# Monolithic Integration of Barium Titanate on Silicon for High-Speed and Power-Efficient Optical Modulator Applications

Min-Hsiang Hsu

Promotoren: prof. dr. ir. D. Van Thourhout, dr. C. Merckling
Proefschrift ingediend tot het behalen van de graad van
Doctor in de ingenieurswetenschappen: fotonica

UNIVERSITEIT
GENT

Vakgroep Informatietechnologie
Voorzitter: prof. dr. ir. B. Dhoedt
Faculteit Ingenieurswetenschappen en Architectuur
Academiejaar 2016 - 2017

ISBN 978-94-6355-027-7
NUR 959, 965
Wettelijk depot: D/2017/10.500/62

Universiteit Gent
Faculteit Ingenieurswetenschappen en Architectuur
Vakgroep Informatietechnologie

**Promotoren**: prof. dr. ir. Dries Van Thourhout,
dr. Clement Merckling

## Examencommissie:

| | |
|---|---|
| prof. dr. ir. Daniël De Zutter (voorzitter) | Universiteit Gent, |
| prof. dr. ir. Dries Van Thourhout (promotor) | Universiteit Gent |
| dr. Clement Merckling (promotor) | imec, Leuven |
| prof. dr. ir. Roel Baet (secretaris) | Universiteit Gent |
| prof. dr. ir. Jeroen Beeckman | Universiteit Gent |
| prof. dr. ir. Jan Genoe | KU Leuven |
| dr. Jean Fompeyrine | IBM Research Zurich |

Universiteit Gent
Faculteit Ingenieurswetenschappen en Architectuur

Vakgroep Informatietechnologie
Technologiepark-Zwijnaarde 15, B-9052 Gent, België

Tel.: +32-9-264.33.41
Fax.: +32-9-331.35.93

Dit werk kwam tot stand in het kader van het imec Optical IO programma.

Proefschrift tot het bekomen van de graad van
Doctor in de ingenieurswetenschappen: fotonica
Academiejaar 2016-2017

# Dankwoord

The 4-year PhD training made me become a stronger and mature person. Looking back on the past several years, I received so many supports from different people between the application and completion of my PhD. I'd like to use the section to express my gratitude briefly.

First, I'd like to thank my promotor, Prof. Dr. Dries Van Thourhout. I appreciate his guidance and valuable feedback during the period. I feel so blessed to be his student. Thanks to his tremendous support and patience, I could finish my PhD in a good manner and in time. Although I was not working at Gent University, I knew whenever or wherever I need him, he would always help me.

Dr. Clement Merckling deserves my special thank. He led me to the Epitaxy wonderland and takes care of me on a daily base in imec. During my PhD, I appreciate the freedom and flexibility that he provided with me. This helped me to become a truly independent thinker and problem solver not only in research but also in my daily life. I enjoy every single moment working, chatting and even having fun with him.

Then, I'm grateful to my PhD examination committee members: Prof. Dr. Daniël De Zutter (Universiteit Gent), Prof. Dr. Roel Baet (Universiteit Gent), Prof. Dr. Jeroen Beeckman (Universiteit Gent), Prof. Dr. Jan Genoe (KU Leuven) and Dr. Jean Fompeyrine (IBM Research Zurich). I thank all of them for their endorsement on my PhD work and giving me their valuable feedback to polish this dissertations.

Besides, I thank the whole team of 3D and Optical/IO Technologies in imec, led by Dr. Philippe Absil. I'm pretty thankful for all the resources and assistance that I obtained during 4 years. Without their helps and trust, I can't make all the achievements presented here. Especially, I thank Dr. Joris Van Campenhout, who patiently guided me during the whole period. His knowledge and enthusiasms on research and industry always inspire me to move forward. In addition, Dr. Marianna Pantouvaki is also a very important mentor in my PhD career. I appreciate very much her patience to teach me every detail of process knowledge. For several times, she even worked with me in the lab during her off-hours. No matter how busy she is, she always shows her care both in my research and in my life. Without her guidance and supports, many results here can't be done.

Next, I want to thank Dr. Salim El Kazzi, Hans Costermans and Linda Vanmeerbeek, who are like my family here. During 4 years, I experienced many down time from all aspects of lives. Thanks to their supports and loves, I can get through those difficulties and finish this PhD.

Also I want to thank Kevin Dubois, also a part of MBE team. I will miss all the great time and bad time when we worked on the tool. I appreciate his efforts and cares for our MBE system very much.

In addition, I want to thank the whole team of Materials and Components Analysis in imec. Thanks to their fantastic analysis techniques, I was able to explore my materials and devices very deeply.

Furthermore, I'd like to show my appreciation to the colleagues in Epitaxy team, other PhD students and Taiwanese folks in Leuven. I want to thank them for accompanying me to finish 4 year period.

I'd also like to thank Dr. Aaron Thean, who gave me some encouragement from time to time. His insightful knowledge in both academy and industry broaden my vision to the semiconductor field.

What's more, I'm very thankful to Prof. Dr. Ming-Hwei Hong, who has been my important mentor since I was studying in university. It was him to make me dare to dream big, setting a plan for studying abroad, working and even competing with all the intelligent people around the world. Thanks to his suggestions, I chose imec, having an incredible 4-year period of my life.

A very special thank goes to my wife, Sandy Huang. She is the greatest woman in my life, who is always patient with me, sacrificing herself to fulfill me and taking care of me without asking rewards. My contribution to this work belongs to her and it's she to complete this work and me, myself.

Last but not least, I want to thank my parents, two older sisters and brother-in-law. I'm grateful to them for sacrificing themselves to let me realize the dream. I appreciate their selfless considerations, understandings and supports. Although, during 4 years, we experienced a lot of difficulties, loves make us strong to face those challenges firmly. Also, my dearest grandma from heaven must be very happy for me to obtain this PhD tittle.

There were too many people to list each of them who also played an important role in my PhD studies. Please accept my humble apologies and thank you for your supports during these years. This thesis can't be finished without any of you.

# Table of Contents

**Dankwoord** **i**

**Samenvatting** **vii**

**Summary** **x**

**1 Introduction** **1-1**

1.1 Silicon Photonics Opportunities....1-1
1.2 Silicon Photonics Building Blocks ....1-7
1.3 Novel Si Optical Modulators ....1-11
1.3.1 Carrier Dispersion Effect ....1-11
1.3.2 Electro-Absorptive Effect ....1-13
1.3.3 Pockels Effect ....1-14
1.4 BTO Properties ....1-19
1.5 Integration of Epitaxial BTO and Si(001)....1-22
1.6 Thesis Outline ....1-24
1.7 Publications....1-26
1.7.1 Published SCI Journals ....1-26
1.7.2 SCI Journals under Preparation ....1-26
1.7.3 Publications in International Conferences ....1-26
References....1-28

**2 Molecular Beam Epitaxy & Characterization Methods** **2-1**

2.1 Principle of Epitaxial Growth ....2-1
2.1.1 Kinetics of Atoms on the Sample Surface ....2-2
2.1.2 Surface Energy and Growth Modes....2-3
2.2 Molecular Beam Epitaxy ....2-4
2.2.1 MBE Cluster System ....2-5
2.3 Reflection High Energy Electron Diffraction ....2-7
2.4 X-Ray Diffraction ....2-9
2.5 Spectroscopic Ellipsometry....2-12
2.6 Scanning Probe Microscopy ....2-13
2.6.1 Atomic Force Microscopy ....2-13
2.6.2 Conductive Atomic Force Microscopy ....2-14
2.6.3 Piezo-response Force Microscopy ....2-15
2.7 Transmission Electron Microscopy....2-15
2.8 X-ray Photoelectron Spectroscopy....2-16

2.9 Rutherford Backscattering Spectroscopy .....2-18
2.10 Conclusion .....2-18
References .....2-19

**3 Calibration of BTO Stoichiometry 3-1**

3.1 Methodology for Growing Epitaxial BTO on Ge(001) .....3-2
3.2 BTO Crystal Structure on Ge(001) .....3-6
3.2.1 BTO RHEED Analysis .....3-6
3.2.2 XRD Analysis .....3-7
3.2.3 TEM Analysis .....3-11
3.3 Stoichiometry-Dependent Diffraction Phenomenon .....3-12
3.4 Conclusion .....3-16
References .....3-18

**4 Effects of Process Conditions on BTO 4-1**

4.1 Experiments .....4-2
4.2 BTO Crystallinity Optimization .....4-4
4.2.1 Growth Temperature Effect .....4-4
4.2.2 Oxygen Plasma Power Effects .....4-8
4.3 Post-Process Annealing Effect .....4-11
4.3.1 TEM Analysis of Crystal Structure .....4-11
4.3.2 Post-Growth Annealing Effects on Polarization Switching ...4-15
4.4 Conclusion .....4-19
References .....4-21

**5 Understandings of BTO Domains 5-1**

5.1 Si-Integrated Waveguides Using Different BTO Orientations and Electrode Designs .....5-2
5.2 Controlled BTO Orientation by Thickness Engineering .....5-4
5.2.1 Thickness Effects on Epitaxial STO on Si(001) .....5-4
5.2.2 Thickness Effects on BTO/5nm STO/Si(001) .....5-7
5.2.3 STO Thickness Effects on BTO/STO/Si(001) .....5-10
5.2.4 Summary .....5-11
5.3 Orientation-Dependent EO Response Studied By Spectroscopic Ellipsometry .....5-12
5.3.1 Crystal Structures and Domain Orientations .....5-12
5.3.2 Electrical Properties .....5-15
5.3.3 EO Characterization Using Spectroscopic Ellipsometry .....5-16
5.3.4 EO Comparison of c-Oriented & a-Oriented BTO .....5-18

5.3.5 Summary.....5-20
References.....5-22

**6 Optimizing BTO Domain Dynamics for Hybrid BTO/Si Modulators 6-1**

6.1. Generalized EO Models for Multi-Domain a-Oriented BTO.....6-1
6.2. Fabrication Process Comparisons for Hybrid BTO/Si Optical Components .....6-3
6.3. Characteristics of Hybrid BTO/Si Passive Waveguides on the Patterned SOI .....6-5
6.4 Annealing Effect .....6-8
6.5 Linear EO Modulation in Hybrid BTO/Si Mach-Zehnder-Ring Modulators .....6-13
6.5.1 Different Bias-Sweeping Measurements .....6-16
6.5.2 Hysteresis Mechanisms.....6-18
6.5.3 Further Discussions: Polarization Stability.....6-23
6.5.4 Further Discussions: Percentage of Poled Domain Area .....6-26
6.5.5 Further Discussions: Mach-Zehnder Modulator or Ring? .....6-27
6.6 Benchmarks of the Performance for the Hybrid BTO/Si Optical Components .....6-28
6.7 Conclusion .....6-30
References.....6-31

**7 Conclusions and Perspectives 7-1**

7.1. Conclusions.....7-1
7.2. Perspectives .....7-4
7.2.1 BTO Thin Film Preparation.....7-4
7.2.2 Hysteresis Mechanisms.....7-4
References.....7-6

**Appendix A EO Response in Single-Domain BTO/Si Hybrid Waveguides**

A.1. EO Effect in BTO.....A-1
A.2. c-Oriented BTO/Si Hybrid Waveguides Using Vertical Electrodes..A-2
A.3. c-Oriented BTO/Si Hybrid Waveguides Using In-Plane Electrodes .A-3
A.4. a-Oriented BTO/Si Hybrid Waveguides Using Vertical Electrodes..A-4
A.5. a-Oriented BTO/Si Hybrid Waveguides Using In-Plane Electrodes .A-5
References.....A-7

# Samenvatting

Vanwege de centro-symmetrisch kristalstructuur vertoont silicium geen lineair elektro-optisch effect (ook Pockels effect genoemd). Een rechttoe-rechtaan methode om dit op te lossen bestaat erin een materiaal dat wel een Pockels effect vertoont monolithisch te integreren met silicium. Ferro-elektrische oxides die een sterke polarisatie vertonen zijn zo'n materialen. Daarom was er recent veel interesse in de integratie van deze ferro-elektrische oxides met silicium voor de realisatie van optische modulatoren. Van de vele mogelijke ferro-elektrische oxides is $BaTiO_3$ (BTO) in het bijzonder veelbelovend. BTO vertoont een van de meest uitgesproken Pockels coëfficiënten, > 1000 pm/V. Bovendien is BTO intrinsiek compatibel met modulatie aan hoge snelheid. Maar bovenal is het mogelijk om hoogwaardige epitaxiale BTO lagen op standaard (001) silicium substraten te integreren, ook al hebben beide materialen een heel verschillende kristalstructuur en heel verschillende chemische eigenschappen.

Om dunne filmen van BTO op silicium te integreren wordt een MBE-process gebruikt (molecular beam epitaxy). In de MBE-reactor wordt het substraat voorbereidt, en worden dan een submonolaag template-laag en een $SrTiO_3$ (STO) bufferlaag gegroeid. Het bereiken van de juiste stoichiometrie bij het groeien van de eigenlijke BTO-laag op deze STO bufferlaag is dan een van de grootste uitdagingen. Om dit probleem te vereenvoudigen, wordt eerst een germanium-substraat, dat quasi geen verschil in roosterconstante vertoont met BTO, gebruikt voor de kalibratie van de BTO-stoichiometrie. Daarbij wordt beroep gedaan op verschillende diffractietechnieken waaronder "reflection high-energy electron diffraction" (RHEED), "X-ray diffraction" (XRD) en "selected-area electron diffraction" (SAED) in transmissie elektronen microscopy (TEM). De exacte Ba en Ti compositie in de BTO laag wordt gemeten met Rutherford backscattering spectroscopy (RBS). Vermits Ba en Ti atomen een verschillend aantal elektronen hebben, diffracteren lagen met verschillende stoichometrie de elektronenbundel op een verschillende manier. Op basis van de resultaten bekomen met de hierboven vermelde experimentele technieken konden we besluiten dat de stoichiometrie van de lagen een duidelijke invloed heeft op de 3 laagste-orde Bragg pieken $(001)_{BTO}$, $(101)_{BTO}$ en $(111)_{BTO}$. Om deze observaties te verklaren stellen we een model voor dat op basis van diffractietheorie verklaart hoe extra [Ba] of [Ti] in de laag het diffractiepatroon beïnvloed. Belangrijk is dat deze studie veralgemeend kan worden naar andere types perovskieten van het type $ABO_3$, wat het mogelijk maakt ook hun stoichiometrie efficiënt te kalibreren, op een efficiënte en niet-destructieve manier, gebruikmaken van XRD en in-situ RHEED tijdens de dunne-film synthese.

Eens de stoichiometrie van de BTO lagen onder controle is worden 20 nm dikke stoichiometrische BTO lagen gegroeid op een p-type substraat, gebruikmakend van een 10 nm dikke STO bufferlaag. Vervolgens worden, gebruik makend van XRD, de procesparameters zoals temperatuur, vermogen van het zuurstofplasma en temperatuur van het postgroei annealproces geoptimaliseerd, met als doel een c-georiënteerde BTO laag te bekomen. Alhoewel inderdaad kristallijne BTO lagen worden bekomen, zorgt de thermische instabiliteit ter hoogte van de interface tussen de STO laag en het Si(001) substraat ervoor dat een 3 nm dik amorf silicaat gevormd wordt. Voor optische modulator toepassingen is het van belang dat een sterk veld kan worden opgebouwd in de BTO laag. Een hoge lekstroom is dan ook niet gewenst. Om het elektrisch gedrag te begrijpen wordt een analyse op basis van ”conductive atomic force microscopy” (CAFM) uitgevoerd. Ondanks het 3 nm dikke silicaat, bepaald de bandalignering tussen de BTO en STO lagen het elektrisch gedrag. Bij een voorwaartse spanning tot 4 Volt blijft de lekstroom laag maar een achterwaartse spanning leidt onmiddellijk tot hoge lekstromen. Na een annealprocess wordt echter zowel bij voorwaartse als achterwaartse spanning een lage lekstroom gemeten. Volgend op dit annealproces (in een zuurstofatmosfeer) kan poling en schakelen van de BTO domeinen worden bekomen. Volgend op deze procesoptimalisatie wordt een systematisch onderzoek uitgevoerd om beter te begrijpen hoe de BTO domeinoriëntatie kan worden gecontroleerd door een correcte keuze van de diktes van de BTO en STO lagen. Analyse van de kristalstructuur als functie van de laagdikte toont dat de BTO domeinoriëntatie verandert van c-type naar a-type als ofwel de dikte van de BTO-laag ofwel de dikte van de STO bufferlaag toeneemt. Dit biedt verschillende mogelijkheden voor het bekomen van een gewenste BTO domeinoriëntatie, afhankelijk van de specifieke applicatie.

Vervolgens bespreken we de invloed van de BTO domeinoriëntatie op het elektro-optisch gedrag. Ellipsometrie wordt gebruikt om het elektro-optisch effect van 100nm dikke c- en a-georiënteerde lagen gegroeid op respectievelijk een 40nm en 10nm dikke STO bufferlaag te onderzoeken. Daarnaast, gebaseerd op een eerder gepubliceerd model, wordt het gebruik van c- en a-georiënteerd BTO voor de realisatie van optische modulatoren samengevat. Daarbij worden verschillende elektrodeconfiguraties en zowel TE als TM polarisatie beschouwd.

Om een hybride BTO/Si modulator te realiseren wordt een 170 nm dikke BTO laag gegroeid op SOI substraten met optische golfgeleiders gefabriceerd in imec’s 200mm platform. Gezien de patronen in het SOI-substraat resulteren in temperatuurs niet-uniformiteit bevat de BTO laag echter defecten en slagen we er niet in licht door de golfgeleiders te geleiden Daarom wordt een annealstap uitgevoerd die het verlies reduceert tot 85dB/cm. Het effect van deze stap op de kristalstructuur wordt ook onderzocht.

Finaal wordt het elektro-optisch effect van BTO geïntegreerd met een Mach-Zehnder-Ring interferometer onderzocht. BTO vertoont een intrinsiek hysteresis gedrag, gezien zijn bias-afhankelijke domein-dynamiek. Om deze hysteresis te vermijden is een stabiele polarisatie van de domeinen vereist. Dat kan verwezenlijkt worden door het toevoegen van een polarisatiestap, het aanleggen van een voldoende hoge spanning, voor de meting. Toepassen van deze aanpak toont dat de hybride BTO/Si MZR modulator (Mach-Zehnder interferometer met een ring in een van beide armen) een lineair EO-effect vertoont, met een gemiddelde Pockels constante $r_{eff}$ ~ 185 pm/V (c.f. 30 pm/V in LNO). De daarmee corresponderende $V_{\pi}L$ is ~1.6 Vcm. Om de domaindynamica in het vlak te visualiseren wordt ook een piezo-force microscopie-experiment uitgevoerd. Zowel polarisatie als schakelen van de domeinen in het vlak wordt geobserveerd met deze techniek. Dit is consistent met de optische metingen uitgevoerd op de MZR componenten. Samenvattend, alhoewel het propagatieverlies in onze hybride BTO/Si golfgeleiders 85 dB/cm is, een grootteorde hoger dan de 6 dB/cm die eerder in de literatuur werd gerapporteerd, zijn de effectieve elektro-optische constante $r_{eff}$ and $V_{\pi}L$ bekomen in ons werk wel competitief met andere resultaten.

# English Abstract

Given its centro-symmetric crystal structure, Si exhibits no linear electro-optical (EO) effect, also known as the Pockels effect. An intuitive approach to overcome this is via the monolithic integration of silicon with a Pockels material. Ferroelectric oxides, which exhibit a strong spontaneous polarization, show the desired strong EO performance. Therefore, the integration of Si with those ferroelectric oxides for optical modulator applications has attracted considerable research interest. Among various ferroelectric oxides, $BaTiO_3$ (BTO) is a promising candidate given several reasons. Bulk BTO material shows one of the most pronounced Pockels coefficients, > 1000 pm/V. Also, BTO naturally allows high-speed optical modulation. Most of all, it is feasible to obtain high-quality integration of epitaxial BTO thin films with Si(001) substrates although they have greatly different crystal structure and chemical properties.

To facilitate the monolithic integration on Si of BTO thin films, molecular beam epitaxy is used to prepare the Si surface, a submonolayer crystal template and a high quality $SrTiO_3$ (STO) buffer layer. Even so, achieving the correct BTO stoichiometry is the main challenge for thin film preparation. To simplify the problem, a Ge substrate, with a quasi-zero lattice mismatch with respect to BTO, is used for the calibration of the stoichiometry by various diffraction techniques, including reflection high-energy electron diffraction (RHEED), X-ray diffraction (XRD) and selected-area electron diffraction (SAED) in transmission electron microscopy (TEM). The exact Ba and Ti compositions in the BTO layer are measured by Rutherford backscattering spectroscopy (RBS). Since Ba and Ti atoms possess a different number of electrons, the diffractive behavior observed using the above mentioned techniques is stoichiometry-dependent and can be observed through the 3 lowest-order Bragg peaks: $(001)_{BTO}$, $(101)_{BTO}$ and $(111)_{BTO}$. To explain the observations, we propose a model based on diffraction theory explaining how excess [Ba] or [Ti] in the layer influences the diffraction response. This study can be generalized to other types of perovskite oxides of the type $ABO_3$, facilitating the calibration of their stoichiometry by efficient and non-destructive XRD and in-situ RHEED during the thin film synthesis.

Thanks to the calibration of the stoichiometry using diffraction techniques as described above, 20-nm-thick stoichiometric BTO layers grown on a p-type Si(001) substrate using a 10-nm-thick STO buffer can be obtained. Then, performing a series of XRD characterizations, the different process conditions such as growth temperature and oxygen plasma power are optimized to achieve a BTO layer with optimal c-oriented domains. Although the BTO crystallinity is indeed optimized, the thermal instability at the interface between STO and Si(001)

leads to the formation of a 3-nm-thick amorphous silicate. For optical modulator applications, it is important to build up a strong electric field within the BTO layer. Therefore, a high leakage current in the BTO/STO/silicate/p-type Si heterostructure is unfavorable. To understand the electrical properties, a conductive atomic force microscopy (CAFM) analysis is carried out. Despite the 3 nm silicate in the as-deposited sample, the band offsets between BTO and STO govern the current behavior: A forward bias up to 4 V still results in a low current but a reverse bias directly results in a breakdown of the device. After post-process annealing under an oxygen ambient, the amorphous silicate thickens and influences the electrical properties of the heterostructure. Because of the wide energy barriers created by the silicate, a low current is now obtained for both bias directions, enabling to generate strong electric fields with different directions in the BTO layer. Following this treatment, via piezo-response force microscopy (PFM), now poling and switching of the BTO domains can be achieved in both bias directions. In addition, improvement of the polarization stability in the BTO layer after the oxygen annealing process is also observed.

In practice, the device performance is highly dependent on the BTO domain orientation and the relationship between the BTO domain orientation and the applied electric field. After the process optimization, a systematic investigation is performed to understand how to control the BTO domain orientation through engineering the thickness of the BTO layer and the STO buffer. The BTO orientation is determined by the trade-off between compressive strain from the BTO/STO lattice mismatch and tensile strain from the BTO/Si thermal expansion difference. Analysis of the crystal as function of the layer thickness shows that the BTO orientation changes from c-oriented to a-oriented as the BTO film thickness increases or as the thickness of the underlying STO buffer decreases. This offers different possibilities for obtaining a given BTO orientation as desired for a specific device application.

Then, the effects of BTO domain orientation on the EO behavior is discussed. Ellipsometry is used to compare the EO effect in 100-nm-thick c-oriented and a-oriented BTO grown on Si(001) substrates using a 40 nm and 10 nm STO buffer respectively. In addition, the use of c-oriented and a-oriented BTO for optical modulators employing various electrode configurations with TE- and TM-polarized light are summarized. Since $r_{51}$, $r_{31}$ and $r_{33}$ in the Pockels tensor are all exploited, a-oriented BTO using in-plane electrodes for both TE and TM modulation was found to be the optimal scheme.

For that reason, to realize hybrid BTO/Si optical components, a 170 nm a-oriented BTO layer is grown directly on patterned SOI substrates with c-Si optical waveguides fabricated in imec’s 200mm silicon photonics platform. However, since the patterns on the substrate result in a temperature non-uniformity, the BTO layer is defective and no light is transmitted through the hybrid Si-BTO

waveguide. Therefore, a post-growth oxygen annealing at 800 $^{o}$C is performed, which improves the TE-polarized light propagation loss down to 85 dB/cm. However, the TM-polarized light through the waveguide is still not detectable. In addition, the impact of such annealing process on the crystal structure is investigated relying on XRD and TEM characterizations. Consistent with what is observed for BTO grown on blanket Si(001), the silicate interfacial layer is thickened because of the high-temperature annealing process, which also turns the material from amorphous in a polycrystalline form. Moreover, the amelioration of BTO crystallinity from the oxygen annealing is also observed.

Finally, a study of the BTO EO behavior for TE-polarized light in a Mach-Zehnder-Ring (MZR) modulator is carried out. Ferroelectric BTO exhibits an intrinsic hysteresis behavior due to its bias-dependent domain dynamics. To avoid this hysteresis, a stable polarization is needed and can be obtained by adding a domain poling step before an EO-measurement. Applying this approach shows the hybrid BTO/Si MZR modulators exhibit a linear EO effect, showing an average $r_{eff}$ around 185 pm/V (c.f. 30 pm/V in LNO). The corresponding $V_{\pi}L$ is evaluated to be ~1.6 Vcm. To observe the dynamics of 90$^{o}$-type BTO domains, in-plane PFM on a TEM lamella is also executed. Both poling and switching for in-plane domains are seen by PFM, consistent with the observations in MZR devices. In brief, although the propagation loss in our hybrid BTO/Si waveguides is 85 dB/cm, one order higher than the state-of-the-art result of 6 dB/cm, $r_{eff}$ and $V_{\pi}L$ as obtained in our work are competitive with other key works.

# 1

# Introduction

This chapter gives an overview of silicon photonics opportunities in different interconnect applications, from telecommunications to intra-chip I/O. Then, a brief introduction to the building blocks of a silicon photonics platform is presented. The development of high-speed and power-efficient modulators is reviewed, in particular for Si-based optical modulators. Because $BaTiO_3$ (BTO) possesses one of the most pronounced Pockels effects, a hybrid BTO/Si optical modulator offers an alternative method to introduce pure phase modulation in Si. Therefore, some material properties of BTO and different approaches for BTO integration with Si are given. Finally, the chapter concludes with the outline of this thesis.

## 1.1 Silicon Photonics Opportunities

Over the past 50 years, following Moore's Law for CMOS technology enabled a consistent progress in the state-of-the-art manufacturing process [1]. However, for sub-20-nm technologies, the scaling of CMOS transistors encounters serious challenges in all aspects of the density, performance, and cost [2]. Therefore, several changes in technology, such as strained silicon, high-K/metal gates, multi-gate transistors, integration of germanium and III-V compound semiconductors, and even new lithography technology have been introduced to keep up with Moore's Law. Although transistor dimensions can consistently be scaled down and the number of transistors still soars up, the clock

frequency in integrated circuit (IC) systems where billions of transistors are embedded has already reached its ceiling, as shown in Figure 1.1 [3]. In fact, improvements to the clock frequency of nano-scaled ICs are limited by the parasitic loading in the copper-based wiring and high power consumption [4].

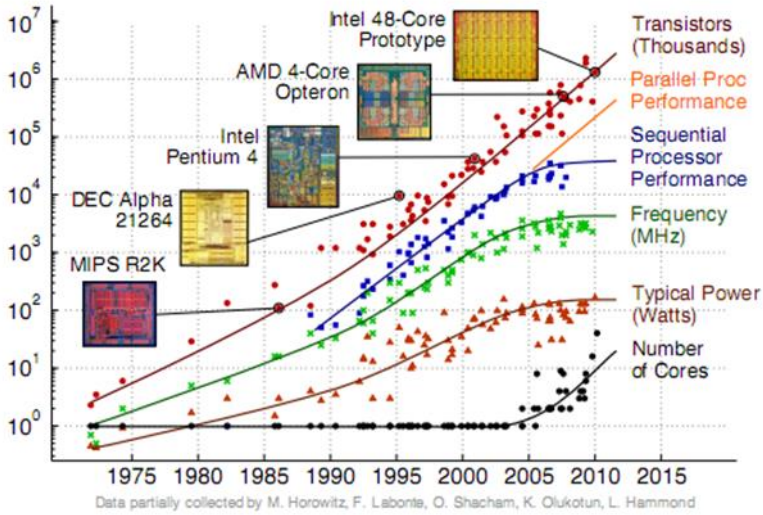


**Figure 1.1:** Illustration of increases in the numbers of transistors following Moore's law, and corresponding evolutions of the clock-rate and performance. The figure is reproduced from the ref [3].

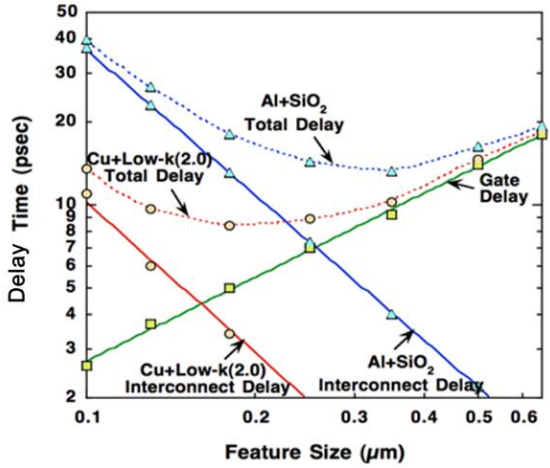


**Figure 1.2:** Delay time as a function of the feature size of the gate length in transistors using copper/low-k(2.0) and Al/$SiO_2$. The figure is reproduced from the ref. [5].

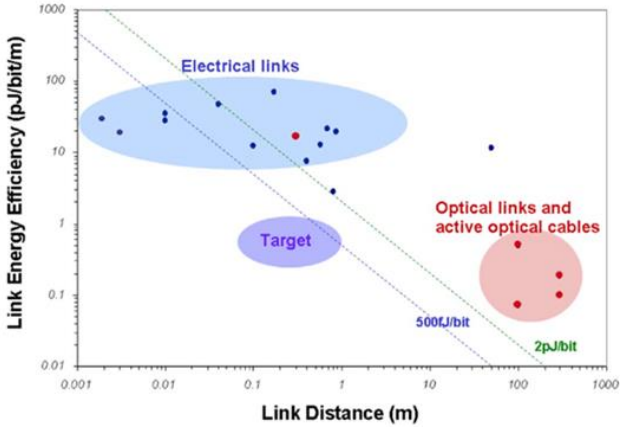


**Figure 1.3:** Energy per bit per meter versus the maximum reach of the link. The figure is reproduced from the ref [7].

As shown in Figure 1-2, when interconnect features of the copper and low-k materials shrink, the delay time, which is calculated as the product (RC) of the resistance (R) and capacitance (C), increases because of increasing resistance in the copper wire [5,6]. Additionally, Figure 1-3 shows the soaring power consumption for denser chips in these systems [7]. Furthermore, a fundamental limit for the bandwidth of electrical wires is given by the formula [8]:

$$B \sim B_0 \frac{A}{L^2} \qquad (1.1)$$

where B is the bandwidth for the electric interconnects; $B_0$ varies from $10^{15}$ to $10^{18}$ b/s, depending on the type of interconnect; and A and L are the cross-sectional area of the electrical wire and the length, respectively. It can be clearly seen that the bandwidth in the electrical interconnects is not enhanced by the smaller cross-section dimensions. These natural limitations for electrical interconnects drive the development of many-core processors which exploit parallelism to obtain an enhancement of processor performance as can be seen in Figure 1.1, whereby each core inside operates at low speed to keep the power consumption low. Although the overall data bandwidth within a processor is still enhanced, some performance is actually sacrificed. To overcome the limitations in electrical interconnects, new initiatives, such as heterogeneous 2-D/3-D IC integration [9], radio frequency [10], and optical interconnects [11] have been pursued to achieve the exponential growth in the demand for high link capacity for intra- and inter-chip interconnections. Among several alternative technologies, optical interconnects show great potential as next-generation interconnects, as reflected in the high data rates achieved over different distances, ranging from millimeters to kilometers, with scalability, low latency, and low energy consumption per bit [7].

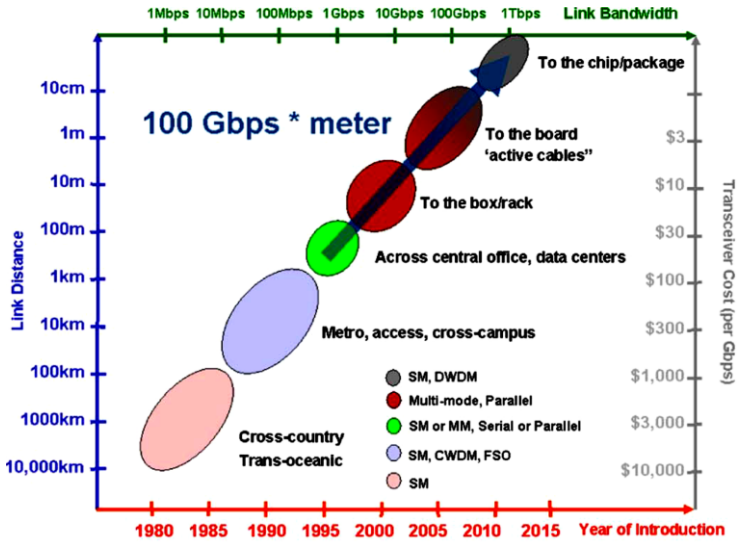


**Figure 1.4:** Chronological roadmap for the introduction of optical interconnects in digital systems, describing the link distance versus link bandwidth and cost. The figure is reproduced from the ref. [7].

According to their reach, interconnects can be classified into different system levels, from several kilometers for a wide area network (WAN), several tens or hundreds of meters for a local area network (LAN), several meters for rack-to-rack or card-to-card interconnects in a cluster, hundreds of millimeter for a multiple-chip module (MCM), to a few millimeters for inter-chip or intra-chip interconnects. Figure 1-4 shows the historical roadmap for digital systems moving toward optical interconnect technology [7]. This figure comprehensively shows that the time for introducing optical interconnects depends on three factors: data bandwidth, reach distance, and cost. A compromise with respect to these three factors brings about a bandwidth-distance product of 100 Gb/s-m as the most favorable point of introducing optical systems.

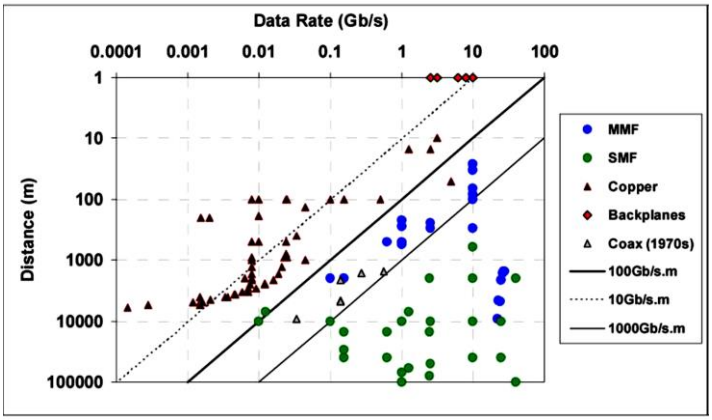


**Figure 1.5:** Data rate versus distance for commercial electrical versus optical links. The figure is reproduced from the ref. [7].

Comparing copper electrical interconnects and optical interconnects with either single-mode fibers or multi-mode fibers in Figure 1-5, systems with bandwidth-distance product beyond 1000 Gb/s-m are based on single-mode fibers, those between 100 Gb/s-m and 1000 Gb/s-m are based on multi-mode fibers, and those below 100 Gb/s-m are based on copper-based electrical interconnects [7]. According to the trend in Figure 1-5, currently, interconnects that use single-mode optical fibers for LAN and WAN with several kilometers of reach distance for telecommunication systems have been deployed. Datacenters primarily deploy optical interconnects for data communications. Today, the most cost-effective solution for data communications in datacenters is to use Vertical-Cavity Surface-Emitting Lasers (VCSEL)-based transceivers with multi-mode fibers. However, because of the dispersion issue in the multi-mode fibers, the transmission rate needs to be optimized with respect to reach distance. For example, OM3 fibers can transmit data over 300 m at 10 Gb/s, while they can transmit data over 70 m at 25 Gb/s. For this reason, to achieve high data capacity, it is necessary to deploy multi-mode fiber ribbons with lower speed to maintain sufficiently long reach distance. However, multi-mode fibers would not be practical for providing bandwidths as high as 1 Tb/s over 300 m, for example. In this case, 100 pairs of fibers are required, bringing about different challenges: installation of large numbers of fibers on the limited area of line-card boards and significantly higher costs. With these limitations for VCSEL technology, revolutionary solutions taking advantage of wavelength division multiplexers (WDM) in single-mode fibers, such as using silicon photonics, are being actively pursued to increase the transmission bit rate while also extending the reach [12]. For chip-scale interconnects, the power consumption of the optical links needs to be extremely

low, less than one pico-joule per bit. Emerging silicon photonics technology is a promising candidate to achieve low-power optical devices, combining with energy-efficient CMOS drivers and amplifiers by both hybrid electronic–photonics integration and monolithic integration [13, 14]. Chip-scale interconnects also require high capacity. Combining a mode-locked III-V laser source, tunable micro-ring, and tunable detectors with WDM or using the previously mentioned components with advanced modulation formats, the aggregated data rate can be increased by using many wavelength channels. Therefore, for on-chip applications, a silicon photonics chip can be assembled with CMOS interface ICs, a processor, stacked memory chips, and a III-V laser by heterogeneous integration technology to provide switching and processing capacity up to 100 Tb/s in a compact module, as illustrated in Figure 1-6 [15].

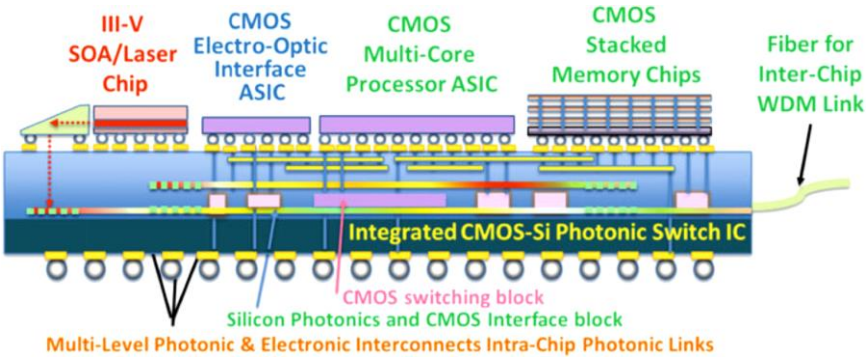


**Figure 1.6:** Schematic diagram of a possible compact terabit silicon photonics integrated circuit assembled with CMOS interface ICs, processor, stacked memory chips and III-V laser by heterogeneous integration technology. The figure is reproduced from the ref. [15].

## 1.2 Silicon Photonics Building Blocks

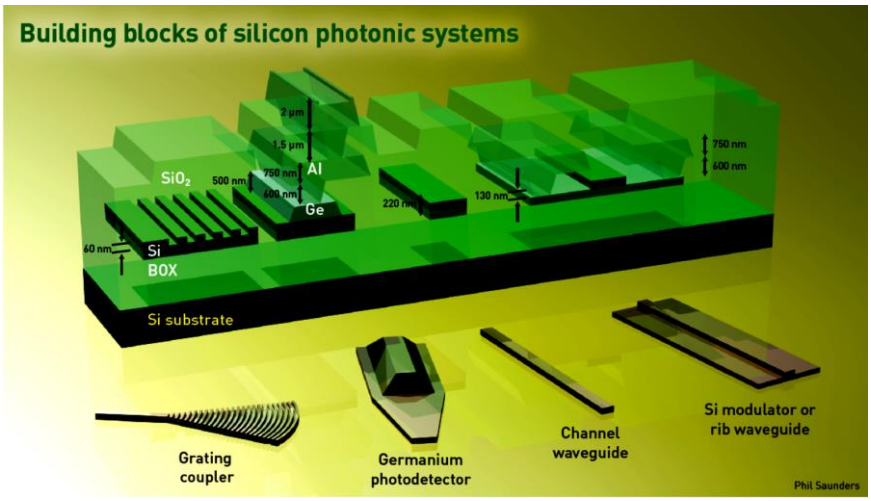


**Figure 1.7:** Schematic for building blocks of silicon photonic systems. The figure is reproduced from the ref. [16].

Typical silicon photonics circuits are composed of several basic building blocks, as shown in Figure 1-7 [16]. For passive components, there are waveguides, couplers, and filters. For active devices, there are lasers, modulators, and photodetectors. Additionally, silicon photonics circuits could include electronic circuitry to realize electrical-to-optical (EO) and optical-to-electrical (OE) signal transitions. A simplified optical link is composed of the transmitter and receiver chips. We are going to take the 4x12.5 Gb/s transmitter and receiver chips in Figure 1.8 as an example to explain the operation steps as follows [17]:

- 4 lasers are pumped electrically and emit O-band (1260 nm to 1360 nm), C-band (1530 nm to 1565 nm) or L-band (1565 nm to 1625 nm) radiation.
- The output light from the laser in each channel is coupled in waveguides, which have a high refractive index in the core region to confine the light.
- Modulators are used to encode the light with the 12.5 Gb/s speed of the electric signal by intensity or phase or polarization modulation in each channel.
- Encoded light from each channel is combined with the multiplexer, and is coupled to the fiber by couplers.
- When light carrying the signals are arriving at the receiver, the demultiplexer separates the light to 4 channels.
- Photodetectors are then used to decode the optical signal with 12.5 Gb/s back to an electric signal for further processing.

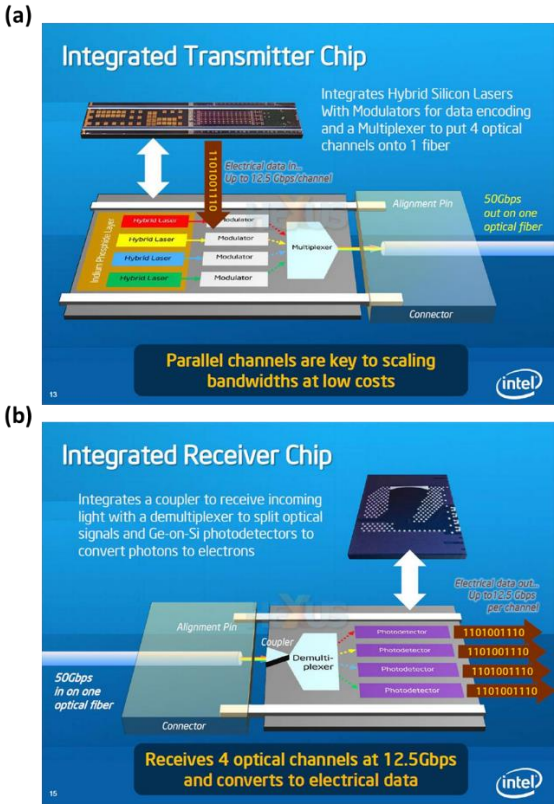


**Figure 1.8:** Schematic for 50 Gb/s transmitter and receiver chips from Intel. The figure is reproduced from the ref. [17].

Because of its transparency in the telecommunication wavelength range and high refractive index, silicon is an ideal material for passive devices such as waveguides, filters, resonators, and gratings. The high index contrast between the Si core (n=3.47) and the $SiO_2$ cladding (n=1.44) results in a highly confined waveguide, enabling components with small footprints. Figure 1.9 describes the effect of the index contrast between the core and cladding on the bending radius [18]. This allows the fabrication of high-density chips on wafers. However, for active (electrically-driven) components, such as photodetectors, lasers, and optical modulators, Si also has some limitations, which will be discussed later.

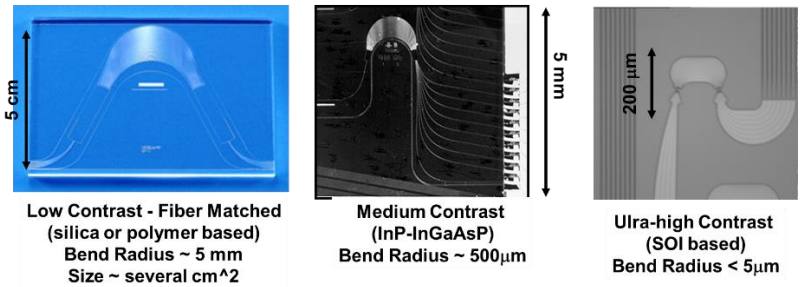


**Figure 1.9:** The effect of the index contrast between the core and cladding on the bending radius. The figure is reproduced from the ref. [18].

For photodetector applications, Si is not a suitable material because it has very poor light absorption for wavelengths beyond 1100 nm. Therefore, III–V-based materials, primarily used in telecommunications, can also be option. The hybrid integration of III–V materials on Si allows the fabrication of high-speed and efficient photodetectors. However, the integration via wafer-bonding or epitaxy techniques makes this approach unfavorable because it is not cost-effective. Thus, it would be more desirable to find another solution to use CMOS technology to reduce costs and allow monolithic integration with Si. The hetero-epitaxy of Ge on Si offers a solution that is simple, low-cost, and fully compatible with CMOS processes [19]. In addition, Ge grown on silicon has a strong absorption up to approximately 1600 nm. Thus, it can be considered an ideal material for infrared optical detection. However, a lattice mismatch of more than 4% makes the integration of Ge on Si challenging. Currently, Ge photodetectors show a bandwidth higher than 50 GHz, a responsivity around 1 A/W, and a dark current below 1 μA [20-24]. Figure 1.10 shows the cross-sectional TEM for Ge epitaxy on Si and the device schematic of the Ge photodetectors [25].

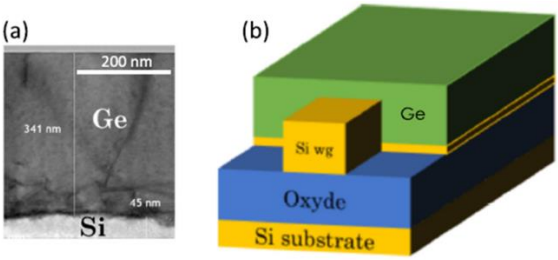


**Figure 1.10:** The cross-sectional TEM for Ge epitaxy on Si and the device schematic of the Ge photodetectors. The figure is reproduced from the ref. [25].

A light source is another key component in optical interconnects and is also the most challenging device to realize. Because its indirect band gap, Si is not an

efficient light emitter either. A method to introduce efficient electrically pumped sources is to utilize III–V gain regions placed directly on silicon [26, 27]. There are three approaches to achieve this [25]. The first is to use III–V chips bonded on silicon and fabricate the laser cavity subsequently. A second approach is the direct epitaxial growth of III–V layers on patterned SOI using buffer layer engineering to prevent dislocations from propagating into the active region. The third method is to take advantage of the first two methods: grow III–V gain material on silicon and then bond it to patterned SOI wafers. The main challenges for the direct growth of III-V on silicon are threading dislocations coming from lattice and thermal mismatches. Figure 1.11(a) shows the schematic of a hybrid Si Fabry–Pérot laser, which is fabricated by using the wafer bonding to transfer the III-V films after patterning Si waveguides [28]. Figure 1.11(b) displays the monolithically integrated InGaAs/InP DFB lasers on Si(001) without the buffer layer using a selective growth process [29]. Other possibilities to achieve light emission in Si are by strain engineering of Si and Ge to obtain a direct bandgap, as shown in Figure 1.11(c) [30], or by Raman effect in Si, as shown in Figure 1.11(d) [31]. However, all of these methods still encounter many challenges in building high-performance lasers. Currently, the main method to obtain the light source in silicon photonics is either to use heterogeneous integration by wafer bonding or to use a hybrid method involving edge or grating-coupling with precise assembly.

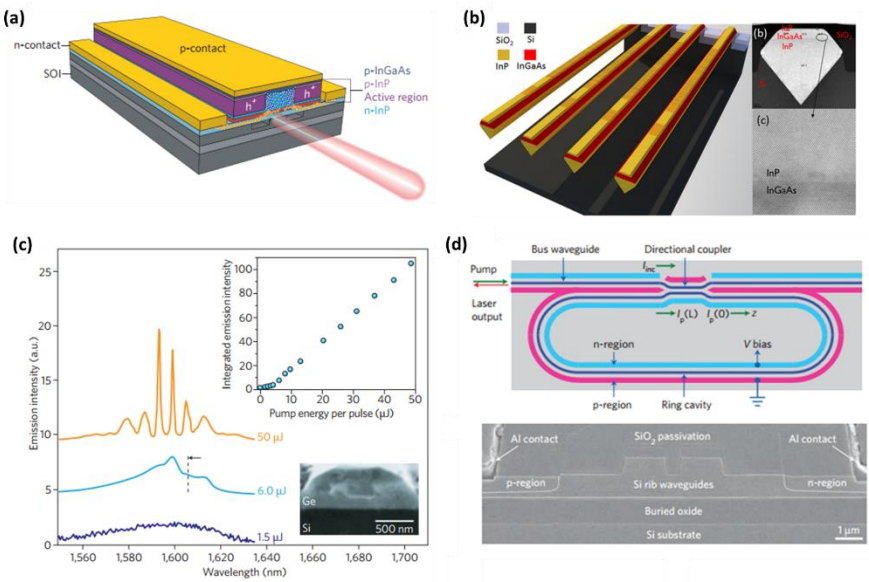


**Figure 1.11:** Different approaches for achieving the laser sources on Si. These figures are reproduced from the ref. [28-31].

The third important class of active optical devices, optical modulators, will be discussed in more detail in the following sections.

# 1.3 Novel Si Optical Modulators

## 1.3.1 Carrier Dispersion Effect

Different from $LiNbO_3$ and III-V materials, Si is not naturally a good candidate for optical modulator applications because of its centro-symmetric crystal lattice and transparency at telecommunication wavelengths. In silicon, light modulation is usually obtained by the free-carrier plasma dispersion effect, as described in Formulas 1.2 and 1.3 [32]:

$$\Delta n = -[8.8\times10^{-22}\Delta N_e + 8.5\times10^{-18}\Delta N_h^{0.8}] \qquad (1.2)$$

$$\Delta\alpha = [8.5\times10^{-18}\Delta N_e + 6.0\times10^{-18}\Delta N_h] \qquad (1.3)$$

A change in carrier concentration of electrons ($\Delta N_e$) or holes ($\Delta N_h$) will lead to a change in the refractive index ($\Delta n$) and absorption ($\Delta\alpha$) of Si. Several Si-based optical modulators using the free-carrier plasma dispersion effect have been demonstrated. According to the mode of operation, they can be categorized as carrier-injection (Figure 1-12), carrier-accumulation (Figure 1-13), or carrier-depletion (Figure 1-14) [33]. For the carrier injection modulator, practically, a p-i-n diode structure is used to manipulate carrier concentration in the path of light propagation. To avoid high optical loss from free carrier absorption, the optical mode is designed within the intrinsic region. Meanwhile, the p- and n-doped regions, as well as the electrodes, are positioned away from the waveguide. However, if the distance between the two electrodes is so far that the resistance is increased, the bandwidth of the modulator will be limited by the product of resistance and capacitance (RC). For this reason, the dimensions and shapes of the modulators need to be optimized. For the carrier injection modulator, the minority carrier lifetime of several nanoseconds for the Si limits the switching speed to approximately 1 GHz. Xu et al. demonstrated 1.5 Gb/s for a ring modulator using the p-i-n structure [34]. Additionally, the authors used a pre-emphasis driving signal to break through the limitations of the minority carrier lifetime, achieving 16 Gb/s in the same device structure [35, 36]. Although Gan et al. showed via simulation that the reduction of the minority carrier lifetime to 10 ps can boost the modulation speed to 24 GHz, it is difficult to engineer the minority carrier lifetime [37]. For this reason, it is necessary to find other modes of operations for Si optical modulators using the free carrier dispersion effect. Instead of using the carrier injection, in 2004, the Intel group took advantage of free carrier accumulation to achieve a modulation speed beyond 1 GHz [38]. Unlike carrier injection modulators, the modulation speed for carrier

accumulation is primarily determined by the RC constant, which is easier to adjust than the minority carrier lifetime. Using the carrier accumulation, a speed of 15 Gb/s is reported in the ring device [39]. Carrier depletion is the other approach to change the optical index, using free carrier dispersion without being limited by the minority carrier lifetime. The light in the carrier depletion modulator interacts with the p-n junction at a reverse bias. When the device is operated, the depletion width and free carrier concentration are varied with the applied bias. To avoid excessive loss resulting from the free carrier absorption, the highly doped regions, which can reduce resistance for the contacts, are required to be placed at the extremities of the waveguide, remaining at a sufficient distance from the light. In addition, according to Formula (1.2), the index change is more sensitive to the hole concentration than to the electron concentration. Thus, in the waveguide region, the p-type region is larger than the n-type region such that more holes can be used during the modulation, as shown in Figure 1.14 [33]. To optimize the modulation speed, it is necessary to carefully design the implantation of carriers and different dimensions of the device, which influence the resistance and capacitance. Recently, a 56-Gb/s ring modulator using carrier depletion has been successfully demonstrated in a 300-mm pilot line by imec [40]. A review can be found here [41]

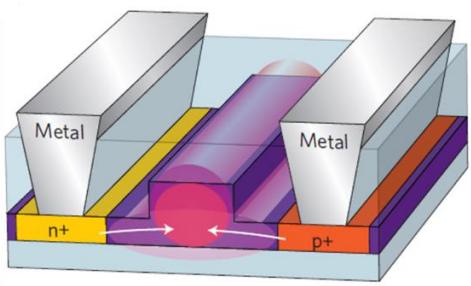


**Figure 1.12:** Cross-section of the device structure implementing the carrier injection mechanism. Highly doped p- and n-regions are separated by an 'intrinsic region' in which the waveguide is formed. Forward-biasing the device causes free electrons and holes to be injected into the 'intrinsic' waveguide region. The figure is reproduced from the ref. [33].

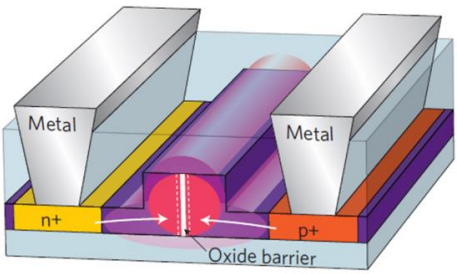

**Figure 1.13:** Cross-section of the device structure implementing the carrier accumulation mechanism. A thin insulating layer of $SiO_2$ is used to isolate two halves of the waveguide to form a capacitor structure. The figure is reproduced from the ref. [33].

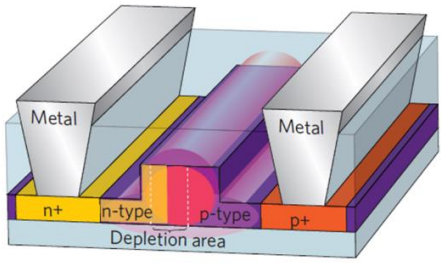


**Figure 1.14:** Cross-section of the device structure implementing the carrier depletion mechanism. Lightly doped p- and n-type regions abut in the waveguide to form a p–n diode. The depletion area of the diode becomes larger with increasing reverse bias voltage. The figure is reproduced from the ref. [33].

### 1.3.2 Electro-Absorptive Effect

An alternative route to achieving high-speed modulation is to introduce other materials with strong electro-optic effects to the silicon platform. According to their modulation mechanism, novel hybrid modulators can be categorized into two groups: electro-absorptive and electro-refractive types. To introduce electro-absorption modulation in transparent Si at O-band and C-band wavelengths, some materials have been successfully integrated with Si and show promising performance. For example, Feng et al. took advantage of the Franz-Keldysh effect to show a frequency of 40.7 GHz for a GeSi electro-absorption modulator monolithically integrated on SOI [42]. Recently, imec demonstrated 56Gb/s non-return-to-the-zero (NRZ) eye diagram at 1565 nm for a 16x GeSi electro-absorption modulator transmitter array [43]. Also, the broad and electrically adjustable optical absorption in graphene makes it an interesting material for electro-absorption modulators. Hu et al. reported the first silicon integrated graphene optical electro-absorption modulator capable of 10 Gb/s modulation speed [44]. For III-V material applications, Tang et al. exploited the quantum confined stark effect in an InAlGaAs quantum well to achieve a frequency of greater than 67 GHz for an electro-absorption modulator monolithically integrated with Si by wafer-bonding [45]. Another promising and novel approach is a plasmonic modulator. The possibility of achieving highly efficient devices that can in turn be operated at a low drive voltage, be compact, and have a reasonable

loss has already been demonstrated; because these are the first results, significant improvements can be expected [46].

### 1.3.3 Pockels Effect

Because of centro-symmetry in the Si crystal, there is no linear electro-optical effect, also known as the Pockels effect. As mentioned before, Si-based photonic integrated circuits have mostly employed carrier dispersion effects to achieve high-speed Si modulators. However, for photonic systems using higher-order modulation schemes, such as quadrature phase shift keying, exploiting the carrier dispersion effect with amplitude modulation leads to sub-optimal performance [47]. Thus, for these applications, it would be more advantageous to employ a pure phase modulator that utilizes the Pockels effect, rather than the carrier dispersion effect, to avoid unbalanced amplitude modulation.

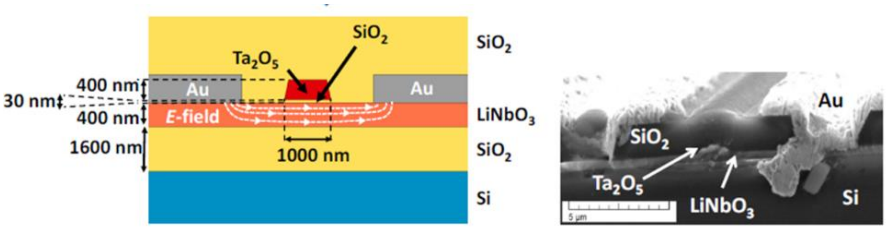


**Figure 1.15:** Schematic of the cross-section of the device structure and a scanning electron microscopy (SEM) image. These figures are reproduced from the ref. [49].

One approach is to deposit silicon nitrides, as a stressor, on Si to break the crystal symmetry and to bring about a Pockels coefficient of approximately 2.2 pm/V [48]. However, the Pockels effect from the silicon nitride stressor is still one order smaller than that of a commercial Pockels material, $LiNbO_3$, which has a value of 33 pm/V in the bulk material [49]. Intuitively, another method to introduce the Pockels effect in Si is to employ wafer bonding to directly transfer the $LiNbO_3$ thin film onto the SOI substrate. Rabiei et al. showed that a $LiNbO_3$ thin film, transferred by wafer bonding onto SOI, has a Pockels coefficient of 30 pm/V, which is comparable to that of the bulk, as shown in Figure 1.15 [49].

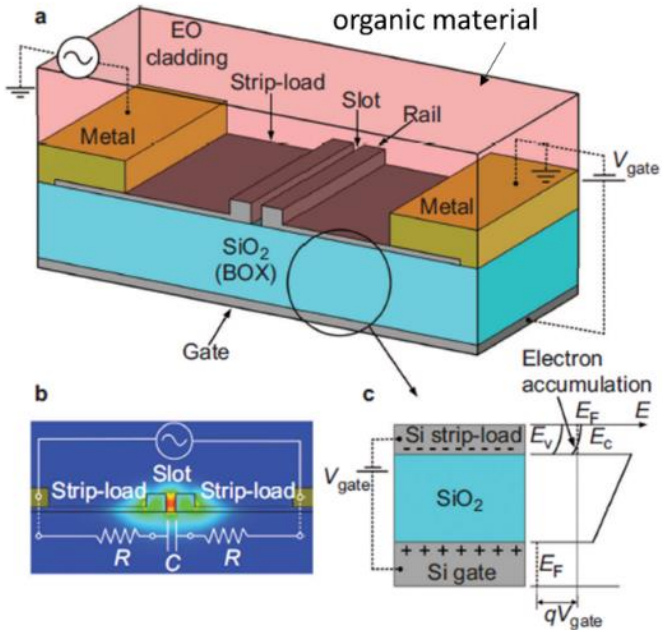


**Figure 1.16:** Schematic of the silicon-organic hybrid optical modulator. These figures are reproduced from the ref. [50, 51].

Additionally, organic ferroelectric thin films also show a strong Pockels effect. Alloatti et al. reported that a silicon-organic hybrid modulator can achieve a modulation speed of 100 GHz and a Pockels coefficient of 180 pm/V, as shown in Figure 1.16 [50, 51].

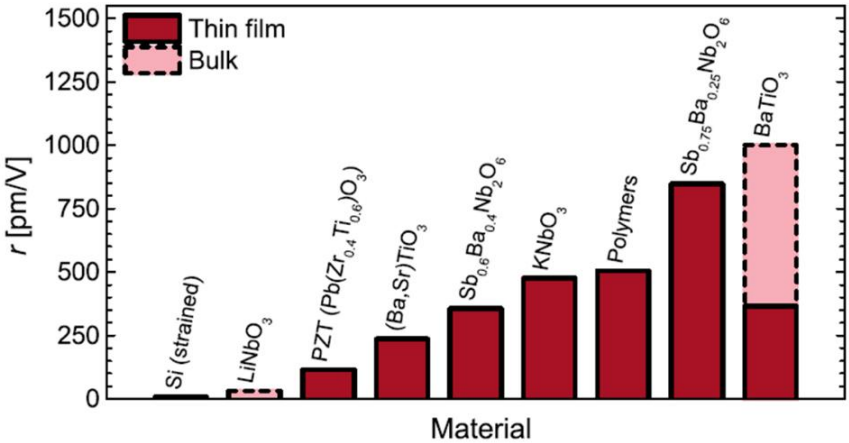


**Figure 1.17:** Comparison of the effective Pockels coefficients r of common bulk and thin-film nonlinear materials. The figure is reproduced from the ref. [52-55]: BTO exhibits one of the largest Pockels coefficients of all

known materials. Rabiei et al. integrated $LiNbO_3$ with the SOI substrate by wafer-bonding, showing an r value of approximately 30 pm/V [49].

Several ferroelectric oxides, such as $BaTiO_3$ (BTO), $BaSrTiO_3$, and $PbZrTiO_3$, have larger Pockels effects than $LiNbO_3$, as shown in Figure 1.17 [49, 52-55]. Therefore, the integration of those ferroelectric oxides with Si for optical modulator applications has attracted much research interest. The correlation between ferroelectricity and electro-optical effect will be discussed in the next section. Among the materials listed in Figure 1.17, BTO is a promising candidate given several reasons: bulk BTO material shows one of the most pronounced Pockels coefficients, > 1000 pm/V [52]. Also, BTO naturally allows high-speed optical modulation: recently, a frequency of 5 GHz has been successfully demonstrated in a ring device structure, as shown in Figure 1.18 [56]. In addition, a promising modulation speed of 72 Gb/s has been successfully achieved in a BTO/Si hybrid plasmonic optical modulator, as presented in Figure 1.19 [57].

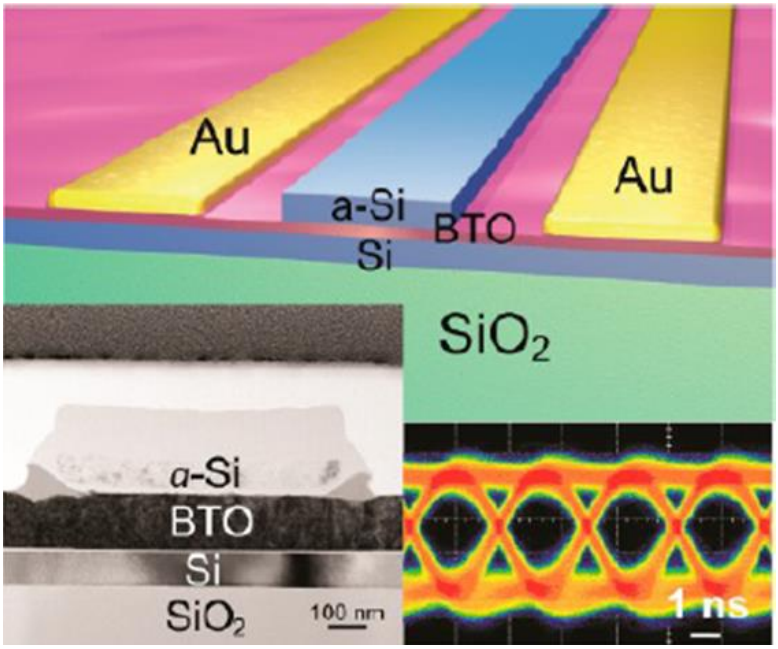


**Figure 1.18:** Schematic, transmission electron microscopy (TEM), and eye diagram of a BTO/Si hybrid optical modulator. These figures are reproduced from the ref. [56].

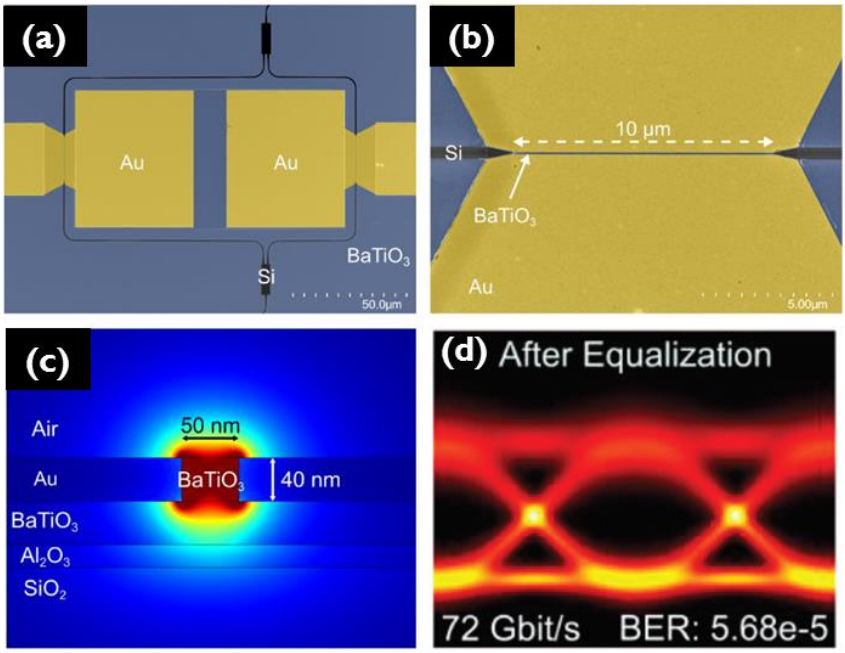


**Figure 1.19:** (a) and (b) Scanning electron microscopy (SEM) of the BTO/Si hybrid plasmonic modulator. (c) Simulated mode profile of the device. (d) Eye diagram of the data transmission. These figures are reproduced from the ref. [57].

Table 1.1 summarizes key metrics for different Si-based optical modulators as introduced in Section 1.3. The hybrid optical modulators exploiting the Pockels effect in BTO or in organic materials show great potential to enable high-speed and power-efficient optical links. However, the non-linear organic material is still not CMOS-compatible. For that reason, BTO, which can be epitaxially grown on a Si(001) substrate using CMOS compatible tools, has a clear advantage. In the next sections, more BTO properties and BTO/Si integration will be introduced. Besides, Chapter 6 will benchmark state-of-the-art results for different types of hybrid Pockels material/Si optical modulators.

**Table 1.1:** Summary of characteristics in Si-based modulators using different modulation mechanisms and device structures. The metrics are collected from the ref. [40, 45, 50, 51, 57-62].

| Modulator Type | Ref. | Mechanism | Footprint | Wavelength | Voltage Swing | Optical Range | ER | IL | Power | | 3dB Bandwidth | Max. Bit Rate |
|---|---|---|---|---|---|---|---|---|---|---|---|---|
| | | | | | | | | | Static | Dynamic | | |
| | | | $\mu m^2$ | nm | V | nm | dB | dB | mW | fJ/bit | GHz | Gb/s |
| **BTO/Si Plasmonic** | **[57]** | **Pockels Effect** | **~10x2** | **1542** | **2.8** | **-** | **15** | **25** | **-** | **-** | **-** | **72** |
| **Organic/Si MZI** | **[50, 51]** | **Pockels Effect** | **-** | **1550 [50, 51]** | **0.95 [50, 51]** | **-** | **11 [50, 51]** | **~6 [50, 51]** | **-** | **1.6 @ 12.5Gb/s [50]** | **100 [51]** | **40 [50]** |
| GeSi FK | [58] | Franz-Keldysh | ~40×10 | 1560 | 2.0 | 30 | 4.2 | 4.4 | 1.7 | 13.8 | >50 | 56 |
| GeSi FK | [59] | Franz-Keldysh | ~50×10 | 1540 | 3.0 | >40 | 5.9 | 4.8 | 11.3 | 147 | 38 | >50 |
| Ge FK | [60] | Franz-Keldysh | ~40×10 | 1615 | 2.0 | >22.5 | 4.6 | 4.9 | 1.2 | 12.8 | >50 | 56 |
| Si MZI | [61] | Carrier Dispersion | ~3000×500 | 1300 | 1.5 | >80 | 3.4 | 7.1 | ~20 | ~450 | 30 | 50 |
| Si Ring | [62] | Carrier Dispersion | ~10×10 | 1550 | 0.5 | <0.1 | 6.4 | 1.2 | <0.01 | ~1 | 21 | 44 |
| Si Ring | [40] | Carrier Dispersion | ~5×5 | 1566.5 | 2.5 | <0.1 | 4.5 | 2.4 | - | 45 | 40 | 56 |
| III-V on Si | [45] | QCSE | >100×350 | 1300 | 2.2 | >30 | >10 | 4.8 | 6.2 | 484 | 74 | 50 |

## 1.4 BTO Properties

Because of its crystal symmetry, rare earth cations, and ionic bonding, the crystalline perovskite oxides $ABO_3$ exhibit several unique properties that are useful for applications such as dielectrics, piezoelectrics, pyroelectrics, and ferroelectrics. One representative $ABO_3$ material that has been studied for over 70 years is BTO. Figure 1.20 shows the BTO crystal structure, which is composed of BaO and $TiO_2$ planes alternately. The in-plane ($a_{//}$) and out-of-plane ($a_{\perp}$) lattice constants in a unit cell are denoted *a* and *c*, respectively.

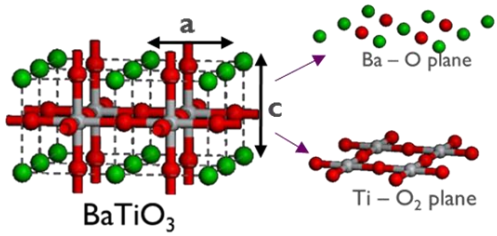


**Figure 1.20:** BTO perovskite crystal structure, with lattice constants *a* and *c*.

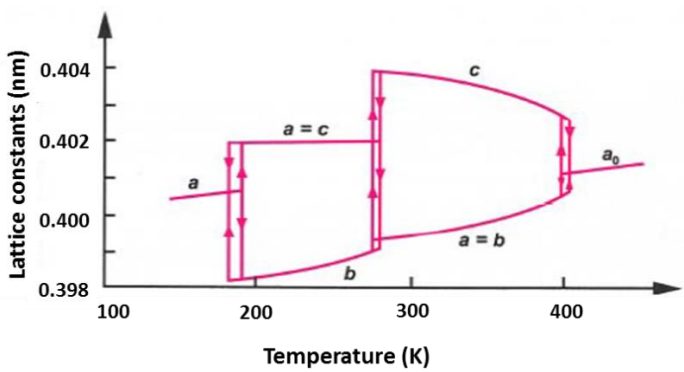


**Figure 1.21:** Lattice constants *a* and *c* as a function of temperature. The figure is reproduced from the ref. [63].

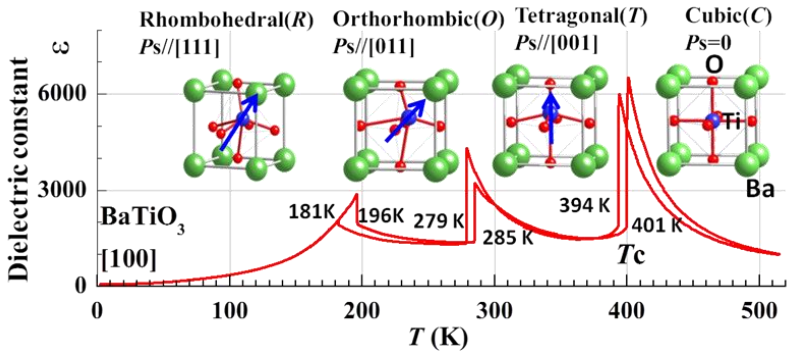


**Figure 1.22:** Dielectric constant, crystal structure, and spontaneous polarization as functions of temperature. The figure is reproduced from the ref. [64].

To obtain the minimum free energy, there is a displacement of the Ti atom away from the center of the BTO unit crystal. Thanks to that, BTO offers multiple excellent properties. By varying the temperature, a phase transition occurs: its lattice constants and several material properties, such as dielectric constant and spontaneous polarization, are changed simultaneously, as presented in Figures 1.21 and 1.22 [63, 64]. At room temperature, BTO exhibits the P4mm crystal symmetry for the tetragonal crystal structure, showing spontaneous polarization along $<100>_{BTO}$. Thus, there are six directions of spontaneous polarization, as follows: 2 c-oriented domains with out-of-plane dipoles and 4 a-oriented domains with in-plane dipoles. The lattice parameters for a-oriented and c-oriented bulk BTO are summarized in the Table 1.2:

| | Numbers of Equivalent Directions | c (nm) | a (nm) | Tetragonality (c/a) |
|---|---|---|---|---|
| c-oriented BTO | 2 | 0.4036 | 0.3992 | 1.011 |
| a-oriented BTO | 4 | 0.3992 | 0.4036 | 0.989 |

**Table 1.2:** Lattice parameters for a-oriented and c-oriented bulk BTO at room temperature.

When the temperature is beyond the Curie temperature (approximately 396 K for bulk BTO), the crystal structure becomes centro-symmetric cubic. Then, BTO no longer exhibits the Ti displacement, losing all of the properties induced by the spontaneous polarization. However, the Curie temperature of thin-film BTO is highly dependent on the strain caused by the underlying materials, defects, stoichiometry, and crystallinity [65, 66]. Figure 1.23 shows the phase diagram of BaO and $TiO_2$ [67]. Because the chemical formula of BTO shows ternary

compounds composed of the stoichiometric ratio Ba:Ti:O=1:1:3, it is crucial to control the compositions precisely to obtain the desired material properties. However, as shown in the phase diagram, it is very easy to form compounds other than BTO when the stoichiometric ratio is slightly off. Therefore, controlling the stoichiometry is one of the main challenges in BTO synthesis. The stoichiometry calibration during the BTO synthesis using various diffraction techniques will be discussed in Chapter 3.

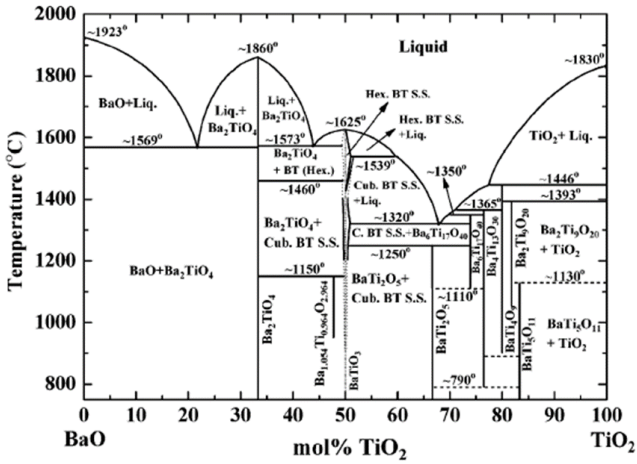


**Figure 1.23:** Phase diagram of BaO and $TiO_2$. The figure is reproduced from the ref. [67].

Fundamentally, BTO possesses a variety of properties because the Ti ion surrounded with six oxygens ($TiO_6$ octahedron) can be displaced by an electric field. Ferroelectric, piezoelectric, dielectric, elasto-optical, thermo-optical electro-optical, and photo-refractive effects have been reported in BTO materials [68-70]. All of the above properties can respond to an electric field, which can result not only from an external applied bias or light polarization, but also from the built-in field induced by spontaneous polarizations or extra charges in domain boundaries. Therefore, all the physical properties are coupled with each other, contributing to the overall experimental results. In order to understand the fundamental origin of the electro-optical effect in the ferroelectric perovskite oxide, DiDomenico and Wemple in 1969 developed a microscopic theory using tensorial analysis to explain the measured electro-optical phenomenon [71, 72]: They claimed that a large electro-optical coefficient would be observed in materials with large dielectric constant and spontaneous polarizations. Therefore, ferroelectric oxides with a strong spontaneous polarization show a strong electro-optical performance too. From their works, they established insightful pictures to

study different perovskite oxides in the context of a wide range of applications. Forty five years after, Veithen and Ghosez exploited the first-principle approach to study the electro-optical properties of BTO, coming to the same conclusion as Didomenico and Wemple's work [73]. Those theoretical studies are discussing the behavior in bulk materials. Recently, some qualitative models to explain the electro-optical effects for the BTO thin films have been reported [74, 75]. However, the less controllable thin film synthesis still makes quantitative analysis very difficult. In chapter 6, more details for the electro-optical response within our hybrid BTO/Si devices will be given.

## 1.5 Integration of Epitaxial BTO and Si(001)

In thin film applications, the functional properties of BTO, as mentioned in Section 1.4, depend on its crystallinity, with single-crystalline BTO displaying the best properties [66, 76, 77]. However, it is challenging to integrate high-quality crystalline BTO thin films on a Si(001) substrate because of their greatly different crystal structure and chemical properties [66]. The in-plane lattice constant ($a_{//}$) of BTO is 0.3992 nm, while that of silicon is 0.5431 nm; this constitutes a lattice mismatch of 27%. In addition, BTO is chemically unstable when being deposited directly on silicon, resulting in the formation of an amorphous silicate layer and inhibiting the synthesis of high-quality epitaxial BTO. Furthermore, to obtain high-quality BTO thin films, sufficient oxidation is important for the stoichiometry. However, the surface of Si is very reactive with oxygen, forming amorphous silicon oxide, which, again, prevents the epitaxial growth of BTO. Therefore, avoiding Si surface oxidation at the beginning of oxide growth and solving the chemical stability issue between BTO and Si are needed for BTO/Si integration. This particular problem was not resolved until the late 1990s, when McKee et al. utilized a ½ monolayer (ML) of SrO to obtain a high-quality $SrTiO_3$ (STO) layer using molecular beam epitaxy (MBE), as shown in Figure 1.24 [78].

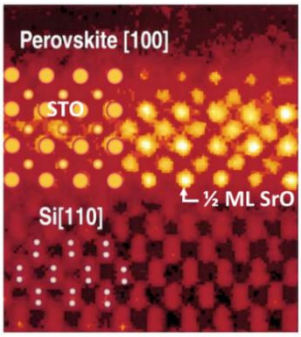


**Figure 1.24:** Z-contrast image of $SrTiO_3$ on (001) silicon. The figure is reproduced from the ref. [78].

There is no formation of the amorphous silicate when ½ ML SrO is in contact with the Si surface, i.e., SrO is thermodynamically stable with respect to the Si surface, as described in Figure 1.25 [79]. This ½ ML of SrO acts as a protection layer to prevent the Si surface from being oxidized during the STO growth. Although bulk STO and Si still have a cubic-to-cubic lattice mismatch of approximately 28% ($a_{//}$ for STO is 0.3905 nm), a ½ ML of SrO can also be used as a lattice template to initiate a 45° rotation of the STO lattice with respect to the Si lattice, reducing the remaining lattice mismatch to 2% (Si/ √2 = 0.3840 nm). Building further on this development, the chemical instability between BTO and Si can now be resolved via the insertion of STO, which presents a crystal and chemical structure similar to BTO [77, 79]. Moreover, the lattice mismatch between BTO and STO is only 2%. Thus, STO can be used to facilitate the monolithic integration of BTO thin films on Si(001) using MBE.

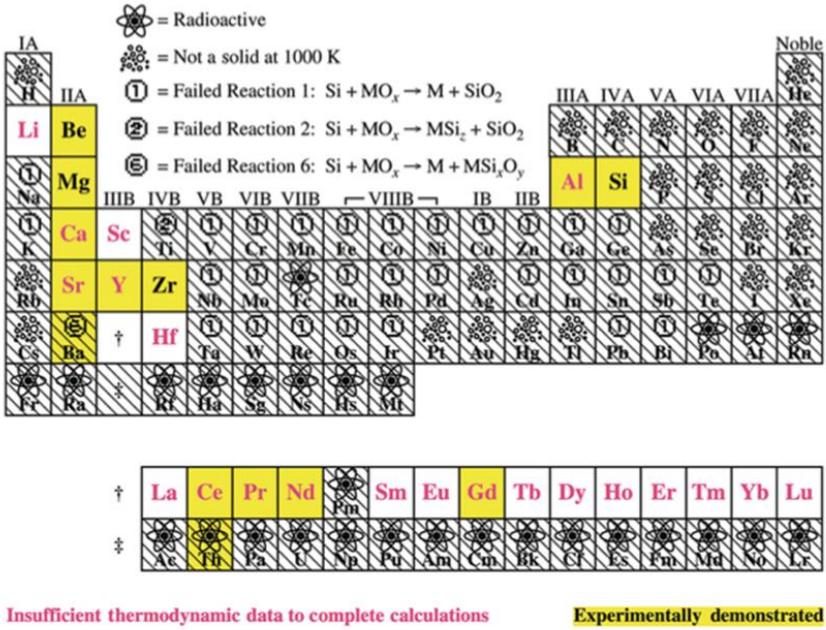


**Figure 1.25:** Thermo-dynamical stability of the oxides of elements in contact with Si at1000K. The figure is reproduced from the ref. [79].

In addition to using the STO buffer for BTO/Si integration, another option is to use Ge, which has a quasi-zero lattice mismatch with respect to BTO (Ge/ √2 = 0.3995 nm), as a buffer layer. Thanks to recent CMOS developments, fabrication of Ge-on-Si pseudo-substrates has become a standard process. The

thickness of the Ge buffer layer in this work is 1000 nm, which is much thicker than that of the STO buffer layer (less than 40 nm in this work). Although the BTO lattice is matched to the Ge lattice, using ½ ML BaO prior to the BTO growth is still necessary to avoid the formation of amorphous germanate or germanium oxide [80, 81]. The integration of BTO with a Ge-on-Si pseudo-substrate also offers a wide spectrum of potential device applications in both electronics and photonics [82, 83].

There are several routes to grow BTO on STO-buffered Si(001) or Ge-on-Si(001) substrates, such as MBE, radio-frequency sputtering, pulsed laser deposition (PLD), and chemical vapor deposition (CVD). Recently, Kormondy et al. compared the EO performance of BTO layers grown by various approaches [84]. They concluded that the effective Pockels coefficient is correlated with BTO porosity, which is derived from spectroscopic ellipsometry. Among the various techniques, MBE gives the best EO performance for the BTO layer, as shown in Figure 1.26.

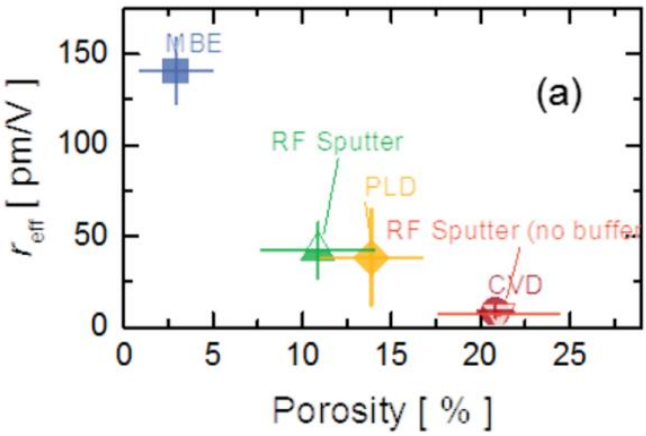


**Figure 1.26:** Effective Pockels coefficient $r_{eff}$ for BTO vs porosity using different deposition techniques. The figure is reproduced from the ref. [84].

## 1.6 Thesis Outline

In this work, high-quality integration of an epitaxial BTO thin film with a STO-buffered Si(001) substrate is achieved by MBE for hybrid BTO/Si optical modulator applications. Although bulk BTO has been studied for over 70 years and epitaxial STO on Si(001) has been demonstrated for over 15 years, there are still many unresolved aspects, from the thin film preparation to the device behavior of optical modulators. Therefore, the thesis structure is developed

according to various questions arising at different stages. The main points of each chapter are as follows:

- **Chapter 2**: The physical principles of epitaxy and introduction of the MBE system employed for oxide growth are presented in this chapter. Additionally, the various in-situ and ex-situ characterization methods are also described.

- **Chapter 3**: As mentioned in Section 1.4, achieving the correct BTO stoichiometry is the main challenge for thin film preparation. To simplify the problem, in this chapter, a Ge substrate, with a quasi-zero lattice mismatch with respect to BTO, is used for the calibration of the stoichiometry by various diffraction techniques. Meanwhile, a model is proposed to explain how excess [Ba] or [Ti] in non-stoichiometric BTO layers induces different experimental diffraction behavior from the stoichiometric layer.

- **Chapter 4**: Based on the results from chapter 3, a high-quality STO buffer layer on a Si(001) substrate is also obtained. Then, a series of optimizations for different growth conditions is performed. This chapter investigates the effects of the BTO growth conditions on its crystallinity, interface, electrical properties, and ferroelectricity.

- **Chapter 5**: Although the growth conditions for both BTO and STO have been optimized, controlling the BTO domain orientation is still difficult. To understand the role of BTO orientation in the device performance, this chapter starts by a discussion about how BTO domain orientations impact the BTO/Si hybrid modulator. Then, the demonstration of controlling BTO orientations by thickness engineering of BTO and the STO buffer layer is presented. Finally, studying the influence of BTO domain orientation on the EO response is also performed by spectroscopic ellipsometry (SE).

- **Chapter 6**: In the last stage, a hybrid BTO/Si optical modulator is realized by direct BTO growth on a patterned SOI wafer. In this chapter, the effect of the domain poling on the device behavior is investigated. Using different bias sweeping modes, the domains are controlled such that the device behavior can be analyzed systematically. Besides, microscopic and macroscopic views of the domain dependent EO response is discussed. Further, the benchmarks of the device performance for various Si-based hybrid modulators are presented.

- **Chapter 7**: Summary and Perspectives

# 1.7 Publications

## 1.7.1. Published SCI Journals

1. **M. H. M. Hsu**, A. Marinelli, C. Merckling, M. Pantouvaki, J. Van Campenhout, P. Absil, D. Van Thourhout, "Orientation-Dependent Electro-Optical Response of $BaTiO_3$ on $SrTiO_3$-Buffered Si(001) Studied via Spectroscopic Ellipsometry" *Opt. Mat. Express* **7**, 2030 (2017).
2. **M. H. M. Hsu**, D. Van Thourhout, M. Pantouvaki, J. Meersschaut, T. Conard, O. Richard, H. Bender, P. Favia, M. Vila, R. Cid, J. Rubio-Zuazo, G. R. Castro, J. Van Campenhout, P. Absil, C. Merckling, "Controlled Orientation of Molecular-Beam-Epitaxial $BaTiO_3$ on Si(001) Using Thickness Engineering of $BaTiO_3$ and $SrTiO_3$ Buffer Layers" *Appl. Phys. Express* **10**, 065501 (2017).
3. **M. H. M. Hsu**, C. Merckling, S. El Kazzi, M. Pantouvaki, O. Richard, H. Bender, J. Meersschaut, J. Van Campenhout, P. Absil, and D. Van Thourhout, "Diffraction studies for stoichiometry effects in $BaTiO_3$ grown by molecular beam epitaxy on Ge(001)," *J. Appl. Phys.* **120**, 225114 (2016).

## 1.7.2. SCI Journals under Preparation

1. "Crystal Structures and Ferroelectricity for Epitaxial $BaTiO_3$ on $SrTiO_3$-on-Si Pseudo-Substrate Using Plasma-Assisted Molecular Beam Epitaxy"
2. "Effects of $90^o$-Domain Dynamics on Electrical and Optical Properties of MBE-Grown BTO on Si."

## 1.7.3. Publications in International Conferences

1. D. Van Thourhout, M. Pantouvaki, H. D'Heer, K. Alexander, B. Kuyken, I. Asselberghs, S. Brems, C. Huyghebaert, L. A. Shiramin, C. Alessandri, J. P. George, J. Beeckman, **M. H. M. Hsu**, C. Merckling, J. Van Campenhout "New materials for modulators and switches in silicon photonics," 2017 SPIE OPTO.

2. D. Van Thourhout, Z. Wang, B. Tian, Y. Shi, M. Pantouvaki, C. Merckling, Y. Hu, I. Asselberghs, S. Brems, L. Abdollahi Shiramin, C. Alessandri, J. George, J. Beeckman, **M. H. M. Hsu**, P .Absil, J. Van Campenhout, "New Materials for Multifunctional Photonic ICs," Conferencia Española de Nanofotonica (2016). (Invited)

3. **M. H. M. Hsu**, M. Pantouvaki, C. Merckling, A. Marinelli, J. Van Campenhout, P. Absil, D. Van Thourhout, "Design of thin film stacks for non-destructive electro-optical characterizations by spectroscopic ellipsometry," Proceedings of the 19th Annual Symposium of the IEEE Photonics Society Benelux Chapter, Belgium, 65-68 (2016).

4. **M. H. M. Hsu** et al, "Orientation-Dependent Electro-Optical Properties Of Molecular-Beam-Epitaxial BaTiO3 On Si For Optical Switches", European Materials Research Society Fall Meeting (2016)

5. D. Van Thourhout, Z. Wang, B. Tian, Y. Hu, J. P. George, J. Beeckman, M. Pantouvaki, C. Merckling, I. Asselberghs, S. Brems, P. Absil, M. H. M. Hsu, J. Van Campenhout "New materials and devices for optical interconnect," Opto-Electronics and Communications Conference (OECC), 2015 (2015).

6. **M. H. M. Hsu** et al, "MBE growth of $BaTiO_3$ on Ge/Si and $SrTiO_3$/Si pseudosubstrates for electro-optical modulators integration on silicon", European Materials Research Society Spring Meeting (2015)

7. **M. H. M. Hsu** et al, "Stoichiometry studies for molecular beam epitaxial $BaTiO_3$ on Ge-on-Si(001)", European Materials Research Society Fall Meeting (2014)

8. S. El Kazzi, **M. H. M. Hsu**, M. Ezzedini and C. Merckling, "MBE studies for In0.53Ga0.47As growth using strained buffer layers and in-situ high-k gate passivation" Compound Semiconductor Week 2014 (2014).

# References

[1] G.E. Moore, “Lithography and the future of Moore’s law”, in SPIE’s 1995 Symposium on Microlithography (1995)

[2] B. Sheu, K. Wilcox, A.M. Keshavarzi, D. Antoniadis, “Moore’s law challenges below 10 nm: technology, design and economic implications”, in IEEE Solid-State Circuits Conference (ISSCC), EP1 (2015)

[3] https://scs.senecac.on.ca/~gpu610/pages/content/intro.html

[4] R. G. Beausoleil, P. J. Kuekes, G. S. Snider, W. Shih-Yuan, and R. S. Williams, "Nanoelectronic and Nanophotonic Interconnect," Proceedings of the IEEE, vol. 96, no. 2, pp. 230-247, 2008.

[5] M. T. Bohr, "Interconnect scaling-the real limiter to high performance ULSI," in Proceedings of International Electron Devices Meeting, 1995, pp. 241-244.

[6] M. Haurylau et al., "On-Chip Optical Interconnect Roadmap: Challenges and Critical Directions," IEEE Journal of Selected Topics in Quantum Electronics, vol. 12, no. 6, pp. 1699-1705, 2006.

[7] A. V. Krishnamoorthy et al., "Progress in Low-Power Switched Optical Interconnects," IEEE Journal of Selected Topics in Quantum Electronics, vol. 17, no. 2, pp. 357-376, 2011.

[8] D. Miller, "Device Requirements for Optical Interconnects to Silicon Chips," Proceedings of the IEEE, vol. 97, no. 7, pp. 1166-1185, 2009.

[9] A. Karim, K. Samadi, Y. Du, “3D VLSI: a scalable integration beyond 2D”, in Proceedings of the Symposium on International Symposium on Physical Design (ACM, 2015)

[10] E. Socher, M. Chang, “Can RF help CMOS processors?” IEEE Commun. Mag. 45(8), 104–111 (2007)

[11] M. Haurylau, G. Chen, H. Chen, J. Zhang, N.A. Nelson, D.H. Albonesi, P.M. Fauchet, “On-chip optical interconnect roadmap: challenges and critical directions.” IEEE J. Sel. Top. Quantum Electron. 12(6), 1699–1705 (2006)

[12] V. Vujicic, C. Calò, R. Watts, F. Lelarge, C. Browning, K. Merghem, L.P. Barry, “Quantum dash passively mode-locked lasers for Tbit/s data interconnects.” OFC2015, Tu3I-4

[13] S. Assefa, W.M.J. Green, A. Rylyakov, C. Schow, F. Horst, Y.A. Vlasov, “Monolithic integration of silicon nanophotonics with CMOS,” in IEEE Photonics Conference (2012), pp. 626–627

[14] J.E. Cunningham, I. Shubin, H.D. Thacker, J.-H. Lee, G. Li, X. Zheng, J. Lexau, R. Ho, J.G. Mitchell, L. Ying, J. Yao, K. Raj, A.V. Krishnamoorthy, “Scaling hybrid-integration of silicon photonics in Freescale 130 nm to TSMC 40 nm-CMOS VLSI drivers for low power communications,” in IEEE 62nd Electronic Components and Technology Conference (ECTC) (2012), 1518–1525

[15] L. Pavesi and D.J. Lockwood, “*Silicon Photonics III*”, Springer New York Heidelberg Dordrecht London, 2016, Chapter 14.

[16] M. Streshinsky et al., "The Road to Affordable, Large-Scale Silicon Photonics," Optics and Photonics News, vol. 24, no. 9, pp. 32-39, 2013/09/01 2013.

[17] http://hexus.net/tech/news/mainboard/25707-intel-takes-next-step-silicon-photonics/

[18] http://www.photonics.intec.ugent.be/download/pub_2062.pdf

[19] Hartmann J M et al 2004 “Reduced pressure-chemical vapor deposition of Ge thick layers on Si(001) for 1.3–1.55-μm photodetection,” J. of Appl. Phys. 95 5905

[20] L. Vivien et al., "Zero-bias 40Gbit/s germanium waveguide photodetector on silicon," Optics Express, vol. 20, no. 2, pp. 1096-1101, 2012/01/16 2012.

[21] L. Vivien et al., "42 GHz p.i.n Germanium photodetector integrated in a silicon-on-insulator waveguide," Optics Express, vol. 17, no. 8, pp. 6252-6257, 2009/04/13 2009.

[22] T. Yin et al., "31GHz Ge n-i-p waveguide photodetectors on Silicon-on-Insulator substrate," Optics Express, vol. 15, no. 21, pp. 13965-13971, 2007/10/17 2007.

[23] T. Torikai and K. Makita, "40-Gbps high-sensitive waveguide photodetectors," 2005, vol. 6020, pp. 602024-602024-8.

[24] C. T. DeRose et al., "Ultra compact 45 GHz CMOS compatible Germanium waveguide photodiode with low dark current," Optics Express, vol. 19, no. 25, pp. 24897-24904, 2011/12/05 2011.

[25] D. Thomson et al., "Roadmap on silicon photonics," Journal of Optics, vol. 18, no. 7, p. 073003, 2016.

[26] M. J. R. Heck et al., "Hybrid Silicon Photonic Integrated Circuit Technology," IEEE Journal of Selected Topics in Quantum Electronics, vol. 19, no. 4, pp. 6100117-6100117, 2013.

[27] S. Keyvaninia et al., "Heterogeneously integrated III-V/silicon distributed feedback lasers," Optics Letters, vol. 38, no. 24, pp. 5434-5437, 2013/12/15 2013.

[28] A. W. Fang, E. Lively, Y.-H. Kuo, D. Liang, and J. E. Bowers, "A distributed feedback silicon evanescent laser," Optics Express, vol. 16, no. 7, pp. 4413-4419, 2008/03/31 2008.

[29] B. Tian et al., "Room Temperature O-band DFB Laser Array Directly Grown on (001) Silicon," Nano Letters, vol. 17, no. 1, pp. 559-564, 2017/01/11 2017.

[30] J. Liu, X. Sun, R. Camacho-Aguilera, L. C. Kimerling, and J. Michel, "Ge-on-Si laser operating at room temperature," Optics Letters, vol. 35, no. 5, pp. 679-681, 2010/03/01 2010.

[31] H. Rong et al., "Low-threshold continuous-wave Raman silicon laser," Nat Photon, vol. 1, no. 4, pp. 232-237, 04//print 2007.

[32] G. T. Reed and C. E. Jason Png, "Silicon optical modulators," Materials Today, vol. 8, no. 1, pp. 40-50, 2005.

[33] G. T. Reed, G. Mashanovich, F. Y. Gardes, and D. J. Thomson, "Silicon optical modulators," Nature Photonics, vol. 4, no. 8, pp. 518-526, 2010.

[34] Q. Xu, B. Schmidt, S. Pradhan, and M. Lipson, "Micrometre-scale silicon electro-optic modulator," Nature, vol. 435, no. 7040, pp. 325-7, May 19 2005.

[35] S. Manipatruni, Q. Xu, B. Schmidt, J. Shakya, and M. Lipson, "High Speed Carrier Injection 18 Gb/s Silicon Micro-ring Electro-optic Modulator," in LEOS 2007 - IEEE Lasers and Electro-Optics Society Annual Meeting Conference Proceedings, 2007, pp. 537-538.

[36] S. Manipatruni, M. Lipson, and I. A. Young, "Device Scaling Considerations for Nanophotonic CMOS Global Interconnects," IEEE Journal of Selected Topics in Quantum Electronics, vol. 19, no. 2, pp. 8200109-8200109, 2013.

[37] F. Gan and F. X. Ka, "High-speed silicon electrooptic Modulator design," IEEE Photonics Technology Letters, vol. 17, no. 5, pp. 1007-1009, 2005.

[38] A. Liu et al., "A high-speed silicon optical modulator based on a metal-oxide-semiconductor capacitor," Nature, 10.1038/nature02310 vol. 427, no. 6975, pp. 615-618, 02/12/print 2004.

[39] M. Sodagar et al., "Compact, 15 Gb/s electro-optic modulator through carrier accumulation in a hybrid Si/SiO(2)/Si microdisk," Opt Express, vol. 23, no. 22, pp. 28306-15, Nov 02 2015.

[40] M. Pantouvaki, P. Verheyen, J. D. Coster, G. Lepage, P. Absil, and J. V. Campenhout, "56Gb/s ring modulator on a 300mm silicon photonics platform," in 2015 European Conference on Optical Communication (ECOC), 2015, pp. 1-3.

[41] S. S. Azadeh et al., "Low V(pi) Silicon photonics modulators with highly linear epitaxially grown phase shifters," Opt Express, vol. 23, no. 18, pp. 23526-50, Sep 07 2015.

[42] D. Feng et al., "High speed GeSi electro-absorption modulator at 1550 nm wavelength on SOI waveguide," Optics Express, vol. 20, no. 20, pp. 22224-22232, 2012/09/24 2012.

[43] P. De Heyn et al., "Ultra-Dense 16x56Gb/s NRZ GeSi EAM-PD Arrays Coupled to Multicore Fiber for Short-Reach 896Gb/s Optical Links," in Optical Fiber Communication Conference, Los Angeles, California, 2017, p. Th1B.7: Optical Society of America.

[44] Y. T. Hu et al., "Broadband 10Gb/s graphene electro-absorption modulator on silicon for chip-level optical interconnects," in 2014 IEEE International Electron Devices Meeting, 2014, pp. 5.6.1-5.6.4.

[45] Y. Tang, J. D. Peters, and J. E. Bowers, "Over 67 GHz bandwidth hybrid silicon electroabsorption modulator with asymmetric segmented electrode for 1.3 μm transmission," Optics Express, vol. 20, no. 10, pp. 11529-11535, 2012/05/07 2012.

[46] HaffnerC et al., "All-plasmonic Mach–Zehnder modulator enabling optical high-speed communication at the microscale," Nat Photon, Letter vol. 9, no. 8, pp. 525-528, 08//print 2015.

[47] E. L. Wooten, K. M. Kissa, A. Yi-Yan, E. J. Murphy, D. A. Lafaw, P. F. Hallemeier, D. Maack, D. V. Attanasio, D. J. Fritz, G. J. McBrien and D. E. Bossi, “A review of lithium niobate modulator for fiber-optic communications systems,” IEEE J Sel Top Quantum Electron 6, 69-82 (2000).

[48] P. Damas et al., "Wavelength dependence of Pockels effect in strained silicon waveguides," Opt Express, vol. 22, no. 18, pp. 22095-100, Sep 08 2014.

[49] P. Rabiei, J. Ma, S. Khan, J. Chiles, and S. Fathpour, "Heterogeneous lithium niobate photonics on silicon substrates," Opt Express, vol. 21, no. 21, pp. 25573-81, Oct 21 2013.

[50] R. Palmer et al., "High-speed silicon-organic hybrid (SOH) modulator with 1.6 fJ/bit and 180 pm/V in-device nonlinearity," in 39th European

Conference and Exhibition on Optical Communication (ECOC 2013), 2013, pp. 1-3.

[51] L. Alloatti et al., "100 GHz silicon–organic hybrid modulator," Light: Science & Applications, vol. 3, no. 5, p. e173, 2014.

[52] S. Abel et al., "A Hybrid Barium Titanate–Silicon Photonics Platform for Ultraefficient Electro-Optic Tuning," Journal of Lightwave Technology, vol. 34, no. 8, pp. 1688-1693, 2016.

[53] B. Chmielak, M. Waldow, C. Matheisen, C. Ripperda, J. Bolten, T. Wahlbrink, M. Nagel, F. Merget, and H. Kurz, “Pockels effect based fully integrated, strained silicon electro-optic modulator,” Opt. Exp., vol. 19, no. 18, pp. 17212–17219, 2011.

[54] B. W. Wessels, “Ferroelectric epitaxial thin films for integrated optics,” Annu. Rev. Mater. Res., vol. 37, no. 1, pp. 659–679, 2007.

[55] L. R. Dalton, P. A. Sullivan, and D. H. Bale, “Electric field poled organic electro-optic materials: State of the art and future prospects,” Chem. Rev., vol. 110, no. 1, pp. 25–55, 2010.

[56] C. Xiong et al., "Active silicon integrated nanophotonics: ferroelectric BaTiO3 devices," Nano Lett, vol. 14, no. 3, pp. 1419-25, Mar 12 2014.

[57] A. Messner et al., "Integrated Ferroelectric Plasmonic Optical Modulator," in Optical Fiber Communication Conference Postdeadline Papers, Los Angeles, California, 2017, p. Th5C.7: Optical Society of America.

[58] A. Srinivasan, et al. “50Gb/s C-band GeSi Waveguide Electro-Absorption Modulator”, Tu3D.7, OFC 2016.

[59] D. Feng, et al. “High-Speed GeSi Electroabsorption Modulator on the SOI Waveguide Platform”, IEEE Journal of Selected Topics in Quantum Electronics, 19, 64, 2013.

[60] A. Srinivasan, et al. “56Gb/s Germanium Waveguide Electro-Absorption Modulator”, Journal of Lightwave Technology, vol.34, pp.419, 2016.

[61] M. Streshinsky, et al. “Low power 50 Gb/s silicon traveling wave Mach-Zehnder modulator near 1300 nm”, Opt. Express 21, 30350-30357, 2013.

[62] E. Timurdogan, et al. “An ultralow power athermal silicon modulator”, Nature Communications, 5, 4008, 2014.

[63] H. F. Kay and P. Vousden, "XCV. Symmetry changes in barium titanate at low temperatures and their relation to its ferroelectric properties," The

London, Edinburgh, and Dublin Philosophical Magazine and Journal of Science, vol. 40, no. 309, pp. 1019-1040, 1949/10/01 1949.

[64] https://www.intechopen.com/books/ferroelectric-materials-synthesis-and-characterization/role-of-ca-off-centering-in-tuning-ferroelectric-phase-transitions-in-ba-zr-ti-o3system

[65] K. J. Choi et al., "Enhancement of ferroelectricity in strained BaTiO3 thin films," Science, vol. 306, no. 5698, pp. 1005-9, Nov 05 2004.

[66] A. A. Demkov and A. B. Posadas, Integration of functional oxides with semiconductors (Springer, 2014).

[67] S. Lee, C. A. Randall, and Z.-K. Liu, "Modified Phase Diagram for the Barium Oxide–Titanium Dioxide System for the Ferroelectric Barium Titanate," Journal of the American Ceramic Society, vol. 90, no. 8, pp. 2589-2594, 2007.

[68] P. Guenter, "Electro-optical and nonlinear-optical materials," Ferroelectrics, vol. 24, no. 1, pp. 35-42, 1980/01/01 1980.

[69] M. Zgonik et al., "Dielectric, elastic, piezoelectric, electro-optic, and elasto-optic tensors of BaTiO3 crystals," Physical Review B, vol. 50, no. 9, pp. 5941-5949, 09/01/ 1994.

[70] P. Bernasconi, M. Zgonik, and P. Günter, "Temperature dependence and dispersion of electro - optic and elasto - optic effect in perovskite crystals," Journal of Applied Physics, vol. 78, no. 4, pp. 2651-2658, 1995.

[71] M. D. Jr. and S. H. Wemple, "Oxygen - Octahedra Ferroelectrics. I. Theory of Electro - optical and Nonlinear optical Effects," Journal of Applied Physics, vol. 40, no. 2, pp. 720-734, 1969.

[72] S. H. Wemple and M. D. Jr., "Oxygen - Octahedra Ferroelectrics. II. Electro - optical and Nonlinear - Optical Device Applications," Journal of Applied Physics, vol. 40, no. 2, pp. 735-752, 1969.

[73] M. Veithen and P. Ghosez, "Temperature dependence of the electro-optic tensor and refractive indices of BaTiO3 from first principles," Physical Review B, vol. 71, no. 13, p. 132101, 04/13/ 2005.

[74] P. Castera, D. Tulli, A. M. Gutierrez, and P. Sanchis, "Influence of BaTiO3 ferroelectric orientation for electro-optic modulation on silicon," Opt Express, vol. 23, no. 12, pp. 15332-42, Jun 15 2015.

[75] P. Castera et al., "Electro-Optical Modulation Based on Pockels Effect in BaTiO3 With a Multi-Domain Structure," IEEE Photonics Technology Letters, vol. 28, no. 9, pp. 990-993, 2016.

[76] J. W. Reiner, A. M. Kolpak, Y. Segal, K. F. Garrity, S. Ismail - Beigi, C. H. Ahn, and F. J. Walker, "Crystalline oxides on silicon," Advanced Materials 22, 2919-2938 (2010).

[77] D. G. Schlom, L.-Q. Chen, X. Pan, A. Schmehl, and M. A. Zurbuchen, "A Thin Film Approach to Engineering Functionality into Oxides," Journal of the American Ceramic Society 91, 2429-2454 (2008).

[78] R. McKee, F. Walker, and M. Chisholm, "Crystalline oxides on silicon: the first five monolayers," Physical Review Letters 81, 3014 (1998).

[79] D. G. Schlom and J. H. Haeni, ‘‘A Thermodynamic Approach to Selecting Alternative Gate Dielectrics,’’ MRS Bull., 27 [3] 198–204 (2002).

[80] C. Merckling, G. Saint-Girons, C. Botella, G. Hollinger, M. Heyns, J. Dekoster, and M. Caymax, “Molecular beam epitaxial growth of BaTiO3 single crystal on Ge-on-Si(001) substrates” Appl. Phys. Lett. 98, 092901 (2011).

[81] M. H. M. Hsu, C. Merckling, S. El Kazzi, M. Pantouvaki, O. Richard, H. Bender, J. Meersschaut, J. Van Campenhout, P. Absil, and D. Van Thourhout, "Diffraction studies for stoichiometry effects in BaTiO3 grown by molecular beam epitaxy on Ge(001)," Journal of Applied Physics 120, 225114 (2016).

[82] P. Ponath et al., "Carrier density modulation in a germanium heterostructure by ferroelectric switching," Nat Commun, vol. 6, p. 6067, Jan 14 2015.

[83] L. Kornblum, M. D. Morales-Acosta, E. N. Jin, C. H. Ahn, and F. J. Walker, "Transport at the Epitaxial Interface between Germanium and Functional Oxides," Advanced Materials Interfaces, vol. 2, no. 18, pp. 1500193-n/a, 2015, Art. no. 1500193.

[84] K. J. Kormondy et al., "Microstructure and ferroelectricity of BaTiO3 thin films on Si for integrated photonics," Nanotechnology, vol. 28, no. 7, p. 075706, 2017.

# 2

# Molecular Beam Epitaxy & Characterization Methods

In this chapter, we present the physical principles of epitaxy and introduce the MBE system employed for the oxide growth. The different in-situ and ex-situ characterization methods used are also described.

## 2.1 Principle of Epitaxial Growth

As introduced in Chapter 1, arising from the Ti displacement in the BTO unit cell, this ferroelectric oxide possess several excellent properties, including large dielectric constant, piezoelectric, pyroelectric, and Pockels effects. Therefore, BTO possesses wide potential applications in novel devices. However, any disorder of the crystal lattice will impede the movement of the Ti atom inside the lattice, limiting the properties of the material and therefore device performance. Hence, it has been widely reported that the above-mentioned effects are superior in single crystalline BTO compared with poly-crystalline and amorphous BTO. The process, used to achieve single crystalline thin films on single crystalline substrates, is called heteroepitaxy. In the following section, we give a brief introduction to the mechanism of epitaxial growth [1].

### 2.1.1. Kinetics of Atoms on the Sample Surface

MBE is an ultra-high vacuum (UHV) process in which thin films are formed by the deposition of vaporized atoms or molecules onto a heated substrate. The extremely low pressure as well as moderate substrate temperature makes MBE growth dominated more by kinetics rather than being a thermodynamic equilibrium process. Therefore, the growth mechanism is mainly based on physiochemical interactions between adatoms from the vapor and the substrate surface.

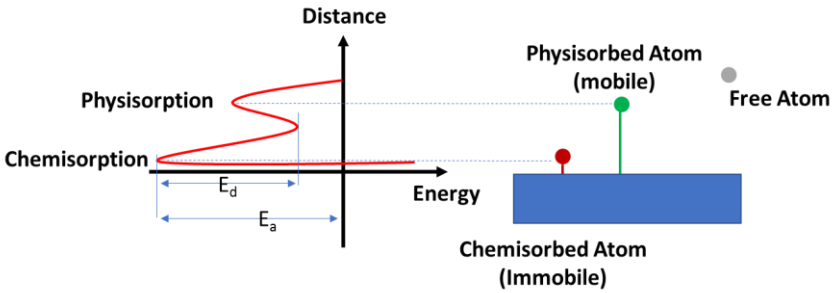


**Figure 2.1:** Physicochemical interactions between adatoms from vapor and substrate surface. The figures are reproduced from the ref. [2].

The adsorption of incoming atoms on the surface of the substrate can be categorized into two types according to bonding energy, as described in Figure 2.1 [2]: (1) Chemisorption: The adatoms form either covalent, ionic, or metallic bonds with the substrate surface. Therefore, when the thermal energy is insufficient owing to a low substrate temperature, the chemisorbed atoms cannot move on the surface, limiting the deposition to a monolayer instead of multi-layers. (2) Physisorption: The adatoms bond to the substrate surface via the weaker Van der Waals force. As a result, when the thermal energy overcomes the Van der Waals bonding, the atoms become mobile on the surface, and organize to form multi-layers. If, initially, the adatoms are chemisorbed on the surface, thermal energy between $E_a$ and $E_d$ can make the atoms become physisorbed and mobile on the surface. However, when the substrate temperature offers energy beyond $E_a$, the desorption process happens: the adatoms will desorb from the surface and re-vaporize. Therefore, only an appropriate substrate temperature and pressure conditions can make the epitaxial process take place to form an epitaxial film. Under such appropriate conditions, the adatoms diffuse on the surface from one site to another, and groups of several atoms combine to form metastable nuclei. These nuclei grow until they reach a critical size, at which they become stable

nuclei. The stable nuclei then become incorporated together and form a complete layer. The above process is dynamic and its different steps always occur simultaneously. The whole atomic process of nucleation and growth is illustrated in Figure 2.2. [3]

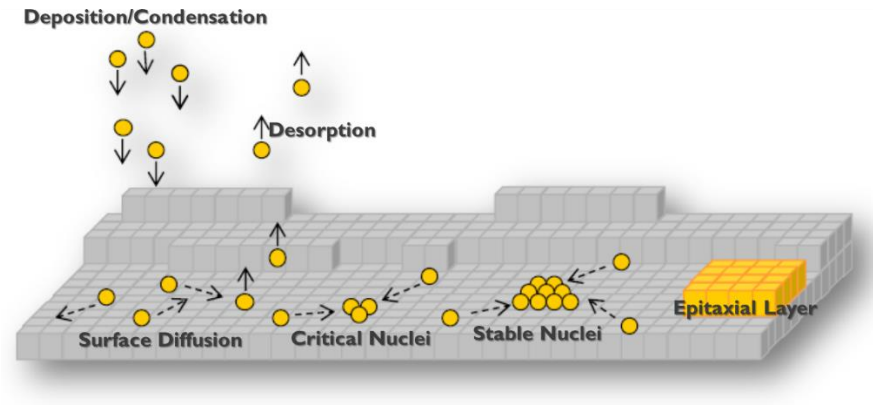


**Figure 2.2:** Atomic process of nucleation and epitaxy. The figure is reproduced from the ref. [2]

## 2.1.2. Surface Energy and Growth Modes

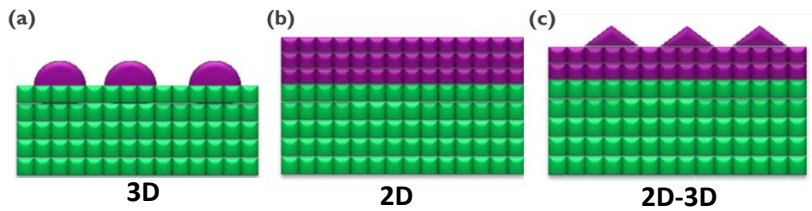


**Figure 2.3:** Three modes of thin-film growth: (a) Volmer-Weber (island growth), (b) Frank-van der Merwe (layer-by-layer growth), and (c) Stranski-Krastanov. These figures are reproduced from the ref. [3].

The growth mode can be classified into one of three types according to the morphology of the grown layer, as described in Figure 2.3 [3]. The first is the Volmer-Weber mode, also known as the 3D island growth mode. The deposited atoms assemble into small nuclei on the surface and grow into islands because the bonding between adatoms is stronger than that with surface atoms on the substrate. Conversely, if the interaction between adatoms and atoms on the substrate surface is greater than that between adatoms, the growth tends to progress layer-by-layer,

which is known as the Frank-van der Merwe mode or called the 2D growth. The intermediate growth mode is the Stranski-Krastanov mode or called the 2D-3D growth mode. This mode begins as layer-by-layer growth until a certain critical thickness, after which it becomes island growth. As mentioned, all these growth modes are dependent on interactions between adatoms and substrate surface atoms. Therefore, understanding of the thermodynamics considering the surface energy between growth layer, substrate, and interface can also give insight into the growth modes. To discuss this, we first introduce the surface wettability in terms of surface energies in the system, as described in Figure 2.4. Young's equation describes the relationship between the surface energy of the substrate ($\gamma_S$), growth layer ($\gamma_L$), interface ($\gamma_i$), and contact angle ($\theta$) as follows:

$$\gamma_s = \gamma_i + \gamma_L \times \cos(\theta). \qquad (2.1)$$

In the case of low contact angle, as shown in Figure 2.4(a), the growth layer makes the substrate surface hydrophilic, which facilitates layer-by-layer growth. According to Equation 2.1, $\gamma_S > \gamma_i + \gamma_L$ for the Frank-van der Merwe mode (2D growth) or Stranski-Kranstanov mode (2D-3D growth). Conversely, as shown in Figure 2.4(b), a large contact angle makes the substrate surface hydrophobic, which enables island growth. Thus, Equation 2.1 shows $\gamma_S < \gamma_i + \gamma_L$ for the Volmer-Weber mode (3D growth).

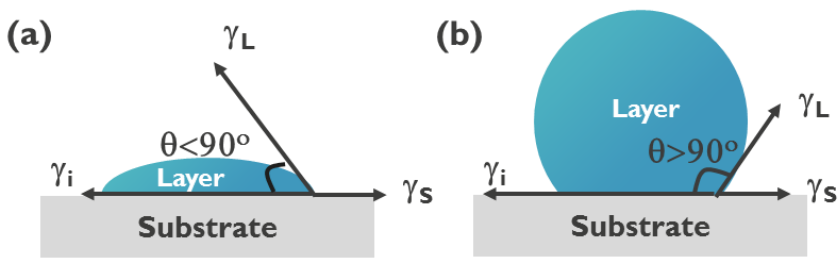


**Figure 2.4:** (a) Hydrophilic and (b) hydrophobic surfaces corresponding to layer-by-layer and island growth modes, respectively.

## 2.2 Molecular Beam Epitaxy

In the 1960s, A.Y. Cho and J.R. Arthur of Bell Labs introduced the first molecular beam epitaxy (MBE) process for the growth of GaAs [4, 5]. Since then, many applications of MBE have been developed for the preparation of different materials, including metals, semiconductors, and insulators. An ultra-high

vaccum (UHV) is used during the MBE process. In the traditional III-V growth process, the base pressure is on the level of $10^{-10}$ Torr. Under such a pressure, the mean free path inside the chamber can be up to $10^{6}$ m, whereas the distance from the material source to the substrate is around 1 m. This means that the element beam will directly be ejected to the substrate. Owing to the UHV, MBE can not only be used to control thin film growth at an atomic level, but can also be combined with in-situ surface characterization such as reflection high energy electron diffraction (RHEED), spectroscopic ellipsometry, and X-ray photoemission spectroscopy (XPS) [6]. These characteristics make MBE stand out among the different growth techniques for crystalline oxide/Si integration. [7, 8]

### 2.2.1. MBE Cluster System

In this thesis, we use the Riber49 200mm MBE cluster system, which comprises a loadlock chamber and three reactors for III-V, 2-D, and oxide materials. The sample size is varied from 2- to 4- and 8-inch substrates. During the operation of the process, first, the sample is introduced into the loadlock chamber. After the pressure is pumped to around $10^{-7}$ torr, the sample is transported by a robotic arm to the cluster chamber, where the pressure is maintained at $10^{-10}$ torr by the cryo pump. The sample can then be transferred to any of the reactors for the deposition of III-V, 2-D, or oxide materials.

(a)

(b)

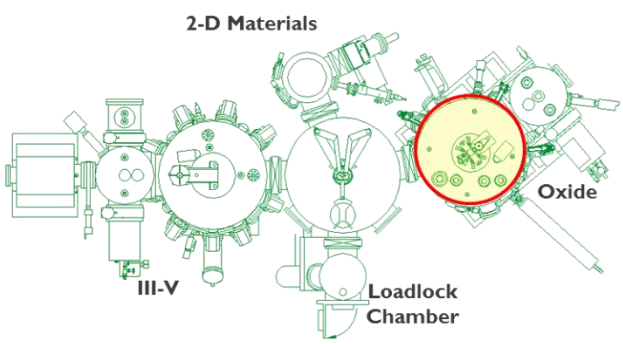

**Figure 2.5:** (a) Photograph and (b) schematic diagram of the Riber49 200mm MBE cluster system.

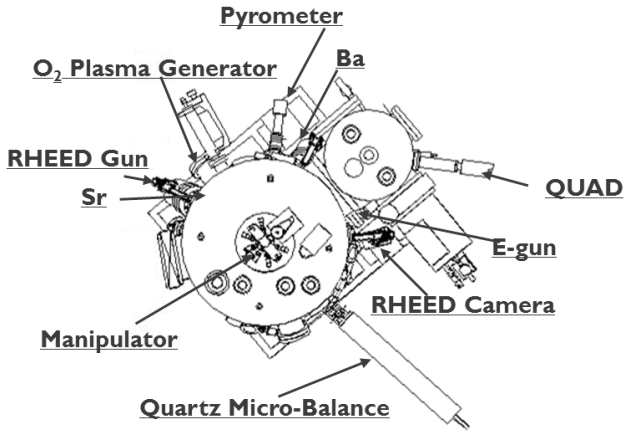


**Figure 2.6:** Components of the oxide chamber.

Figure 2.6 illustrates the components of the MBE oxide chamber, which contains Ba, Sr, Ti, $Al_2O_3$, and $HfO_2$ sources. In this work, only Ba, Sr, and Ti are used. Ba and Sr are evaporated from thermal effusion Knudsen cells. The element is placed in the crucible, which is surrounded by heating filaments. When the temperature reaches the evaporation point, under UHV, the element sublimes to the gas phase and forms an atomic beam projected towards the sample. Owing to the design of Knudsen cells, the temperature can be well controlled and, thus, the flux is stable. Given its high evaporation point, Ti is heated using an electron gun (E-gun). First, electrons are generated by thermal emission from a heated filament. The electron beam is then accelerated by an electric field and moved by a magnetic field towards the Ti source. The electron bombardment is used to heat the Ti until it reaches the temperature at which the desired flux rate is obtained. The quadrupole mass spectrometer (QUAD) mounted near the E-gun detects the Ti partial pressure during operation. The read-out signal of the partial pressure is sent to the E-gun, forming a feedback loop that is used to control the E-gun power for the stabilization of the Ti flux. A shutter is installed in the front of each cell to stop the flux. The flux of all of the materials is calibrated prior to the growth using the quartz crystal microbalance. The observed change in the oscillation frequency of the quartz is used to evaluate the deposition quantity. During BTO or STO growth, oxygen is introduced to react with Sr, Ba, and Ti. The oxygen flux is controlled using a mass flow controller. To improve the oxidation state of the Sr, Ba and Ti metals, a remote plasma source is used to produce atomic oxygen at a plasma power of up to 600 W.

## 2.3 Reflection High Energy Electron Diffraction

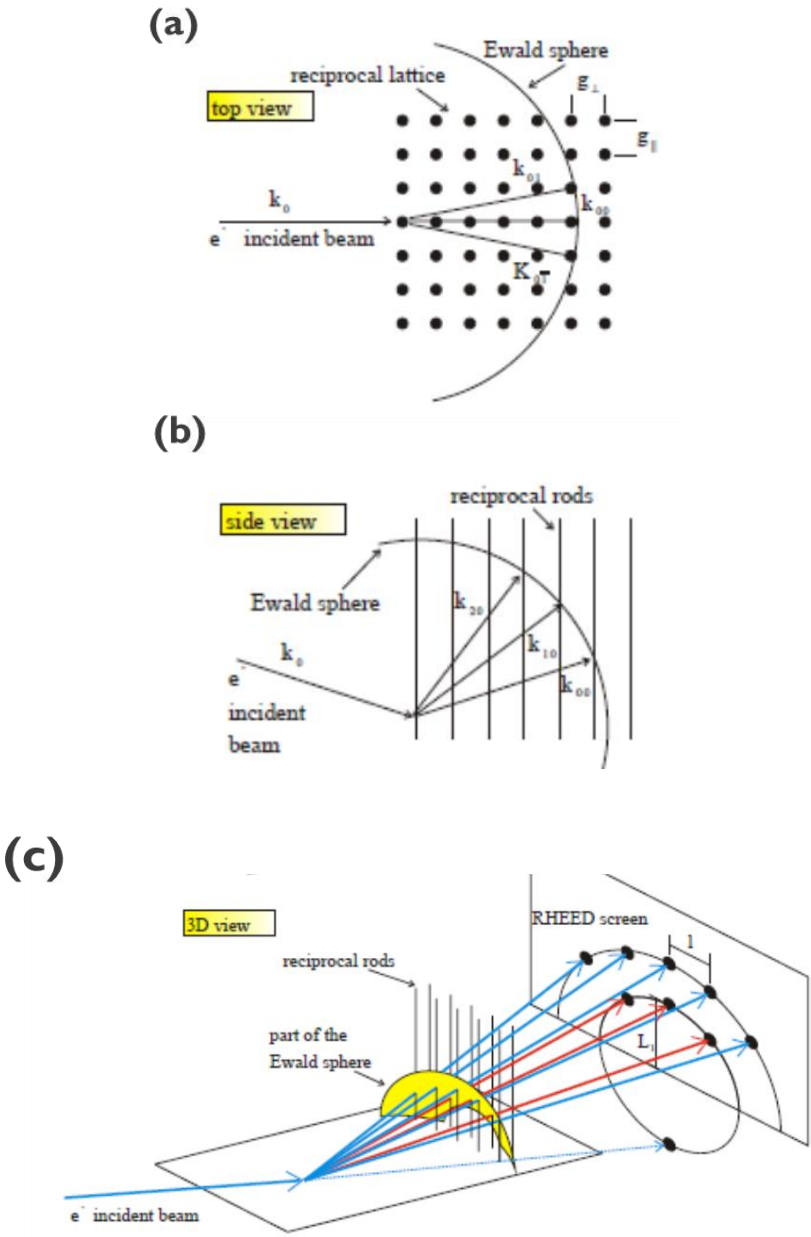

**Figure 2.7:** (a) Top view and (b) side view of reciprocal rods and Ewald spheres for electron beam diffraction. (c) 3-D diagram illustrating the formation of RHEED patterns in MBE. These figures are reproduced from the ref. [10].

RHEED is a technique that can be used for in-situ and real-time observation of surface dynamics during MBE growth. A high energy (20 keV in our setup) electron beam is incident to the surface at a grazing angle (1–3°). Such a grazing incidence makes RHEED sensitive to the top few monolayers. Additionally, the short electron wavelength allows atomic information on the surface to be resolved. The resulting diffraction patterns are projected onto a fluorescent screen and captured by a CCD camera. To obtain good film uniformity, the sample is rotated during the growth. Therefore, RHEED can reveal surface structure along different orientations.

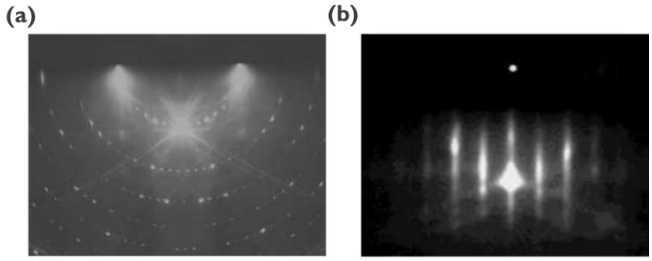


**Figure 2.8:** (a) Ideal and (b) typical RHEED patterns for 2-dimensional layers. [9]

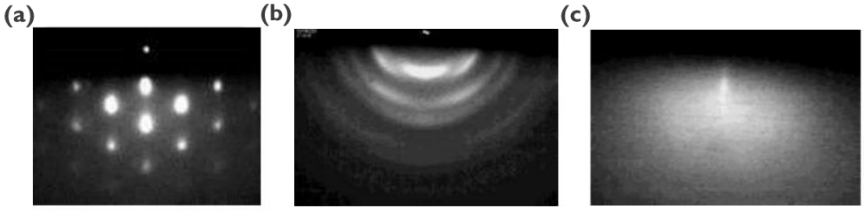


**Figure 2.9:** RHEED patterns for a (a) rough surface, (b) polycrystalline surface, and (c) amorphous surface. These figures are reproduced from the ref. [9].

In principle, a RHEED pattern results from the constructive interference of the electrons diffracted by the certain crystal plane [9]. As shown in Figure 2.7(a) [10], the Ewald sphere can be defined by the wave vector ($k_0$) of the incident electrons. Then, meeting the momentum conservation, the intersection between the reciprocal lattice of that certain crystal plane and the Ewald sphere makes the corresponding RHEED pattern observable. Because the detection depth of

grazing-incident electrons in RHEED is only few monolayers, the effective detected material can be regarded as a 2-dimensional layer. In this case, the reciprocal lattice becomes a series of rods elongated vertically with respect to the substrate surface. The Ewald sphere radius is inversely proportional to the electron wavelength, which is very small, around 10 pm. Therefore, the Ewald sphere is so large that the peripheral intersections with the reciprocal lattice of the layer become "flat", as seen in Figure 2.7(a) and (b) [10]. Electron diffraction patterns like that shown in Figure 2.7(c) will be projected onto the screen [10]. However, the RHEED pattern in Figure 2.7(c) presents the ideal case for a perfect 2-dimensional layer and good electron beam condition. In reality, some imperfections in the electron beam and crystals always prevent RHEED patterns from appearing as perfect spots like those shown in Figure 2.8(a). For example, the shell of the Ewald sphere is thickened by energy variations from the electron beam. Also, phonon vibrations or lattice imperfections broaden and shorten the reciprocal lattice rods. Thus, the diffraction pattern of a smooth surface shows elongated streaks. Figure 2.8(b) presents the typical RHEED patterns for the 2-D layer. Differences in crystallinity and morphology also produce different features in RHEED patterns: the rough surface that results from island growth produces a RHEED pattern that is spotty (Figure 2.9(a)). For poly-crystalline layers, the RHEED pattern becomes ring-like (Figure 2.9(b)), while amorphous films result in a diffuse background (Figure 2.9(c)).

## 2.4 X-Ray Diffraction

X-ray diffraction (XRD) is a non-destructive and efficient approach for the characterization of crystal structures [11]. By controlling the impinging angle of the incident beam, the surface, interface, and bulk properties of a material may be determined from its XRD pattern. The basic XRD principle follows Bragg's Law: $2d\sin\theta = n\lambda$, where d is the inter-planar distance, $\theta$ is Bragg's angle, and $\lambda$ is the X-ray wavelength. Based on Bragg's Law, XRD can reveal a large amount of crystal information, including strain, lattice constant, crystal orientation, and crystallite size. XRD is also applicable to the characterization of some complicated heterostructure systems, such as multiple layers or even superlattices, revealing the thickness, density, and even roughness of each layer stack.

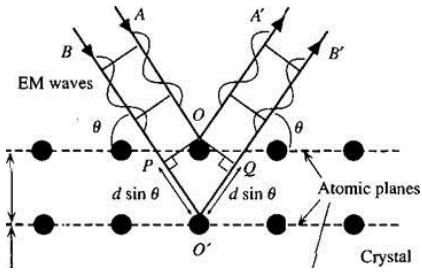


**Figure 2.10:** Schematic of Bragg's condition. The figure is reproduced from the ref. [11].

The XRD system used in this work was a Panalytical X'Pert Pro diffractometer (PANalytical). Figure 2.11 shows a photograph of the equipment and a schematic diagram describing all the angle definitions. Before the analysis, the substrate material was used as a reference to execute a series of careful beam/setup alignments. Then, according to the information required, different scans, such as ω-2θ, ω-scans, azimuthal ϕ scans, reciprocal space mapping (RSM), or pole figure (PF) mapping, could be carried out. Although RSM and PF reveal all the details contained in the reciprocal space of the crystal, it takes too much time to obtain such mappings. Therefore, instead, one dimensional scans like ω-2θ, rocking curve, and azimuthal ϕ scans are usually executed. A brief introduction to RSM and PF is given below.

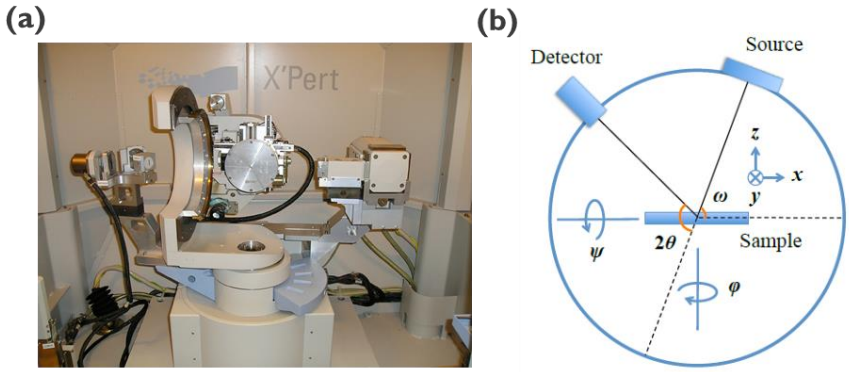


**Figure 2.11:** (a) A photograph of the equipment and (b) diagram describing all the angle definitions.

*RSM*: RSM measurements characterize the relationship between the substrate and crystalline thin film in reciprocal space. A RSM consists of a number of ω-2θ scans for different ω angles. The composition, strain relaxation, and defect density

in the thin film can then be deduced from its shape and position relative to the substrate in the RSM, as shown in Figure 2.12. [12]

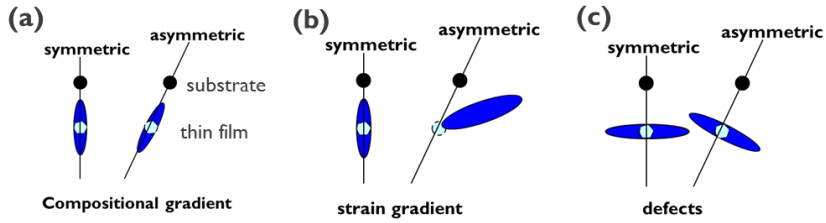


**Figure 2.12:** Relationships between layer and substrate in RSM illustrating the effect of (a) a compositional gradient, (b) a strain gradient, and (c) defects. The green dot-like signals indicate the ideal crystallinity in the thin film. However, different imperfect properties makes the signal become an ellipse and show different tilt angles as well as positions. These figures are reproduced from the ref. [12].

*PF*: PF measurement is a method used to analyze the crystal symmetry, preferred orientation, epitaxial relationship between layer and substrate, and degree of sample orientation. During the measurement, the crystal plane expressed by the miller index, (hkl), is first chosen ($\omega$ and $2\theta$ are fixed) and the azimuthal angle $\phi$ and tilt angle $\Psi$ are then scanned simultaneously. As shown in Figure 2.13, PF can be interpreted by considering the intersection of the normal to the selected hkl-planes with an imaginary hemisphere situated above the sample surface. The projection of this hemisphere on a planar surface results in a pole figure.

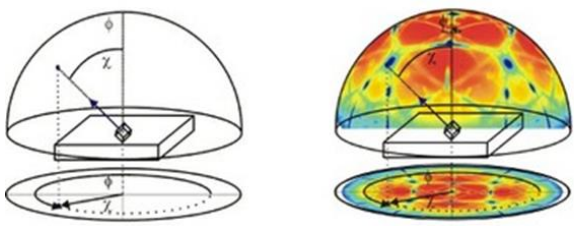

**Figure 2.13:** Schematic illustrating the construction of a pole figure by scanning $\phi$ and $\Psi$ in XRD. These figures are reproduced from the ref. [11].

## 2.5 Spectroscopic Ellipsometry

Spectroscopic ellipsometry (SE) is a fast and non-destructive technique used to characterize thin-film materials [13]. It can be used to determine layer thickness as well as optical constants (complex refractive index or dielectric function). In principle, SE measures the ratio between the reflection coefficients of TE ($r_{TE}$) and TM ($r_{TM}$) polarized light waves incident on the stack under study. This ratio is then expressed as a function of the characteristic terms tan(Ψ) and Δ as follows:

$$\frac{r_{TM}}{r_{TE}} = tan(\Psi)e^{i\Delta} \qquad (2.2)$$

Based on the number of TE- and TM-polarized light waves that are reflected by the sample, Eq. (2.2) can be used to reveal information about its polarization state. SE obtains Ψ and Δ spectra as described in Fig. 2.14. Because it is difficult to interpret the measurement results directly from the absolute values of Ψ and Δ, it is necessary to construct an optical model for data analysis. Physical properties including the optical constants and film thickness of the sample can then be extracted. Then, the reflectance R and transmittance T at a different angle of incidence can be calculated. Furthermore, measurements carried out in the UV/visible region can be used to analyze the band structure. Particularly, the bandgap $E_g$ can be deduced from the onset of increasing optical absorption. Because the band structure generally varies according to surface temperature, alloy composition, phase structure, and crystal grain size, these properties can also be determined from spectral analysis of the optical constants of the sample. Moreover, in the infrared region, SE can be used to investigate the presence of carriers, phonons, and local structure via free-carrier and infrared absorption.

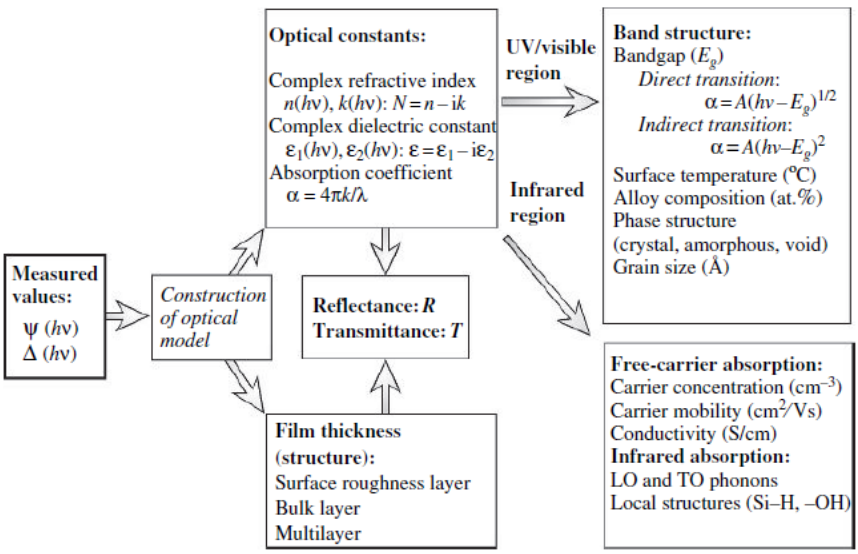

**Figure 2.14:** Flow chart describing characterization of physical properties by SE. This figure is reproduced from the ref. [13].

## 2.6 Scanning Probe Microscopy

### 2.6.1. Atomic Force Microscopy

The surface morphology of the grown samples was examined by atomic force microscopy (AFM) operated in tapping mode. AFM allows the imaging of surface morphology at a resolution that can reach an atomic step in the direction perpendicular to the sample surface. It is therefore one of the most powerful tools for imaging, measuring, and manipulating matter at the nanoscale. The AFM apparatus consists of a cantilever with a sharp tip (probe) at its end which is used to scan the sample surface (Figure 2.15) [14]. The cantilever is typically made with silicon and has a tip radius on the order of a few nanometers (around 10 nm max) in curvature. When the tip is brought into proximity with a surface, force gradients between the tip and the sample interact with the harmonic oscillator formed by the cantilever. This effect induces both energy dissipation and a shift in the frequency of the oscillator. The feedback loop formed by the laser detection maintains the same level of energy dissipation and frequency shift by moving the Z height on the sample surface. The surface topology is then obtained by scanning the surface and reading the Z movement.

AFM has several advantages over scanning electron microscopy (SEM). AFM provides a true three-dimensional surface profile, whereas SEM gives a two-dimensional projection. Besides, samples viewed by AFM do not require any special treatments and can be measured well in ambient air or even in liquid. This makes it possible to study biological macromolecules and living organisms. In principle, AFM can provide higher resolution than SEM. UHV AFM is comparable in resolution to scanning tunneling microscopy (STM) and transmission electron microscopy (TEM). However, a disadvantage of AFM compared with SEM is the image size: SEM can be used to image an area on the order of millimeters by millimeters with a depth on the order of millimeters, but AFM cannot. Besides, owing to the nature of AFM probes, it is also difficult to measure features with high aspect ratio.

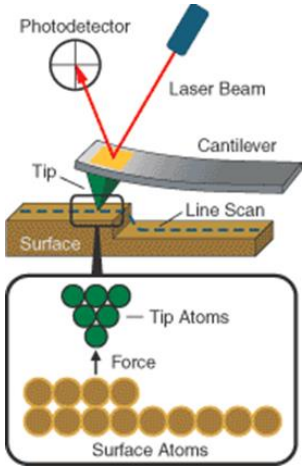


**Figure 2.15:** Schematic illustration of AFM. The figure is reproduced from the ref. [14].

### 2.6.2. Conductive Atomic Force Microscopy

Conductive AFM (CAFM) characterizes local conductivity variations across conducting and semiconducting materials. Its operation is similar to the tapping mode of AFM. In conductive AFM, a DC bias is applied to the tip while the sample is grounded. A linear amplifier senses the current flowing through the sample, with detectable range of 10 pA to 1 μA. For currents ranging from 100 fA to 100 pA, tunneling AFM (TUNA) can be used. TUNA works similarly to CAFM but has higher current sensitivity, allowing ultra-low currents (<1 pA) to be determined through the thickness of thin films, and is of particular importance when electrical characterization of such low-conductivity samples is needed at high lateral resolution.

### 2.6.3. Piezo-response Force Microscopy

Piezo-response force microscopy (PFM) is used to characterize the piezo-response of a thin film surface. Its operation is similar to that of AFM and CAFM. During the measurement, an electric field is applied to the sample surface via the cantilever. A piezo-effect on the sample surface causes its morphology to experience minor deformation induced by the external field. To decouple the deformation caused by the piezo-effect from the surface morphology, a lock-in amplifier with AC bias signal is used to read the local piezo-response. Then, after

scanning over the whole sample surface, the piezo-response mapping can be obtained. The operation of PFM is depicted in Figure 2.16 [15]. Moreover, by applying a DC bias prior to PFM measurement, we can also write polarization on the surface locally, and thus produce different piezo-response on the sample surface.

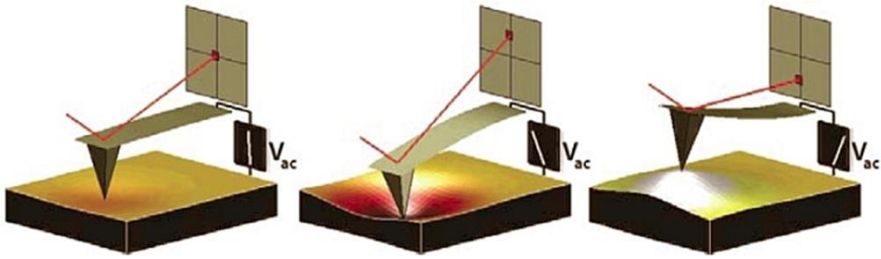


**Figure 2.16:** Illustration of PFM operation. The sample deforms in response to the applied voltage. This, in turn, causes the cantilever to deflect, which can then be measured and interpreted in terms of the piezoelectric properties of the sample. These figures are reproduced from the ref. [15].

## 2.7 Transmission Electron Microscopy

Exploiting the wave-particle duality of electrons, a transmission electron microscope (TEM) uses a beam of electrons instead of light to analyze a specimen. Figure 2.17 shows the major components of the TEM instrument. The TEM apparatus consists of an electron emission source, electromagnetic lenses, and an electron detector. A very thin sample is placed in the electron beam path. The electron beam is generated, accelerated, and focused on the sample using the electromagnetic lenses. The beam penetrates the sample, and is modified by the interaction between the electrons and sample material. The beam is then magnified by other lenses and detected, for example, using fluorescence. TEM allows images of very thin samples down to atomic resolution to be obtained, because the wavelength of an electron can be as small as few picometers. The image resolution obtainable using electrons is therefore much greater than that using visible wavelengths, like with optical microscopes. Besides, like many imaging techniques, the original TEM image comprises the diffraction patterns of the specimen, i.e., the image in the reciprocal space. The image is reconstructed by Fourier transformation to obtain the real-space image.

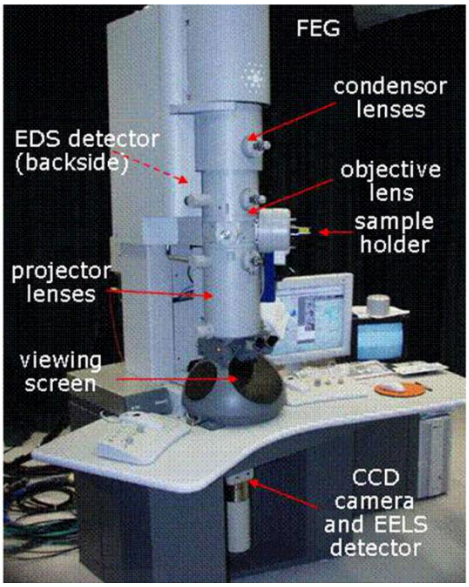


**Figure 2.17:** Major components of the TEM instrument.

## 2.8 X-ray Photoelectron Spectroscopy

X-ray Photoelectron Spectroscopy (XPS) is an analysis technique that uses x-rays in an UHV environment to investigate the chemical compounds on a sample surface. Although the principle is simple, XPS reveals a vast amount of information about a sample; including composition and chemical states. The XPS measurement is actually composed of two processes, which are the interactions between x-ray and electrons. The first is Compton scattering. An incident x-ray collides with a core electron. The collision causes the electron to be ejected from the electronic shell with a certain kinetic energy. Based on energy conservation, the binding energy of the electron to the atom can be extracted according to:

$$Binding\ Energy = \mathrm{h}\nu - \text{Kinetic Energy} - \text{correction constant}$$

The ejection of the inner core electron leads to the second process; the missing inner core electron results in an unstable hole in the electronic shell. An electron from the valance shell then fills the newly formed hole, causing an Auger electron to be emitted from the valence shell to conserve energy. Again, the kinetic energy

of the emitted electron is directly related to the binding energy of the electron to the atom. These two processes are used to identify the elements in the sample since the binding energy of the electrons is unique for every element. Figure 2.18 shows the basic components of a monochromatic XPS system and illustrates the schematics of the mechanisms during the measurement [16].

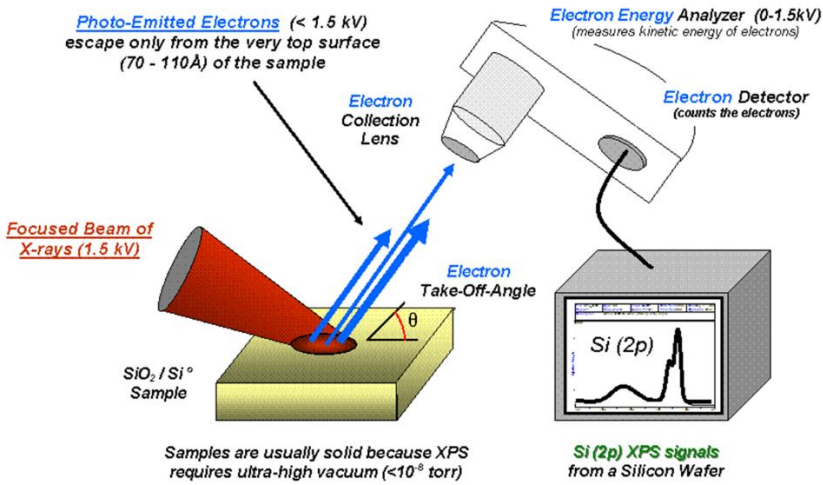


**Figure 2.18:** Basic components of the monochromatic XPS system. These figures are reproduced from the ref. [16].

## 2.9 Rutherford Backscattering Spectroscopy

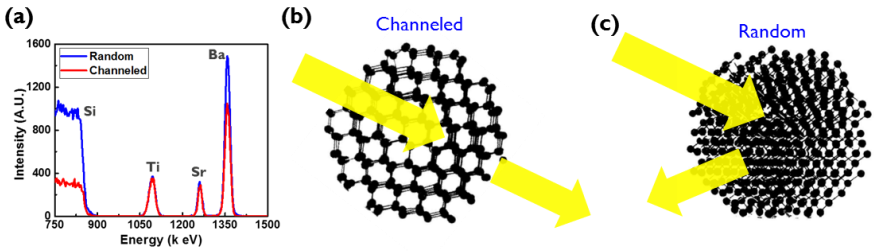


**Figure 2.19:** (a) The typical random and channeled RBS spectra for BTO on STO-buffered Si(001) substrate. The schematic of the (b) channeled and (c) random cases.

In this thesis work, Rutherford Backscattering Spectroscopy (RBS) is used to determine the composition or crystallinity of the oxide thin film. In principle, the RBS exploits the high-energy alpha particle ($He^{2+}$) to collide on the specimen. By measuring the energy of the backscattered alpha particle, the composition inside the thin film can be evaluated. In addition, the thin film crystallinity can also be quantitatively characterized by the RBS channeling analysis. Figure 2.19(a) presents the typical RBS result with random and channeled spectra. As illustrated in Figure 2.19(b), when the beam is well-aligned, the specimen can be channeled through by the alpha particle beam, resulting in the channeled spectrum. Then, by tilting the sample with $2^o$ intentionally, the aligned crystal becomes random. Thus, the beam will be blocked and backscattered by the disordered crystal, having the random spectrum, as plot in Figure 2.19(c). Finally, according to the minimum yield ($\chi_{min}$), defined by the signal ratio of the channeled and random particles, the crystallinity can be quantitatively analyzed. The Ba $\chi_{min}$ in Figure 2.19(a) is around 70%.

## 2.10 Conclusion

This chapter begins with a brief physical principle of the epitaxial growth. Then, the MBE system as well as in-situ RHEED are introduced. Besides, the different thin film characterization methods that we extensively use in the following chapters are explained.

## References

[1] J. A. Venables, Introduction to Surface and Thin Film Processes. Cambridge: Cambridge University Press, 2000.

[2] G. Saint-Girons, HDR, “Epitaxie des systemes heterogenes”, Ecole Centrale de Lyon and University of Lyon, 2009.

[3] Courtesy of Clement Merckling.

[4] A.Y. Cho, “Film Deposition by Molecular Beam Techniques”, J. Vac. Sci. Tech. 8, S31, (1971)

[5] A. Y. Cho and J. R. Arthur, “Molecular Beam Epitaxy”, Prog. Solid State Chem. 10, 157, (1975)

[6] M. A. Herman and H. Sitter, “Molecular Beam Epitaxy: Fundamentals and Current Status”, Springer Science & Business Media, 2013.

[7] D. G. Schlom, "Perspective: Oxide molecular-beam epitaxy rocks!," APL Materials, vol. 3, no. 6, p. 062403, 2015.

[8] A. A. Demkov and A. B. Posadas, “Integration of functional oxides with semiconductors” Springer, 2014.

[9] W. Braun, “Applied RHEED”, Springer Berlin Heidelberg, 1999.

[10] J. Klein. “Epitaktische Heterostrukturen aus dotierten Manganaten”. PhD thesis, University of Cologne, 2001. pages 24, 25.

[11] C. Ferrari and C. Bocchi, "4 - Strain and composition determination in semiconducting heterostructures by high-resolution X-ray diffraction A2 - Lamberti, Carlo," in Characterization of Semiconductor Heterostructures and Nanostructures, Amsterdam: Elsevier, 2008, pp. 93-132.

[12] http://prism.mit.edu/xray/oldsite/Introduction%20to%20HRXRD.pdf

[13] H. Fujiwara, "Spectroscopic Ellipsometry”, John Wiley & Sons, Ltd, 2007.

[14] G. Niu, “Epitaxy of crystalline oxides for functional materials integration on silicon”, Ecole Centrale de Lyon and University of Lyon, 2010.

[15] Image courtesy S. Jesse, ORNL.

[16] https://en.wikipedia.org/wiki/X-ray_photoelectron_spectroscopy#/media/File:System2.gif

# 3

# Calibration of BTO Stoichiometry[a]

Given the unique physical properties of thin-film perovskite oxides ($ABO_3$), exhibiting at the same time strong ferroelectric, piezo-electric and electro-optical effects, their monolithic integration with compound semiconductors offers many new degrees of freedom for advanced device generations [1-3]. It is widely reported that the above-mentioned effects are superior in single crystalline $ABO_3$ compared to poly-crystalline or amorphous layers [4-6]. However, obtaining high-quality integration of crystalline $ABO_3$ with semiconductors remains challenging due to the huge discrepancy in their respective crystal lattices and chemical properties [5-6].

As explained in chapter 1, the path towards the integration of crystalline $ABO_3$ thin films with semiconductors wasn't opened until the late 1990s. McKee et al utilized an alkaline earth metal submonolayer to achieve high quality $SrTiO_3$ (STO) epitaxy on Si by molecular beam epitaxy (MBE) [7]. Since then, the epitaxy of STO onto Si substrates was heavily investigated, given its compatibility with several other functional oxides and its interesting material characteristics [8-10]. Nevertheless, its properties are highly dependent on the exact epitaxial conditions such as substrates used, growth temperature and, especially, stoichiometry [11-14]. Even if several techniques for realizing high quality STO thin films have been developed [15-17], avoiding local or global non-stoichiometry is still difficult [18]. In order to well control material properties, it is important to develop an efficient method to understand the stoichiometry inside the layer during and after the growth. To evaluate the composition of the STO

[a] This is the enhanced version of the paper published in *J. App. Phys.* **120**, 225114 (2016)

layer, several diffraction techniques are commonly applied [19-21]. During the growth, many groups utilize reflection high energy electron diffraction (RHEED) to monitor the Sr and Ti flux ratio ([Sr]/[Ti]) in the layer in real-time, and to control the stoichiometry [19,20]. After the growth, the out-of-plane lattice constants retrieved from a ω-2θ scan along the [001] axis in X-ray diffraction (XRD) can also qualitatively reveal the ratio [Sr]/[Ti] [19, 21].

However, for other $ABO_3$ oxides, these are much less discussed than for STO. Even though all $ABO_3$ have a similar crystal structure, the different electron numbers, atom sizes and composition from various elements will lead to different diffraction behaviors [22]. Given its strong ferroelectric and electro-optical properties, lead-free $BaTiO_3$ (BTO) has been studied for over 70 years [23, 24]. With the successful development of an STO on Si epitaxial process, also BTO recently is getting considerable research interest, in particular for the integration in novel Si-based devices. For example, the authors of [2, 25] showed high speed silicon integrated modulators, exploiting the excellent electro-optical properties of a hybrid integrated BTO layer. However, as with STO, the characteristics of such BTO layers are greatly dependent on the [Ba]/[Ti] composition [26-28], so accurately controlling the stoichiometry of the deposited BTO is crucial.

Therefore, in this chapter, we will mainly investigate the impact of the stoichiometry of an epitaxially grown BTO layer on its diffraction characteristics. The BTO layers are grown by MBE onto Ge(001), which has a quasi-zero lattice mismatch of 0.2% to BTO in a 45° crystal rotation epitaxial relationship [29]. First, the [Ba]/[Ti] ratio is measured by Rutherford backscattering spectroscopy (RBS). Then, the results of RHEED, XRD and transmission electron microscope (TEM) experiments are systematically presented and discussed. Moreover, a model for the diffraction by non-stoichiometric BTO is developed, which explains several of the unique observations in our experiments.

## 3.1 Methodology for Growing Epitaxial BTO on Ge(001)

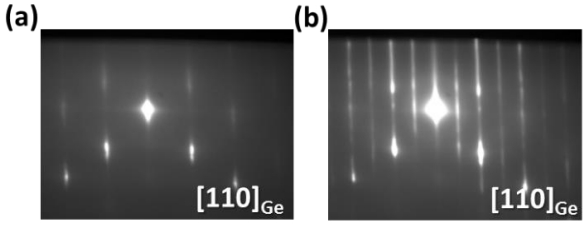


**Figure 3.1:** RHEED patterns along $[110]_{Ge}$ for Ge(001) substrate (a) with and (b) without native oxide.

Four samples with varying [Ba]/[Ti] ratio and denoted A to D are prepared. All of them are grown on a 4-inch Ge(001) substrate in a Riber49 200 mm production MBE reactor. Ti is evaporated with an electron beam controlled by a feedback loop from a QUAD mass spectrometer to control a constant flux during growth. The Ba atomic flux is obtained using a standard Knudsen effusion cell and the [Ba]/[Ti] flux ratio is tuned with the help of a quartz crystal microbalance. A radio frequency (RF) remote plasma source is used to produce atomic oxygen during the growth.

Prior to BTO deposition, native oxide removal from Ge surface is necessary. Figure 3.1(a) demonstrates the 1x1 RHEED reconstruction pattern along $[110]_{Ge}$ for a Ge(001) substrate covered with native oxide. The Ge native oxide is, then, thermally desorbed by heating the substrate to 800 °C for 30 minutes. Dangling bonds on the Ge surface form dimers to obtain lower surface energy, as shown in Figure 3.2(a), resulting in a bright (2x1) RHEED reconstruction pattern in Figure 3.1(b). Since BTO has 29% lattice mismatch against the Ge lattice constant (BTO: 3.992 Å and Ge: 5.658 Å), a 45$^{o}$ rotation of the BTO lattice with respect to the Ge substrate is required to obtain quasi-zero lattice mismatch. In order to achieve this, insertion of exact 0.5 monolayer (ML) BaO between BTO and Ge is needed [29]. Next, we are going to use RHEED to assist us to control Ba coverage on the Ge surface. Therefore, calibration of the RHEED intensity and Ba coverage is performed. RHEED intensity is monitored at the ½-ordered streakline; meanwhile, the Ba coverage is measured by RBS. Figure 3.3(a) shows that the RHEED intensity is a function of the Ba coverage (deposited at 550 $^{o}$C). Figure 3.3(b) presents the corresponding RHEED patterns. The decreasing RHEED intensity suggests that when Ba addition starts, the Ge surface roughens. When the Ge surface is covered with 0.5 ML Ba, the RHEED intensity reaches a maximum, suggesting the Ge surface is flattened again. From a first principle calculation, it is proved that the most favorable site for a Ba atom on a Si(001) surface is position A, which has the lowest surface energy, as shown in Figure 3.2(b) [30]. Inferring from Ba atoms on a Si(001), Ba atoms on the Ge(001) surface are believed to be located at the corresponding positions as shown in Figure 3.2(c). This atom configuration also explains why we observe a 1x2 reconstruction from RHEED. If we add Ba until 0.75 ML, the RHEED intensity becomes blurry, indicating the surface is roughened again. Therefore, Figure 3.3(a) shows that 0.5 ML Ba can be obtained by controlling the RHEED intensity of an ½-order line. Subsequently, we introduce oxygen to oxidize the 0.5 ML Ba to BaO, which can be a crystal template guiding BTO to register on Ge with 45$^{o}$ lattice rotation. Then, the substrate temperature is increased to 630 °C for BTO growth under an oxygen partial pressure of ~$1.6\times10^{-6}$ torr.

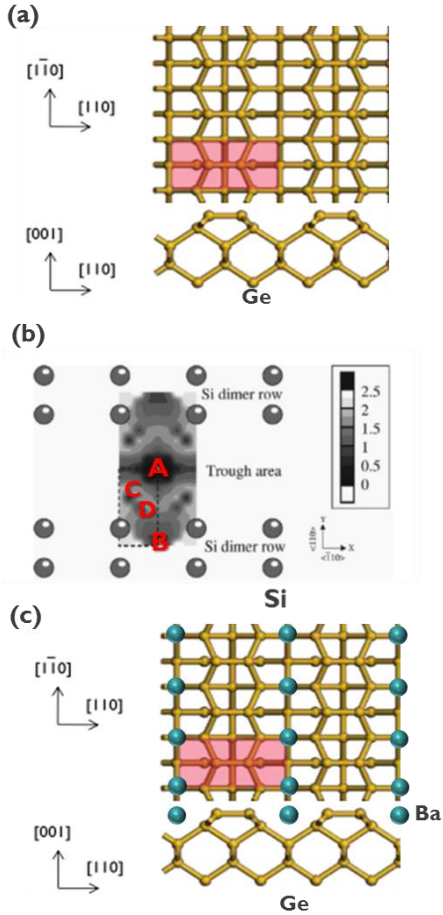


**Figure 3.2:** (a) Schematic of 1x2 reconstructed Ge surface with dimers (b) Map of surface potential energy for a Ba atom on a Si(001) surface. The figure is reproduced from the ref. [30]. (c) Schematic of Ba atoms on Ge(001) surface to form 1x2 reconstruction.

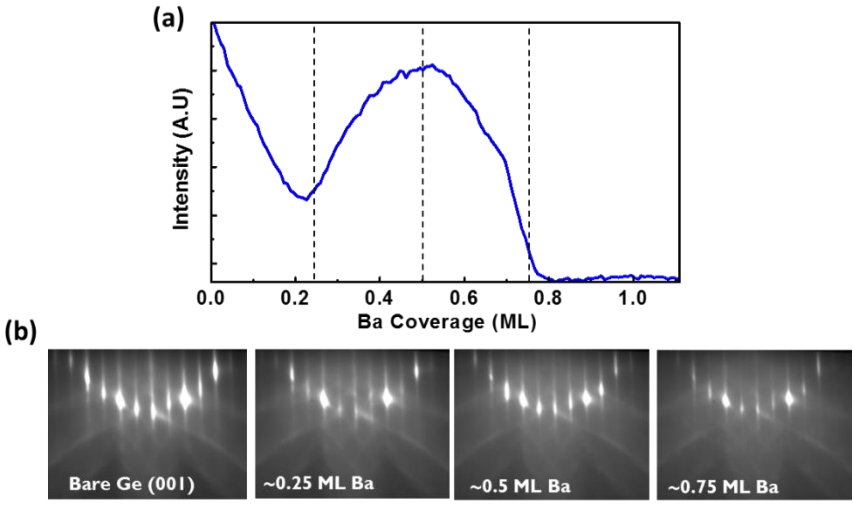


**Figure 3.3:** (a) The RHEED intensity for 1/2-order streak line as function of Ba coverage (b) corresponding RHEED patterns.

For all samples, [Ba] and [Ti] were measured by Rutherford backscattering spectrometry (RBS) and the results are summarized in Table 3.1, where the [Ba] excess ε is defined as $Ba_{1+\varepsilon}TiO_{3-\zeta}$. The [Ba] excess in the BTO films varies from -90% to 28%. The 4 samples used in the present study are representative for each unique phenomenon, which will be detailed in the following. XRD measurements show that above 28% the films become completely amorphous and these are therefore not included in the current study. In the next section we provide and discuss the detailed structural and diffraction behavior as observed from RHEED, XRD and TEM experiments as function of the ratio [Ba]/[Ti] for the different samples.

**Table.3.1** Summary of RBS-measured [Ba]/[Ti] ratio in the different BTO-layers grown.

| | [Ba]/[Ti] in RBS | Excessive [Ba][a] |
|---|---|---|
| Sample A | 0.10 | -90% |
| Sample B | 0.96 | -4% |
| Sample C | 1.08 | +8% |
| Sample D | 1.28 | +28% |

[a][Ba] excess, ε, is defined by $Ba_{1+\varepsilon}TiO_{3-\zeta}$.

## 3.2 BTO Crystal Structure on Ge(001)

### 3.2.1 Reflection High Energy Electron Diffraction Analysis

Figure 3.4 presents the evolution of the RHEED diffraction patterns and the corresponding schematics for the samples A, B, C and D. In Figure 3.4(a), sample A with -90% [Ba] excess in the BTO shows spotty RHEED patterns indicating 3D growth with a rough surface. The corresponding miller-indexed planes can be defined from the tetragonal BTO crystal lattice. Given the excess [Ti], the oxygen content in the BTO is decreased, leading to both Ti-rich and O-deficient BTO compounds, $BaTi_{1+\Delta}O_{3-\delta}$ [31]. It has been reported that O-deficient BTO contains $(111)_{BTO}$ twins [32, 33], which can be observed in the RHEED patterns along $[100]_{BTO}$ in Figure 3.4(a). With a [Ba]/[Ti] ratio closer to the stoichiometric composition, the RHEED patterns of sample B (4% extra [Ti]) change (Figure 3.4(b)): instead of a spot-only 3D pattern, they now show streak-lined patterns overlaid with a few spots, representing a 2D layer with much improved roughness on the surface. Diffraction lines at (11), (-1-1), (01), (0-1) can be observed revealing that the diffraction behavior is changed as the [Ba]/[Ti] ratio reaches unity. Figure 3.4(c) shows RHEED patterns of sample C, which has 8% extra [Ba]. One can notice that the extra Ba roughens the surface again, resulting in more spotty patterns overlaid on the streak lines. In addition, there are extra spots between the diffraction lines along $[110]_{BTO}$ and $[100]_{BTO}$ directions, denoted by the gray ellipses in the schematic representations. With further increasing the [Ba] content to 28% in sample D, the spottier patterns in both azimuthal directions, as presented in Figure 3.4(d), indicate the surface roughens further. In addition, more extra spots between the diffraction lines emerge, labeled gray in the schematic. Those extra spots between the diffraction lines in Figure 3.4(c) and 3.4(d) originate from $(111)_{BTO}$ twins in the crystalline layer. In order to incorporate extra BaO in the Ba-rich BTO, $(111)_{BTO}$ nanotwins and $(001)_{BTO}$ Ruddlesden-Popper planar faults are usually generated [19,33]. Therefore, more [Ba] will induce more twins as observed in the RHEED patterns of Figure 3.4(c) and 3.4(d) respectively. Generally, none of the samples show extra x2 reconstruction lines in the RHEED pattern along $[110]_{BTO}$ and $[100]_{BTO}$ resulting from the BaO for the Ba-rich and $TiO_2$ for the Ti-rich BTO, respectively. This might be because the [Ba]/[Ti] element ratio is too far away from the stoichiometric condition to observe this extra x2 reconstruction lines. Despite being with a wide range of the [Ba]/[Ti] cation ratios for $Ba_{1+\varepsilon}TiO_{3-\zeta}$, other works on oxide substrates also show similar stoichiometry-dependent RHEED patterns to our results. [34, 35].

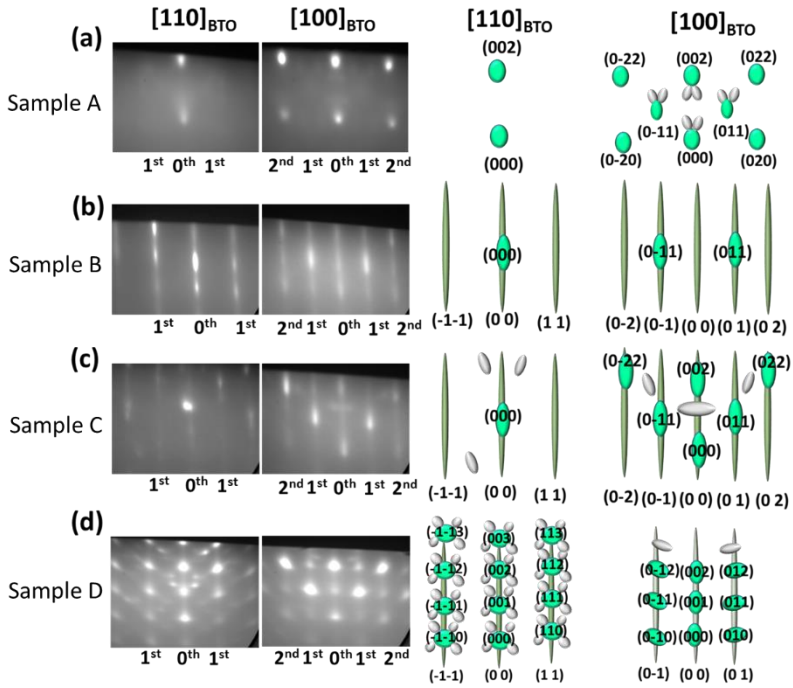


**Figure 3.4:** The RHEED diffraction patterns and corresponding schematics along $[100]_{BTO}$ and $[110]_{BTO}$ of (a) sample A with 90% extra [Ti], (b) sample B with 4% extra [Ti], (c) sample C with 8% additional [Ba] and (d) sample D with 28% additional [Ba], respectively.

### 3.2.2 X-ray Diffraction Analysis

Figure 3.5 describes a series of XRD scans for different BTO samples with using the 1-degree slit in front of the rocking-curve detector. Figure 3.5(a) presents the azimuthal $\phi$ scans for all four samples. While measuring $(\pm1\pm11)_{BTO}$ in samples B to D, $(\pm2\pm24)_{BTO}$ was measured for sample A indicating the absence of the $(\pm1\pm11)_{BTO}$ in the latter. Despite large discrepancies in the [Ba]/[Ti] ratio, surprisingly, all samples still exhibit the same epitaxial relationship with the Ge-substrate, <100>BTO(001)//<110>Ge(001), i.e. a 45° in-plane rotation of the BTO lattice with respect to the Ge lattice. Such 4-fold symmetry also corresponds with azimuthal RHEED scans for all the samples. The symmetrical $\omega$-2$\theta$ scan along the $[001]_{BTO}$ direction shown in Figure 3.5(b) reveals that all BTO layers are seemingly single-crystalline, only showing $(00l)_{BTO}$ Bragg reflection peaks. However, for sample A, the first-order Bragg peak, $(001)_{BTO}$, is missing. This agrees with the absence of this Bragg reflection on the RHEED patterns from sample A, confirming the diffraction behavior changes due to the [Ti] excess.

Also an asymmetrical ω-2θ scan along $[101]_{BTO}$ is conducted and shows a poly-crystalline diffraction spectrum with multiple peaks for all samples except for sample C. These multi-peaks can be filtered by using a narrower slit (<1 degree) in front of the XRD detector or using a detector in the triple-axis configuration. They result from the poly-crystalline and non-stoichiometric BaO and $TiO_2$ compounds contained in the films such as, $Ba_2TiO_4$, $BaTi_2O_5$, $BaTi_4O_9$ ...etc [28]. The diffraction spectra for these compounds are too complicated to be resolved with our measurement setup [36, 37]. Among the different peaks in the spectrum, the $(101)_{BTO}$ peak can be identified by ϕ-scan measurements: only the $(101)_{BTO}$ peak belonging to epitaxial BTO can show 4-fold symmetry as shown in Figure 3.5(a). From the ϕ-scan of $(101)_{BTO}$, we found that the $(101)_{BTO}$ is not observable only in sample A revealing the unique diffraction behavior triggered by extra [Ti]. Finally, Figure 3.5(d) shows the asymmetrical ω-2θ scan along $[111]_{BTO}$. By measuring the ϕ-scan of $(111)_{BTO}$, this Bragg reflection does not appear for sample A suggesting again the 90% excessive [Ti] induces different diffraction behaviors. Besides, all samples, including sample A, show a poly-crystalline diffraction spectrum, presenting even more peaks than for the scan along $[101]_{BTO}$. From this, we conclude the ω-2θ scan along $[111]_{BTO}$ is a better measure for the assessment of the crystallinity of the ideal stoichiometric [Ba]=[Ti] BTO thin films. This correlates with the fact that the non-stoichiometric compounds tend to precipitate in the grain boundaries of twinned $(111)_{BTO}$ [38]. Yet, it is important to realize that the traditional ω-2θ scan along $[001]_{BTO}$ is not sufficient to determine the crystalline quality of the layer.

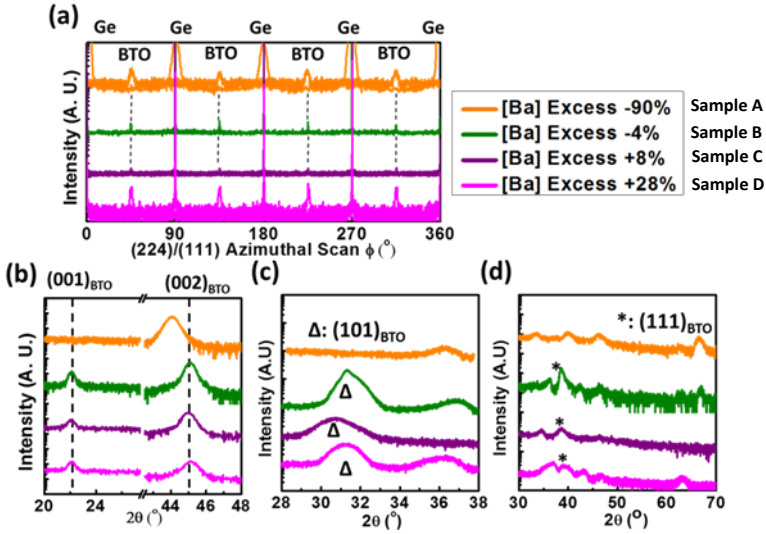

**Figure 3.5:** (a) The azimuthal $\phi$ scan of $(\pm1\pm11)_{BTO/Ge}$ for the samples B to D, and that of $(\pm2\pm24)_{BTO/Ge}$ for the sample A. The $\omega$-$2\theta$ scan along (b) $[001]_{BTO}$, (c) $[101]_{BTO}$ and (d) $[111]_{BTO}$ for all the samples.

To understand the XRD diffraction behavior as function of the [Ba]/[Ti] ratio, the intensity ratio of the three lowest-ordered Bragg peaks ($(001)_{BTO}$, $(101)_{BTO}$ and $(111)_{BTO}$) relative to the $(002)_{BTO}$ peak is calculated and summarized in Figure 3.6. Note that only sample A does not show $(001)_{BTO}$, $(101)_{BTO}$ and $(111)_{BTO}$. We can observe that the ratio $I_{(001)}/I_{(002)}$ is increasing with increasing Ba-content in the BTO. On the other hand, $I_{(101)}/I_{(002)}$ and $I_{(111)}/I_{(002)}$ decrease when evolving from Ti-rich to Ba-rich BTO. When further increasing the [Ba] content, those ratios are increasing again, even above those obtained for sample B, which is closer to the ideal stoichiometric condition. We will discuss the observed variations and the relation to our model later in this chapter.

From the symmetric and asymmetric $\omega$-$2\theta$ scans presented in Figure 3.5, the in-plane and out-of-plane lattice constants for sample B to sample D can be calculated. To determine the in-plane lattice constant of sample A, we have to rely on the $\omega$-$2\theta$ scan of $(224)_{BTO}$ (not shown here) because the $(101)_{BTO}$ and $(111)_{BTO}$ peaks are missing. The out-of-plane lattice constant, $a_\perp$, and the in-plane lattice constant, $a_{//}$, are summarized in Figure 3.7(a). The local minimum for $a_\perp$ is obtained for the sample with [Ba]/[Ti]=1, similar to what is observed for $a_\perp$ of STO [19]. The in-plane lattice constant $a_{//}$ on the other hand decreases with increasing [Ba] content inside the layer. The trend for the lattice constants $a_\perp$ and $a_{//}$ for excessive [Ti] can be explained by Coulomb repulsion induced by the extra [Ti]. Since the extra [Ti] induces oxygen vacancies $V_o$ in the BTO to keep charge neutrality, the neighboring Ti-ions show charge repulsion due to the absence of [O] atoms in the crystal. Therefore, excessive [Ti] will also result in an expansion of the crystal lattice. For sample C and sample D with excess [Ba], the out-of-plane lattice constant $a_\perp$ is seemingly independent of the [Ba] content. However, the in plane lattice constant $a_{//}$ decreases as more [Ba] is incorporated inside the layer, probably related to the smaller lattice constants of $Ba_2TiO_4$ [37]. Therefore, when evaluating the tetragonality ($a_\perp/a_{//}$) to understand the BTO polarization in Figure 3.7(b), sample D with 28% [Ba] excess shows a dramatic increment, indicating strong out-of-plane polarization. All other samples show $a_\perp/a_{//}$ below 1, indicating in-plane polarization. This is believed to stem from the large mismatch in the thermal expansion coefficients of BTO ($\alpha_{BTO}=1.1\times10^{-5}$ $K^{-1}$) and Ge ($\alpha_{Ge}=5.8\times10^{-6}$ $K^{-1}$) [39, 40]. Summarizing, from our studies, the stoichiometry of the BTO-sample also provides a route to control its tetragonality, optimizing it for a given device application [35, 41].

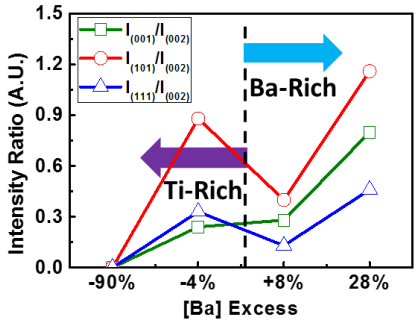


**Figure 3.6:** The XRD intensity ratio of $(001)_{BTO}$, $(101)_{BTO}$ and $(111)_{BTO}$ to $(002)_{BTO}$ for all samples, evaluated from the ω-2θ scans shown in Figure 3.5.

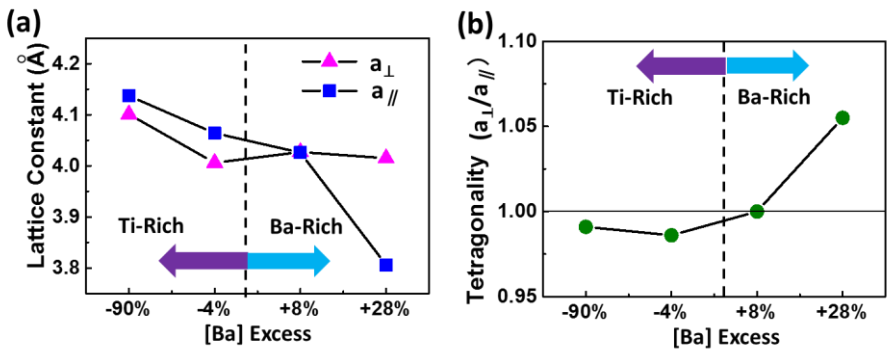


**Figure 3.7:** (a) The in-plane ($a_{//}$) and out-of-plane ($a_{\perp}$) lattice constants, derived from ω-2θ scans shown in Figure 3.5. (b) The corresponding tetragonality ($a_{\perp}$/ $a_{//}$) for all samples

### 3.2.3 Transmission Electron Microscopy Analysis

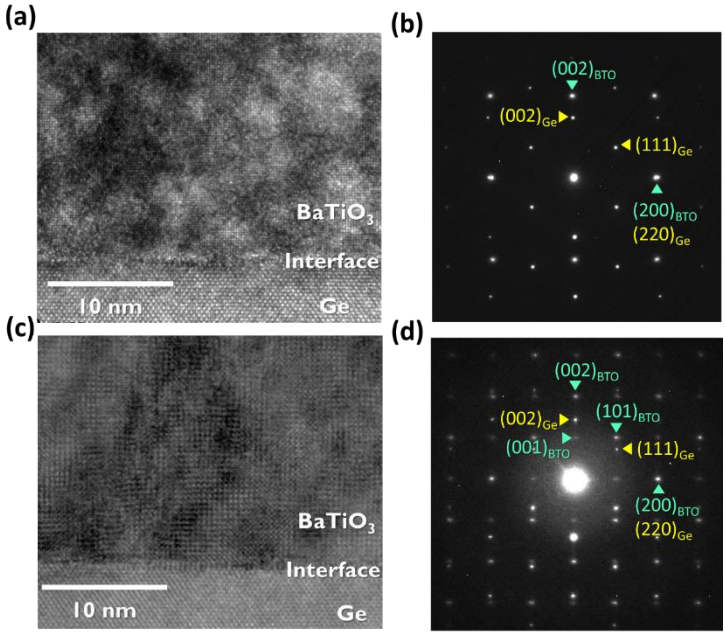


**Figure 3.8:** (a) and (b) are HR-TEM and SAED images of sample A with 90% [Ti] respectively; (c) and (d) are those images for sample B with 4% extra [Ti]. The miller planes in the SAED images are indexed based on the tetragonal lattice system and Ge(001) reference

Figure 3.8 presents the comparison of cross-sectional high resolution TEM (HRTEM) images with the corresponding Selected Area Electron Diffraction (SAED) images for sample A and B. The samples were prepared by taking a cross-section along the $[100]_{BTO}//[110]_{Ge}$ zone axis and $[001]_{BTO}//[001]_{Ge}$ vertical direction. The black shadows in the HRTEM images are believed to originate either from the presence of defects or from roughness of the TEM sample lamella. The corresponding SAED Bragg peaks are defined based on the reference of the Ge substrate. In Figure 3.8(a) and 3.8(c), the HRTEM images for respectively sample A and B show a sharp BTO/Ge interface without the formation of amorphous $GeO_x$ suboxides at the hetero-interfaces. Also, the bright SAED spots in both samples (Figure 3.8(b) and 3.8(d)) agree with the good crystallinity already deduced from the ω-2θ scan in figure 3.5. However, compared to sample A, the SAED pattern for sample B shows more diffraction spots. It confirms that

the 90% excessive [Ti] generates a change in the diffraction behavior, explaining the observed diffraction behavior of the different BTO layers.

## 3.3 Stoichiometry-Dependent Diffraction Phenomenon

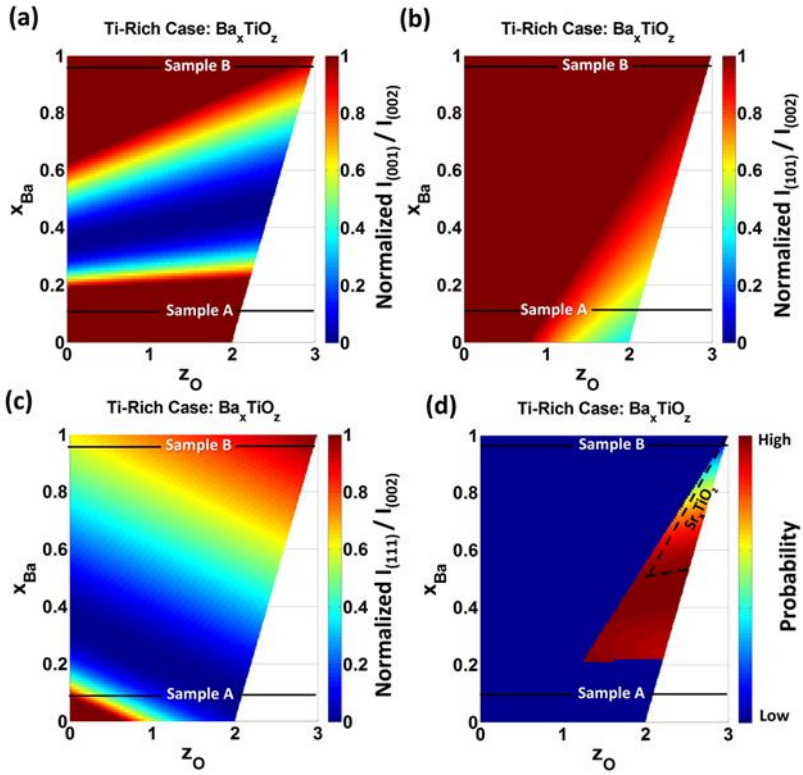


**Figure 3.9:** The calculated mappings of (a) $I_{(001)}/I_{(002)}$,(b) $I_{(101)}/I_{(002)}$ and (c) $I_{(111)}/I_{(002)}$ for the Ti-rich compound $Ba_xTiO_z$, which are normalized by those ratios for the stoichiometric $BaTiO_3$. (d) the probability distribution for having lower $I_{(001)}/I_{(002)}$, $I_{(101)}/I_{(002)}$ and $I_{(111)}/I_{(002)}$ at the same time. The RBS-measured [Ba]/[Ti] ratios for samples A and B are denoted by the solid lines on all mappings. The Ti-rich STO case is indicated by the black dashed lines in (d).

To qualitatively understand the relation between the observed diffraction patterns and the ratio [Ba]/[Ti], we calculate the peak diffraction intensity and position corresponding to various planes simply based on diffraction theory without considering instrument geometry [22]. In the calculation, we assume the

BTO structure is cubic for simplicity. The diffraction intensity can be described by the following formula:

$$I_{hkl} \propto \frac{\lambda^3 \times |F_{hkl}|^2 \times M \times L.P.}{V_c^2 \mu_\varrho} \quad (3.1)$$

$$F_{hkl} = f_{Ti} + f_{Ba}(-1)^{h+k+l} + f_O[(-1)^{h+k} + (-1)^{k+l} + (-1)^{h+l}] \quad (3.2)$$

$$L.P. = \frac{(1+\cos^2 2\theta_{hkl})}{\sin 2\theta_{hkl} \sin \theta_{hkl}} \quad (3.3)$$

where $f_{Ti}$, $f_{Ba}$ and $f_O$ are the atomic form factors of Ti, Ba and O, respectively, and $\theta_{hkl}$ is the Bragg peak position for a given plane (hkl). Due to the large atomic form factor of Ba, there are no (hkl) conditions for which the structure factor $F_{hkl}$ disappears. In addition, according to Formula (3.3), the lower order peaks at low $\theta_{hkl}$ show a relatively large L.P. factor value, giving larger diffraction intensity. Therefore, all reflections of stoichiometric BTO should be clearly observable. For sample A, however, with 90% excessive [Ti], the 3 lowest-ordered Bragg's peaks, $(001)_{BTO}$, $(101)_{BTO}$ and $(111)_{BTO}$ are missing in the RHEED patterns (Figure 3.4) as well as in the XRD (Figure 3.5) and TEM (Figure 3.8) figures, indicating the extra [Ti] results in a unique diffraction phenomenon. To understand this, we consider the $Ba_xTiO_z$ compound with Ba composition x from 0 to 1, and oxygen content z from 0 to 2+x, assuming charge neutrality. We further assume the atomic form factor of deficient [Ba] and oxygen can be expressed by $xf_{Ba}$ and $zf_O/3$, respectively. Then, combining Equation 3.1 to Equation 3.3 taking into account those non-stoichiometric atomic form factors, the diffraction intensity for each plane (hkl) can be derived. In order to see how the stoichiometry influences the diffraction pattern, we evaluate again the intensity ratio of the 3 lowest-ordered peaks with respect to the (002) peak, in functions of various x and z composition. Afterwards, the intensity ratios $I_{(001)}/I_{(002)}$, $I_{(101)}/I_{(002)}$, and $I_{(111)}/I_{(002)}$ for $Ba_xTiO_z$ are normalized to those for stoichiometric $BaTiO_3$ and color-mapped in Figures 3.9(a) to 3.9(c) respectively. The black solid lines in each mapping show the [Ba]/[Ti] ratio measured using RBS. Any colors other than the deep red in the color bar define a composition of $Ba_xTiO_z$ with smaller diffraction intensity ratio than that for stoichiometric $BaTiO_3$, which is the unique phenomenon that we are interested in. Figure 3.9(a)-3.9(c) show the windows of $Ba_xTiO_z$ having smaller $(001)_{BTO}$, $(101)_{BTO}$ and $(111)_{BTO}$ diffraction intensity than that for the stoichiometric BTO respectively. In order to describe the diffraction behavior observed in sample A for which the $(001)_{BTO}$, $(101)_{BTO}$ and $(111)_{BTO}$ Bragg peaks are unobservable, Figure 3.9(d) defines the area where the 3 composition windows of Figures 3.9(a) to 3.9(c) overlap. The resulting triangular region shows that sample A is not only Ti-rich but also O-deficient. From RBS we found a [Ba]

deficiency of -90% for sample A, which is beyond the lower bound of the triangular area (-80%). Yet, from the XRD-data shown in Figure 3.5 we know that some poly-titanate compounds formed in sample A and precipitated in the grain boundaries of twinned $(111)_{BTO}$, evidenced by multi-peaks in the ω-2θ scans of the $(101)_{BTO}$ and $(111)_{BTO}$ planes. Therefore, we can infer that more than 10% [Ti] is not incorporated in the BTO lattice but forms a poly-titanate. Besides, the lattice expansion observed in Figure 3.7 indicates plenty of $V_o$ exists in sample A, in agreement with Figure 3.9(d). This explains the disappearance of the 3 lowest-ordered Bragg peaks for sample A, as observed in our diffraction analysis.

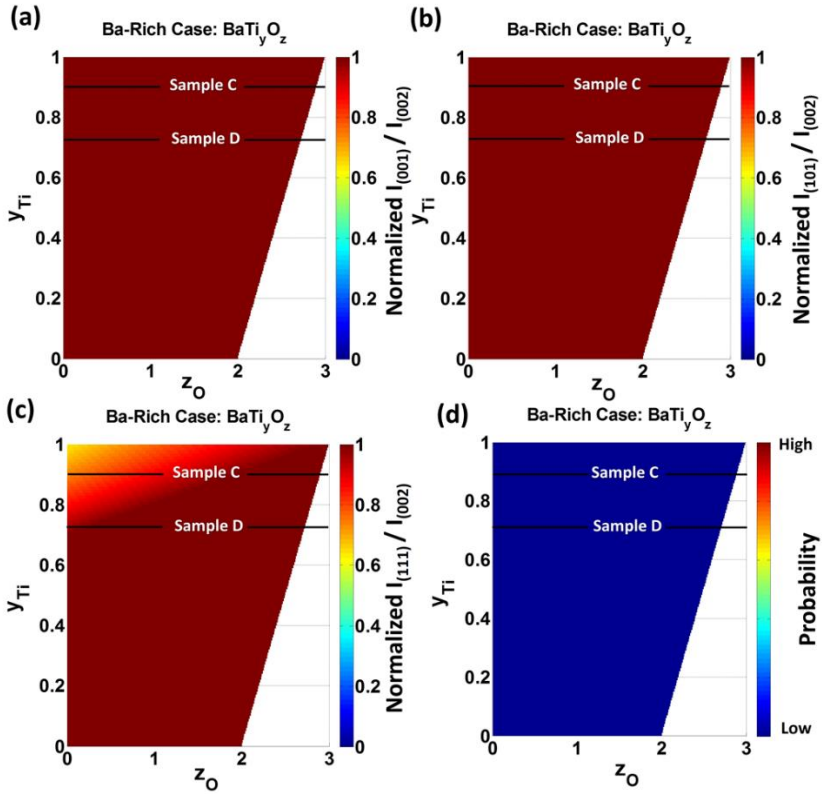


**Figure 3.10:** The calculated mappings of (a) $I_{(001)}/I_{(002)}$,(b) $I_{(101)}/I_{(002)}$ and (c) $I_{(111)}/I_{(002)}$ for the Ba-rich compound $BaTi_yO_z$, which are normalized by those ratios for the stoichiometric $BaTiO_3$. (d) the probability distribution for having lower $I_{(001)}/I_{(002)}$, $I_{(101)}/I_{(002)}$ and $I_{(111)}/I_{(002)}$, at the same time. The RBS-measured [Ba]/[Ti] ratios for samples C and D are denoted by the solid lines on all mappings.

To describe the Ba-rich samples we use $BaTi_yO_z$ as our model, where y ranges from 0 to 1 and z from 0 to 2+y. Similar to the Ti-rich case, we assume the atomic form factors of deficient [Ti] and oxygen are expressed by $yf_{Ti}$ and $zf_O/3$,

respectively. Then, the normalized diffraction efficiencies $I_{(001)}/I_{(002)}$, $I_{(101)}/I_{(002)}$, and $I_{(111)}/I_{(002)}$ can be evaluated as illustrated in Figure 3.10(a) to 3.10(c) respectively. The RBS-measured [Ba]/[Ti] ratios are indicated by the black solid line in these figures. Different from the Ti-rich case, in the Ba-excess case no combination of y and z leads to a decrease of the intensity of the $(001)_{BTO}$ and $(101)_{BTO}$ peaks. Yet, there is still a small region with an excess [Ba] between 0% and 30% and with some Vo which shows a lower $I_{(111)}/I_{(002)}$ than that for the stoichiometric BTO, as visible in Figure 3.10(c). Combined with the $I_{(001)}/I_{(002)}$, $I_{(101)}/I_{(002)}$, and $I_{(111)}/I_{(002)}$ mappings however, there is no overlapping region where all 3 peaks disappear at the same time, as can be seen from Figure 3.10(d).

Comparing the experimental results of Figure 3.6 and the modelling results presented in Figure 3.9 and Figure 3.10, the trend of the relative diffraction efficiencies $I_{(001)}/I_{(002)}$, $I_{(101)}/I_{(002)}$, and $I_{(111)}/I_{(002)}$ with stoichiometry can be further discussed. In Figure 3.6, $I_{(001)}/I_{(002)}$, $I_{(101)}/I_{(002)}$, and $I_{(111)}/I_{(002)}$ are all decreasing with more [Ti] being incorporated inside the BTO layer. This is in agreement with the triangular region delineated for the Ti-rich case in Figure 3.9(d): excess [Ti] and O-deficiency in the BTO layer can lead to an intensity degradation of diffraction at the $(001)_{BTO}$, $(101)_{BTO}$ and $(111)_{BTO}$ planes. On the other hand, for the Ba-rich case (Figure 3.10), the calculated diffraction efficiencies $I_{(001)}/I_{(002)}$ and $I_{(101)}/I_{(002)}$ color red, indicating that both should increase with increasing [Ba]. This is in agreement with the experiments for $I_{(001)}/I_{(002)}$ but not for $I_{(101)}/I_{(002)}$ in the whole case, which, as can be seen from Figure 3.6, with increasing the [Ba] content from -4% (sample B) to 8% (sample C), increases. This disagreement might result from the calculation which does not take the setup geometry into account. Figure 3.10(c) shows a triangular region defining the Ba-rich, oxygen-deficient composition window, where the relative diffraction efficiency $I_{(111)}/I_{(002)}$ is smaller than that for stoichiometric BTO. With further increasing [Ba], the ratio $I_{(111)}/I_{(002)}$ will increase again and become larger than for stoichiometric BTO. This trend matches well with the experimental trend seen comparing samples C and D in Figure 3.6. Therefore, at least qualitatively, the diffraction models we propose for both Ti- and Ba-rich BTO can explain the experimentally observed phenomena very well.

Interestingly, within the wide literature on STO, and even though STO has the same perovskite crystal structure as BTO, to our knowledge, there is no report of a diffraction behavior similar to what we describe in this work. Since $Sr^{2+}$ (36) has less electrons than $Ba^{2+}$(54), the atomic form factor of Sr is smaller than that of Ba. Therefore, $Sr^{2+}$ in an STO-film cannot exhibit such large electron or X-ray scattering as Ba. Therefore, compared to Ti-rich BTO, the composition window for Ti-rich STO to have the 3 lowest-ordered Bragg peaks missing simultaneously shrinks, as indicated by the dashed lines in Figure 3.9(d). Therefore, this unique diffraction phenomenon becomes comparatively more difficult to be observed in

STO-films. For that reason, Sr-rich STO behaves similar to Ba-rich BTO, and equally does not exhibit a composition window where all 3 lowest-ordered peaks disappear.

## 3.4 Conclusion

In this chapter, we utilized RBS to measure the exact [Ba]/[Ti] ratio in BTO-films and developed diffraction models to understand the effect of the precise stoichiometry on the diffraction phenomenon observed in RHEED, XRD and TEM diffraction studies. In the RHEED patterns, non-stoichiometric BTO does not show x2 surface reconstructions along the $[100]_{BTO}$ and $[110]_{BTO}$ directions, presumably because the [Ba]/[Ti] ratio is too far away from unit in these layers. However, we observe that excess [Ba] and [Ti] in the non-stoichiometric BTO-layers generates twinning planes and induces a rougher surface, as revealed in the RHEED patterns. Besides, excess [Ti] is observed to change the BTO diffraction behavior, making the ±1st-ordered RHEED lines along the $[100]_{BTO}$ and $[110]_{BTO}$ directions disappear. Further, despite we considered a very broad range of [Ba]/[Ti] ratios, all samples still show a four-fold tetragonal symmetry in the crystal structure. Additionally, we found that the ω-2θ scan along $[001]_{BTO}$ does not provide sufficient information to judge if a given BTO layer is single-crystalline and stoichiometric. The non-stoichiometric BTO samples show poly-crystalline-like diffraction patterns, which might result from any non-stoichiometric compound precipitation. Besides, evaluated from ω-2θ scans, the out-of-plane lattice constant $a_{\perp}$ for BTO follows a similar trend as function of the stoichiometry as STO, having a local minimum for the composition [Ba]/[Ti] around 1. On the other hand, the variation of $a_{//}$ as function of the layer stoichiometry shows a completely different behavior: it is decreasing with more [Ba] inside the layer. Therefore, adjusting the ratio [Ba]/[Ti] offers a route to adjust the BTO tetragonality and hence to control the ferroelectricity of the BTO layer for device applications. In addition, the 3 lowest-ordered Bragg peak relative intensity ratios $I_{(001)}/I_{(002)}$, $I_{(101)}/I_{(002)}$ and $I_{(111)}/I_{(002)}$ derived from the ω-2θ scan depend on BTO stoichiometry in a characteristic way. Compared with the intensity ratios of stoichiometric BTO, extra [Ti] will decrease all three ratios $I_{(001)}/I_{(002)}$, $I_{(101)}/I_{(002)}$ and $I_{(111)}/I_{(002)}$ simultaneously, making the 3 lowest-ordered Bragg peaks unobservable for sample A (with the highest excess [Ti]). This peak disappearance is also in good agreement with the RHEED and SAED patterns for sample A. On the other hand, for Ba-rich BTO, the ratios of $I_{(001)}/I_{(002)}$, $I_{(101)}/I_{(002)}$ and $I_{(111)}/I_{(002)}$ are not all increasing. To understand this, we proposed a model that explains how excess [Ba] or [Ti] in non-stoichiometric BTO layers indeed induces different experimental diffraction behavior from the stoichiometric layer. Therefore, this chapter provides insight and better understanding in how the

stoichiometry of a BTO layer influences different diffraction phenomena, thereby assisting in precisely controlling the properties of a BTO-layer for a given applications.

# References

[1] R. Guo, Z. Wang, S. Zheng, Kun, Han, L. Huang, D. G. Schlom, T. Venkatesan, Ariando and J. Chen, "Functional ferroelectric tunnel junctions on silicon," Scientific Reports, 5, 12576 (2015).

[2] C. Xiong, W. H. P. Pernice, J. H. Ngai, J. W. Reiner, D. Kumah, F. J. Walker, C. H. Ahn, and H. X. Tang, "Active silicon integrated nanophotonics: ferroelectric $BaTiO_3$ devices," Nano Lett. 14, 1419 (2014).

[3] S. H. Baek, J. Park, D. M. Kim, V. a. Aksyuk, R. R. Das, S. D. Bu, D. a. Felker, J. Lettieri, V. Vaithyanathan, S. S. N. Bharadwaja, N. Bassiri-Gharb, Y. B. Chen, H. P. Sun, C. M. Folkman, H. W. Jang, D. J. Kreft, S. K. Streiffer, R. Ramesh, X. Q. Pan, S. Trolier-McKinstry, D. G. Schlom, M. S. Rzchowski, R. H. Blick, and C. B. Eom, "Giant piezoelectricity on Si for hyperactive MEMS," Science 334, 958 (2011).

[4] D. G. Schlom, L.-Q. Chen, X. Pan, A. Schmehl, and M. A. Zurbuchen, "A thin film approach to engineering functionality into oxides," J. Am. Ceram. Soc. 91, 2429 (2008).

[5] A. A. Demkov and A. B. Posadas, *Integration of Functional Oxides with Semiconductors* (Springer New York Heidelberg Dordrecht London, 2014).

[6] J. W. Reiner, A. M. Kolpak, Y. Segal, K. F. Garrity, S. Ismail Beigi, C. H. Ahn, F. J. Walker, S. Ismail-Beigi, C. H. Ahn, and F. J. Walker, "Crystalline oxides on silicon," Adv. Mater. 22, 2919 (2010).

[7] R. McKee, F. Walker, and M. Chisholm, "Crystalline oxides on silicon: the first five monolayers," Phys. Rev. Lett., vol. 81, 3014 (1998).

[8] H. L. Yu, Y. Z. Wu, X. F. Jiang, M. Q. Cai, L. P. Gu, and G. W. Yang, "Ferroelectric functionality in SrTiO3/Si heterojunctions," J. Appl. Phys. 114, 173502 (2013).

[9] A. Kalabukhov, R. Gunnarsson, J. Börjesson, E. Olsson, T. Claeson, and D. Winkler, "Effect of oxygen vacancies in the SrTiO3 substrate on the electrical properties of the LaAlO3/SrTiO3 interface," Phys. Rev. B, 75, 121404 (2007).

[10] L. Ji, M. D. McDaniel, S. Wang, A. B. Posadas, X. Li, H. Huang, J. C. Lee, A. A. Demkov, A. J. Bard, J. G. Ekerdt, and E. T. Yu, "A silicon-based photocathode for water reduction with an epitaxial SrTiO3 protection layer and a nanostructured catalyst," Nat. Nanotechnol. 10, 84 (2014).

[11] F. S. Aguirre-Tostado, A. Herrera-Gómez, J. C. Woicik, R. Droopad, Z. Yu, D. G. Schlom, P. Zschack, E. Karapetrova, P. Pianetta, and C. S. Hellberg, "Elastic anomaly for SrTiO3 thin films grown on Si(001)," Phys. Rev. B 70, 201403 (2004).

[12] A. M. Kolpak and S. Ismail-Beigi, "Thermodynamic stability and growth kinetics of epitaxial SrTiO3 on silicon," Phys. Rev. B, 83, 165318 (2011).

[13] C. J. Fennie and K. M. Rabe, “Structural and dielectric properties of Sr2TiO4 from first principles,” Phys. Rev. B 68, 184111 (2003).

[14] Y. Y. Guo, H. M. Liu, D. P. Yu, and J.-M. Liu, “Ferroelectricity and superparamagnetism in Sr/Ti nonstoichiometric SrTiO3,” Phys. Rev. B 85, 104108 (2012).

[15] C. Dubourdieu, H. Roussel, C. Jimenez, M. Audier, J. P. Sénateur, S. Lhostis, L. Auvray, F. Ducroquet, B. J. O’Sullivan, P. K. Hurley, S. Rushworth, and L. Hubert-Pfalzgraf, “Pulsed liquid-injection MOCVD of high-K oxides for advanced semiconductor technologies,” Mater. Sci. Eng. B 118, 105 (2005).

[16] M. Vehkamäki, T. Hänninen, M. Ritala, M. Leskelä, T. Sajavaara, E. Rauhala, and J. Keinonen, “Atomic Layer Deposition of SrTiO3 Thin Films from a Novel Strontium Precursor- Strontium-bis(tri-isopropylcyclopentadienyl),” Chem. Vap. Depos. 7, 75 (2001).

[17] M. D. McDaniel, A. Posadas, T. Q. Ngo, A. Dhamdhere, D. J. Smith, A. A. Demkov, and J. G. Ekerdt, “Epitaxial strontium titanate films grown by atomic layer deposition on SrTiO3-buffered Si(001) substrates,” J. Vac. Sci. Technol. A, 31, 01A136 (2013).

[18] P. Fisher, H. Du, M. Skowronski, P. a. Salvador, O. Maksimov, and X. Weng, “Stoichiometric, nonstoichiometric, and locally nonstoichiometric SrTiO3 films grown by molecular beam epitaxy,” J. Appl. Phys. 103, 013519 (2008).

[19] C. M. Brooks, L. F. Kourkoutis, T. Heeg, J. Schubert, D. A. Muller, and D. G. Schlom, “Growth of homoepitaxial SrTiO3 thin films by molecular-beam epitaxy,” Appl. Phys. Lett. 94, 162905 (2009).

[20] Z. Yu, Y. Liang, C. Overgaard, X. Hu, J. Curless, H. Li, Y. Wei, B. Craigo, D. Jordan, R. Droopad, J. Finder, K. Eisenbeiser, D. Marshall, K. Moore, J. Kulik, and P. Fejes, “Advances in heteroepitaxy of oxides on silicon,” Thin Solid Films, 462–463, 51 (2004).

[21] J. M. LeBeau, R. Engel-Herbert, B. Jalan, J. Cagnon, P. Moetakef, S. Stemmer, and G. B. Stephenson, “Stoichiometry optimization of homoepitaxial oxide thin films using x-ray diffraction,” Appl. Phys. Lett. 95, 142905 (2009).

[22] B. Fultz and J. Howe, *Transmission Electron Microscopy and Diffractometry of Materials* (Springer-Verlag Berlin Heidelberg 2013) Chapter 1.

[23] E. Heymann and H. Bloom, “High permittivity crystalline aggregates,” Nature 156, 480 (1945).

[24] J. B. Murgatroyd and R. F. Sykes, “Dielectric constants of some titanates,” Nature 156, 717 (1945).

[25] S. Abel, T. Stöferle, C. Marchiori, C. Rossel, M. D. Rossell, R. Erni, D. Caimi, M. Sousa, A. Chelnokov, B. J. Offrein, and J. Fompeyrine, “A strong electro-optically active lead-free ferroelectric integrated on silicon,” Nat. Commun. 4, 1671 (2013).

[26] T. Suzuki, Y. Nishi, and M. Fujimoto, “Ruddlesden–Popper planar faults and nanotwins in heteroepitaxial nonstoichiometric Barium Titanate thin films,” J. Am. Ceram. Soc. 83, 3185 (2000).

[27] G. Y. Yang, G. D. Lian, E. C. Dickey, C. a. Randall, D. E. Barber, P. Pinceloup, M. a. Henderson, R. a. Hill, J. J. Beeson, and D. J. Skamser, “Oxygen nonstoichiometry and dielectric evolution of BaTiO3. Part II—insulation resistance degradation under applied dc bias,” J. Appl. Phys. 96, 7500 (2004).

[28] A. Lotnyk, A. Graff, S. Senz, N. D. Zakharov, and D. Hesse, “Topotaxial formation of titanium-rich barium titanates during solid state reactions on (110) TiO2 (rutile) and (001) BaTiO3 single crystals,” Solid State Sci. 10, 702 (2008).

[29] C. Merckling, G. Saint-Girons, C. Botella, G. Hollinger, M. Heyns, J. Dekoster, and M. Caymax, “Molecular beam epitaxial growth of BaTiO3 single crystal on Ge-on-Si(001) substrates,” Appl. Phys. Lett. 98, 092901 (2011).

[30] J. Wang et al., "Bonding and diffusion of Ba on a Si(001) reconstructed surface," Physical Review B, vol. 60, no. 7, pp. 4968-4971, 08/15/ 1999.

[31] J. L. Wang, J. Leroy, G. Niu, G. Saint-Girons, B. Gautier, B. Vilquin, and N. Barrett, “Chemistry and structure of BaTiO3 ultra-thin films grown by different O2 plasma power,” Chem. Phys. Lett. 592, 206 (2014).

[32] Y. L. Zhu, M. J. Zhuo, X. L. Ma, and H. B. Lu, “Microstructural characteristics in the BaTiO2.52 thin films showing metallic behavior,” Mater. Lett. 61,1971–1973 (2007).

[33] T. Suzuki, Y. Nishi, and M. Fujimoto, “Defect structure in homoepitaxial non-stoichiometric strontium titanate thin films,” Philos. Mag. A, 80, 621 (2000).

[34] K. Shimoyama, K. Kubo, M. Lida, and K. Yamabe, “Changes in surface states during epitaxial growth of BaTiO3 on SrTiO3 substrate in connection with composition deviation,” J. Vac. Sci. Technol. A 19, 2083 (2001).

[35] S. Abel, Ph.D. thesis, Universite Grenoble Alpes, 2014.

[36] M. Yashima, R. Tu, T. Goto, and H. Yamane, “Crystal structure of the high-temperature paraelectric phase in barium titanate BaTi2O5,” Appl. Phys. Lett. 87, 101909 (2005).

[37] J. Bland, “The Crystal Structure of Barium Orthotitanate, Ba2TiO4,” Acta Crystallogr. 14, 875 (1961).

[38] S. Stemmer, S. K. Streiffer, N. D. Browning, and A. I. Kingon, “Accommodation of nonstoichiometry in (100) fiber-textured (BaxSr1−x)Ti1+yO3+z thin films grown by chemical vapor deposition,” Appl. Phys. Lett. 74, 2432 (1999).

[39] Y. He, “Heat capacity, thermal conductivity, and thermal expansion of barium titanate-based ceramics,” Thermochim. Acta, 419, 135 (2004).

[40] D. F. Gibbons, “Thermal expansion of some crystals with the diamond structure,” Phys. Rev. 112, 136 (1958).

[41] S. Sakai and M. Takahashi, “Recent progress of ferroelectric-gate field-effect transistors and applications to nonvolatile logic and FeNAND flash memory,” Materials 3, 4950 (2010).

# 4

# Effects of Process Conditions on BTO

Although the goal of this thesis is to use BTO to realize optical modulators, it will take much time to carry out the growth optimization by fabricating the real optical device and performing the electro-optical (EO) characterizations as a starting point. In this chapter, we start from simple and non-destructive techniques including X-ray diffraction (XRD) and some scanning probe microscopy (SPM) analysis to understand the BTO crystallinity and ferroelectricity-related properties, which will be the main metrics to define the optimal BTO growth conditions.

Recently, BTO ferroelectricity, one of the most intriguing BTO characteristics, in logic applications has provided an alternative route for technologies beyond Complementary Metal-Oxide-Semiconductor (CMOS) [1-3]. Several studies have successfully demonstrated switchable BTO ferroelectricity for non-volatile Si- and Ge-hybrid logic transistors using MBE [4-6]. Since current FeFET designs are still primarily based on planar stacks of metal-ferroelectric oxide-semiconductors, practical FeFET applications require out-of-plane polarization in the active layer [4, 6, 7]. It has been extensively reported that polarization in ferroelectric materials is sensitive to growth conditions such as temperature, oxygen partial pressure, and cations stoichiometry [5, 8, 9]. Nevertheless, the growth of ternary BTO is difficult to be controlled, and its Si integration is even more challenging. To obtain high device performance, it is crucial to understand how growth parameters influence both material and device behavior during BTO thin film preparation. Although much research has been devoted to obtaining high-quality STO epitaxy on semiconductors using MBE, little information is available for the case of BTO growth [7].

Therefore, in this chapter, we will focus on how process conditions impact the crystal structure and ferroelectricity of epitaxial BTO on a Si substrate. The 20 nm BTO thin films are grown by plasma-assisted MBE on Si(001) using a 10 nm STO buffer layer. First, a series of BTO crystallinity optimization steps in terms of growth temperatures and plasma power are executed based on RHEED, XRD and channeling analysis in RBS. Then, the effect of post-growth annealing is also studied. Comparisons of detailed TEM characterization and current-voltage (I-V) of the as-deposited and annealed samples are presented and discussed. We find that oxygen annealing not only improves leakage current in the BTO but also ameliorates switching and stability of ferroelectric polarizations, as shown using a PFM.

## 4.1 Experiments

All of the samples are grown on 8-inch-diameter Si(001) substrates in a 200 mm Riber49 MBE production reactor. A co-deposition approach is used to deposit STO and BTO. Both Ba and Sr atomic fluxes are obtained using standard Knudsen effusion cells. The [Sr]/[Ti] and [Ba]/[Ti] flux ratios are calibrated in-situ using a quartz crystal microbalance and ex-situ by RBS analysis. The ([Ba]+[Sr])/[Ti] in the optimal sample is around 0.88. A radio frequency remote plasma source is used to produce atomic oxygen during growth.

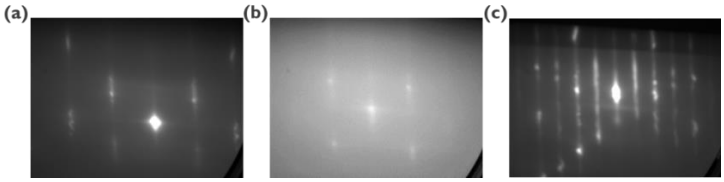


**Figure 4.1:** RHEED patterns along $[110]_{Si}$ for Si(001) surface, which is covered with (a) native $SiO_2$ (b) 2 monolayer Sr on the native oxide (c) ½ ML Sr.

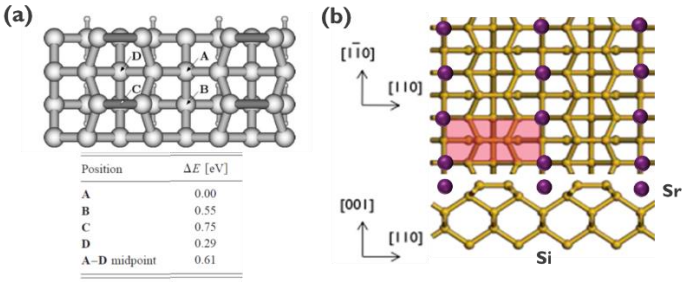


| Position | $\Delta E$ [eV] |
|---|---|
| A | 0.00 |
| B | 0.55 |
| C | 0.75 |
| D | 0.29 |
| A–D midpoint | 0.61 |

**Figure 4.2:** (a) Map of surface potential energy for a Sr atom on a Si(001) surface with 1x2 reconstruction. The figure is reproduced from the ref. [13]. (b) Schematic of Sr atoms on Si(001) surface to form 1x2 reconstruction.

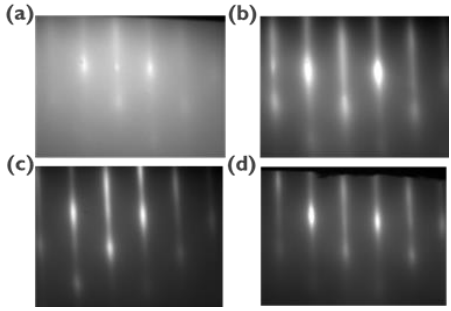


**Figure 4.3:** RHEED patterns along $[100]_{STO}$ for (a) 6 ML (2.4 nm) STO which was deposited at 150 ℃ (b) 6 ML (2.4 nm) STO which was recrystallized at 550℃ (c) 12 ML (4.8 nm) STO after 2 times of deposition and recrystallization process. (d) 10 nm STO.

Since STO has 28% lattice mismatch against Si lattice constant (STO: 0.3905 nm and Si: 0.5431nm), a 45° rotation of the STO lattice with respect to the Si substrate is needed through an insertion of 0.5 ML SrO on the Si(001) surface. Prior to STO deposition, native oxide removal from Si surface is necessary. Figure 4.1(a) shows 1x1 RHEED reconstruction pattern along $[110]_{Si}$ for Si(001) substrate covered with native oxide. Then, the native oxide is removed with an assistance of Sr monolayers. Two monolayer (ML) of Sr is deposited on the substrate at 650 °C. The RHEED, which is presented in Figure 4.1(b), shows a blurry contrast and a white background. Afterwards, the substrate temperature is further increased to 800 °C. When being at this high temperature under ultra-high vacuum (UHV), the desorption of the native oxide $SiO_2$ is facilitated by the formation of volatile SrO and SiO. The two ML Sr is consumed [10]. Meanwhile, the RHEED reconstructions are changed until a bright 2×1 reconstruction pattern is observed. After cooling the substrate back to 600 °C, the RHEED pattern evolves to a 2×3 reconstruction, corresponding to a 0.167 ML of Sr remaining on the surface [11-12]. Additional Sr is added to 0.5 ML Sr (confirmed by RBS), showing back a 2×1 RHEED pattern. From a first principle calculation [13], it is proven that the most favorable site for a Sr atom on a Si(001) surface is position A, as shown in Figure 4.2(a). Thus, Sr atoms will be located at the corresponding positions on the Si surface as illustrated in Figure 4.2(b). This atom configuration also explains why we observe a 1x2 reconstruction pattern from RHEED for 0.5 ML Sr on the Si surface. Then, the substrate is cooled down to 150 °C and we introduce oxygen to oxidize the 0.5 ML Sr to SrO, which can be a crystal template

guiding STO to register on Si with a 45° lattice rotation. Moreover, such a 0.5 ML SrO can also act as an oxidation barrier for the silicon surface during the following STO growth.

Subsequently, the process for growing the STO buffer is carried out. First, 6 ML (2.4 nm) STO is deposited at 150 °C under a molecular oxygen pressure of ~$4\times10^{-7}$ Torr. In Figure 4.3(a), the RHEED pattern with the white background indicates that the STO layer is mostly amorphous, resulting from the too low oxygen concentration and growth temperature. Even so, there are some noticeable streak diffraction lines overlaying on the background, suggesting that some epitaxy still happens during the growth. Then, the substrate is heated up to 550 °C to recrystallize the STO material in UHV until the RHEED diffraction pattern presents sharp streak lines again, as shown in Figure 4.3(b). To ensure the quality of the initial STO crystallinity, we repeat the above STO steps again until we reach a STO thickness of 5 nm on a Si(001) substrate and Figure 4.3(c) presents its RHEED pattern. To obtain STO layers thicker than 5 nm after the second recrystallization at 550 °C, the rest of the STO is allowed to continue growing under an oxygen chamber pressure of ~$1.2\times10^{-6}$ Torr. Figure 4.3(d) shows the RHEED for 10 nm STO. One can notice that the thicker STO exhibits the better crystallinity as suggested by RHEED sharpness. As soon as the desired STO thickness (10 nm STO is used in this chapter) is reached, the substrate temperature is increased to 630 °C to grow the BTO layer under an oxygen chamber pressure of ~$1.6\times10^{-6}$ Torr. Then, the thickness of the layers is measured by ellipsometry (calibrated using the TEM images).

## 4.2 BTO Crystallinity Optimization

### 4.2.1 Growth Temperature Effect

BTO spontaneous polarization originates from displacement of the Ti ion in the unit cell, leading to a tetragonal crystal structure. For this reason, any disordered crystallinity will impede Ti movement and polarization switching during device operation [9]. Thus, optimization of the BTO crystal quality is critical. Figure 4.4 presents a series of crystallinity analyses for 20 nm BTO on 10 nm STO-buffered Si(001) prepared under growth temperatures ($T_G$) from 600 °C to 660 °C with a plasma power of 300 W. The 2-D streak-lined RHEED patterns in Figure 4.4(a) imply flatness on the surface of all the samples. Nevertheless, among samples using different $T_G$, the difference in the intensity and background contrast of RHEED patterns is not distinguishable. To quantitatively compare crystal quality over all samples, we performed RBS to quantify BTO crystallinity. Figure 4.4(b) displays random and channeled RBS spectra for the BTO grown at $T_G$=630 °C. In principle, the minimum yield ($\chi_{min}$), defined by the ratio of channeled and random signal intensity, is directly linked to the crystallinity of the

thin film. Therefore, the better the film crystallinity in the measured sample, the lower the magnitude of $\chi_{min}$. For this reason, the lowest $\chi_{min}$ of Ba in Figure 4.4(c) suggests that the optimal $T_G$ for BTO crystallinity is 630 °C. In addition, we also performed a symmetrical ω-2θ scan along $[001]_{BTO}//[001]_{STO}//[001]_{Si}$, as shown in Figure 4.4(d). The signal profile at $T_G$=630 °C appears slightly different. There are some observable thickness fringes at the tails of both $(002)_{BTO}$ and $(002)_{STO}$ (labelled by *). This finding indicates that such a growth temperature provides better lattice coherence in the stack of BTO, STO and Si(001) than do the other temperatures. Its periodicity is also consistent with the corresponding layer thickness of 20 nm BTO and 10 nm STO. Moreover, Figure 4.4(c) includes the full width at half maximum (FWHM) of the $(002)_{BTO}$ rocking curve, Δω. The lowest FWHM of the $(002)_{BTO}$ rocking curve, Δω, also occurs at $T_G$=630 °C in agreement with RBS results. Consequently, under 300 W of oxygen plasma power, the optimal $T_G$ in terms of crystallinity in 20 nm BTO on a 10 nm STO-on-Si(001) pseudo-substrate is confirmed to be 630 °C.

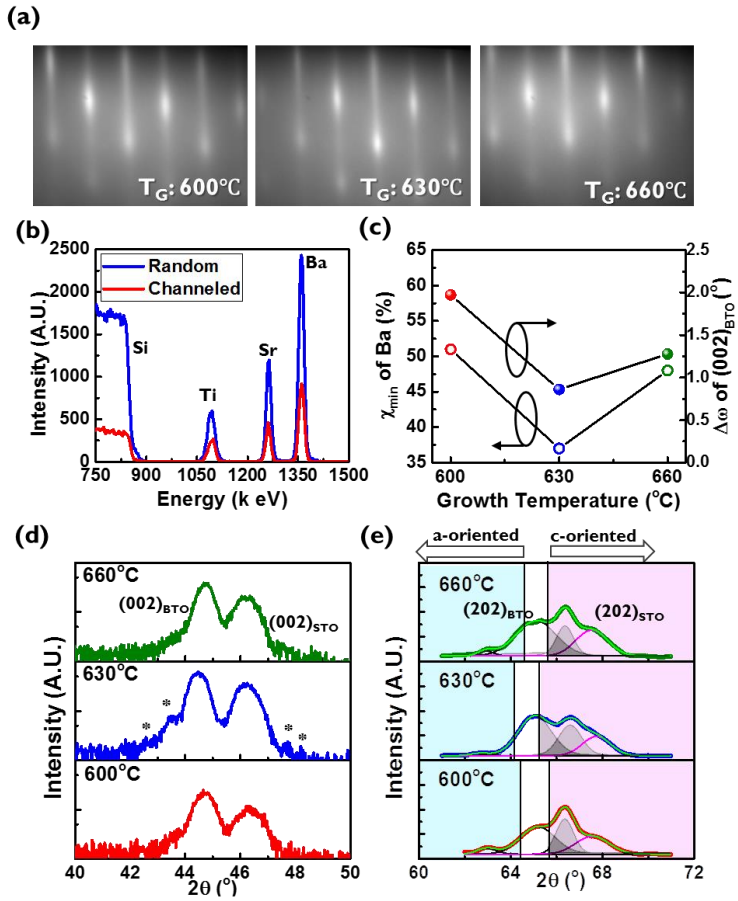

**Figure 4.4:** A series of crystal characterizations for BTO samples, which were prepared under $T_G$=600 °C, $T_G$=630 °C and $T_G$=660 °C with 300 W of plasma power: (a) RHEED patterns for all the samples. (b) The RBS spectrum under random and channeled configurations for the BTO prepared at $T_G$=630 °C. (c) The minimum yield of the RBS channeling analysis and the FWHM of the $(002)_{BTO}$ rocking curves. (d) The ω-2θ scans of $(002)_{BTO/STO}$. (e) The ω-2θ scans of $(202)_{BTO/STO}$ and fitted profiles.

According to Bragg's law, the positions of the Bragg peaks $(002)_{BTO/STO}$ in Figure 4.4(d) and $(202)_{BTO/STO}$ in Figure 4.4(e) can be used to evaluate the out-of-plane ($a_{\perp}$) and in-plane ($a_{//}$) lattice constants of both BTO and STO. In addition, tetragonality, defined by $a_{\perp}/a_{//}$, can also be calculated, revealing domain orientations. In Figure 4.4(d), single peak profiles for both BTO and STO suggest that one $a_{\perp}$ is present in the BTO and STO layers. In Figure 4.4(e), however, double shoulders in $(202)_{BTO}$ (2θ near 65° and 66°) reveal two distinct BTO $a_{//}$ values, and the single peak in $(202)_{STO}$ indicates one STO in-plane lattice parameter. Therefore, BTO tetragonality has two different values, implying two distinct groups of domains inside the layer. To resolve the peaks and find the positions correctly, we fitted the data for $(002)_{BTO/STO}$ and $(202)_{BTO/STO}$ via Gaussian functions and Lorentzian functions, respectively. Table 4.1 summarizes $a_{\perp}$, $a_{//}$ and the resulting tetragonality for BTO and STO prepared under different process conditions. Due to the ionic bond in the $ABO_3$, the in-plane and out-of-plane strain/relaxation can be non-uniform, generating different domains [12]. Suggested by the single $a_{\perp}$ and double $a_{//}$, BTO shows uniform out-of-plane strain ($\varepsilon_{\perp}$) but inhomogeneous in-plane strain. Therefore, based on the lattice constants shown in Table 4.1, the BTO layers exhibit two domain phases according to tetragonality: cubic-like and c-oriented tetragonal phases. In contrast, STO exhibits homogeneous strains in both $\varepsilon_{\perp}$ and $\varepsilon_{//}$, possessing a cubic or slightly out-of-plane tetragonal lattice in the layer. In addition, Table 4.1 indicates that the BTO tetragonal phase results from strain applied by the STO, as indicated by nearly equal $a_{//}$ in both BTO and STO. In principle, due to the larger $a_{//}$ in bulk BTO than in bulk STO (as described in Table 1), BTO undergoes compressive strain from the STO lattice, leading to elongation in the out-of-plane direction. Thus, it becomes more c-oriented. Nevertheless, cubic-like BTO $a_{//}$ shows comparatively larger values than expected in bulk BTO $a_{//}$, expanding towards BTO $a_{\perp}$. This result can be explained by either the coexistence of the c-oriented and in-plane-oriented (a-oriented) domains or, indeed, a cubic crystal with a larger lattice constant. In addition, from the perspective of FeFET applications, out-of-plane polarization is preferable. According to the tetragonality strength in Table

4.1, $T_G$=630 °C is the more favorable growth temperature due to the associated strong out-of-plane polarization.

In an ideal crystal, the Bragg peak in the ω-2θ scan is a delta function indicating only one exact lattice constant in the material. However, in Figure 4.4(d), the broadness of the peaks suggests that there are multiple crystallite grains in BTO with slight variations in lattice constant. Following Scherrer's Equation, we are able to evaluate the size of the BTO grains:

$$\boldsymbol{L} = \frac{\boldsymbol{k\lambda}}{\boldsymbol{BCos(\theta)}} \tag{4.1}$$

where L is the grain size; k is Scherrer's constant, usually taken as 0.9 [14]; λ is 1.54056 Å; θ is Bragg's peak position, and B is the FWHM of 2θ. The calculated grain sizes for the three samples range from 11 nm to 13 nm. In polycrystalline BTO, the grain size is as large as several tens of μm and each grain contains many domains [15, 16]. However, the grain with the size below 300 nm can only possess one domain [16]. Therefore, the grain is equivalent to the domain for the following discussions. Then, we take such lattice variation into account to discuss how growth temperature influences BTO tetragonality. Based on the FWHM of $(002)_{BTO}$ in Figure 4.4(d), the range of peak position for $(202)_{BTO}$ giving a-oriented and c-oriented BTO domains can be evaluated, as shown by the shaded area in Figure 4.4(e). The white region depends on the peak width in $(002)_{BTO}$ and represents the mixture of c-oriented, a-oriented or cubic-phase BTO. To consider the preferable BTO properties for FeFET applications, we are only interested in the c-oriented area, where fitted BTO Bragg's peaks are highlighted by gray shades in Figure 4.4(e). We observe that among different growth temperatures, $T_G$=630 °C exhibits twice as large gray-shaded area below the fitting curves as do the other growth temperatures. For this reason, $T_G$=630 °C produces the most c-oriented BTO domains, which are preferable for FeFET applications. We should stress that even though most grains are c-oriented, the peak tail spreading to the white and cyan regions indicates that some a-oriented domains also exist in BTO. In summary, after a series of characterizations of BTO crystallinity and orientations, $T_G$=630 °C is concluded to be the optimized temperature for 20 nm BTO on a 10 nm STO buffer using 300 W oxygen plasma power.

**Table 4.1** Summary of lattice constants of BTO and STO derived from fittings of Bragg's peak $(002)_{BTO/STO}$ and $(202)_{BTO/STO}$.

| Sample[a)] | $a_{\perp BTO}$ [b)] (Å) | $a_{//BTO}$ [b)] #1 (Å) | BTO Tetra-gonality [b)] #1 | $a_{//BTO}$ #2 (Å) | BTO Tetra-gonality #2 | $a_{\perp STO}$ [c)] (Å) | $a_{//STO}$ [c)] (Å) | STO Tetra-gonality [c)] |
|---|---|---|---|---|---|---|---|---|
| 660 °C +300 W | 4.049 | 4.047 | 1.000 | 3.911 | 1.035 | 3.926 | 3.913 | 1.003 |
| 630 °C +300 W | 4.071 | 4.031 | 1.010 | 3.870 | 1.052 | 3.925 | 3.894 | 1.008 |
| 600 °C +300 W | 4.052 | 4.037 | 1.003 | 3.910 | 1.036 | 3.915 | 3.921 | 0.999 |
| 630 °C +600 W | 4.077 | 4.002 | 1.019 | - | - | 3.896 | 3.964 | 0.983 |

[a)] Growth temperature and plasma power
[b)] Bulk BTO: $a_{\perp}$=4.036 Å, $a_{//}$=3.992 Å and tetragonality: 1.011 The value can be found in ref. [12]
[c)] Bulk STO: $a_{\perp}$=3.905 Å, $a_{//}$=3.905 Å and tetragonality: 1 The value can be found in ref. [12]

### 4.2.2 Oxygen Plasma Power Effects

To oxidize metal cations during perovskite oxide growth, it has been reported that the use of atomic oxygen, generated by a radio frequency plasma, is more efficient than using molecular oxygen [17, 18]. With the optimal $T_G$ determined to be 630 °C, in this section, we will investigate how oxygen plasma powers between 300 W and 600 W will influence the BTO and STO crystal structures. Already the RHEED patterns in Figure 4.5(a) reveal that the sharpness and intensity are much improved after the plasma power is increased from 300 W to 600 W. In Figure 4.5(b), the ω-2θ scan for 600 W also exhibits clearer thickness fringes in both $(002)_{BTO}$ and $(002)_{STO}$. In addition, the 600 W plasma power reduces Δω of the $(002)_{BTO}$ rocking curve and $\chi_{min}$ of Ba to 0.5° and 18%, respectively. Thus, a 600 W plasma power unambiguously improves crystallinity of the BTO/STO/Si stack prepared at $T_G$=630 °C.

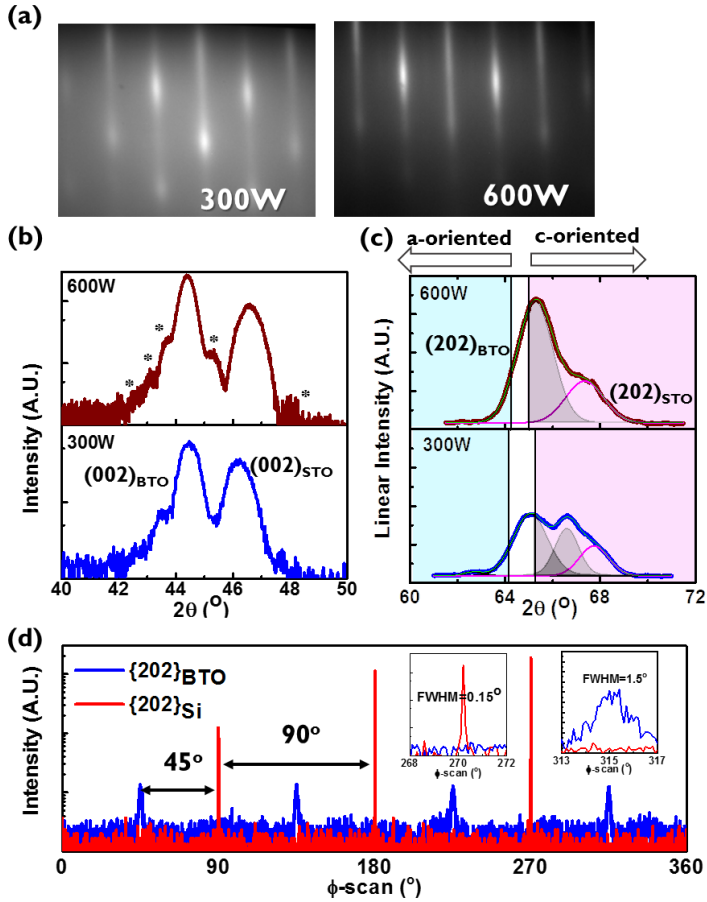


**Figure 4.5:** (a) RHEED patterns for BTO prepared at 630 °C with 300 W and 600 W. (b) The ω-2θ scans of $(002)_{BTO/STO}$ for samples prepared at 300 W and 600 W. (c) The ω-2θ scans of $(202)_{BTO/STO}$ for samples prepared at 300 W and 600 W. (d) The ϕ-scan of $\{202\}_{BTO/Si}$ for the sample prepared at 600 W. Insets show magnifications of the BTO and Si peaks and their corresponding FWHM.

As in the previous section, to extract $a_{\perp}$ and $a_{//}$ for BTO orientation analysis, we fit Bragg's peaks $(002)_{BTO/STO}$ (Figure 4.5(b)) by a Gaussian function and $(202)_{BTO/STO}$ (Figure 4.5(c)) by a Lorentzian function. The $(202)_{BTO}$ shown in Figure 4.5(c) indicates that 600 W produces only a single Bragg's peak instead of the double shoulders occurring at 300 W. Therefore, different from using 300 W, there is only one BTO phase under 600 W. After peak fittings, the $a_{\perp}$, $a_{//}$, and tetragonality for BTO grown at 630 °C with 600 W are also included in Table 4.1. To compare 300 W to 600 W, we observe that 600 W does not change BTO $a_{\perp}$

but produces a BTO $a_{//}$ in between the two BTO $a_{//}$ values measured previously for 300 W. The tetragonality for 600 W is between those of the two phases observed for 300 W. Furthermore, 600 W causes STO to have a smaller $a_{\perp}$ value but a larger $a_{//}$ value than those for 300 W. Consequently, the effect of 600 W on STO tetragonality shows that the STO domain orientation is flipped from slightly c-oriented (tetragonality=1.008) to a-oriented (tetragonality=0.983). By thermal expansion mismatch between STO and Si, such STO lattice constants $a_{//}$ and $a_{\perp}$ can be quantitatively explained. The detailed discussions for the thermal effects on STO crystals will be presented in Section 5.2.2. By the calculations explained in Section 5.2.2, the evaluated $a_{//}$ and $a_{\perp}$ are 0.3920 nm and 0.3895 nm, respectively, which are consistent with our observed values, $a_{\perp}$=0.3896 nm and $a_{//}$=0.3964 nm. This result suggests that the BTO growth using 600 W plasma makes the STO buffer layer fully relaxed to the bulk STO lattice constant during the high-temperature growth.

In addition, performing a similar analysis as described in the last section, we consider lattice variation to investigate the plasma power effect on BTO orientation. We observe in Figure 4.5(b) that the FWHM of 2θ in $(002)_{BTO}$ for 600 W is narrower than that for 300 W, giving a larger grain size at approximately 16 nm, according to Equation (4.1). Thus, for $(202)_{BTO}$ in Figure 4.5(c), there is a smaller white region for 600 W containing a mixture of cubic, a-oriented and c-oriented domains. According to the $(202)_{BTO}$ fittings, the gray-shaded areas within the c-oriented region occupy equally for both 300 W and 600 W. However, 600 W plasma power induces more single-like domain phases instead of manifesting double domains for 300 W. In practice, the existence of multiple domains in the ferroelectric layer hinders polarization switching. Therefore, 600 W is considered to be a preferred plasma power condition over 300 W.

Figure 4.5(d) presents the azimuthal ϕ scan of $(202)_{BTO}$ and $(202)_{Si}$ for the sample prepared at 600 W plasma power. Due to the 4-fold symmetry for both BTO and the Si crystal, the periodicity in the ϕ-scan spectrum is 90°. In addition, the ½ monolayer (ML) of SrO at the interface between STO and Si enables 45° lattice rotation, making an epitaxial STO buffer layer on Si(001) feasible. Then, the BTO layer can be epitaxially grown onto the STO buffer. Thus, the epitaxial relationship for the BTO/STO/Si(001) stack is as follows: <100>BTO(001)//<100>STO(001)//<110>Si(001). Indeed, consistent with this crystal system, the ϕ scan in Figure 4.5(d) also shows a 45° shift between the BTO and Si peaks. However, the insets in Figure 4.5(d) indicate that the FWHM of $(202)_{BTO}$ is 1.5°; whereas that of $(202)_{Si}$ is only 0.15°. This finding indicates that BTO crystallites exhibit a certain amount of azimuthal randomness with in-plane lattice twists of approximately ±0.75° [19].

# 4.3 Effect of Post-Process Annealing

## 4.3.1 TEM Analysis of Crystal Structure

The effects of annealing on the BTO and STO crystallinity were also investigated by XRD and TEM. In XRD analysis, oxygen annealing at 600 °C for 30 minutes does not produce a detectable change. However, the comparison of HR-TEM images in Figure 4.6(a) suggests some differences at the interface. In the as-deposited sample, an amorphous interfacial layer (IL) between STO and the Si(001) substrate can be observed. After annealing, the thickness of the amorphous layer increases. To further analyze the interface, high-angle annular dark-field scanning TEM (HAADF-STEM) measurements for both samples were also performed, as shown in Figure 4.6(b). The IL is actually composed of two layers. Since the image contrast in HAADF-STEM is proportional to the square of the atomic number ($Z^2$), the double layers at the interface suggest different compositions. From electron dispersion spectroscopy (EDS), the spatial atomic concentration for the annealed sample in Figure 4.6(c) reveals the existence of certain diffusion mechanisms: Si diffuses towards the STO, while Sr, Ti and O diffuse to the Si substrate. Figures 4.6(d)-4.6(h) show EDS results for each element in the STO/IL/Si substrate stacks. We find that the entire IL is a silicate compound with graded distributions of Si, O, Sr and Ti. Although the top layer contains more Sr and Ti, the bottom layer is identified as more $SiO_x$-rich. The high temperature from the annealing process triggers the diffusion of mostly O and some Sr and Ti to the Si, turning the crystalline Si to a $SiO_x$-rich silicate due to the Si thermal instability with these compounds [20]. For that reason, we observe from Figure 4.6(a) and 4.6(b) that the IL thickening is towards the Si side. In addition, in Figure 4.6(c) and Figure 4.6(h), some Ti atoms are clearly located within the Si substrate, which can explain why some of the Si area has local brighter contrast, as shown in Figure 4.6(i), which is the HAADF image in Figure 4.6(d) with different image contrast and brightness. To determine the origin of such a mechanism, we compare the HAADF-STEM results for a 10-nm-thick STO layer. In Figure 4.7, the absence of a local brightness difference in the HAADF-STEM result for only 10 nm STO suggests that the Ti diffusion process towards the Si(001) substrate does not occur during STO growth. In contrast, in Figure 4.8, several local bright spots at the top of the Si substrate in the HAADF-STEM image for the as-deposited BTO can be noticed. Thus, such a mechanism happens during the BTO growth, where the $T_G$ is 630 °C offering sufficient energy to trigger Ti diffusion from STO to the Si surface. As the STO is prepared under an oxygen-deficient environment, many oxygen vacancies and sub-oxidized $Ti^{3+}$ (fully-oxidized state is $Ti^{4+}$) are existing in the STO. From First-Principle calculations [21], Ti diffusion is an energy-favorable process in $TiO_{2-x}$. This, to some extent, explains our observations that the BTO growth at 630 ºC leads to Ti

diffusion to the Si surface. Moreover, from the HAADF-STEM images in Figure 4.6(b) and Figure 4.9, the double IL are thickened during the BTO growth. More details of the effects of BTO growth on the IL as well as the STO will be given in Chapter 5.

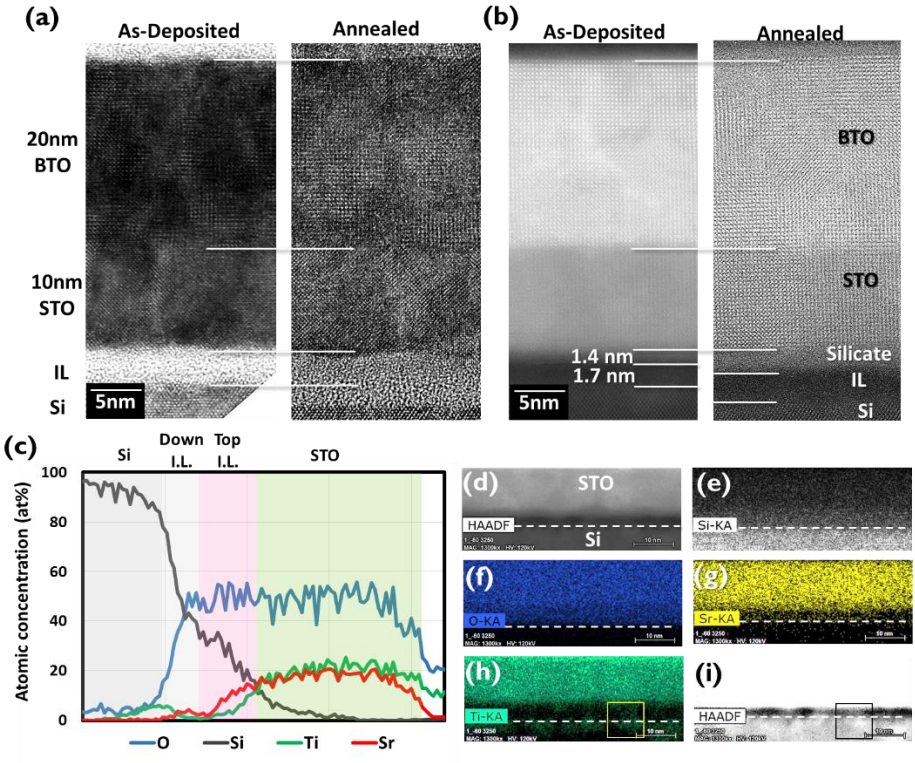


**Figure 4.6:** (a) HR-TEM and (b) HAADF-STEM images of as-deposited and annealed BTO samples. (c) Spatial atomic concentration for the annealed BTO (d) HAADF-STEM image with EDS analysis. EDS detection results for (e) Si (f) O (g) Sr and (h) Ti. (i) The HAADF-STEM image with different brightness and contrast from (d).

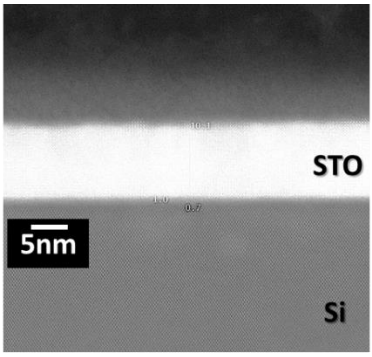


**Figure 4.7:** The HAADF-STEM for 10 nm STO on a Si(001) substrate with high brightness and contrast to indicate the Si region.

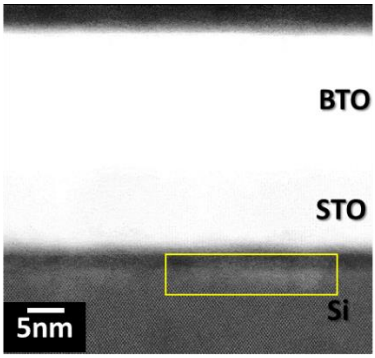


**Figure 4.8:** The HAADF-STEM for as-deposited 20 nm BTO on a Si(001) substrate using a 10 nm STO buffer. The image is presented with high brightness and contrast to indicate the Si region.

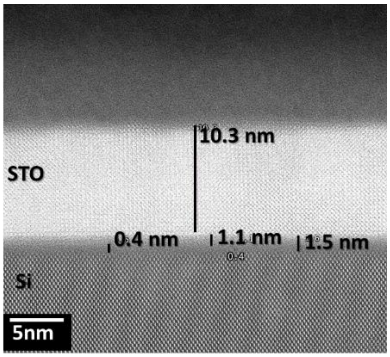


**Figure 4.9:** The HAADF-STEM for 10 nm STO on the Si(001) substrate.

Figure 4.10(a) presents the enlarged HAADF-STEM image. Several regions with different lattices are shown to exist in the BTO layer, highlighted by yellow lines. Even though the STO layer also exhibits this local difference, it is less easily detected than what we observe in BTO. These areas indicate the existence of randomness in the BTO lattice, such as crystal distortion, tilt or twists. As discussed in Section 4.2.1, given by the broadness of 2θ, the BTO layer possesses a grain size of approximately 16 nm, containing a lattice-constant variation. In addition, the azimuthal ϕ-scan shows that those grains have in-plane lattice twists with ±0.75°. Therefore, XRD analysis generally supports the conclusion that the local difference in the HAADF-STEM image originates from the BTO grains.

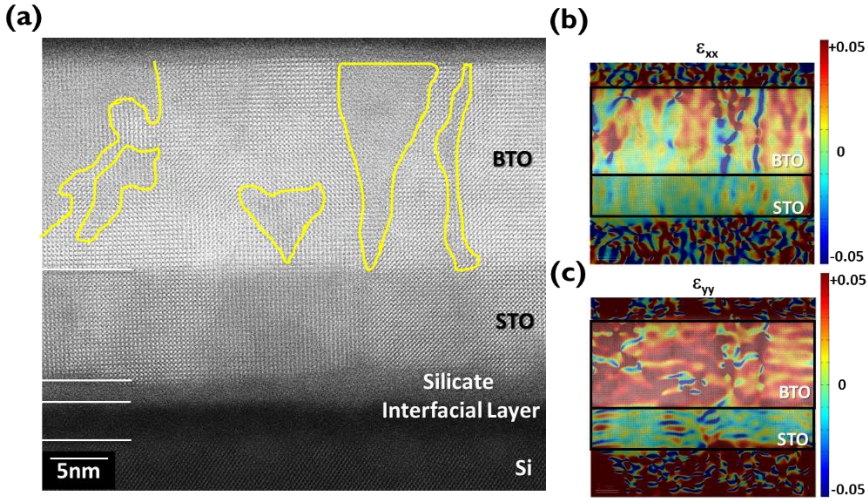


**Figure 4.10:** (a) HAADF-STEM of the annealed sample highlighted with detectable domain boundaries. The mappings of (b) in-plane ($\varepsilon_{xx}$) and (c) out-of-plane ($\varepsilon_{yy}$) strains obtained from GPA analysis.

For further investigation, we applied a geometrical phase algorithm (GPA) to analyze the strain distribution in the BTO and STO layers. Figure 4.10(b) and Figure 4.10(c) show the mappings of $\varepsilon_{xx}$ and $\varepsilon_{yy}$, respectively. The analysis is baselined with respect to STO $a_{//}$ and $a_{\perp}$. In Si, even though the strains are homogeneous, the mappings exhibit random colors. These random colors do not represent actual strains; instead, they are produced by the GPA calculation when analyzing a complex epitaxial relationship: 45° lattice rotation for BTO and STO versus Si. In STO, overall, the $\varepsilon_{xx}$ and $\varepsilon_{yy}$ mappings are fairly uniformly showing approximately zero strain. In contrast, $\varepsilon_{xx}$ in BTO starts from zero strain at the bottom and rises when reaching the BTO surface, as revealed by the color transition from yellow green to dark red. Therefore, BTO $a_{//}$ is strained with STO

$a_{//}$ at the BTO/STO interface; then, it is relaxed to larger $\varepsilon_{xx}$. Nevertheless, the $\varepsilon_{yy}$ shows a different trend in terms of BTO height. The $\varepsilon_{yy}$ at the BTO bottom is larger than that at the surface, according to the color change from dark red to red. The origin of this phenomenon is as follows: at the interface of BTO and STO, when BTO $a_{//}$ is strained with STO $a_{//}$, compressive strain will induce larger $\varepsilon_{yy}$ resulting from $a_{\perp}$ elongation. When reaching the BTO surface, BTO $a_{//}$ is relaxed from STO $a_{//}$; consequently, the compressive strain is decreased, leading to smaller BTO $a_{\perp}$ at the surface. Therefore, supported by Figure 4.10(b) and 4.10(c), in general, BTO has c-oriented domains, according to the presence of more dark red in $\varepsilon_{yy}$ than $\varepsilon_{xx}$. In addition, the degree of tetragonality decreases when moving towards the BTO surface. As described by the derivative calculation used in GPA analysis, grain boundaries shown in the HAADF-STEM image can also be observed in Figure 4.10(b) and 4.10(c) by discontinuities in $\varepsilon_{xx}$ and $\varepsilon_{yy}$.

### 4.3.2 Effect of Post-Growth Annealing on Polarization Switching

In this section, we conduct a series of SPM based studies including atomic force microscopy (AFM), conductive AFM (CAFM) as well as piezo-response force microscopy (PFM) to study how annealing influences BTO polarization switching. During ferroelectric transistor operation, a high leakage current will deteriorate the electric field in the BTO and hinder polarization switching. Therefore, it is important for BTO FeFET applications to understand the current-voltage (I-V) behavior and to know how to obtain a low leakage current in the BTO/STO/p-type Si heterostructure. First, a nanoscale current-voltage (I-V) measurement is performed by CAFM without bottom or top electrodes. In Figure 4.11(a), the as-deposited BTO/STO/p-Si substrate stack shows a dramatic increase in the current when applying a reverse bias. On the contrary, a forward bias of up to +4 V results in a low current of a few pA. Above +4 V the current increases rapidly. Still, a bias of +6 V yields a current smaller than 50 pA. This rectifying phenomenon observed in the forward bias but not in the reverse bias can be explained by the band diagram illustrated in Figure 4.11(b). Although there is around 3 nm silicate in between STO and Si as shown in Figure 4.6(a), such a thin layer might not be seen by the carriers due to tunneling. For that reason, the carrier transport is governed by the band offset at the STO/Si interface, where the conduction band offset is -0.14 eV and the valence band offset is 2.4 eV. On one hand, for the forward bias, the electrons and holes are injected to the Si and BTO respectively, and need to overcome band offsets at both the conduction band and the valence band at the STO/Si interface, leading to a rectifying I-V curve. On the other hand, for the reverse bias, the negative conduction band offset between STO

and Si is favorable for electrons to inject towards the STO, resulting in a huge increase of the current. As soon as post-growth annealing is conducted under oxygen at 600 °C for 30 minutes, we observe a dramatic decrease in the current under a negative bias. Thus, the annealed sample exhibits a low current (±50 pA) starting from -6 V to approximately +6 V. The current reduction after the post-process oxygen annealing is involved with two mechanisms: reducing oxygen vacancies and thickening the silicate IL. Given the ultra-high vacuum (UHV) epitaxial process, it is challenging to avoid the generation of oxygen vacancies in the as-grown samples. Besides, the slight non-stoichiometry in the BTO and STO layer contributes the creations of oxygen vacancies, too. The post-process annealing under ambient oxygen can suppress the oxygen vacancies, reducing the leakage current. However, the effect of reducing the oxygen vacancies is not sufficient to explain the rectifying in I-V. From the previous section we know that the thermo-instability at the STO/Si interface leads to thickening the silicate IL after the annealing process. Since the silicate thickness becomes thicker, the silicate affects the I-V in the whole heterostructure. The silicate is composed of $SiO_x$, $SrO_x$ and $TiO_x$ compounds, so the band offsets of the conduction band and valence band with respect to the Si will be sufficient to block the carriers from both sides now. Figure 4.11(c) takes $SiO_2$ as an example to illustrate the band diagram of BTO/STO/Silicate/Si heterostructure. Therefore, the currents at both positive and negative bias for the oxygen annealed sample remain low, behaving like an insulator.

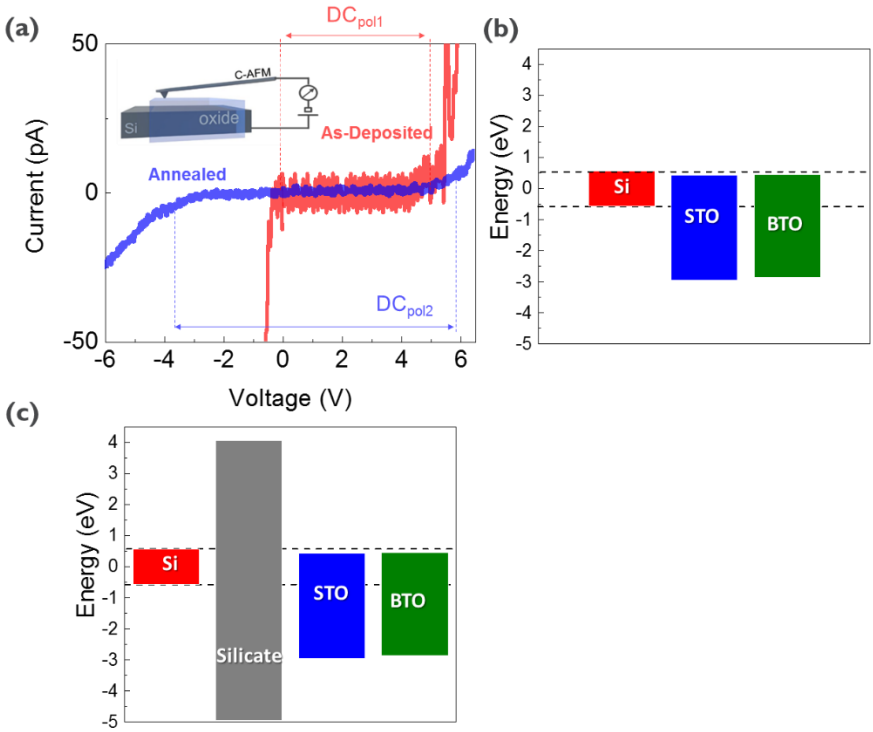


**Figure 4.11:** (a) The I-V measured by CAFM for as-deposited and annealed samples. The band diagram of (b) BTO/STO/Si and (c) BTO/STO/Silicate/Si heterostructure.

Figure 4.12(a) shows the surface morphology of an as-deposited sample measured by AFM. It shows a flat surface with an average roughness of 0.2 nm, consistent with the streak-line RHEED patterns shown in Figure 4.5(a). The I-V curve in Figure 4.11(a) indicates that the operating voltage for an as-deposited sample can only be positive and up to +6 V. Therefore, we conduct domain poling on an as-deposited sample using a DC bias of +6 V with 5 scans and record the piezo-response at AC 3 V and 50 kHz. Figure 4.12(a) presents piezo-response mapping detected by PFM. A poled region with aligned domains shows 50 mV difference in piezo-response relative to an un-poled region where the domains are random. However, even though we can write a domain state using +6 V, the high leakage current at -6 V prevents the switching of domain polarizations. Figure 4.12(b) shows that when we apply a DC bias of -6 V after +6 V, the domains stay the same piezo-response state, meaning that a polarization switch does not occur. According to Figure 4.11(a), a negative bias results in a high leakage current in the as-deposited sample. In this case, carriers are flowing directly through the oxide, and it is difficult for them to accumulate to build up enough electric field

to drive polarization switching. However, the annealed sample with low leakage current for both bias directions can achieve domain switching, as shown in Figure 4.12(c). Originally, domains of the annealed sample are written by +4 V with 5 scans in a large square, showing a piezo-amplitude of up to 700 mV. Subsequently, in the middle area, the domains are poled by -6 V with 5 scans, decreasing the piezo-amplitude to 450 mV. This finding indicates that some domain dipoles are flipped by a reverse bias; thus, the piezo-amplitude is reduced. Therefore, it is important to obtain low leakage current in both bias directions such that a sufficient electric field will be built up and trigger the switching of ferroelectric polarization.

In addition, the time-evolution of the PFM response was also measured to study stability of ferroelectric polarization. First, both samples were poled by a DC voltage at +6 V with 5 scans; then, we monitored how the PFM response changed with time by normalizing the measurements to the original PFM response. Figure 4.12(d) shows the stability comparisons of ferroelectric polarization between as-deposited and annealed samples. The PFM response for the as-deposited sample decays from the beginning of the measurement. However, for the annealed sample, there are two different stages for degradation: Up to 2300 seconds, the PFM response is stable and decays less than 5%; thereafter, the PFM response drops quickly. Such degradation implies that there is a depolarization or back-switching process in both samples. However, the mechanisms behind this phenomenon in our BTO layers are still not clear. It has been reported that domain and grain boundaries in ferroelectric oxides create depolarization fields, contributing to loss of the polarization [16]. As shown in the HAADF-STEM image in Figure 4.10(a), different domains exist simultaneously in the BTO layer. In addition, the ω-2θ scan in Figure 4.5 reveals that they are mostly c-oriented but still with a-oriented domains in the BTO. Thus, the existence of multi-domain boundaries is confirmed and it might be associated with depolarization in both as-deposited and annealed BTO. Nevertheless, to understand the effects of annealing on the depolarization mechanisms, more studies are needed.

Chapter 6 will give another discussion about the analysis for polarization stability.

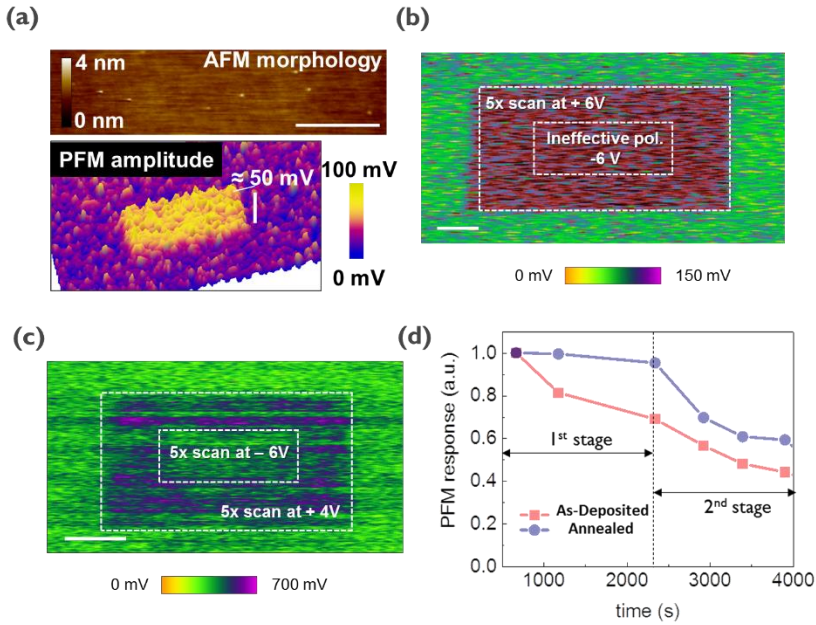


**Figure 4.12:** (a) The AFM morphology and PFM response mapping for as-deposited BTO. The square area in the PFM image is written by DC +6 V with 5 scans. The PFM response mapping of (b) as-deposited and (c) annealed BTO with different poling bias values. Scale bars represent 500 nm. (d) The time evolution of the PFM response for as-deposited and annealed BTO polarized by +6 V with 5 scans.

## 4.4 Conclusion

In conclusion, we investigated how process conditions impact the properties of a 20 nm layer BTO grown by MBE on a Si(001) substrate using a 10 nm STO buffer. First, we executed a series of optimizations for growth temperature and oxygen plasma power to obtain the desired crystallinity and out-of-plane orientation for practical FeFET applications. For the as-deposited BTO film, the I-V measured by CAFM shows a low leakage current up to +4 V. However, a reverse bias induces a high current immediately. This one-sided rectifying behavior allows the BTO domain to be poled only by the forward bias. After oxygen annealing at 600 °C for 30 minutes, the current under reverse bias can be highly suppressed, ameliorating the ferroelectric switching behavior. Even though annealing increases the thickness of the amorphous silicate IL, general crystallinity remains the same based on the ω-2θ scan. In addition, the degradation in the time evolution of the PFM response suggests that depolarization occurs in the BTO layer during device operation. This depolarization can be attributed to

the existence of multi-domains in the layer, confirmed by both XRD and TEM observations. Since BTO is a ternary compound, its properties are highly sensitive to preparation conditions. Therefore, this chapter provides a better understanding and new insights into how to control BTO characteristics by process conditions. All the BTO and STO samples described in the coming chapters will be prepared under the optimal process condition defined in this chapter.

# References

[1] R. Soni et al., "Giant electrode effect on tunnelling electroresistance in ferroelectric tunnel junctions," Nat Commun, vol. 5, p. 5414, Nov 17 2014.

[2] S. Sakai and M. Takahashi, "Recent Progress of Ferroelectric-Gate Field-Effect Transistors and Applications to Nonvolatile Logic and FeNAND Flash Memory," Materials, vol. 3, no. 11, pp. 4950-4964, 2010.

[3] Tsymbal, E. Y. & Kohlstedt, H. Tunneling across a ferroelectric. Science 313, 181–183 (2006)

[4] P. Ponath et al., "Carrier density modulation in a germanium heterostructure by ferroelectric switching," Nat Commun, vol. 6, p. 6067, Jan 14 2015.

[5] E. Bousquet, M. Dawber, N. Stucki, C. Lichtensteiger, P. Hermet, S. Gariglio, J. M. Triscone, and P. Ghosez, "Improper ferroelectricity in perovskite oxide artificial superlattices," Nature 452, 732-736 (2008).

[6] C. Dubourdieu, J. Bruley, T. M. Arruda, A. Posadas, J. Jordan-Sweet, M. M. Frank, E. Cartier, D. J. Frank, S. V. Kalinin, A. A. Demkov, and V. Narayanan, "Switching of ferroelectric polarization in epitaxial BaTiO3 films on silicon without a conducting bottom electrode," Nat Nanotechnol 8, 748-754 (2013).

[7] L. Mazet et al., "Structural study and ferroelectricity of epitaxial BaTiO3 films on silicon grown by molecular beam epitaxy," Journal of Applied Physics, vol. 116, no. 21, p. 214102, 2014.

[8] L. Mazet, S. M. Yang, S. V. Kalinin, S. Schamm-Chardon and C. Dubourdieu, “A review of molecular beam epitaxy of ferroelectric BaTiO3 on Si, Ge and GaAS substrates and their applications,” Sci. Technol. Adv. Mater. 16, 036005 (2015).

[9] J. W. Reiner, A. M. Kolpak, Y. Segal, K. F. Garrity, S. Ismail‐Beigi, C. H. Ahn, and F. J. Walker, "Crystalline oxides on silicon," Advanced Materials 22, 2919-2938 (2010).

[10] Y. Wei et al., "Mechanism of cleaning Si(100) surface using Sr or SrO for the growth of crystalline SrTiO3 films," Journal of Vacuum Science & Technology B: Microelectronics and Nanometer Structures, vol. 20, no. 4, p. 1402, 2002.

[11] A. A. Demkov and X. Zhang, "Theory of the Sr-induced reconstruction of the Si (001) surface," Journal of Applied Physics, vol. 103, no. 10, p. 103710, 2008.

[12] A. A. Demkov and A. B. Posadas, Integration of functional oxides with semiconductors (Springer, 2014).

[13] C. R. Ashman, C. J. Först, K. Schwarz, and P. E. Blöchl, "First-principles calculations of strontium on Si(001)," Physical Review B, vol. 69, no. 7, p. 075309, 02/17/ 2004.

[14] J. Langford and A. J. C. Wilson, “Scherrer after sixty years: A survey and some new results in the determination of crystallite size,” Journal of Applied Crystallography, vol. 11, p. 102-113, 1978.

[15] H. Takuya, T. Kayo, L. Jianyong, K. Takeshi, K. Hirofumi, and T. Takaaki, "Domain Size Effect on Dielectric Properties of Barium Titanate Ceramics," Japanese Journal of Applied Physics, vol. 47, no. 9S, p. 7607, 2008.

[16] Z. Zhao et al., "Grain-size effects on the ferroelectric behavior of dense nanocrystalline BaTiO3 ceramics," Physical Review B, vol. 70, no. 2, p. 024107, 07/30/ 2004.

[17] J. L. Wang et al., "Chemistry and structure of BaTiO3 ultra-thin films grown by different O2 plasma power," Chemical Physics Letters, vol. 592, pp. 206-210, 1/30/ 2014.

[18] K. J. Kormondy et al., "Analysis of the Pockels effect in ferroelectric barium titanate thin films on Si(001)," Microelectronic Engineering, vol. 147, pp. 215-218, 2015.

[19] Z. Boekelheide and F. Hellman, "Cr(110) texture induced by epitaxy on Al2O3(0001) substrates: Preferential grain growth in the <001> direction," Applied Physics Letters, vol. 102, no. 14, p. 141601, 2013.

[20] D. G. Schlom, L.-Q. Chen, X. Pan, A. Schmehl, and M. A. Zurbuchen, "A Thin Film Approach to Engineering Functionality into Oxides," Journal of the American Ceramic Society 91, 2429-2454 (2008).

[21] H. Iddir et al, “Diffusion mechanisms of native point defects in rutile TiO2: Ab initio total-energy calculations,” Phys. Rev. B 75, 073203 (2007).

# 5

# Understandings of BTO Domains[a]

The strain owing to the remaining mismatch of the lattice constants and the different thermal expansion coefficients results in multi-domains within the BTO layers grown on STO-buffered Si(001) [1-3]. BTO has a tetragonal crystal structure, with its optical axis along $<100>_{BTO}$, resulting in six possible domain orientations: two 180°-type domains (c-oriented, out-of-plane optical axis) and four 90°-type domains (a-oriented, in-plane optical axis). Given the optical anisotropy of BTO, the EO behavior of a BTO-based modulator will be dependent on the relationship between the BTO domain orientation (i.e. the BTO optical axis), the externally applied electric field, and the polarization of the optical signal [4]. To design a high performance BTO-integrated Si modulator, it is important to understand how these mixtures of the domains influence its EO properties.

To understand the role of BTO orientation on the device behavior and to learn how to control BTO orientation from the growth process, this chapter consists of three sections. Section 5.1 presents the summary of EO response in the practical Si-integrated waveguides using different electrode configurations and BTO orientations. Section 5.2 demonstrates how thickness engineering of BTO and STO buffer layer control BTO orientations. On section 5.3, we adopted Spectroscopic ellipsometry (SE) approach to study how domain orientations on two different BTO films affect the EO response.

[a] This is the enhanced version of the papers:

- "Controlled Orientation of Molecular-Beam-Epitaxial BaTiO3 on Si(001) Using Thickness Engineering of BaTiO3 and SrTiO3 Buffer Layers" *Appl. Phys. Express* **10** 065501(2017)
- "Orientation-Dependent Electro-Optical Response of BaTiO3 on SrTiO3-Buffered Si(001) Studied via Spectroscopic Ellipsometry" *Optics Mat. Express* **7** 2030 (2017)

## 5.1 Si-Integrated Waveguides Using Different BTO Orientations and Electrode Designs

In this section, we will start from the ideal BTO with purely out-of-plane orientation (c-oriented) or purely in-plane orientation (a-oriented) to understand how the Pockels effect responds to an external electric-field in practical waveguides. This will give us the insights required to understand the generalized cases that will be discussed in Chapter 6.

| Orientation | c-oriented BTO | | a-oriented BTO | |
|---|---|---|---|---|
| | Vertical | In-Plane | Vertical | In-plane |
| | 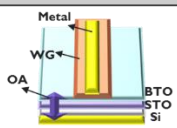 | 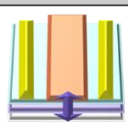 | 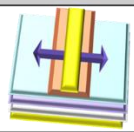 | 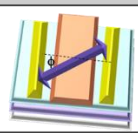 |
| TE | $-\frac{1}{2}n_o^3 r_{13}E$ | 0 | 0 | $-\frac{1}{2}n_{z'}^3 r_{z'}E$ |
| TM | $-\frac{1}{2}n_o^3 r_{13}E - \frac{1}{2}n_e^3 r_{33}E$ | 0 | 0 | $-\frac{1}{2}n_x^3 r_x E - \frac{1}{2}n_{y'}^3 r_{y'}E$ |

**Figure 5.1:** Summary of the index modulations (Δn) for c-oriented and a-oriented BTO with various electrode configurations for TE- and TM- polarized light. The derivations for each case can be found in Appendix A.

The EO modulation for TE- and TM-polarized light in BTO/Si hybrid waveguides using different domain orientations and electrode configurations are summarized in Figure 5.1, where

$$n_x = n_o \tag{5.1}$$

$$r_x = r_{13}cos\phi \tag{5.2}$$

$$n_{y'} = \frac{n_o n_e}{\sqrt{n_e^2 cos^2\phi + n_o^2 sin^2\phi}} \tag{5.3}$$

$$r_{y'} = [(r_{13}cos^3\phi) + (r_{33} + 2r_{51})sin^2\phi cos\phi] \tag{5.4}$$

$$n_{z'} = \frac{n_o n_e}{\sqrt{n_o^2 cos^2\phi + n_e^2 sin^2\phi}} \tag{5.5}$$

$$r_{Z'} = [(r_{33}cos^3\phi) + (r_{13} - 2r_{51})sin^2\phi cos\phi] \tag{5.6}$$

The detailed derivations for each case can be found in Appendix A. To make a comparison of the index modulations over different cases, the extraordinary index $n_e$=2.383, ordinary index $n_o$=2.444, Pockels tensor components $r_{13}$=8 pm/V, $r_{33}$=28 pm/V, $r_{51}$= 800 pm/V, the angle between the a-oriented domain and the electric field $\phi$= 45$^o$ and the electric field E=2x10$^6$ V/m are used [5 , 6]. Figure 5.2 presents the index change as function of the electric field for the different device schemes shown in Figure 5.1. One can clearly see that the Si-integrated waveguides using the in-plane electrodes on the a-oriented BTO have stronger modulation than those using vertical electrodes on the c-oriented BTO. The difference between TE and TM polarizations for the cases of a-oriented BTO is barely noticeable. Therefore, the modulator device using different BTO orientations will lead to distinct EO behaviors. To achieve high performance BTO/Si hybrid modulators, controlling the BTO orientation becomes important. In the next section, we will demonstrate how to engineer the layer thickness of both BTO and STO layers to obtain the desired BTO orientations. Besides, characterizing EO response via the bias-dependent ellipsometry will be presented. Then, more discussions about the optimal device schemes using the in-plane electrodes on the a-oriented BTO will be given in Chapter 6.

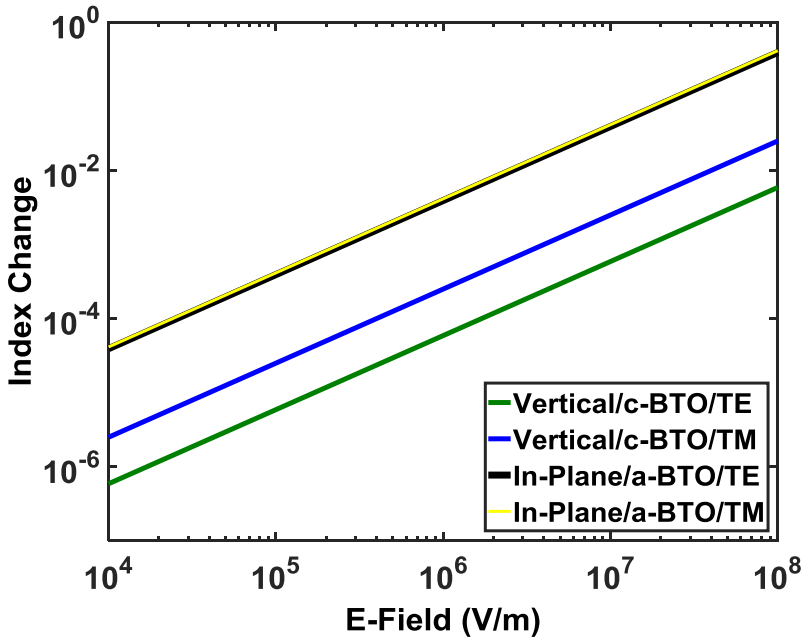


**Figure 5.2:** The index modulations in functions of the electric field for different device schemes described in Figure 5.1. For the a-oriented BTO, the angle between the domain and the electric field $\phi$=45$^{o.}$

## 5.2 Controlled BTO Orientation by Thickness Engineering

In principle, the biaxial strain exerted on the BTO layer will determine its orientation: compressive and tensile strain induce c-oriented and a-oriented BTO, respectively. However, the flexible ionic bonds in BTO and the complicated strain/relaxation mechanisms, which depend on the differential thermal expansion and lattice differences between BTO and the underlying substrate, make it very difficult to control the orientation of BTO on Si(001) substrates [2]. Several groups have reported that using a few nanometer thick STO buffer layer, which has a smaller lattice constant, on Si(001) can cause thin BTO layers (thicknesses below 20 nm) to be more c-oriented [2, 7]. However, for BTO layer thicknesses above 50 nm, the BTO layer will become more a-oriented owing to the tensile strain caused by the difference in the thermal expansion coefficients of Si and the BTO layer [8-10]. For intermediate BTO thicknesses between 20 nm to 50 nm, a mixture of both a- and c-orientation has been reported. Therefore, for BTO/STO/Si(001) heterostructures, the orientation of BTO is mainly determined by a trade-off between the strain originating from respectively the difference in lattice constant and the difference in thermal expansion of the various layers.

Hence, in this section, we systematically study the orientation of BTO in response to this strain, as function of the thickness of the BTO layer itself and that of the underlying STO buffer layer. We use MBE to epitaxially grow the STO buffer layer followed by the BTO layer with various thicknesses of both layers on Si(001) substrates. First, we investigate the effect of the STO thickness on the crystal structure and the interface between STO and Si(001). Then, we analyze the crystallinity and orientation of samples with different BTO thicknesses on top of a 5-nm-thick STO buffer layer. In addition, we study the orientation of BTO layers grown on STO buffer layers with various thicknesses.

### 5.2.1 Thickness Effects on Epitaxial STO on Si(001)

Figure 5.3 presents the results of the crystal and interface analysis, obtained through high-resolution X-ray diffractometry (HRXRD), synchrotron radiation grazing incidence X-ray diffractometry (SR-GIXRD) [11], transmission electron microscopy (TEM) and X-ray photoemission spectroscopy (XPS), for a series of samples with different STO thicknesses on a Si(001) substrate. To extract the STO out-of-plane lattice constants ($a_{\perp}$), the $\omega$-$2\theta$ spectrum measured by HRXRD is fitted by Lorentzian functions. Then, according to (002)STO peak positions, the STO out-of-plane lattice constants ($a_{\perp}$) for layer thicknesses between 2.5 to 40 nm are extracted, as presented in Figure 5.3(a). The error bars are related to the

uncertainty of the peak positions during the fitting process. Bulk STO on Si with a "cube-on-cube" epitaxial relationship shows a lattice mismatch of around 28% (bulk STO: 0.3905 nm; Si: 0.5431 nm) [12]. However, the introduction of ½ ML of Sr at the interface promotes 45° rotation of the STO lattice with respect to the Si lattice, thereby reducing the effective lattice mismatch down to 2% (Si/ √2: 0.3840 nm). Therefore, Si inherently exerts compressive strain on the STO layer, prolonging the lattice in the out-of-plane direction, as measured for the 2.5-nm-thick STO sample, which has a large $a_{\perp}$ (Figure 5.3(a)). This also indicates that the strain in the thin STO layer does not fully relax during the recrystallization step. For STO thicknesses greater than 5 nm the relaxation happens gradually, reducing the lattice constant toward that of bulk STO. In the 5-nm-thick STO layer, $a_{\perp}$ is partially relaxed (larger $a_{\perp}$ than bulk STO). The in-plane relaxation for the 5-nm-thick STO layer is measured by reciprocal space mapping (RSM) of $(220)_{Si}$ using SR-GIXRD. The RSM results show that the STO peak tracks the relaxation line (indicated by the white dotted line) and is located at $(1.967\ 1.967\ 0)_{Si}$, suggesting a full relaxation in plane (in-plane lattice constant $a_{//}$ = 0.3905 nm). Therefore, the 5-nm-thick STO layer exhibits a different degree of relaxation in the in- and out-of-plane directions. As the layer thickness is increased to 40 nm, $a_{\perp}$ relaxes below the bulk value. Conversely, the value of $a_{//}$ is found to be 0.3927 nm beyond the bulk value, from a ω-2θ scan of $(202)_{STO}$ using HRXRD. The main cause of the strain/relaxation imbalance in the STO layer is caused by the flexible ionic bonds. Further, the mismatch of the thermal coefficient of STO ($\alpha_{STO}$=8.8×10$^{-6}$ °C$^{-1}$ for bulk STO) and that of Si ($\alpha_{Si}$=2.6×10$^{-6}$ °C$^{-1}$ for Si) needs to be considered. To quantitatively explain the thermal effect on the STO lattice, we assume that, at the recrystallization temperature of 550 °C, the STO thin film will be relaxed in the plane to the bulk STO lattice constant ($a^{550°CSTO_Bulk}$), which is given by

$$a^{550°CSTO_Bulk} = a^{20°CSTO_Bulk}[1+ \alpha_{STO}(550-20)] \quad (5.7)$$

where $a^{20°CSTO_Bulk}$ the bulk STO lattice constant at 20 °C is equal to 0.3905nm. Thus, the lattice constant of the STO thin film at 550 °C is 0.3923 nm. Since the STO thin film adheres onto the Si surface, when cooling down to 20 °C, the contraction of the STO in-plane lattice is driven by the thermal expansion coefficient of Si [13, 14] and hence the in-plane lattice constant of the STO thin film at 20 °C ($a_{//}^{20°CSTO_film}$) is given by

$$a_{//}^{20°CSTO_film} = a^{550°CSTO_Bulk}[1+ \alpha_{Si}(20-550)] \quad (5.8)$$

Therefore, the $a_{//}^{20°CSTO_film}$ becomes 0.3918 nm, in good agreement with our experimental value of 0.3927 nm. Furthermore, according to

$$(a_{\perp}^{20°CSTO_film} - a^{20°CSTO_Bulk}) = 2\cdot(C_{12}/C_{11})\cdot(a_{//}^{20°CSTO_film} - a^{20°CSTO_Bulk}) \quad (5.9)$$

where $a_{\perp}^{20°CSTO_film}$ is the out-of-plane lattice constant of the STO thin film at 20 °C and $C_{12}/C_{11}$=0.3228, we find $a_{\perp}^{20°CSTO_film}$ = 0.3897 nm, which is consistent with our measured value 0.3895 nm. To summarize, the strain of the 2.5-nm-thick STO layer is mainly governed by compressive strain from Si leading to a large $a_{\perp}$. But the strain/relaxation mechanism for the thicker STO layer is determined more by thermal expansion, which leads to tensile strain, thereby reducing $a_{\perp}$.

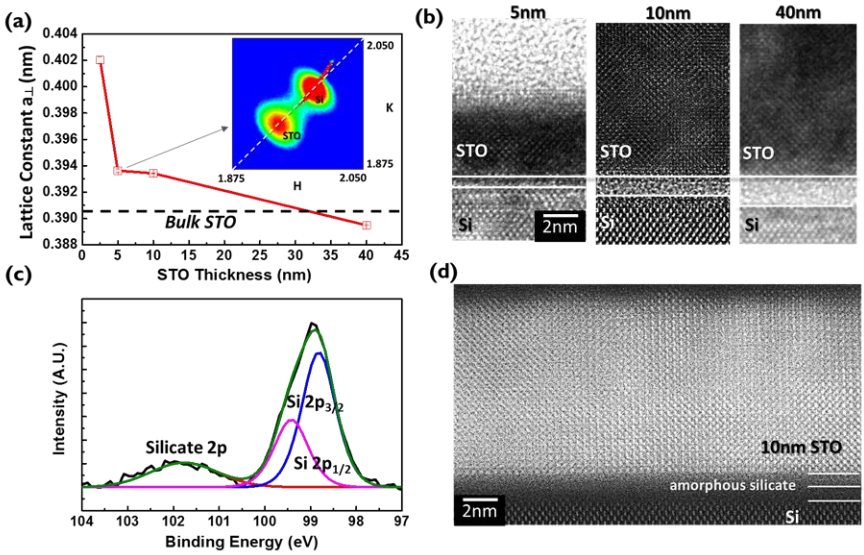


**Figure 5.3:** (a) The lattice constant $a_{\perp}$ as a function of the STO layer thickness on a Si(001) substrate. The inset shows the RSM of $(220)_{Si}$ for a 5-nm-thick STO layer. (b) HRTEM of 5, 10, and 40-nm-thick layers of STO on Si(001). (c) A Si2p XPS scan of the 5-nm-thick STO layer on Si(001). (d) HAADF-STEM of a 10-nm-thick STO layer on Si(001)

Figure 5.3(b) shows cross-sectional high resolution TEM (HR-TEM) images along the $[110]_{Si}$ zone axis for 5-, 10-, and 40-nm-thick STO layers on Si. The relative orientation of the structures is $[100]_{STO}//[110]_{Si}$ zone axis and $[001]_{STO}//[001]_{Si}$ in vertical direction. Because of the thermodynamic instability of the system [15], an amorphous interfacial layer (IL) is formed between the STO and the Si(001) substrate. However, for the 5-nm-thick STO layer, this interfacial layer is barely observable. Hence, we conduct XPS on 5-nm-thick STO/Si heterostructures to analyze the interface further, as shown in Figure 5.3(c). The

silicate peak near the Si 2p core level can be observed near ~102 eV. By fitting its peak area, the thickness of the IL is determined to be around 0.7 nm. The combination of TEM and XPS characterization allows the thickness of each amorphous layer to be extracted and compared (as shown in Figure 5.3(b)), showing that the IL grows with the STO thickness. From the high-angle annular dark field scanning TEM (HAADF-STEM) image shown in Figure 5.3(d), we can derive that this IL is actually composed of two layers. Since the contrast in HAADF-STEM images is proportional to the square of the atomic number ($Z^2$), the brightness of the double layers at the interface indicate that they have different compositions. Electron dispersion spectroscopy (EDS) measurements show that the whole IL is composed of a silicate compound with a graded distribution of Si, O, Sr, and Ti, which is the result of diffusion processes during the STO recrystallization step at high temperature. The top layer contains more Sr and Ti, while the bottom layer is more $SiO_x$-rich.

### 5.2.2 Thickness Effects on BTO/5nm STO/Si(001)

Further, we also study the influence of the BTO thickness on both the BTO and STO crystal structure and investigate the interface stability. BTO layers with thicknesses ranging from 5 to 100 nm are grown on Si(001) with a 5-nm-thick STO buffer layers. For the BTO thicknesses below 20nm, the BTO in-plane lattice constant $a_{//}$ is evaluated using a scan from the origin to $(220)_{Si}$ in reciprocal space using SR-GIXRD. The thicker layers are evaluated using ω-2θ scans of $(202)_{BTO}$ Bragg reflections using HRXRD. The values of $a_{\perp}$ for all the BTO layer sample are determined by studying $(002)_{BTO}$ using HRXRD. It should be noted that for a-oriented BTO, the 4 equivalent domain orientations in the plane should result in a double peak corresponding to $(202)_{BTO}$ and $(220)_{BTO}$ related to the distinct in-plane lattice constants, c and a. However, it is challenging to resolve the double peaks in our HRXRD setup due to the small difference of the lattice constants. For that reason, the in-plane lattice constant ($a_{//}$) for BTO used in this work is the average value. Figure 5.4(a) presents the evolution of the BTO lattice constant, including $a_{\perp}$, $a_{//}$, and the tetragonality ($a_{\perp}/a_{//}$) as a function of the BTO thickness grown on a 5-nm-thick STO buffer layer on Si(001). We clearly observe that for increasing BTO thicknesses, the out-of-plane lattice $a_{\perp}$ is reduced, while the in-plane lattice constant $a_{//}$ is increased. The evolution of the tetragonality suggests that the orientation of BTO flips from c- to a-oriented as the thickness is increased. When the thickness of the BTO layer is below 20 nm, compressive strain originating from the larger in-plane BTO lattice constant (bulk c-oriented BTO: $a_{//}$=0.3992 nm vs bulk STO $a_{//}$=0.3905 nm) dominates. This causes BTO to

become more c-oriented. However, for BTO thicknesses greater than 20 nm, the strain caused by the thermal expansion starts to play a role: Since the BTO spaced by the 5nm STO buffer is close to the Si surface, when cooling down after the growth, the thermal expansion of Si drives the contraction of the BTO in-plane lattice. Given by the huge difference in the thermal expansion coefficient of BTO ($\alpha_{BTO} = 11 \times 10^{-6}$ $K^{-1}$ for bulk BTO) and that of Si, the tensile strain causes the BTO orientation to change from out-of-plane to in-plane. It should be also noted that the volume of a BTO unit cell on 5nm STO is larger than the bulk BTO unit cell volume, which indicates that some point defects are generated during growth. Further, the change of $a_{\perp}$ for the 5-nm-thick STO film covered with BTO layers with various thicknesses is compared in Figure 5.4(b). When a 5-nm-thick BTO layer is grown on the 5-nm-thick STO layer, the value of $a_{\perp}$ for STO is relaxed and remains low for BTO layer thicknesses between 20 and 100 nm. Such an initial STO relaxation can be linked to the effect of the oxygen plasma during the BTO growth, as discussed in Section 4.2.2. Besides, the same can also be observed in the HAADF-STEM image in Figure 5.4(c). BTO layers that are 20 and 100 nm thick have a similarly thick amorphous silicate region at the interface between the 10-nm-thick STO layer and the Si substrate. Figure 5.4(d) presents the ω-2θ scans of the $(002)_{BTO/STO}$ using the HRXRD for the thinnest (5 nm) and the thickest (100 nm) BTO on the 5-nm-thick STO buffer layer. When the BTO thickness is increased, the width of the $(002)_{BTO}$ peak is decreased, indicating the crystallite size within the BTO layer is enlarged. According to the Scherrer equation, the evaluated crystallite size for the 100 nm BTO layer is around 25 nm.

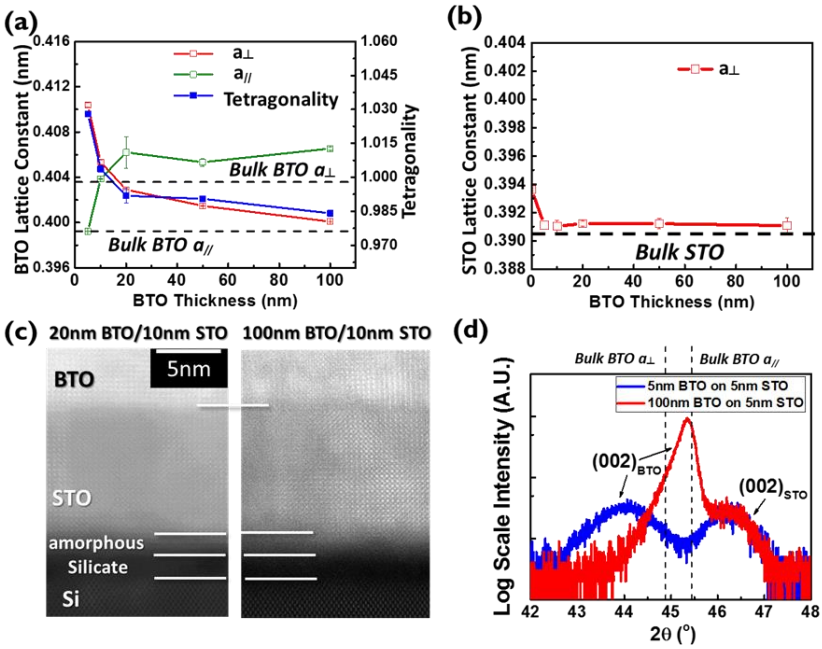

**Figure 5.4:** (a) The lattice constants, $a_{\perp}$, $a_{//}$, and tetragonality for BTO with different layer thicknesses on a 5-nm-thick STO layer. (b) $a_{\perp}$ of the STO for samples with different BTO layer thicknesses on top of a 5-nm-thick STO layer. (c) The HAADF-STEM image for 20- and 100-nm-thick BTO layers on a 10-nm-thick STO buffer layer. (d) The ω-2θ scans of the (002)BTO/STO for 5-nm-thick and 100-nm-thick BTO on a 5-nm-thick STO layer.

In addition, we investigate the dependency of the crystallinity of the BTO layers on their thickness. First of all, RBS channeling is performed to quantitatively analyze the BTO crystallinity. Figure 5.5(a) shows the random and channeled RBS spectra for the 5-nm-thick BTO layer grown on a 5-nm-thick STO buffer layer. In principle, the better the layer quality, the more alpha particles can be channeled without being scattered. Therefore, better quality layers will have a lower minimum yield ($\chi_{min}$), defined by the signal ratio of the channeled and random particles. In Figure 5.5(b), Ba $\chi_{min}$ reveals that the BTO quality improves as the BTO thickness increases. Figure 5.5(b) also shows the full width at half maximum (FWHM) of the $(002)_{BTO}$ rocking curve (Δω) acquired using HRXRD. The evolution of the FWHM shows the same trend as Ba $\chi_{min}$: the FWHM is reduced as the BTO thickness increases. Additionally, the RHEED streak line patterns in Figure 5.5(c) show that thicker BTO layers have better intensities, sharpness, and contrast against the background. Thus, the data obtained from RBS channeling, HRXRD, and RHEED all confirm that the quality of the BTO layer improves as the thickness is increased.

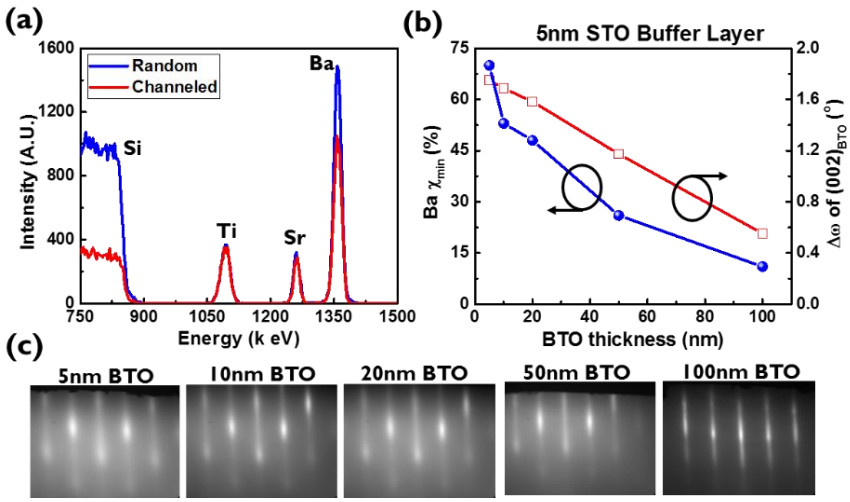


**Figure 5.5:** (a) The RBS spectra for a 5-nm-thick BTO layer with a random or channeled configuration on a 5-nm-thick STO layer on a Si substrate. (b) Ba $\chi_{min}$ for RBS channeling and FWHM of the $(002)_{BTO}$ rocking

curve, Δω, for various BTO layer thicknesses on 5-nm-thick STO layers. (c) a series of RHEED images with different BTO layer thicknesses on a 5-nm-thick STO buffer layer..

### 5.2.3 STO Thickness Effects on BTO/STO/Si(001)

In the previous section, we note that the strain in the 5- and 10-nm-thick BTO layers is dominated by lattice effects of the underlying stacks (STO and Si), which exert compressive strain on the BTO layer. But, for BTO layers thicker than 10 nm, the thermal expansion effect becomes pronounced. To understand the BTO relaxation behavior better, we prepare a series of heterostructures that have BTO layers with several thicknesses (20, 40, and 100 nm) and are grown on STO buffer layers with different thicknesses (5 and 40 nm). In Figure 5.6(a), the values of $a_{\perp}$ for BTO on 5 nm STO layers decrease until they are the same as the bulk BTO $a_{//}$ value when the BTO layer thickness increases. We also note that the value of $a_{\perp}$ in BTO with a 40-nm-thick STO layers is constant regardless of the BTO layer thickness. Further, as can be observed in Figure 5.6(b), with a thicker STO buffer layer, the value of $a_{//}$ for a 20- to 100-nm-thick BTO layer is smaller and close to that of bulk BTO. Thus, the tetragonality in Figure 5.6(c) shows that BTO samples on 5-nm-thick STO layers are a-oriented while those grown on 40-nm-thick STO layers are c-oriented. As mentioned previously, the thick BTO layers on the 5nm STO buffer inherently tend to show a-orientation due to the tensile strain originating from the difference in the thermal expansion coefficient of BTO and that of Si. Nevertheless, when using a 40-nm-thick STO buffer layer as a spacer between the BTO and Si, this effect becomes less important. As a consequence, c-oriented BTO layers can be obtained.

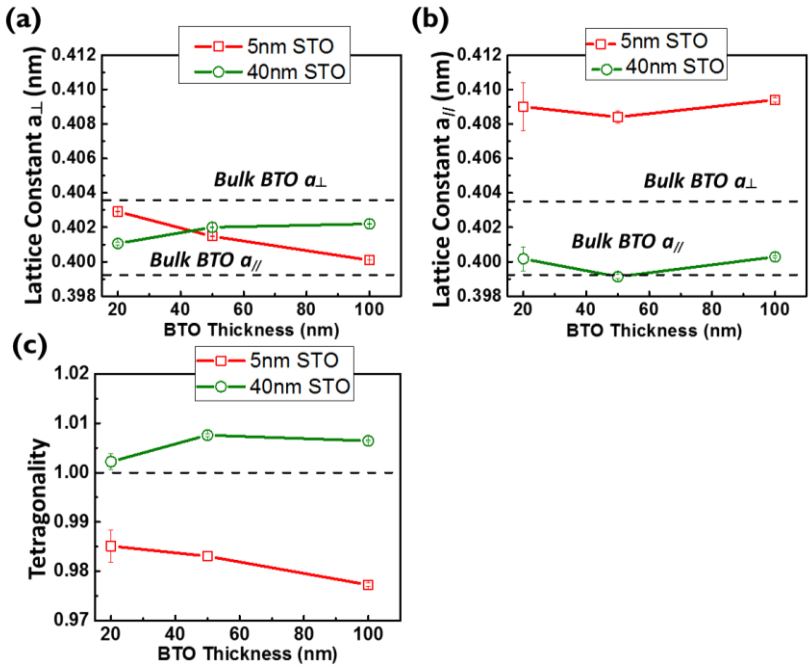


**Figure 5.6:** (a) The $a_{\perp}$, (b) $a_{//}$, and (c) tetragonality of BTO films with different thicknesses on 5- and 40-nm-thick STO buffer layers.

### 5.2.4 Summary

In conclusion, the trade-off between compressive and tensile strain determines the lattice constants as well as the domain orientation of BTO grown on silicon substrates using an STO buffer layer. For BTO/5nm STO/Si(001) heterostructures, the strain in a thin BTO layer is dominated by the compressive strain from the BTO/STO lattice mismatch, leading to more c-oriented BTO. On the contrary, the strain in a thick BTO layer is governed by the tensile strain originating from the different thermal expansion coefficients for Si and BTO, making BTO more a-oriented. In this work, it has been also found that, when using a thick STO buffer layer, c-oriented BTO tends to be obtained, because the impact from the Si thermal expansion on BTO orientation is reduced and the compressive strain dominates. Practically, different applications require different BTO orientations and layer thicknesses. For example, thin c-oriented BTO films are preferable for non-volatile transistor applications owing to CMOS scaling issues and current traditional planar-stack device structures [2]. However, for optical modulator applications, both c-oriented and a-oriented BTO with various thicknesses may be applicable, depending on the exact design and the interplay between polarization of the light, BTO domain orientation, and electrode configuration [5,

7, 15]. Hence, this series of investigations offers different possibilities for controlling the BTO domain orientation for various device applications by engineering the thickness of the BTO and STO buffer layers.

## 5.3 Orientation-Dependent EO Response Studied By Spectroscopic Ellipsometry

The spectroscopic ellipsometry (SE) is used to investigate how the EO response of two differently grown films depends on their respective domain orientation. The 100 nm BTO films are grown using plasma-assisted MBE starting from respectively a 10 nm and a 40 nm STO buffer layer deposited on highly p-doped Si(001) substrates. Via X-ray diffraction (XRD), the BTO film grown on the 10-nm-thick STO buffer is identified as being more a-oriented while the BTO layer grown on 40-nm-thick STO is shown to be more c-oriented. Then, we analyze the EO behavior in a- and c-oriented BTO films by studying the interplay between domain orientations and applied electric field.

### 5.3.1 Crystal Structures and Domain Orientations

In this section, the XRD analysis is performed to identify the domain orientation and crystallinity in 100-nm-thick BTO samples on Si(001) substrate using 10 nm and 40 nm STO buffer layers. Figure 5.7(a) presents ω-2θ XRD scans along $[001]_{BTO}$ and $[101]_{BTO}$. Based on the position of the Bragg peaks along $(002)_{BTO/STO}$ and $(202)_{BTO/STO}$, the average in-plane lattice constant $a_{//}$, the out-of-plane lattice constant $a_{\perp}$, and the tetragonality $a_{\perp}/a_{//}$ of the samples can be extracted. The lattice parameters of bulk BTO can be taken as a reference: bulk c-oriented BTO has $a_{//}$ = 0.3992 nm, $a_{\perp}$ = 0.4036 nm, and tetragonality = 1.011; bulk a-oriented BTO has $a_{//}$ = 0.4036 nm, $a_{\perp}$ = 0.3992 nm, and tetragonality = 0.989.

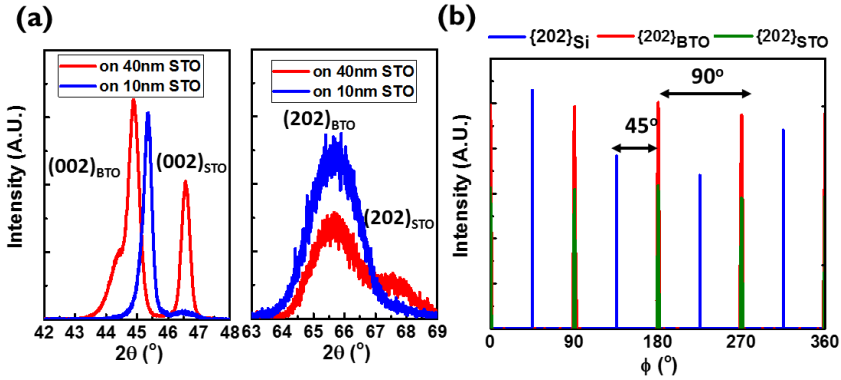


**Figure 5.7:** (a) The ω-2θ XRD scans along $[001]_{BTO/STO}$ and $[101]_{BTO/STO}$ for a 100-nm-thick BTO layer on 10- and 40-nm-thick STO layer. (b) A ϕ-scan of $\{202\}_{Si}$, $\{202\}_{BTO}$, and $\{202\}_{STO}$ for 100-nm-thick BTO on a 40 nm STO layer.

Derived from the data in Figure 5.7(a), the $a_{\perp}$, average $a_{//}$ and tetragonality values for the BTO layer grown on the 40-nm-thick STO buffer layer are 0.4022 nm, 0.4003 nm, and 1.005, respectively. The tetragonality greater than unity indicates that domains in this layer are mostly c-oriented. On the other hand, for the BTO layer grown on the 10-nm-thick STO buffer, $a_{\perp}$ = 0.3997 nm, average $a_{//}$ = 0.4039 nm, and $a_{\perp}/a_{//}$ = 0.990 are evaluated, indicating that a-oriented domains are predominant. The different behavior of both samples is driven by the trade-off between the compressive and tensile strain in the BTO/STO/Si(001) heterostructures. The compressive strain resulted from the smaller a// for the underlying STO layer ($a_{//}$ = 0.3905 nm for bulk STO and $a_{//}$ = 0.3992 nm for bulk c-oriented BTO) tends to favor c-oriented BTO. Conversely, because of the difference in the thermal expansion coefficients of Si and BTO ($\alpha_{Si}$= 2.6 × $10^{-6}$ $K^{-1}$ for Si and $\alpha_{BTO}$ = 11 × $10^{-6}$ $K^{-1}$ for bulk BTO), the tensile strain is also exerted on the BTO layer, favoring a-oriented domains. By using the 10 nm thick STO buffer, the BTO layer is close to the Si surface. When cooling down after the growth, the Si thermal expansion drives the contraction of the BTO in-plane lattice [13, 14]. Therefore, the tensile strain is formed, leading the BTO orientation to be more a-oriented [13]. Nevertheless, by using a 40-nm-thick STO buffer layer as a "spacer" between the BTO and Si, the effect from the Si thermal expansion coefficient, which brings about the tensile strain, is attenuated. Thus, the compressive strain induced by the difference in lattice constants becomes dominant, facilitating more c-oriented domains in the BTO layer. For convenience, in the remainder of this work, we will denote the samples grown on the 10- and 40-nm-thick STO buffer layer as a-oriented and c-oriented, respectively. Figure

5.7(b) presents the azimuthal ϕ scan of $(202)_{STO}$, $(202)_{BTO}$ and $(202)_{Si}$ for c-oriented BTO. Due to the 4-fold symmetry, periodicity in the ϕ-scan spectrum is 90°. In addition, the ½ ML of Sr at the interface between STO and Si initiates 45° lattice rotation, making an epitaxial STO buffer layer on Si(001) feasible. Then, the BTO layer can be epitaxially grown onto the STO buffer. Thus, the epitaxial relationship for the BTO/STO/Si(001) stack is as follows: <100>BTO(001)//<100>STO(001)//<110>Si(001). Indeed, consistent with this crystal system, the ϕ scans of $\{202\}_{Si}$, $\{202\}_{BTO}$, and $\{202\}_{STO}$ in Figure 5.7(b) also shows a 45° shift for the BTO and STO with respect to the Si peaks. Besides, the BTO crystal quality for both orientations is comparable. The full width half maximum of the $(002)_{BTO}$ rocking curve (ω-scan) is 0.8° and 0.7° for the a- and c-oriented BTO, respectively.

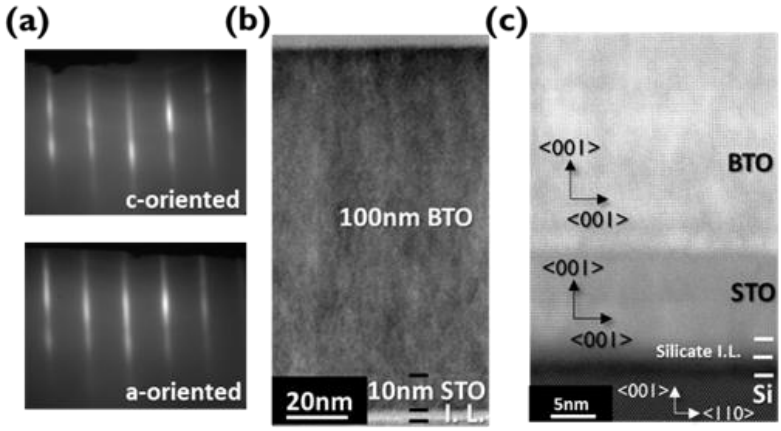


**Figure 5.8:** (a) The RHEED patterns for c- and a-oriented BTO layers on Si(001). TEM (b) and HAADF-STEM (c) images for 100-nm-thick layers of a-oriented BTO on a Si(001) substrate with a 10-nm-thick STO buffer layer.

Similarly, the RHEED patterns of both films, shown in Figure 5.8(a), exhibit sharp streak-lines, revealing a good crystallinity of the BTO as well as a flat surface. This is in agreement with Figure 5.8(b), which shows the transmission electron microscope (TEM) image for a-oriented BTO, illustrating low roughness on the top surface. However, we note that there is a 3.5 nm amorphous interfacial layer between the STO layer and the Si substrate. From the high-angle annular dark field scanning TEM (HAADF-STEM) image shown in Figure 5.8(c), we can derive that this interfacial layer is actually composed of two layers. Since image contrast in HAADF-STEM is proportional to the atomic number squared ($Z^2$), the double layers at interface suggest layers with different compositions. From electron dispersion spectroscopy, the whole interfacial layer is found to be composed of a silicate compound with a graded distribution of Si, O, Sr, and Ti.

The top layer contains more Sr and Ti, while the bottom layer is identified as being more $SiO_x$-rich. Such an amorphous double-layer interface is formed at the beginning of the STO preparation step. From our observations, a thicker STO brings about an increasing silicate thickness. Therefore, the interfacial layer for c-oriented BTO (40-nm-thick STO buffer layer) is thicker than that for a-oriented BTO (10-nm-thick STO buffer). Moreover, in agreement with Figure 5.7(b), Figure 5.8(c) indicates the epitaxial relationship between BTO, STO, and the Si(001) substrate, as labelled by the arrows overlaid on the picture. Despite the existence of the silicate IL, promising modulation bandwidth of 5 GHz [16], effective Pockels coefficient of 300 pm/V [17] and waveguide propagation loss of 6 dB/cm [18] have been successfully demonstrated.

### 5.3.2 Electrical Properties

During operation of the EO devices, the leakage current needs to be low to avoid deterioration of the applied field, limiting optical modulator performance. In this section, we focus on the a-oriented BTO sample and investigate the effect of post-process annealing on the leakage current. The annealing is carried out at different temperatures, under ambient oxygen exposure for 30 min. Then, we sputter a 10-nm-thick gold layer as a top electrode.

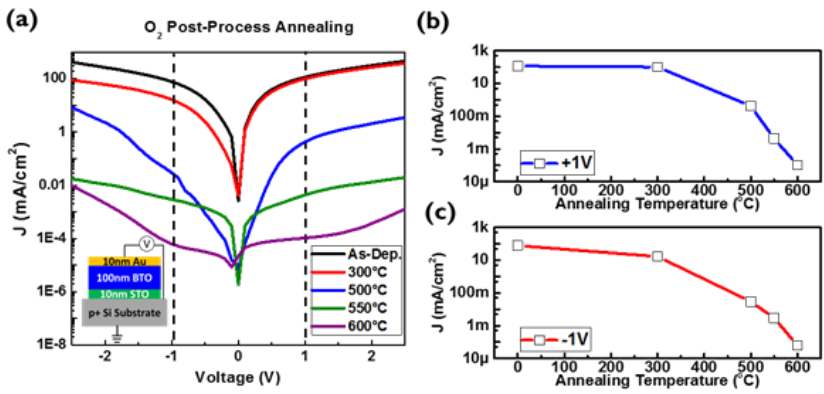


**Figure 5.9:** (a) The J–V curves in terms of various post-process annealing temperatures under 30 min oxygen ambient for 100-nm-thick layers of a-oriented BTO on highly p-doped Si substrates with a 10 nm STO buffer layer. The top electrode is gold (10 nm). (b) and (c) are the current density at +1 V and −1 V, respectively, for different annealing temperatures.

The resulting current density versus voltage (J–V) curves are shown in Figure 5.9(a). The corresponding current densities at +1 V and –1 V are recorded in Figure 5.9(b) and 5.9(c), respectively. The current density results using MBE in

this work are within the range of those by pulsed laser deposition [19]. Given the ultra-high vacuum (UHV) epitaxial process, it is challenging to avoid the generation of oxygen vacancies in the as-grown samples explaining the high leakage current above 100 mA/cm$^2$ at +/- 1 V [10]. According to the chemical equation:

$$O_o = v^{\cdot\cdot}_o + 2e^{/} + 1/2\ O_2(g) \qquad (5.10)$$

at oxygen sites ($O_o$) in the oxide, the creation of one oxygen vacancy with double positive charges ($v^{\cdot\cdot}_o$) will produce two free carriers ($e^{/}$) and one oxygen molecule ($O_2$). Therefore, in an oxygen-deficient condition, carriers created through oxygen vacancy formation cause the oxide to be conductive and absorptive in the near infrared-spectrum [20]. Although the as-deposited sample shows a high leakage current density, post-process annealing under ambient oxygen at increasing temperatures can suppress the leakage current dramatically. Following annealing at 600 °C for 30 minutes, the current density is reduced to $10^{-4}$ mA/cm$^2$ at +/- 1 V. The suppression of the current density at both bias polarities can result from the combinational effects of filling the oxygen vacancies and thickening the silicate IL after the oxygen annealing. In addition, ω-2θ XRD scans show that the BTO crystal structure does not noticeably change under such annealing process. Prior to EO characterizations, both the a- and c-oriented samples studied here are annealed at 600 °C for 30 minutes to improve electrical performance of the heterostructures.

### 5.3.3 EO Characterization Using Spectroscopic Ellipsometry

In principle, spectroscopic ellipsometry (SE) measures the ratio of the reflection coefficients for the TE ($r_{TE}$) and TM ($r_{TM}$) polarized light waves that are incident on the stack under study. This ratio is then expressed as a function of the characteristic terms tan(Ψ) and Δ, as follows:

$$\frac{r_{TM}}{r_{TE}} = tan(\Psi)e^{i\Delta} \qquad (5.11)$$

Fitting an analytical model to the measured data then allows to extract the desired information (refractive index, thickness) of the different layers in the stack. Given that Δ cannot be related to a physical picture of the polarization ellipse in a straightforward manner, in practice one rather uses tan(Ψ) and cos(Δ) for presenting the results of an SE measurement. To enable efficient extraction of the BTO EO properties, we study its effect on the cos(Δ) spectrum in the following analysis.

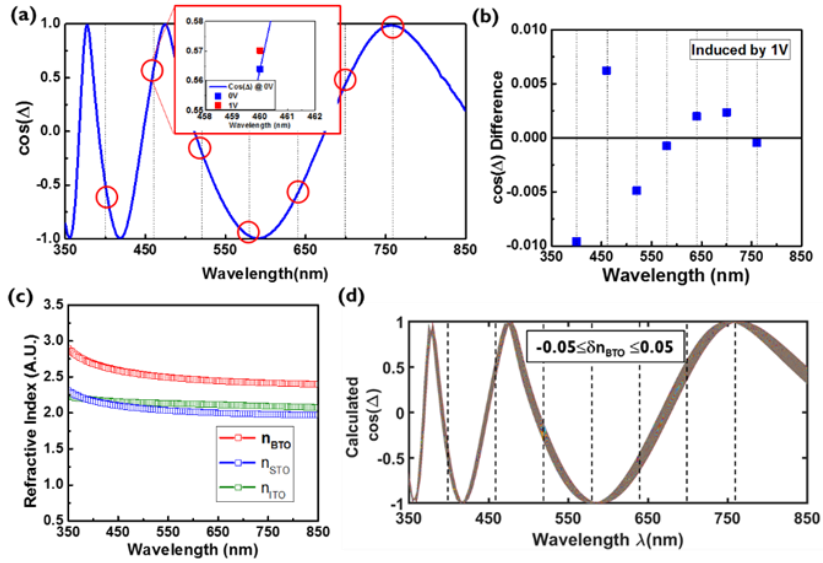


**Figure 5.10:** (a) The measured cos(Δ) spectrum at AOI 65° for a-oriented BTO (100 nm) on a STO-buffered (10 nm) Si substrate at 0 V. The dotted lines indicate the wavelengths where the EO measurements with long acquisition time were executed. The inset shows an EO-induced spectrum shift at 460 nm. (b) The cos(Δ) difference induced by applying 1 V. (c) The refractive indices of BTO, STO, and ITO that are used in the spectrum calculation. (d) A simulated cos(Δ) curve using the TMM with a BTO index variation $\delta n_{BTO}$ of between −0.05 and 0.05.

To perform bias-dependent SE measurements, a transparent electrode must be prepared on the sample surface. The measured samples use a 200 nm indium tin oxide (ITO) layer as the top electrode and a highly p-doped Si substrate as the bottom electrode. In the remainder of this paragraph we use a 200 nm ITO/100 nm a-oriented BTO/10 nm STO/Si structure as an example to explain how the BTO index change induced by an applied voltage is derived. Figure 5.10(a) presents the cos(Δ) spectrum of this structure recorded with a signal acquisition time of 2 s and an applied voltage of 0 V at an angle of incidence (AOI) of 65°. The effect of applying a voltage on the measured cos(Δ) signal is then measured with a much longer acquisition time (90 seconds) as certain discrete wavelengths (labelled by the red dots). Figure 5.10(b) shows the measured difference {cos(Δ(1V)) - cos(Δ(0V))}. As shown in the inset of Figure 5.10(a) and in Figure 5.10(b), the effect on cos(Δ) is small. If a standard parametric spectral fitting method were applied to extract the BTO EO response from such a minor difference in cos(Δ), unphysical results might be obtained, despite a high fitting quality [21]. Therefore, as an alternative, we used a numerical approach to

determine the index change induced by applying a voltage over the BTO layer, based on the transfer matrix method (TMM).

First, a standard parameteric fitting procedure to a dispersion law expressed as a combination of a Tauc-Lorentz model and a Gauss function is used to extract the wavelength dependent refractive indices for BTO, STO and ITO. The results are shown in Figure 5.10(c). Then, based on Equation (5.10), the expected cos(Δ) can be calculated using a TMM with known parameters, including the angle of incidence (AOI), and the thickness and optical indices of the ITO, BTO, STO and Si layers. Subsequently, we vary the BTO index around its measured value with $\delta n_{BTO}$ changing from −0.05 to 0.05, to obtain different cos(Δ) spectra, thus simulating the effect of applying a voltage, as shown in Figure 5.10(d). At each measured wavelength, Figure 5.10(d) can then be used to derive the cos(Δ) difference over the range $0.05 \leqslant \delta n_{BTO} \leqslant 0.05$ with respect to the value at $\delta n_{BTO}=0$. Finally, by comparing Fig. 4(b) with Figure 5.10(d), the measured cos(Δ) difference can be translated in an associated $\delta n_{BTO}$. In the next section, the EO effect as measured in c-oriented and a-oriented BTO using the method described above will be discussed and compared.

### 5.3.4 EO Comparison of c-Oriented & a-Oriented BTO

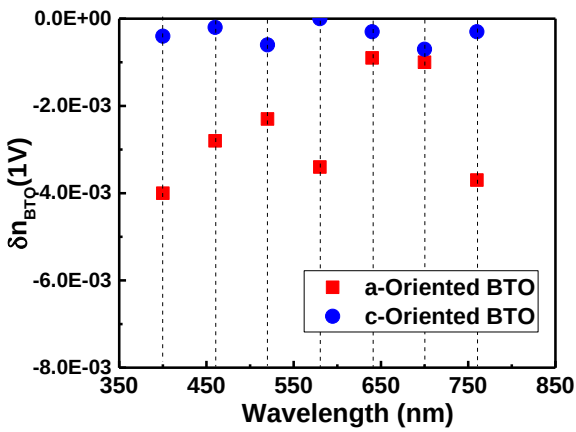


**Figure 5.11:** $\delta n_{BTO}$ at 1 V for a- and c-oriented BTO.

Fig. 5.11 shows $\delta n_{BTO}$(1 V) for a-oriented and c-oriented BTO, calculated by the method described in the previous section. It can be clearly seen that the a-oriented BTO shows a larger $\delta n_{BTO}$ than c-oriented BTO over the whole spectrum. To explain this, we consider single-domain c-oriented BTO, with its domain orientation (optical axis) along the z-axis, as shown in Fig. 5.12(a). Since BTO is

an optically anisotropic material, its ordinary ($n_o$) and extraordinary indices ($n_e$) with respect to the crystal axes can be described through the index ellipsoid shown in Fig. 5.12(a) (without E-field). Then, the effect of applying an electric field is described by the associated deformation of the index ellipsoid according to:

$$(\frac{1}{n_o^2} + r_{13}E_z)x^2 + (\frac{1}{n_o^2} + r_{13}E_z)y^2 + (\frac{1}{n_e^2} + r_{33}E_z)z^2 + 2r_{51}E_x\text{xz} + 2r_{51}E_y\text{yz} = 1 \quad (5.12)$$

with the Pockels tensor

$$r_{ij} = \begin{bmatrix} 0 & 0 & r_{13} \\ 0 & 0 & r_{13} \\ 0 & 0 & r_{33} \\ 0 & r_{51} & 0 \\ r_{51} & 0 & 0 \\ 0 & 0 & 0 \end{bmatrix}; \quad (5.13)$$

in which components $r_{51}$, $r_{13}$ and $r_{33}$ are reported 800, 8 and 28 pm/V for bulk BTO crystals, respectively [5]. Based on equation (5.12), the electric field should be applied perpendicular to the optical axis of the BTO, i.e. along the x- or y-axis, to exploit the strong $r_{51}$ component of the Pockels tensor. Applying an electric field along the z-axis only exploits the much weaker $r_{13}$ and $r_{33}$ components, resulting in a weaker EO effect. Our samples have a top-down electrode configuration resulting in a vertical electric field as shown in Figure 5.12(b). This explains why a stronger EO effect is measured in the a-oriented sample, where the optical axis is perpendicular to the electric field, than in the c-oriented sample, where the electric field is parallel to the optical axis.

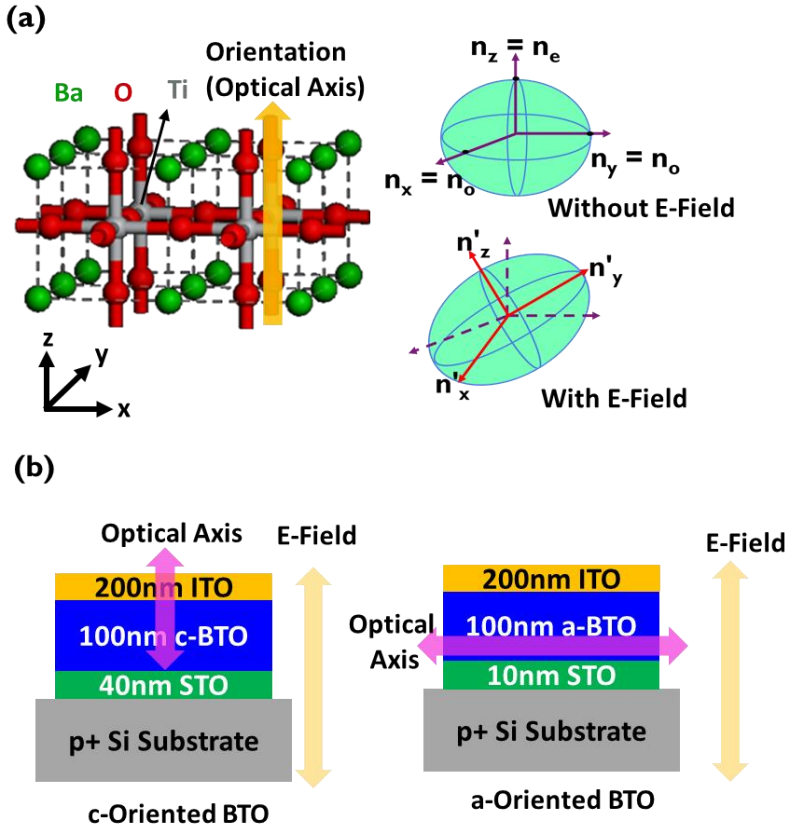


**Figure 5.12:** (a) Lattice structure for c-oriented BTO and its index ellipsoid without and with an applied electric field. (b) Relationship between the electric field and the optical axis in c- and a-oriented BTO.

### 5.3.5 Summary

We prepared 100-nm-thick layers of c- and a-oriented BTO on Si(001) substrates with 40 and 10 nm STO buffer layers. The orientation of the domains was identified by XRD and we utilize RHEED, TEM, and HAADF-STEM analysis to study the crystallinity of the grown BTO layers and the nature of the interface layer between the STO and Si substrate. Even though BTO shows good crystallinity, the UHV MBE process introduces many oxygen vacancies into the layer, resulting in large leakage currents. By post-process annealing in an oxygen ambient at 600 °C for 30 min, the leakage current is efficiently suppressed, ensuring a sufficient electric field can be built up in the BTO layer during device

operation. Then, for both the c-oriented and the a-oriented BTO layers, we investigated how the domain structure influences the EO response, as measured by SE. Given the top-down electrode configuration, the a-oriented BTO layer shows a larger index difference $\delta n_{BTO}$ compared with c-oriented BTO when an external bias of 1 V is applied. This is explained by the fact that the optical axis of a-oriented BTO is perpendicular to the applied electric field, allowing exploiting the strong $r_{51}$ component in this case. The c-oriented BTO sample, however, which has its optical axis parallel to the electric field, shows a weaker EO response, because it relies on the smaller $r_{13}$ and $r_{33}$ components of the Pockels tensor. Therefore, this work provides not only a better understanding in how the domain orientation in a BTO thin film affects its EO response but also provides insights into how to design high performance BTO/Si hybrid modulators, taking into account the domain orientation of the BTO thin films grown on a Si(001) substrate.

# References

[1] K. J. Choi, M. Biegalski, Y. L. Li, A. Sharan, J. Schubert, R. Uecker, P. Reiche, Y. B. Chen, X. Q. Pan, V. Gopalan, L. Q. Chen, D. G. Schlom, and C. B. Eom, "Enhancement of ferroelectricity in strained BaTiO3 thin films," Science 306, 1005-1009 (2004).

[2] C. Dubourdieu, J. Bruley, T. M. Arruda, A. Posadas, J. Jordan-Sweet, M. M. Frank, E. Cartier, D. J. Frank, S. V. Kalinin, A. A. Demkov, and V. Narayanan, "Switching of ferroelectric polarization in epitaxial BaTiO3 films on silicon without a conducting bottom electrode," Nat Nanotechnol 8, 748-754 (2013).

[3] C. Merckling, G. Saint-Girons, C. Botella, G. Hollinger, M. Heyns, J. Dekoster, and M. Caymax, “Molecular beam epitaxial growth of BaTiO3 single crystal on Ge-on-Si(001) substrates” Appl. Phys. Lett. 98, 092901 (2011).

[4] A. Yariv and P. Yeh, Optical waves in crystals (Wiley, New York, 1984), Vol. 10.

[5] P. Castera, D. Tulli, A. M. Gutierrez, and P. Sanchis, "Influence of BaTiO3 ferroelectric orientation for electro-optic modulation on silicon," Opt Express, vol. 23, no. 12, pp. 15332-42, Jun 15 2015.

[6] P. Castera et al., "Electro-Optical Modulation Based on Pockels Effect in BaTiO3 With a Multi-Domain Structure," IEEE Photonics Technology Letters, vol. 28, no. 9, pp. 990-993, 2016.

[7] K. J. Kormondy et al., "Analysis of the Pockels effect in ferroelectric barium titanate thin films on Si(001)," Microelectronic Engineering, vol. 147, pp. 215-218, 2015.

[8] S. Abel et al., "Controlling tetragonality and crystalline orientation in BaTiO3 nano-layers grown on Si," Nanotechnology, vol. 24, no. 28, p. 285701, Jul 19 2013.

[9] D. M. Kim et al., "Thickness dependence of structural and piezoelectric properties of epitaxial Pb(Zr0.52Ti0.48)O3 films on Si and SrTiO3 substrates," Applied Physics Letters, vol. 88, no. 14, p. 142904, 2006.

[10] M.-H. M. Hsu et al., "Diffraction studies for stoichiometry effects in BaTiO3 grown by molecular beam epitaxy on Ge(001)," Journal of Applied Physics, vol. 120, no. 22, p. 225114, 2016.

[11] J. Rubio-Zuazo, P. Ferrer, A. López, A. Gutiérrez-León, I. da Silva, and G. R. Castro, "The multipurpose X-ray diffraction end-station of the BM25B-SpLine synchrotron beamline at the ESRF," Nuclear Instruments and Methods in Physics Research Section A: Accelerators, Spectrometers, Detectors and Associated Equipment, vol. 716, pp. 23-28, 7/11/ 2013.

[12] A. A. Demkov and A. B. Posadas, Integration of functional oxides with semiconductors (Springer, 2014).

[13] G. Delhaye et al., "Structural properties of epitaxial SrTiO3 thin films grown by molecular beam epitaxy on Si(001)," Journal of Applied Physics, vol. 100, no. 12, p. 124109, 2006.

[14] N. Lucas, H. Zabel, H. Morkoç, and H. Unlu, "Anisotropy of thermal expansion of GaAs on Si(001)," Applied Physics Letters, vol. 52, no. 25, pp. 2117-2119, 1988.

[15] A. Petraru, J. Schubert, M. Schmid, and C. Buchal, "Ferroelectric BaTiO3 thin-film optical waveguide modulators," Applied Physics Letters, vol. 81, no. 8, pp. 1375-1377, 2002.

[16] C. Xiong, W. H. Pernice, J. H. Ngai, J. W. Reiner, D. Kumah, F. J. Walker, C. H. Ahn, and H. X. Tang, "Active silicon integrated nanophotonics: ferroelectric BaTiO(3) devices," Nano Lett 14, 1419-1425 (2014).

[17] S. Abel, T. Stoferle, C. Marchiori, D. Caimi, L. Czornomaz, M. Stuckelberger, M. Sousa, B. J. Offrein, and J. Fompeyrine, "A Hybrid Barium Titanate–Silicon Photonics Platform for Ultraefficient Electro-Optic Tuning," Journal of Lightwave Technology 34, 1688-1693 (2016).

[18] F. Eltes, D. Caimi, F. Fallegger, M. Sousa, E. O'Connor, M. D. Rossell, B. Offrein, J. Fompeyrine and S. Abel, "Low-loss BaTiO3–Si waveguides for nonlinear integrated photonics," ACS Photonics, 3, 1698-1703 (2016).

[19] M. Li, J. Zhou, X. Jing, M. Zeng, S. Wu, J. Gao, Z. Zhang, X. Gao, X. Lu, J.M. Liu and M. Alexe, "Controlling resistance switching polarities of epitaxial BaTiO3 films by mediation of ferroelectricity and oxygen vacancies," Adv. Electron. Mater. 1 1500069 (2015).

[20] D. A. Crandles et al., "Optical properties of highly reduced SrTiO3-x" Physical Review B, vol. 59, no. 20, pp. 12842-12846, 05/15/ 1999.

[21] D. V. Likhachev, N. Malkova, and L. Poslavsky, "Modified Tauc–Lorentz dispersion model leading to a more accurate representation of absorption features below the bandgap," Thin Solid Films 589, 844-851 (2015).

# 6

# Optimizing BTO Domain Dynamics for Hybrid BTO/Si Modulators[a]

In this chapter, the correlation between the EO response and the ferroelectricity are investigated by studying the dynamics of BTO domains. In section 6.1, the EO model for multi-domain a-oriented BTO will be generalized according to the results summarized in Section 5.1. In Section 6.2, the pros and cons of different fabrication approaches for hybrid BTO/Si optical components are summarized. In Section 6.3, the epitaxial a-oriented BTO is grown by MBE directly on patterned SOI wafers with Si optical waveguides fabricated by imec's 200 mm silicon photonics platform. The different post-growth annealing to improve the propagation loss of the BTO waveguide will be presented. In Section 6.4, the detailed TEM analysis to investigate the annealing effects on the BTO crystallinity and STO/Si interface is given. In Section 6.5, a series of investigations into the domain poling effect on the EO behaviors is executed. Using different bias sweeping modes, the BTO domains are controlled such that the device behaviors can be analyzed systematically. Microscopic and macroscopic views of the EO response to BTO domains are also discussed. Furthermore, the direct observation of poling effects on a-oriented domains using the PFM technique on the transmission electron microscope (TEM) lamella is presented. Finally, the benchmarks of the optical performance for hybrid BTO/Si optical components are performed.

## 6.1. Generalized EO Models for Multi-Domain a-Oriented BTO

[a] Section 6.1 is partially from *IEEE Photonics Technology Letters*, **28**, 990 (2016) and *Optics Express* **23**, 15332 (2015), done by Castera et al

In Section 5.1, the summary from the single-domain BTO used in Si-integrated waveguides shows that in-plane electrode configurations on the a-oriented BTO can bring about the most efficient modulations for both TE and TM modes. Stepping forward to the real case, the BTO thin film contains multi-oriented domains due to the complicated strain/relaxation mechanisms during the growth, as discussed in Chapter 5. In reality, the a-oriented BTO possesses 4 equivalent domain orientations: $[-100]_{BTO}$, $[100]_{BTO}$, $[0-10]_{BTO}$ and $[010]_{BTO}$. To analyze the practical case, first, reversed domains are not taken into account; i.e. only considering $[100]_{BTO}$ and $[010]_{BTO}$ on the BTO surface. the TE/TM-mode effective Pockels coefficient for the multiple a-oriented domains can be formulated as

$$(1-\alpha)r_{eff}^{TE/TM}(\phi) + \alpha r_{eff}^{TE/TM}(90^o - \phi) \tag{6.1}$$

with respect to the domain along $[100]_{BTO}$ and $[010]_{BTO}$. $\alpha$ is the percentage of the domain along $[100]_{BTO}$ occupation, 1-$\alpha$ is the percentage of the domain along $[010]_{BTO}$ occupation, and $r_{eff}^{TE/TM}$ is described in Section 5.1: on one hand, for TE-polarized light, $r_{eff}^{TE}$ can be described by Equation 5.6. On the other hand, for TM-polarized light, Equation 5.2 is used to describe the x component and Equation 5.4 is used to describe the y component.

In order to fully generalize the model, the order parameter $\beta$ is introduced to consider the reversed domains: when the domains are fully aligned to the positive and negative directions, the $\beta$ are +1 and -1 respectively. If the domains are fully random, the $\beta$ is 0. Then, after taking $\beta$ into account, Equation 6.1 can be re-formulated as:

$$(1-\alpha)\beta_{[010]}r_{eff}^{TE/TM}(\phi) + \alpha\beta_{[100]}r_{eff}^{TE/TM}(90^o - \phi) \tag{6.2}$$

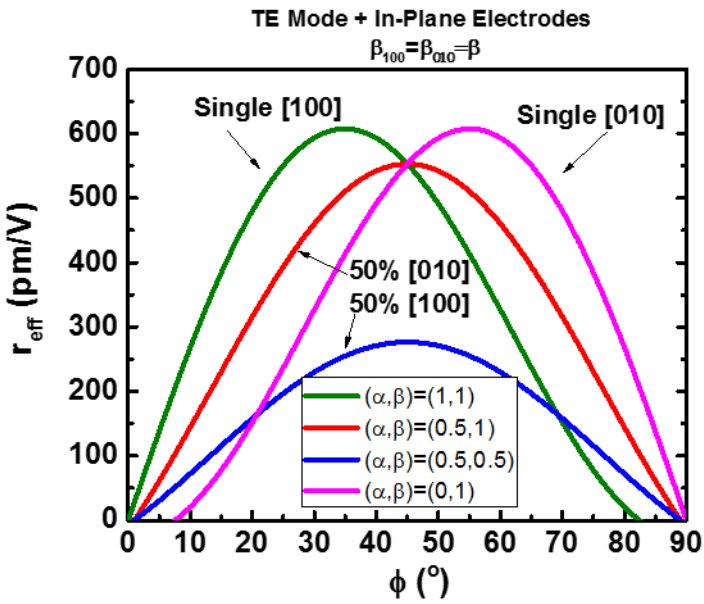


**Figure 6.1:** Calculated $r_{eff}$ under different circumstances of domain randomness and domain orientations in the device for TE modulation.

Figure 6.1 shows the calculated $r_{eff}$ for TE modulation according to Equation 6.2 where we make the assumption of $\beta_{[100]}=\beta_{[010]}$ and use the reported values for $r_{13}$=8 pm/V, $r_{33}$=28 pm/V and $r_{51}$= 800pm/V. Several phenomena can be summarized from Figure 6.1:

- Single-domain BTO shows stronger $r_{eff}$ than multi-domain does.
- Depending on domain occupation, the optimal $\phi$ is within 35° to 55°.
- Any reversed domains cancel out the EO effect, reducing the $r_{eff}$.

These arguments give insight in how to optimize the BTO domains to obtain high-performance optical modulators with strong $r_{eff}$.

## 6.2. Fabrication Process Comparisons for Hybrid BTO/Si Optical Components

Figure 6.2 describes different fabrication approaches for hybrid BTO/Si optical waveguides and make a summary of corresponding pros and cons. Here, the work of the first demonstration from Yale University [1] and the state-of-the-art results from IBM Zurich [2] are presented. IBM Zurich finds that the main cause of the high optical loss in the Yale University's work. During the

amorphous silicon (a-Si) deposition, the hydrogen will incorporate into the BTO and STO buffer, leading to high propagation loss. Thus, IBM Zurich develops the wafer-bonding technique to transfer the BTO layer from one SOI to the other. Then, they remove the substrate handling and pattern the crystalline Si (c-Si) for the waveguide. Finally, the post-process annealing is performed to ameliorate the propagation loss down to 6 dB/cm. However, the approach from IBM Zurich is complicated. In this thesis, to simplify the process, we grow the BTO directly on the patterned SOI with c-Si waveguides. However, the patterns of c-Si and $SiO_2$ claddings make the BTO growth very challenging. Although the post-process annealing can improve the optical loss down to 85 dB/cm, further optimization of the BTO growth is needed. In the following sections, more details of the passive and active hybrid BTO/Si components will be presented

| | Yale University | IBM Zurich | imec |
|---|---|---|---|
| | 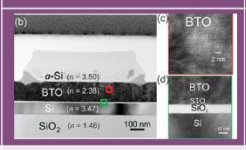  | 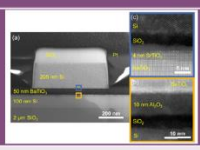 | 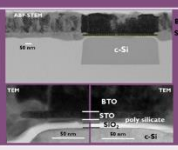  |
| Fabrication Process | • MBE of BTO on the blanket SOI<br>• aSi deposition<br>• Waveguide fabrication by patterning the aSi. | • MBE of BTO on the blanket SOI<br>• Wafer-bonding to transfer BTO to the other SOI<br>• Handling removal<br>• Waveguide fabrication by patterning the c-Si<br>• Post-process annealing | • MBE of BTO on the "**patterned**" SOI<br>• Post-process annealing |
| Pros | • Good control of the BTO quality. | • Good control of the BTO quality.<br>• Low loss (6dB/cm) | • Simple process steps |
| Cons | • Loss from $H_2$ during the aSi deposition (44dB/cm). | • Complicated process steps. | • Challenging control of the BTO quality ➔ high loss (85dB/cm) |

**Figure 6.2:** Pros and Cons of different fabrication approaches for hybrid BTO/Si waveguide applications. The TEM images are reproduced from the ref. [1] and [2].

## 6.3. Characteristics of Hybrid BTO/Si Passive Waveguides on the Patterned SOI

The epitaxial growth starts with 10 nm STO buffer layer followed by 170 nm BTO grown non-selectively on the patterned SOI substrate with the crystalline Si (c-Si) waveguides and the oxide cladding regions, as described in Figure 6.3(a). The distributed patterns composed of c-Si and the $SiO_2$ cladding bring about the thermal non-uniformity on the surface. This temperature inhomogeneity leads to the poor crystallinity with FWHM of the $(002)_{BTO}$ rocking curve ($\Delta\omega$) around 1.9° and rough surface as shown in the scanning electron microscopy image (SEM) Figure 6.3(b). In addition, when characterizing the BTO waveguides, neither TE-polarized nor TM-polarized light transmission through the waveguide can be detected. As we learned from Chapter 5, high temperature annealing under oxygen ambient can improve some device behaviors such as the leakage current and domain switching. For the reason, in this section, a series of comparisons with the waveguide propagation loss and various oxygen annealing conditions will be analyzed.

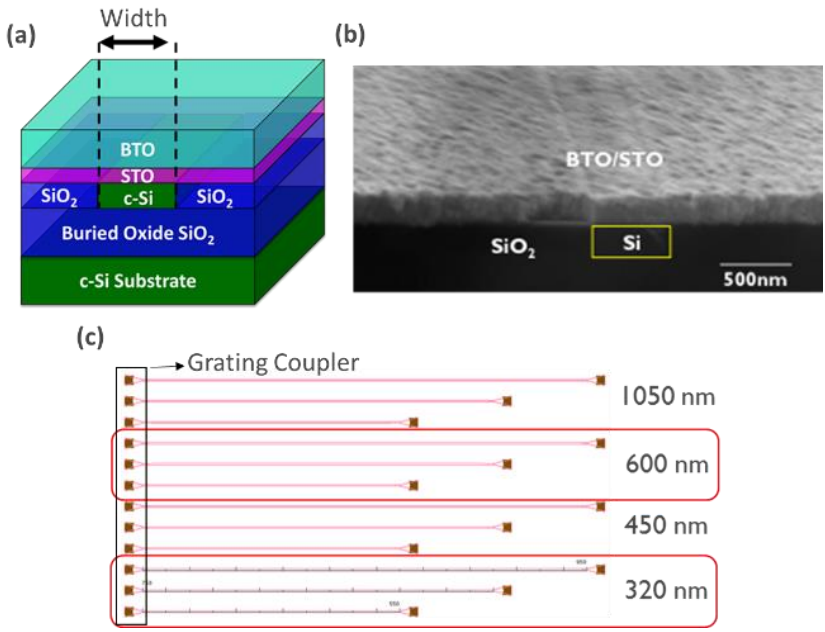


**Figure 6.3:** (a) The structure schematic of the hybrid BTO/Si waveguides. (b) The cross-sectional SEM image of the hybrid BTO/Si waveguides. (c) The waveguide arrays with the width of 320 nm,

450 nm, 600 nm and 1050 nm. Each width has 550-, 750 and 950 μm-long waveguides.

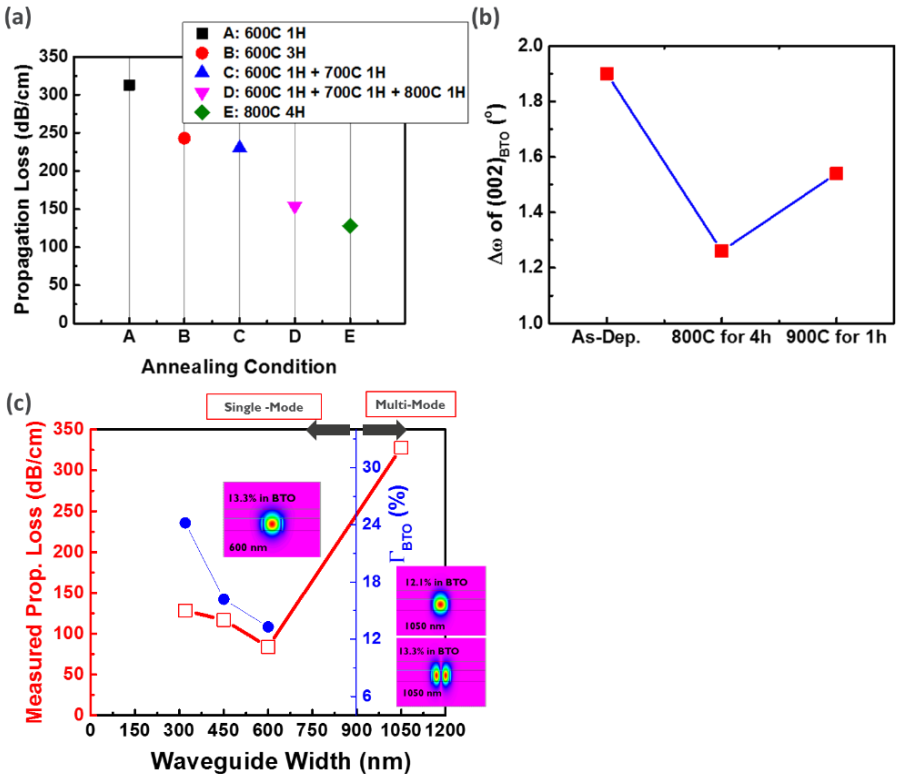


**Figure 6.4:** (a) The measured propagation loss for the 320-nm-wide waveguide under different oxygen annealing temperatures and durations. (b) The FWHM of the $(002)_{BTO}$ Δω. (c) The measured propagation loss of the waveguides, annealed at 800 °C for 4 hours under the oxygen ambient and the calculated BTO light confinement in function of different waveguide widths. The inset presents the corresponding mode distribution as well as the BTO light confinement for the 600- and 1050-nm-wide waveguides.

First, the TE-polarized transmission measurements of 550-, 750- and 950-μm-long waveguides with the 320 nm width, as shown in Figure 6.3(c), are performed. The propagation loss can be obtained by the linear regression with the maximum waveguide transmissions and their corresponding lengths. Figure 6.4(a) shows the evaluated propagation loss of the waveguides

undergone different annealing conditions. The 1-hour annealing under the temperature up to 800 $^{o}$C reduces the propagation loss down to 150 dB/cm. Besides, when prolonging the annealing duration to 4 hours, the propagation loss can be further improved to 120 dB/cm. From the FWHM of the $(002)_{BTO}$ rocking curve ($\Delta\omega$) in Figure 6.4(b), the smaller $\Delta\omega$ of ~1.2$^{o}$ suggests that oxygen annealing process at 800 $^{o}$C for 4 hours improves the crystallinity of the BTO. However, the 1-hour annealing at 900 $^{o}$C degrades the crystallinity as indicated by the increasing $\Delta\omega$. Therefore, the optimal annealing temperature is at 800 $^{o}$C. Besides, in Figure 6.4(a), the reduction of the propagation loss suggests the oxygen vacancies are reduced. As mentioned in Chapter 4 and Chapter 5, oxygen vacancies create extra free carrier absorption within the near infrared, leading to extra light propagation loss caused by the free carrier absorption in the waveguide. As the oxygen vacancies are reduced, the propagation loss is improved. Subsequently, the different widths of the waveguides are also investigated. Figure 6.4(c) presents the measured propagation loss in function of different waveguide widths for the sample annealed at 800$^{o}$C for 4 hours with oxygen. Besides, in order to understand the effect of the width on the optical mode, the finite element calculations are also executed. From the calculation, beyond 900 nm, the single-mode waveguide becomes the multi-mode waveguide. Meanwhile, the light confinements in the BTO with different waveguide widths are also illustrated in Figure 6.4(c). It can be clearly seen that, in the single-mode region, the light propagation loss is reduced with the light confinement in the BTO. The minimal propagation loss of 83 dB/cm can be obtained at the 600-nm-wide waveguide. Since the BTO surface is rough as shown in Figure 6.3(b) and the crystallinity is defective, the light in the BTO is scattered or absorbed during the propagation. Thus, the less light staying in the BTO region, the lower waveguide loss can be obtained. However, for taking advantage of the BTO Pockels effect for the optical modulation, the reasonable light quantity staying in the BTO region is necessary. When the waveguide width is increased up to 1050 nm, the measured propagation loss is increased dramatically due to the existence of multiple TE modes in the waveguide. Despite the improvement of the propagation loss for the TE mode after annealing, the TM light through the waveguide is still barely detectable because of nearly 40% light confinement in the BTO layer.

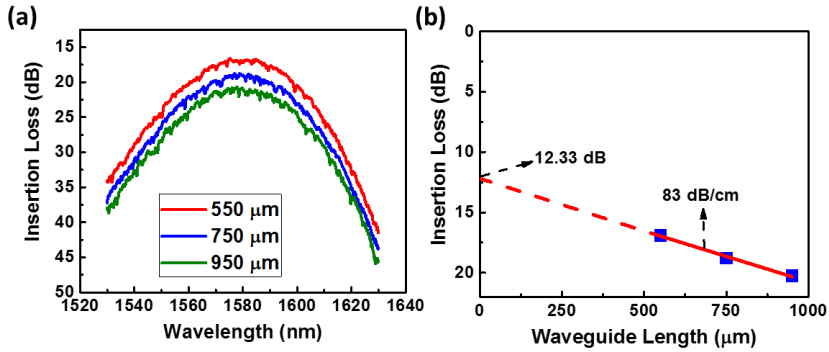


**Figure 6.5:** (a) The measured transmission spectra for the 550 μm, 750 μm and 950 μm waveguides which are annealed with oxygen at 800 °C for 4 hours. (b) The linear regression of the insertion loss with waveguide length. The vertical intersect is -12.33 dB, which reveals the insertion loss of the grating coupler is 6.2 dB. The slope shows the waveguide propagation loss of 83 dB/cm.

Figure 6.5(a) shows the representative transmission spectra for the 550 μm, 750 μm and 950 μm waveguides which are annealed with oxygen at 800 °C for 4 hours. The central wavelength is located at 1580 nm given by the grating coupler. Originally, the grating coupler is designed for the light central at 1550 nm. However, the shift of the spectrum is due to the capping of BTO and STO layers. The insertion loss of the grating coupler can be extracted by the vertical-axis intersect of the linear regression result. As shown in Figure 6.5(b), the intersect is 12.33 dB, a combinational results of the two grating couplers (input and output). Therefore, the insertion loss of one grating coupler can be calculated around 6.2 dB. Also, as previously mentioned, the slope can derive the propagation loss of 83 dB/cm. Although the propagation loss for our current device is still one order higher than the state-of-the-art 6 dB/cm [2], further optimization of the BTO growth on patterned SOI should ameliorate the BTO crystallinity as well as the light propagation loss.

## 6.4. Annealing Effect

Figure 6.6(a) shows the ω-2θ scan of the sample after being annealed at 800°C for 4 hours under oxygen ambient. The BTO crystallinity is biaxially textured along $[001]_{Si}$ of the Si(001)-on-insulator substrate, showing clear Bragg's peaks of the $(001)_{BTO}$ and $(002)_{BTO}$. The $(101)_{BTO}$ is also detectable, revealing there is a poly-crystalline phase existing in the BTO layer. Besides, from ϕ-scan in Figure

6.6(b), both BTO and Si present 4-fold crystal symmetry [3]. The epitaxial relationship between BTO and Si(001): <100>BTO(001)//<110>Si(001) is also observable. Driven by the 1/2 ML SrO during the Si surface preparation, the BTO and the underlying STO crystal lattices are rotated 45° with respect to the Si, as described in Figure 6.6(c).

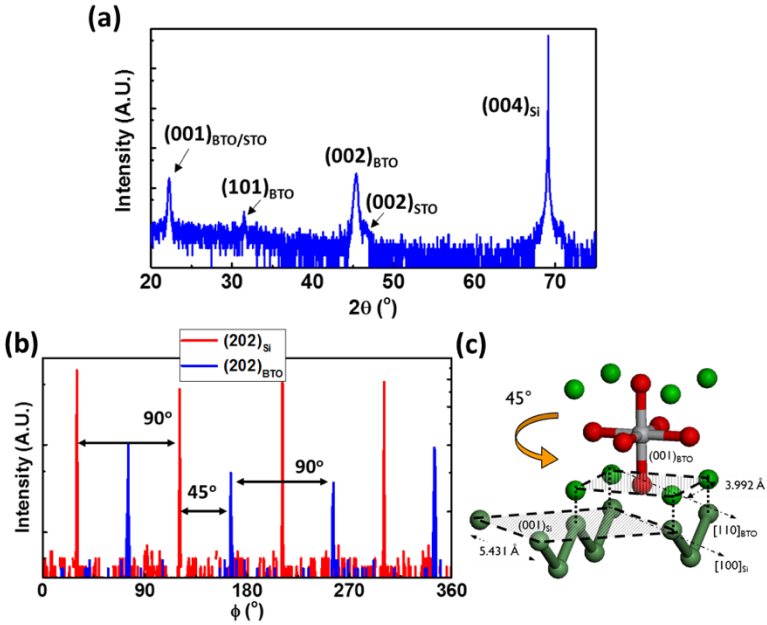


**Figure 6.6:** The (a) ω-2θ and (b) ϕ- scans of the sample annealed with oxygen at 800 °C for 4 hours. (c) The schematic of the epitaxial relationship between BTO and Si(001).

Figure 6.7(a) and 6.7(b) present the annular bright-field scanning transmission electron microscopy (ABF-STEM) images for the oxygen-annealed and as-deposited samples, respectively. The yellow dot lines indicate the original height level of the $SiO_2$ cladding surface before STO and BTO growth. The rough BTO surface is consistent with the cross-sectional SEM in Figure 6.3(b). Clearly, the surface of the $SiO_2$ cladding is changed after $O_2$ annealing at 800 °C for 4 hours, as suggested from the lower level and rougher surface of the $SiO_2$ claddings. Besides, the annealing makes the profile of the top crystalline silicon become more round. In fact, prior to the STO and BTO growth, the crystalline silicon level is 10 nm lower than the level of the $SiO_2$ cladding, as described in Figure 6.7(c). Therefore, there is a deposition at the edge of the $SiO_2$ cladding as indicated by the white circle in Figure 6.7(b). After the oxygen annealing, this

deposition area becomes wider and deeper towards the $SiO_2$, as observed in Figure 6.7(a).

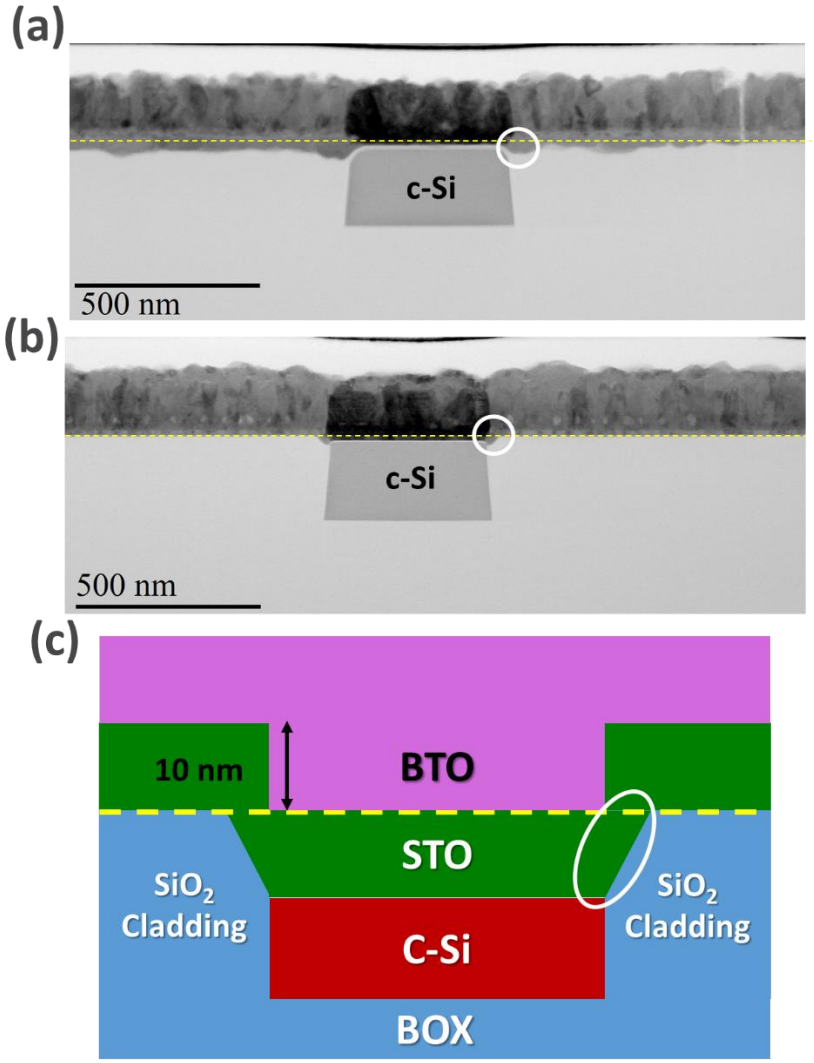


**Figure 6.7:** The ABF-STEM images of (a) oxygen-annealed and (b) as-deposited samples. (c) The structure schematic.

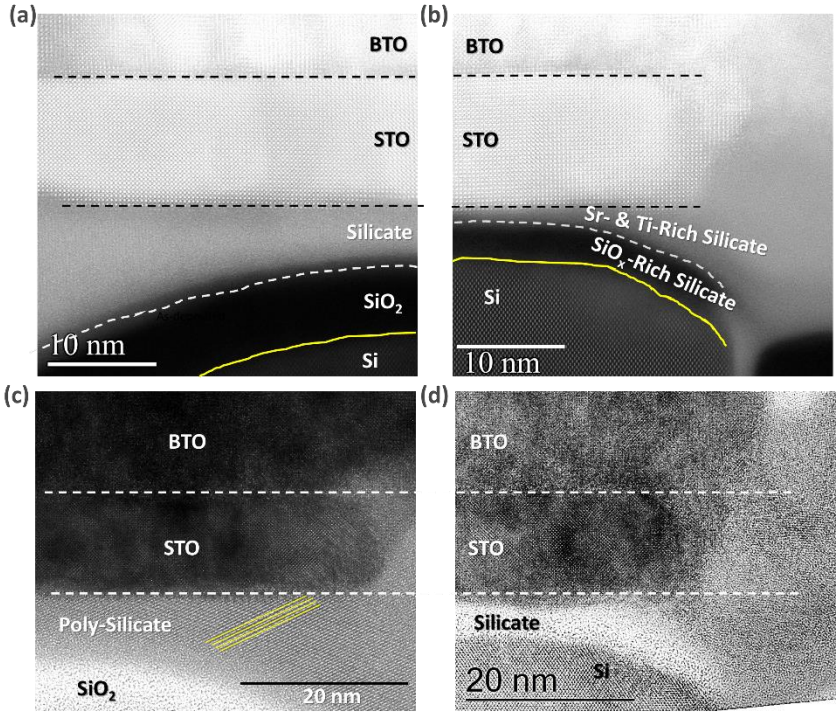


**Figure 6.8:** The HAADF-STEM images of (a) oxygen-annealed and (b) as-deposited samples. The HR-TEM images of (c) oxygen-annealed and (d) as-deposited samples.

Figure 6.8 shows more detailed comparisons of TEM analysis between as-deposited and annealed samples at the interface. In order to make direct comparisons, the height alignment based on the same STO thickness is performed. Figure 6.8(a) and 6.8(b) present the high-angle annular dark-field-STEM (HAADF-STEM) of the oxygen-annealed and as-deposited samples, accordingly. Both samples show the clear crystal lattice of the epitaxial BTO and STO layers on the Si(001). Besides, at the STO and Si interface, there are 2 separated layers observed in both samples. The oxygen-annealed sample has a total interfacial layer of around 12 nm and the as-deposited sample has that of around 4 nm. Besides, for the oxygen-annealed sample, both top and bottom layers are thickened towards the Si, as indicated by the height levels. To analyze the composition at the interface, the energy dispersive spectroscopy (EDS) is executed. For the as-deposited sample, the top layer is identified as the Sr- and Ti-rich silicate and the bottom one is $SiO_x$-rich silicate. This phenomenon suggests the graded element distribution of Ti, Sr, O and Si. After annealing, such a graded distribution continues. In fact, given by the

thermal energy from the high temperature of 800 °C during annealing, O, Sr and Ti are diffusing towards the silicon. Due to the longer diffusion length of O, more O but less Sr and Ti diffuse to the Si surface, turning crystalline Si to be more $SiO_x$-rich silicate. When the interfacial layer thickening continues, in the end, it becomes pure $SiO_2$ at the bottom of the interfacial layer. Therefore, in Figure 6.9, the EDS reveals that, for the oxygen annealed sample, the top interfacial layer is the silicate containing Sr and Ti metal elements. Differently, the bottom one shows the pure $SiO_2$ mostly. In addition, Figure 6.8(c) and 6.8(d) present the high-resolution TEM (HRTEM) for both annealed and as-deposited samples to study the crystallinity at the interface. For the oxygen-annealed sample in Figure 6.8(c), the polycrystalline silicate in the top interfacial layer can be observed. The bottom one is amorphous $SiO_2$. Nevertheless, for the as-deposited sample in Figure 6.8 (d), the whole silicate shows amorphous.

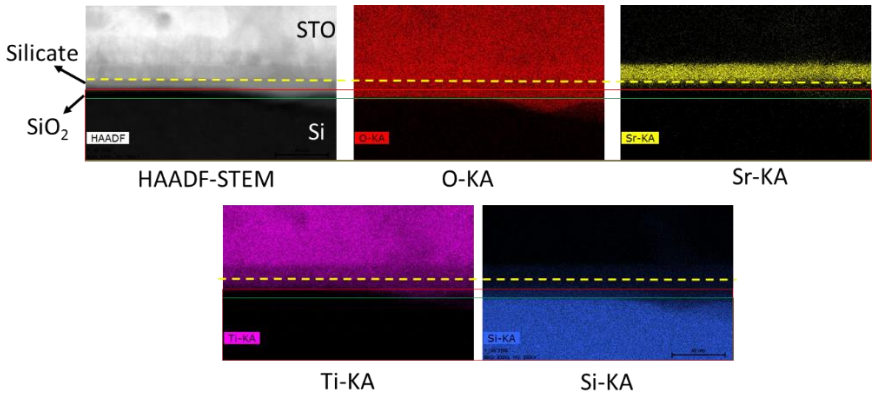


**Figure 6.9:** The EDS analysis at the STO/Si interface for the oxygen-annealed sample.

Figure 6.10(a) shows the ABF-STEM of the oxygen-annealed BTO on the crystalline Si waveguide. The different image contrasts in the BTO can be observed in different locations, indicating the local variation of the BTO crystallinity and layer density. 3 different interesting area are labelled for the zoom-in observations. Figure 6.10(b) and Figure 6.10(c) show the HAADF-STEM images for the bottom-left and at the right edge of the BTO on the waveguide, accordingly. The clear lattice of the epitaxial BTO and STO along the $[100]_{BTO/STO}$ and $[001]_{BTO/STO}$ can be observed in both figures. However, at the right edge in Figure 6.10(c), we can notice that the BTO crystal starts to lose the epitaxy, presenting extra crystal orientations as highlighted by the yellow lines. The HRTEM in Figure 6.10(d) also reveals that some parts of the BTO surface on

the crystalline Si waveguide exhibits polycrystalline phases. However, from our TEM analysis, we find that only minor parts of the whole BTO on the waveguide shows the polycrystalline phases. Therefore, the BTO on top of the crystalline silicon waveguide shows mostly epitaxial. Nevertheless, on the cladding region, only polycrystalline or amorphous can be found due to the lack of the crystal template.

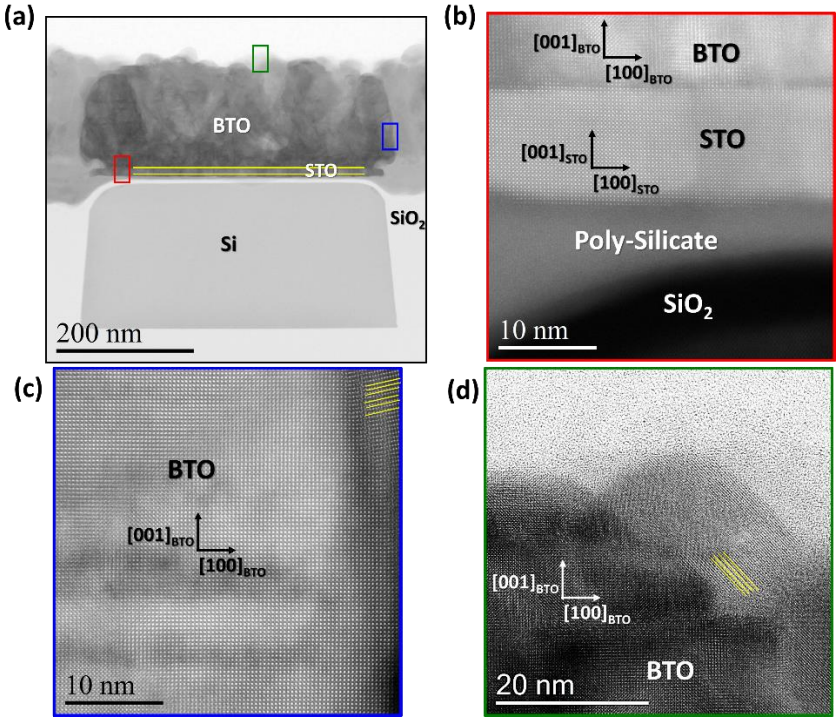


**Figure 6.10:** (a) The ABF-STEM of the oxygen-annealed sample. The different locations for zoom-in analysis are labelled on the BTO/STO on the crystalline Si waveguide region. (b) The HAADF-STEM image at the bottom-right BTO. (c) The HAADF-STEM image at the right edge of the BTO and (d) The HR-TEM at the top of the BTO.

## 6.5. Linear EO Modulation in Hybrid BTO/Si Mach-Zehnder-Ring Modulators

Recently, Abel et al [4] and Xiong et al [1] have demonstrated hybrid BTO/Si mach-zehnder and ring modulators, showing promising performance with VπL around 1.4 Vcm and modulation speed around 5 GHz. However, in their low-

frequency or DC measurements, a hysteresis phenomenon is observed as shown in Figure 6.11(a) and 6.11(b). This is unfavorable for optical modulators, for which a linear electro-optical (EO) effect without hysteresis is preferred, as described in Figure 6.11(c). Although the authors address the origin of the hysteresis EO phenomenon to the ferroelectric domain motions during the biasing, better understanding is needed. For that reason, the objective of this section is to study the fundamental mechanisms behind this effect and learn how to achieve a linear EO effect for the hybrid BTO/Si optical modulator. Because the hybrid BTO/Si mach-zehnder-ring (MZR) modulator provides sufficiently large space for defining contacts in standard contact lithography, we selected it as a starting point for this learning process.

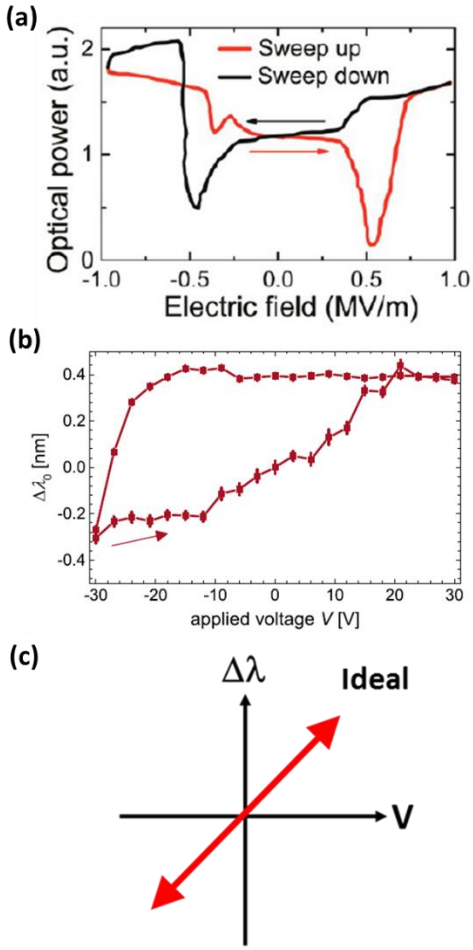


**Figure 6.11:** The (a) optical power and (b) spectral shift as a function of the applied electric field and voltage. These figures are reproduced

from the ref. [4] and [1] respectively. (c) The ideal spectral shift as a linear function of the applied bias.

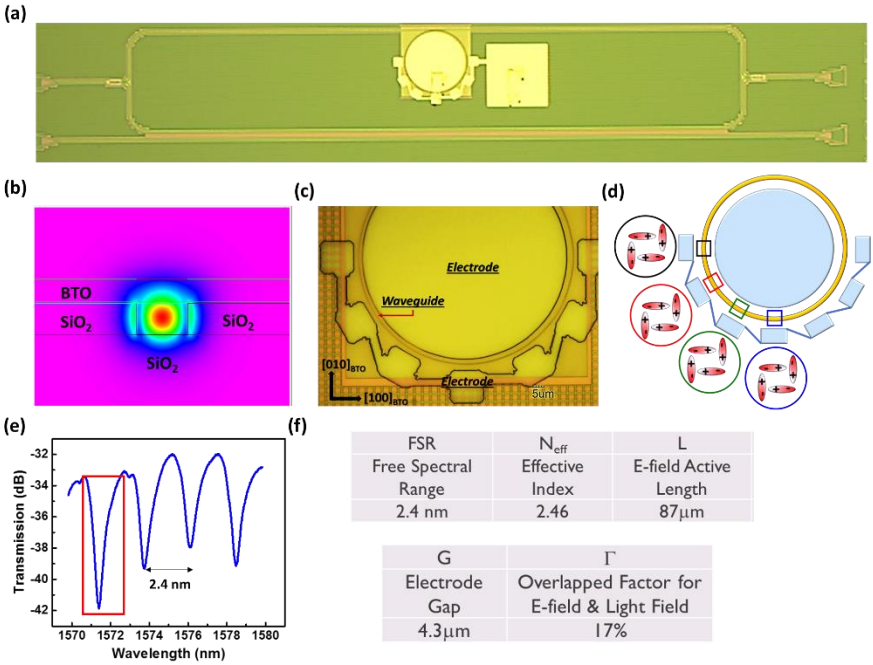


| FSR | $N_{eff}$ | L |
|---|---|---|
| Free Spectral Range | Effective Index | E-field Active Length |
| 2.4 nm | 2.46 | 87μm |

| G | Γ |
|---|---|
| Electrode Gap | Overlapped Factor for E-field & Light Field |
| 4.3μm | 17% |

**Figure 6.12:** (a) The optical microscope image of the hybrid BTO/Si MZR modulator. (b) The mode distribution within the waveguide according to the finite element calculation. (c) The zoom-in image of the ring part. (d) The schematic of the a-oriented domains within the area between the central electrode pad and surrounding electrodes. (e) The transmission spectrum of the MZR modulator without bias. (f) Summary of the main design parameters for the hybrid BTO/Si MZR modulator.

Figure 6.12(a) presents the optical microscope image of the hybrid BTO/Si MZR modulator. Given its balanced arm length, the interference spectrum is mainly dominated by the ring resonator in the top arm. From Section 5.1, we know the optimal scheme for the hybrid BTO/Si modulator is to use a-oriented BTO with both TE- and TM-polarized light and in-plane electrodes. However, since the device doesn't transmit TM light, the following discussions will be focused on the TE modulations in this scheme to perform a series of analysis for the EO response with respect to the BTO domain dynamics. The waveguide width in this device is 450 nm, and Figure 6.12(b) shows the TE mode distribution calculated from the

finite element method. Figure 6.12(c) is the zoomed-in optical microscope image of the ring part and Figure 6.12(d) illustrates the corresponding schematic. There is one electrode connecting 7 pads surrounded the ring. The other electrode is placed inside the ring. By this design, different electric field directions can be applied within the area between the two electrodes as described in Figure 6.12(d). According to the angle $\phi$ defined by the BTO domain and electric field directions as shown in Figure A.5(a), the 7 pads surrounding the ring correspond to $\phi$=0°, 30°, 60°, 90°, 120°, 150° and 180°. Due to the symmetry, the following discussion of BTO domain dynamics can be simply focused on $\phi$=0°, 30°, 60° and 90°. Figure 6.12(e) presents the transmission spectrum of the MZR modulator without any bias. The free spectral range (FSR) is 2.4 nm. Some more features about the MZR modulator are summarized in Figure 6.12(f).

### 6.5.1. Different Bias-Sweeping Measurements

In this section, two different bias-sweeping modes will be introduced to study the BTO domain dynamics, as shown in Figure 6.13. Both bias-sweeping modes are composed of Step A and Step B for domain poling. Following Step A and Step B, the transmission spectrum is measured, while ramping down the bias (Step i and Step ii) and while ramping up (Step iii and Step iv) the bias respectively. In the mode 1, +10 V for $T_1$ minutes in Step A and -10 V for $T_2$ minutes in Step B are used. Differently, in the mode 2, we use -10 V for $T_1$ minutes in Step A and +10 V for $T_2$ minutes in Step B. To study the domain dynamics, we perform Step A and Step B with the symmetric poling durations $T_1$=$T_2$ for 10, 30, 60 and 300 minutes. In Step i, ii, iii and iv, each bias takes only 15 seconds while measuring the spectrum. The reference of the resonant condition is defined at the 0 V between Step i and Step ii. Then, with respect to the reference, the bias-dependent shift of the resonant condition near 1571.5 nm is monitored.

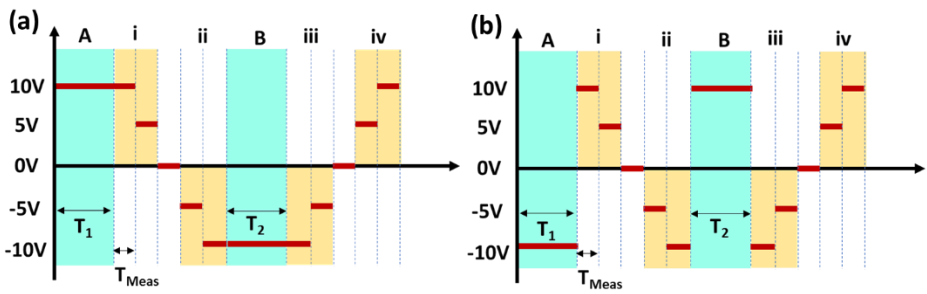


**Figure 6.13:** The bias steps for the (a) sweep mode 1 and (b) sweep mode 2.

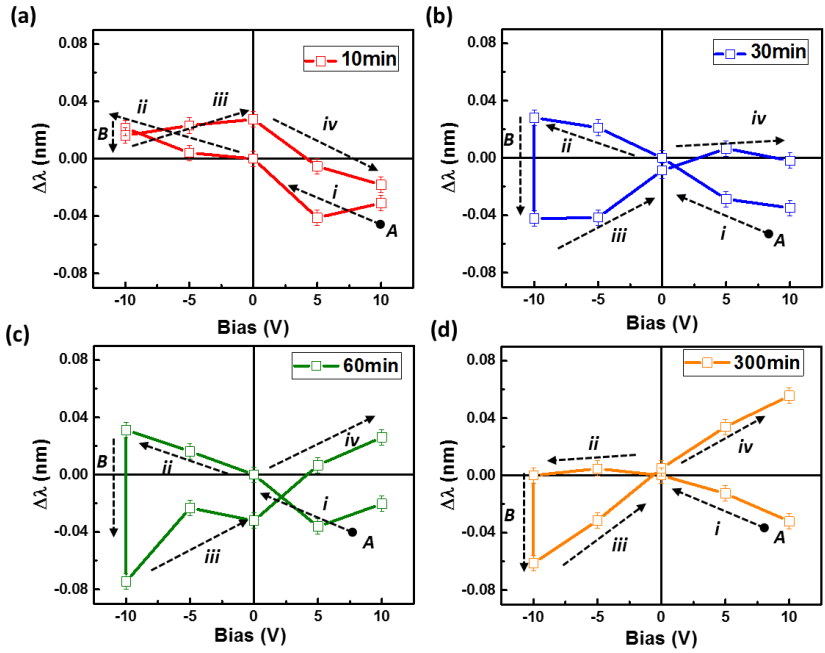


**Figure 6.14:** The bias-dependent spectral shift via the bias-sweeping mode 1 with the poling time $T_1$=$T_2$ varying from (a) 10, (b) 30, (c) 60, and (d) 300 minutes.

Figure 6.14 shows the bias-dependent spectral shift via the bias-sweeping mode 1 with poling time in Step A and Step B varying from 10 to 300 minutes. The corresponding steps and bias-sweeping traces are labelled in the data. All the data show hysteresis. But Figure 6.14(a) with the 10-minute poling process shows very different behavior compared to the others. The latter, with a 30-, 60-, and 300-minute poling process, shows consistent trends when sweeping the bias.

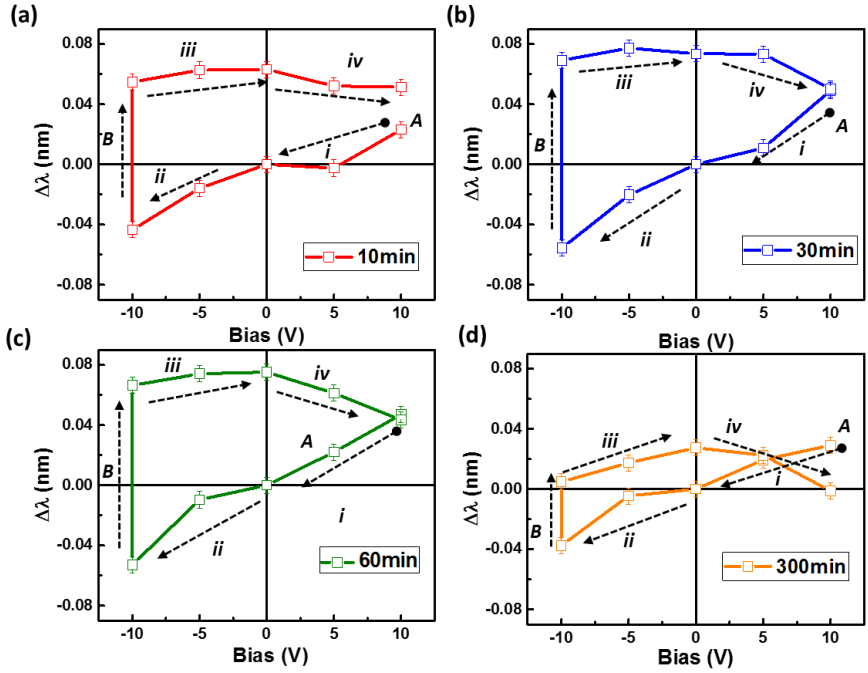


**Figure 6.15:** The bias-dependent spectral shift via the bias-sweeping mode 2 with the poling time $T_1$=$T_2$ varying from (a) 10, (b) 30, (c) 60, and (d) 300 minutes.

Figure 6.15 presents the bias-dependent spectral shift using the bias-sweeping mode 2 with the poling time $T_1$=$T_2$ varying from 10 minutes to 300 minutes. Compared with Figure 6.14, the bias-sweeping mode 2 results in completely different behavior. Among various poling times, the results are now consistent however. In the next section, the detailed mechanisms leading to these results will be discussed.

## 6.5.2. Hysteresis Mechanisms

In Figure 6.14 and Figure 6.15, different bias-sweeping modes and various poling times show clearly distinct results. In order to understand the mechanisms underlying this, a systematic discussion from the microscopic to macroscopic pictures of domain dynamics will be given. Figure 6.16 illustrates the time-evolved microscopic views of the BTO domains response with respect to the applied electric field at different area: $\phi$=0°, 30°, 60° and 90°. As mentioned in previous chapters, the BTO domain orientation is resulted by the Ti displacement in the lattice, leading to the spontaneous (dipole) polarization. Therefore, a dipole-

like schematic is used to describe the polarization direction and its color contrast represents the polarization strength. Without poling, all the area between two pads show the random distribution of the BTO domains along $[100]_{BTO}$, $[-100]_{BTO}$, $[010]_{BTO}$ and $[0\text{-}10]_{BTO}$, as depicted by dipole-like schematics. When applying the bias to create the electric field, which is strong enough to initiate domain movements, the domains start to respond. Since the directions of the electric field are different for $\phi=0^o$, $30^o$, $60^o$ and $90^o$, different response will be involved: For $\phi=0^o$, electric field only along $[100]_{BTO}$, so only $[100]_{BTO}$ and $[-100]_{BTO}$ are responding to be along the $[100]_{BTO}$. Otherwise, the domain polarizations along $[010]_{BTO}$ and $[0\text{-}10]_{BTO}$ perpendicular to the electric field don't respond. Similarly, for $\phi=90^o$, only $[010]_{BTO}$ and $[0\text{-}10]_{BTO}$ are responding to be along the electric field direction, $[010]_{BTO}$. Differently, for $\phi= 30^o$ and $60^o$ with inclined electric field, the horizontal along $[100]_{BTO}$ and vertical along $[010]_{BTO}$ components allow all the domains to be aligned. With the long poling time, the effective polarization (the purple arrow) at each area will increase until all the domains are fully aligned. However, when applying the reversal electric field, the aligned domains will be randomized. Thus, the polarization strength will be decreased and its direction will be switched to the opposite direction if the poling time is sufficiently long.

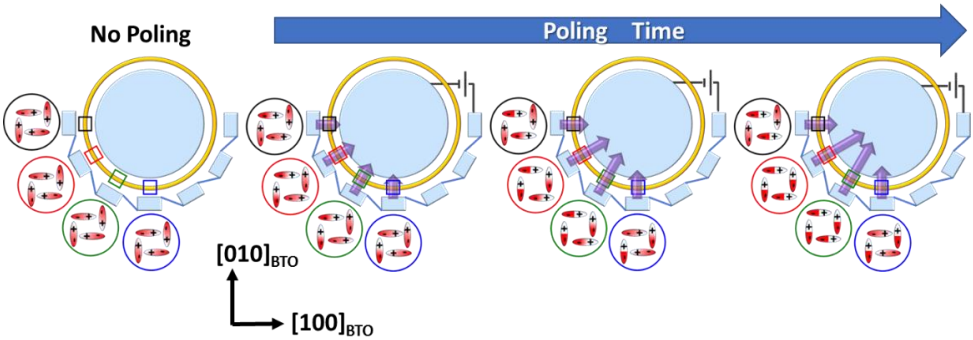


**Figure 6.16:** The time-evolved microscopic views of the BTO domains response with respect to the applied electric field at different regions of $\phi=0^o$, $30^o$, $60^o$ and $90^o$. The purple arrow represents the domain polarization and the arrow length stands for the polarization strength in the macroscopic views. The gradient color for each dipole reveals the polarization strength in the microscopic views.

Figure 6.17 illustrates the macroscopic EO response to the interaction between the applied electric field and BTO domain polarization at different measurement steps. Figure 6.17(a) describes the detailed mechanisms for the ideal bias-dependent spectral shift via the bias-sweeping mode 1. First, Step A sets the

certain polarization state. Then, given by the Pockels effect, the spectral shift follows the linear dependency on the bias in Step i Step ii, sweeping from +10 V to -10 V. In Step B, the BTO is experienced the reversal poling, so the polarization is switched to the opposite direction. Therefore, the spectral shift is changed from the positive to the negative. Then, due to the opposite polarization, the trace of the spectral shift follows different bias linear dependency when sweeping the bias from -10 V to +10 V in Step iii and Step iv. This ideal model of the bias dependency for the spectral shift in Figure 6.17(a) can qualitatively explain the 30- and 60-minute results in Figure 6.14(b) and 6.14(c), respectively. In Figure 6.14(a) undergone the 10-minute poling, spectral shift at Step B doesn't change to the negative value. Instead, the spectral shift value becomes slightly smaller, suggesting that the poling for 10 minutes is too short to complete the polarization switching. For the reason, the polarization direction is kept the same but the strength is weakened at Step B. Therefore, Figure 6.17(b) with the weakened polarization at Step B can explain the trend of the measured data in Figure 6.14(a). Besides, in Figure 6.14(d), 300 minute poling also gives the similar trend of the spectral shift to those for 30- and 60-minute poling cases. However, as noticed in Figure 6.14(d), the spectral shift at Step ii becomes smaller, revealing that the polarization strength is weakened during the measurement. Figure 6.17(c) illustrates the mechanisms for the measurement with 300-minute poling: Step ii gives the opposite electric field to the polarization set in Step A by +10 V, so the reversal field make the polarization weaker than the original. For the reason, the ideal spectral shift at the step ii also shows the smaller value. On the contrary, for the polarization set in Step B by -10 V, the opposite electric field in Step iv is not as influential as what happened in Step ii. This indicate that the polarization set by -10 V is more robust and stable than the one set by +10 V.

Figure 6.17(d) describes the mechanism for using the bias-sweeping mode 2. Because the polarization settings in Step A and Step B in the bias-sweeping mode 2 are opposite to those in the bias-sweeping mode 1, the ideal spectral shift in Figure 6.17(d) shows mirror-like with respect to the Figure 6.17(a). Generally, the model in Figure 6.17(d) can't explain all the results in Figure 6.15. By studying the mechanism step by step, reversal bias in Step i and Step iii will randomize the polarizations set in Step A and Step B respectively. For the measured results from Step A to Step ii as shown in Figure 6.15, the bias-dependent spectral trend is similar to the ideal spectral shift illustrated in Figure 6.17(d). This indicates that, although the reversal electric field in Step i tends to randomize the polarization, the polarization set in Step A by -10 V is still stable and robust. Besides, all the data at Step B in Figure 6.15 show the polarizations are switchable, suggested by the spectral shift from the negative to the positive. However, in Step iii and Step iv, the measured spectral shifts don't follow the ideal one illustrated in Figure 6.17(d), since the randomization of the polarization in Step iii happens. Although

Figure 6.15(d) presents some trends following the ideal spectral shift in Figure 6.17(d), the ideal model can't explain the results from the bias-sweeping mode 2 as good as those from the bias-sweeping mode 1. Ideally, according to the Pockels effect, zero bias should not cause any spectral shift. Nevertheless, all the measured results in Figure 6.15 show that the spectral shift is not crossing to the zero point when sweeping back the bias in Step iii and Step iv. This might result from the extra charges created by the randomization of the polarization. The hysteresis phenomena show that at least BTO domain dynamics and Pockels effect are coupled together, contributing the device behaviors under such DC measurements. In fact, the speed of the bias response for the Pockels can be as fast as several tens of GHz or beyond, much faster than those for the piezoelectric effect, domain dynamics…etc [5-9]. For the reason, performing AC measurements with different speed scales might be helpful to decouple different EO phenomena from the BTO devices. To sum up, the main mechanism leading to the hysteresis phenomena in the bias-dependent spectral shift is due to the polarization switching. Therefore, to obtain the linear EO working condition, find a way to avoid the polarization switching is the key.

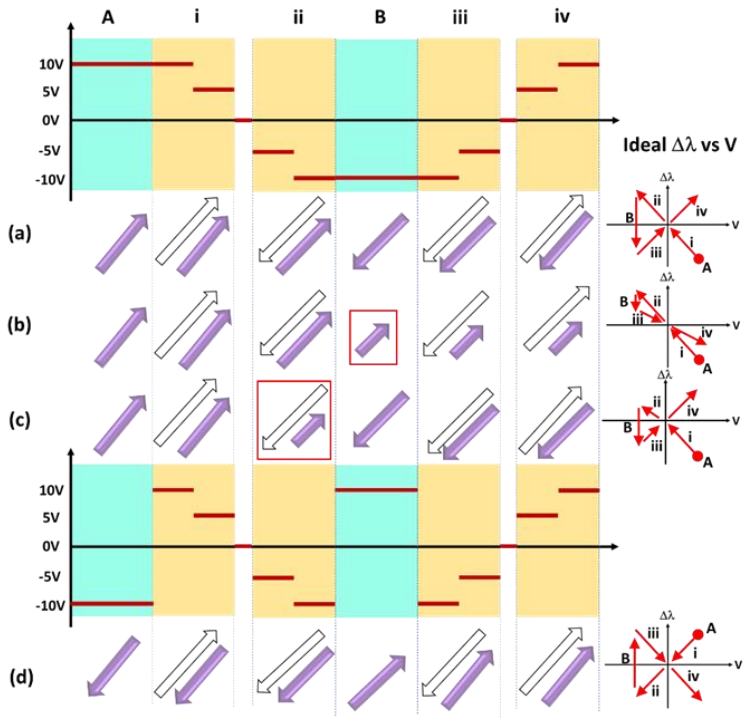


**Figure 6.17:** The macroscopic EO response to the interaction between the applied electric field and BTO domain polarization at different measurement steps. (a) The ideal situation for the bias-sweeping

mode 1. (b) The possible scenario in Figure 6.14(a). (c) The possible scenario in Figure 6.14(d). (d) The ideal situation for the bias-sweeping mode 2. (The purple and white arrows represent the directions of BTO domain polarization and applied electric field.)

One common approach for preventing hysteresis in $LiNbO_3$-based modulators is to use a much larger electric field of few MV/cm to set the polarization, and to use the smaller electric field of few KV/cm while the device is operating [10]. However, choosing the bias polarity for domain poling is another issue: from our measurements, different stability of the domain polarizations set by +10 V and -10 V can be noticed. From Figure 6.14(d) and Figure 6.15, the polarization set by -10 V performs better stability than that set by +10 V. Therefore, a new bias sweeping steps has been planned to use – 10V for 30 minute in Step A and for 300 minute in Step B, as illustrated in Figure 6.18(a). Figure 6.18(b) and 6.18(c) presents the measured spectra with bias swept from +10 V to -10 V and from -10 V back to +10 V. The corresponding spectral shift in function of bias is shown in Figure 6.18(d). Indeed, by using -10V to define the stable BTO domain polarization, a linear EO behavior can be obtained. From the equation [4]:

$$\boldsymbol{V_\pi} = \frac{\mathrm{FSR}}{2\Delta\lambda_V} \times V \qquad \textbf{(6.3)}$$

where FSR is 2.43 nm and $\Delta\lambda_V$ is the spectral shift for the applied bias V, the average $V_\pi$ of 184 V can be evaluated. Then, taking the electrode length of 87 μm into account, the average $V_\pi L$ is ~1.6 Vcm. In order to calculate the $r_{eff}$, another equation is introduced [4]:

$$\boldsymbol{V_\pi L} = \frac{\lambda G}{2 n_{eff}^3 \Gamma r_{eff}} \qquad \textbf{(6.4)}$$

where λ is 1571.5 nm, $n_{eff}$ is the effective refractive index: 2.395, G is the electrode gap: 4.3 μm and Γ is the optical confinement factor in BTO: 16.7%. Then, adapting $V_\pi L$=1.6 Vcm into the Equation 6.4, the average $r_{eff}$ is derived around 185 pm/V, 6 times as large as 30 pm/V for the $LiNbO_3$ [11].

In the next section, the direct observation of this asymmetric bias-poling phenomenon will be presented and discussed.

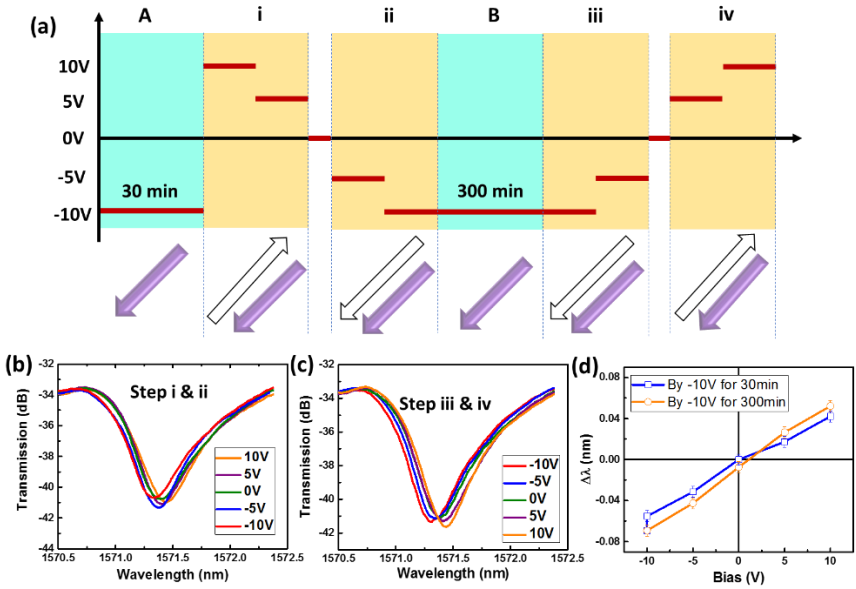


**Figure 6.18:** (a) The bias-sweeping plan with -10 V for 30 and 300 minutes at Step A and Step B respectively to obtain the linear EO condition. The transmission spectra collected in (b) Step i and Step ii and (c) Step iii and Step iv. (d) The measured spectral shift in function of bias showing the linear EO behavior.

### 6.5.3. Further Discussions: Polarization Stability

In the previous section, the importance of the stable BTO domain polarization for optical modulators has been addressed. To investigate the polarization stability of the a-oriented BTO, a new hybrid approach using the TEM lamella for the in-plane piezo-response force microscopy (PFM) is introduced. To perform this characterization, a custom TEM grid is used as shown in Figure 6.19(a). As previously discussed, the direction of the applied electric field decides how many BTO domains can be poled. Setting the applied electric field along $[110]_{BTO}$ at $\phi=45^{o}$ is the most efficient to polarize all the BTO in-plane domains. Therefore, the TEM lamella is prepared along $[100]_{BTO}//[110]_{Si}$ zone axis by the FIB instrument, as illustrated in Figure 6.19(b) and presented in Figure 6.19(c). Then, the lamella is placed on the custom grid for the following in-plane PFM analysis. The sample stack is 100 nm BTO on the 10-nm-thick STO buffer on the blanket Si(001) substrate. Before the PFM analysis, the sample is annealed under oxygen ambient at 600$^{o}$C for 30 minutes. The PFM analysis is performed over a scan area of 300 nm x 600 nm. Figure 6.19(d) presents the result of the PFM amplitude for

the sample being poled by -3 V for 1 hour. The 100 nm BTO/10 nm STO shows different PFM responses from the Pt (platinum)/SoC (spin-on-carbon) and Si area, suggesting the BTO domains are aligned and show distinct piezo-response. In this measurement, the BTO and STO can't be resolved due to the limited spatial resolution.

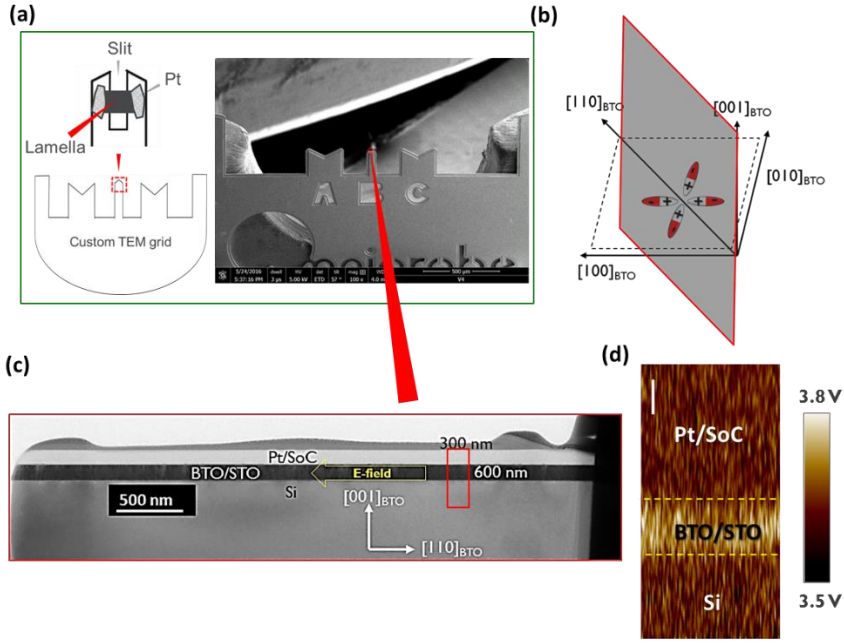


**Figure 6.19:** (a) The custom TEM grid to place the TEM lamella for the in-plane PFM. (b) The schematic illustrating that the TEM specimen is prepared along $[001]_{BTO}$ and $[110]_{BTO}$ by the FIB. The in-plane BTO domains show orientations along $[100]_{BTO}$, $[-100]_{BTO}$, $[010]_{BTO}$ and $[0\text{-}10]_{BTO}$. (c) The TEM lamella for the in-plane PFM (d) The PFM amplitude after the 1-hour poling by -3 V.

Figure 6.20(a) shows the PFM amplitude for the unpoled sample. A minor contrast difference in BTO/STO area against Pt (Platinum)/SoC (Spin-on-Carbon) and Si area can be noticed, suggesting some orderliness of the BTO spontaneous polarization in the layer. This is a counter-intuitive phenomenon for "random" domains in the unpoled sample but this can explain the asymmetry bias-dependent polarization stability observed in Section 6.5.2. However, the origin of this spontaneous orderliness still needs to be further investigated. After the 1 hour poling by -3 V, Figure 6.20(b) presents more PFM amplitude difference within BTO/STO area respectively. This reveals that more BTO domains are aligned

than the unpoled conditions, bringing about more PFM response. In addition, following the 1-hour poling, the local domain switching by +4.5 V for another 1 hour is also performed as indicated by the red rectangular in Figure 6.20(c). From the PFM amplitude in Figure 6.20(c), a shadow contrast within the middle of the stripe can be noticed. Figure 6.20(d) presents the sectional PFM amplitude along the yellow solid line in Figure 6.20(c). The sectional PFM amplitude exhibits the dip of the PFM amplitude, revealing the domain polarization in the location is switched to the other direction. Therefore, from the in-plane PFM analysis, our a-oriented BTO domains are not only polarizable but also switchable, consistent with the hysteresis observations in the EO measurements.

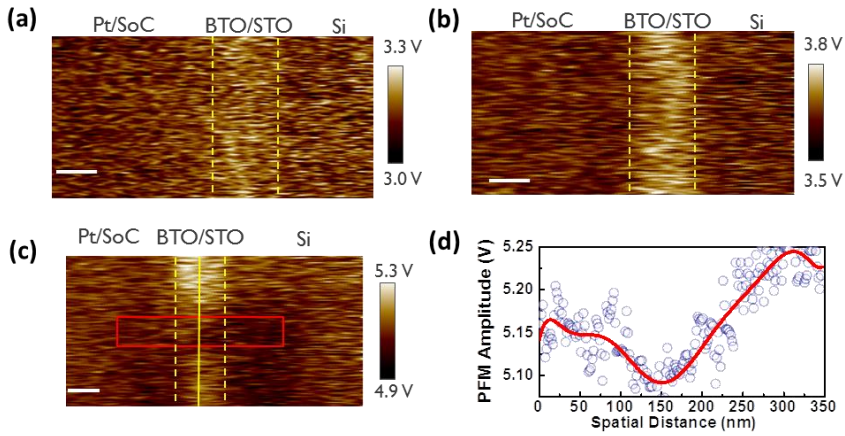


**Figure 6.20:** (a) The PFM amplitude for the un-poled sample. (b) The PFM amplitude for the sample poled by -3V for 1 hour. (c) The PFM amplitude for the sample being reversely poled by + 4.5 V in the red rectangular area. (d) The sectional PFM amplitude along the yellow solid line in (c).

The stability of the polarization over time is also studied. Out-of-plane PFM is performed for the c-oriented 20 nm BTO on the 10-nm-thick STO buffer, which detailed sample information can be found in Section 4.3.2. The in-plane PFM is used for the a-oriented 100 nm BTO on the 10-nm-thick STO as discussed previously in this section. Comparing the polarization stability, the time evolution of the normalized PFM response for both samples is presented in Figure 6.21(a). Before 2800 seconds, the loss rate of the polarization for the c-oriented BTO is better than that for the a-oriented BTO. After, the a-oriented BTO keeps more original polarization than the c-oriented BTO does. The exact reasons for the depolarization still need more investigations. One possible reason is that the charges at the grain and domain boundaries will create the depolarization field. From the ω-2θ scan, the 2θ FWHM of the $(002)_{BTO}$ for the c-oriented BTO is

larger than that for the a-oriented BTO, as displayed in Figure 6.21(b). According to the Scherrer's equation in Equation 4.1, the grain sizes can be evaluated, and their dependency on thickness can also be noticed: ~16 nm domains for the c-oriented 20 nm BTO and ~28 nm domains for the a-oriented 100 nm BTO. In polycrystalline BTO, the grain size is as large as several tens of μm and each grain contains many domains [12]. However, due to a size limitation, the grain below 300 nm can only possess one domain [12, 13]. Therefore, the grain is equivalent to the domain. Then, the larger grain size will lead to the less boundaries of grain and domain in the layer. This may improve the effects of the charge at the grain/domain boundaries to generate the depolarization field [13]. Therefore, to obtain the stable BTO polarization, achieving large-size BTO grain/domain might be favorable for optical modulator applications.

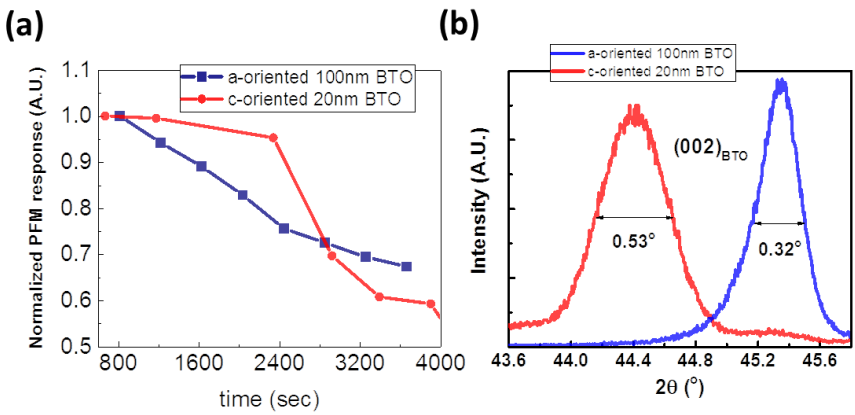


**Figure 6.21:** (a) The comparisons of the polarization stability between a-oriented 100 nm BTO and c-oriented 20 nm BTO. (b) The ω-2θ scan for the a-oriented 100 nm BTO and c-oriented 20 nm BTO.

### 6.5.4. Further Discussions: Percentage of Poled Domain Area

In this section, a quantitative discussion to evaluate how many percentage of domains are poled to obtain 185 pm/V is given. In Section 6.1, two parameters α and β are introduced to fulfill the generalized model for the a-oriented BTO using the in-plane electrode:

$$(1-\alpha)\beta_{[010)]}r_{eff}^{TE/TM}(\phi) + \alpha\beta_{(100)}r_{eff}^{TE/TM}(90^o-\phi) \qquad (6.2)$$

α is the occupation factor, describing how many domains parallel to $[100]_{BTO}$ are occupying the whole BTO layer. $\beta_{[010]}$ and $\beta_{[100]}$ are the order parameters of the

domains along $[010]_{BTO}$ and $[100]_{BTO}$. When the domains are fully aligned to the positive and negative directions, the β are +1 and -1 respectively. When the domains are completely random, β is 0. According to the electrode design around the ring, pads correspond to $\phi$= 0°, 30°, 60°, 90°, 120°, 150° and 180°. Therefore the electric fields along $[100]_{BTO}$ and $[010]_{BTO}$ components can be described as Figure 6.22. Here, we assume the poling mechanism is independent of the poling time and it is only dependent on the electric field strength. The higher strength of the electric field, the more domains can be poled. Therefore, we assume the order parameter (β) is proportional to the electric field. Then, for the domains at $\phi$, its $\beta_{[100]}$ can be written as $\beta\cos(\phi)$ and $\beta_{[010]}$ is $\beta\sin(\phi)$. Closed to the real case of random domains, we consider $\alpha$=0.5, meaning that domains along $[100]_{BTO}$ and $[010]_{BTO}$ are equally distributed. Then, we are using the reported values for the components $r_{51}$=800 pm/V, $r_{13}$=8 pm/V and $r_{33}$=28 pm/V during the calculation. Since several pads are surrounded with ring waveguide, each pad at different $\phi$ contributes the effective Pockels coefficient ($r_{eff}$) differently. Then, in order to have the average $r_{eff}$=185 pm/V, the only unknown parameter β can be solved: β= 99%. Therefore, near 100% of BTO domains are poled contributing 185 pm/V in our hybrid BTO/Si MZR modulator.

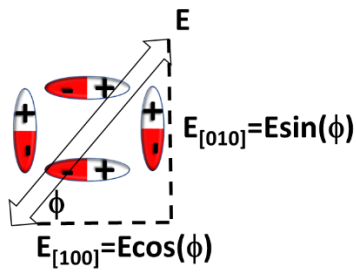


**Figure 6.22:** Relationship between the applied electric field and domains.

### 6.5.5. Further Discussions: Mach-Zehnder Modulator or Ring?

Based on the generalized model, a $r_{eff}$ comparison between the mach-zehnder and ring modulators is also discussed. Here, we assume $\beta_{[100]}$ and $\beta_{[010]}$ are all equal to 1, suggesting that there is no reversal domain in the a-oriented BTO layer. Then, the $r_{eff}$ in function of $\phi$ can be derived according to Equation 6.2, and is presented in Figure 6.23. For the ring modulator with electrodes fully surrounded, the $r_{eff}$ is the average of the $r_{eff}(\phi)$ from $\phi$=0° to $\phi$=90°, and it shows around 325 pm/V. On the other hand, in the mach-zehnder modulator, the $r_{eff}$ can reach 552 pm/V if the electrode is placed at the optimal $\phi$=45°. Therefore, according to the design of the electrode placement around the waveguide determines the value of the $r_{eff}$. Although, seemingly, the mach-zehnder modulator outperforms against

the ring modulator, a design window reveals different possibilities for the hybrid BTO/Si optical modulators. One possible design for this application is the racetrack resonator, which can keep both high Pockels coefficient and ring resonance at the same time.

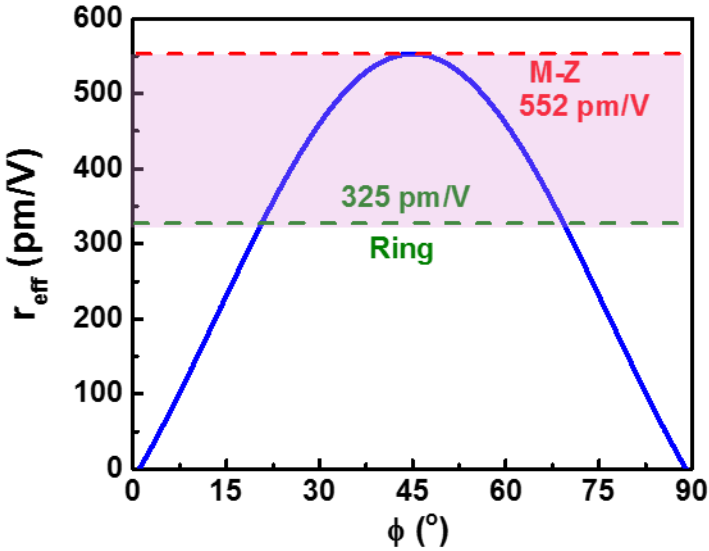


**Figure 6.23:** Evaluated ideal $r_{eff}$ for the ring and mach-zehnder modulators.

## 6.6. Benchmarks of the Performance for the Hybrid BTO/Si Optical Components

Figure 6.24 presents the benchmarks of the propagation loss for different BTO-based TE-mode waveguide [1, 2, 4, 14-16]. All the BTO/Si-related works, BTO on the MgO substrate and the standard Si waveguide are included. The state-of-the-art hybrid BTO/Si waveguide propagation loss is 6 dB/cm [2]. The BTO waveguide propagation loss on the MgO substrate is 4 dB/cm [15]. The standard Si waveguide propagation loss is below 2 dB/cm [16]. Although, the lowest propagation loss for our hybrid BTO/Si waveguide is ~85 dB/cm, the further optimization of the BTO growth on the patterned SOI should much ameliorate the propagation loss.

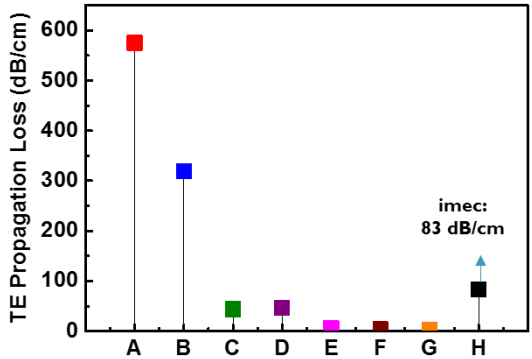


**Figure 6.24:** Benchmarks of the propagation loss for different BTO-based TE-mode waveguides. A: BTO/Si [14]. B: BTO/Si [14]. C: BTO/Si [1]. D: BTO/Si [4]. E: BTO/Si [2]. F: BTO/MgO [15]. G: Si [16]. H: this work.

Besides, Figure 6.25 presents the benchmarks of the $r_{eff}$ and $V_{\pi}L$ which are derived in different hybrid Si-based materials and their optical modulators [1, 4, 17-21]. In addition to the hybrid BTO/Si works [1, 4, 17, 18], $LiNbO_3$/Si [11], $Si_3N_4$/Si [19], organic polymer/Si [20] and PZT/Si [21] are also included in the comparisons. From the benchmarks, our hybrid BTO/Si shows competitive $r_{eff}$~185 pm/V and $V_{\pi}L$~1.6 V/cm against other key results.

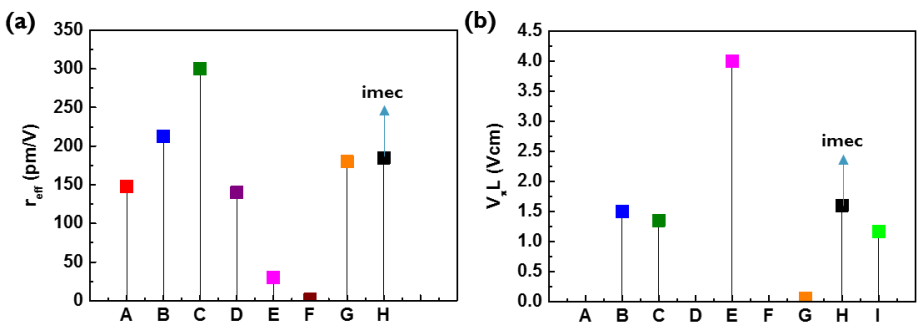


**Figure 6.25:** Benchmarks of the (a) $r_{eff}$ and (b) $V_{\pi}L$, which are derived in different hybrid Si-based materials and their optical modulators. A: BTO/Si from [17]. B: BTO/Si [1]. C: BTO/Si [4]. D: BTO/Si [18]. E: $LiNbO_3$/Si [11]. F: $Si_3N_4$/Si [19]. G: Organic polymer/Si [20]. H: this work. I:PZT/Si [21]

## 6.7. Conclusions

In summary, from the quantitative discussions about different hybrid BTO/Si modulator configurations, the optimal modulator scheme to obtain the large $r_{eff}$ is to use the a-oriented BTO with the TE-polarized light and in-plane electrodes. Due to the temperature non-uniformity, the material and device quality of the BTO on patterned SOI is not as good as those on the blanket substrate. Despite the fact, the post-growth oxygen annealing at 800ºC for 4 hours can improve the FWHM of $(002)_{BTO}$ $\Delta\omega$ to 1.2º and the propagation loss of the 600-nm-wide waveguide down to 83 dB/cm. Besides, a series of the bias-sweeping experiments in hybrid BTO/Si MZR modulators is designed to address the main cause leading to the EO hysteresis behavior. The microscopic and macroscopic views of the EO response to the BTO domains are discussed and we find that the hysteresis behavior is led by the polarization switching during the device operation. In order to avoid the hysteresis, having the stable BTO polarization is important. Therefore, we learn from the 2 different bias-sweeping modes to use -10 V for 30 minute and 300 minutes in Step A and Step B respectively to acquire the stable BTO polarization. Thanks to the robust BTO polarization stability, we demonstrate the linear EO behavior showing the competitive $V_{\pi}L$ of 1.6 Vcm and $r_{eff}$ around 185 pm/V, 6 times as large as the $r_{eff}$ in the $LiNbO_3$. In addition, from the generalized model taking multiple BTO domains and randomness into account, we find that nearly 100% of BTO domains are poled contributing the measured $r_{eff}$ of 185 pm/V. Moreover, the generalized model also points out that, compared with the ring modulators in the ideal situation, mach-zehnder modulators can perform larger $r_{eff}$ when the $\phi$ is set to the optimal angle. However, there is a wide engineering window to design the device according to the wanted characteristics in the device for different applications. Finally, the in-plane PFM for the TEM lamella also presents the direct observations of the domain poling, switching and polarization stability in the a-oriented BTO, consistent with the phenomena in optical modulators.

# References

[1] C. Xiong, W. H. Pernice, J. H. Ngai, J. W. Reiner, D. Kumah, F. J. Walker, C. H. Ahn, and H. X. Tang, "Active silicon integrated nanophotonics: ferroelectric BaTiO(3) devices," Nano Lett 14, 1419-1425 (2014).

[2] F. Eltes et al., "Low-Loss BaTiO3–Si Waveguides for Nonlinear Integrated Photonics," ACS Photonics, vol. 3, no. 9, pp. 1698-1703, 2016.

[3] M.-H. M. Hsu et al., "Diffraction studies for stoichiometry effects in BaTiO3 grown by molecular beam epitaxy on Ge(001)," Journal of Applied Physics, vol. 120, no. 22, p. 225114, 2016.

[4] S. Abel, T. Stoferle, C. Marchiori, D. Caimi, L. Czornomaz, M. Stuckelberger, M. Sousa, B. J. Offrein, and J. Fompeyrine, "A Hybrid Barium Titanate–Silicon Photonics Platform for Ultraefficient Electro-Optic Tuning," Journal of Lightwave Technology 34, 1688-1693 (2016).

[5] B. W. Wessels, "Ferroelectric Epitaxial Thin Films for Integrated Optics," Annual Review of Materials Research 37, 659-679 (2007).

[6] A. Rao et al., "High-performance and linear thin-film lithium niobate Mach-Zehnder modulators on silicon up to 50 GHz," Opt Lett, vol. 41, no. 24, pp. 5700-5703, Dec 15 2016.

[7] P. Tang, D. J. Towner, T. Hamano, A. L. Meier, and B. W. Wessels, "Electrooptic modulation up to 40 GHz in a barium titanate thin film waveguide modulator," Optics Express, vol. 12, no. 24, pp. 5962-5967, 2004/11/29 2004.

[8] E. A. Little, "Dynamic Behavior of Domain Walls in Barium Titanate," Physical Review, vol. 98, no. 4, pp. 978-984, 1955.

[9] S. Kazaoui, J. Ravez, C. Elissalde, and M. Maglione, "High frequency dielectric relaxation in BaTio3derived materials," Ferroelectrics, vol. 135, no. 1, pp. 85-99, 1992.

[10] F. Lucchi et al., "Very low voltage single drive domain inverted LiNbO3 integrated electro-optic modulator," Optics Express, vol. 15, no. 17, pp. 10739-10743, 2007/08/20 2007.

[11] P. Rabiei, J. Ma, S. Khan, J. Chiles, and S. Fathpour, "Heterogeneous lithium niobate photonics on silicon substrates," Opt Express 21, 25573-25581 (2013).

[12] H. Takuya, T. Kayo, L. Jianyong, K. Takeshi, K. Hirofumi, and T. Takaaki, "Domain Size Effect on Dielectric Properties of Barium Titanate Ceramics," Japanese Journal of Applied Physics, vol. 47, no. 9S, p. 7607, 2008.

[13] Z. Zhao et al., "Grain-size effects on the ferroelectric behavior of dense nanocrystalline BaTiO3 ceramics," Physical Review B, vol. 70, no. 2, p. 024107, 07/30/ 2004.

[14] S. Abel, "*Electro-optic photonic devices based on epitaxial barium titanate thin films on silicon.*" Ph.D. thesis, Université de Grenoble, 2014.

[15] D. M. Gill, B. A. Block, C. W. Conrad, B. W. Wessels, and S. T. Ho, "Thin film channel waveguides fabricated in metalorganic chemical vapor deposition grown BaTiO3 on MgO," Applied Physics Letters, vol. 69, no. 20, pp. 2968-2970, 1996.

[16] W. Bogaerts and S. K. Selvaraja, "Compact Single-Mode Silicon Hybrid Rib/Strip Waveguide With Adiabatic Bends," IEEE Photonics Journal, vol. 3, no. 3, pp. 422-432, 2011.

[17] S. Abel et al., "A strong electro-optically active lead-free ferroelectric integrated on silicon," Nat Commun, vol. 4, p. 1671, 2013.

[18] K. J. Kormondy et al., "Microstructure and ferroelectricity of BaTiO3 thin films on Si for integrated photonics," Nanotechnology, vol. 28, no. 7, p. 075706, 2017.

[19] R. S. Jacobsen, K. N. Andersen, P. I. Borel, J. Fage-Pedersen, L. H. Frandsen, O. Hansen, M. Kristensen, A. V. Lavrinenko, G. Moulin, H. Ou, C. Peucheret, B. Zsigri, and A. Bjarklev, "Strained silicon as a new electro-optic material," Nature 441, 199-202 (2006).

[20] R. Palmer et al., "High-speed silicon-organic hybrid (SOH) modulator with 1.6 fJ/bit and 180 pm/V in-device nonlinearity," in 39th European Conference and Exhibition on Optical Communication (ECOC 2013), 2013, pp. 1-3.

[21] J. P. George, "*Integration of Ferroelectric Thin Films on Silicon for Electro-Optic Devices.*" PhD thesis, University Gent, 2016.

# 7

# Conclusions and Perspectives

## 7.1. Conclusions

The goal of this research was to achieve a high-speed and power-efficient hybrid BTO/Si optical modulator. Although a prototype of such a device was demonstrated by Yale University in 2014 and IBM has improved its performance continually since then, several challenges ranging from material growth to understanding the detailed device characteristics still needed to be further understood and solved.

Because BTO is a ternary compound, control of its stoichiometry is the main difficulty during the thin film growth. In the beginning of this thesis, a Ge substrate, exhibiting quasi-zero lattice mismatch with respect to BTO, was used to simplify the problem. We used RBS (Rutherford Backscattering) to measure the exact [Ba]/[Ti] ratio in BTO-films and then developed diffraction models to understand the effect of the precise stoichiometry on the diffraction patterns observed in RHEED, XRD and TEM experiments. In the RHEED patterns, both extra [Ba] and [Ti] in the non-stoichiometric BTO creates twinning planes and roughens the surface, resulting in spotty patterns. In addition, excess [Ti] changes the BTO diffraction behavior, resulting in the disappearance of the ±1st-ordered RHEED lines along the $[100]_{BTO}$ and $[110]_{BTO}$ directions. In both XRD and SAED of the TEM, the 3 lowest-ordered Bragg peak relative intensity ratios $I_{(001)}/I_{(002)}$, $I_{(101)}/I_{(002)}$ and $I_{(111)}/I_{(002)}$ depend on the [Ba] and [Ti] compositions. Extra Ti decreases all three ratios. In the sample with [Ba]/[Ti]~0.1, all the lowest-ordered Bragg peaks even disappeared. For the opposite stoichiometry condition, extra Ba does not increase all three ratios. To understand these observations, we proposed a model that explains how excess [Ba] or [Ti] in non-stoichiometric BTO layers induces a different diffraction behavior compared to that of the stoichiometric

layer. These learnings assist us in optimizing the layer composition relying on different characterization tools relying on diffraction.

As soon as stoichiometric BTO was obtained, we could focus on how the process conditions impact the quality of epitaxial BTO grown on a STO-buffered Si substrate. We find that a growth temperature of 630 ºC and an oxygen plasma power of 600 Watt results in an optimized c-oriented BTO. From the TEM and XRD analysis, multiple domains are observable in the BTO layer. Then, different types of scanning probe microscopy were performed on the as-deposited BTO layer including AFM, CAFM and (out-of-plane) PFM. The surface roughness measured by the AFM is around 0.2 nm. CAFM showed that up to a forward bias of +6 V the current remains low, indicating the structure shows a diode-like rectifying behavior. However, for a reverse bias the current increased immediately due to the fact that the carriers tunnel through the thin amorphous silicate at the interface between the STO and Si. This one-way rectifying behavior makes that the BTO domains can be poled by a forward bias but not by a reverse bias. After oxygen annealing at 600 ºC for 30 minutes, CAFM showed that both bias directions now present a low leakage current. Since the amorphous silicate is thickened after annealing, large conduction and valence band offsets are formed, blocking the current for both bias directions. This allows an electric field to be built up in both directions, enabling the BTO domains to be poled and switched. In addition, we observed that the polarization stability for the oxygen-annealed sample outperformed that of the as-deposited sample.

Following optimization of the process conditions for the growth of the BTO layer, a study of how to control the BTO orientation on the STO-buffered Si(001) substrate was carried out. The BTO orientation is determined by the trade-off between compressive and tensile strain. For BTO/5-nm-thick STO/Si(001) heterostructures, the strain in a thin BTO-layer is dominated by the compressive strain from the lattice mismatch between BTO and STO. For that reason, thin BTO layers tend to show more c-oriented domains. Differently, the strain in a thick BTO layer is determined by the tensile strain resulting from the different thermal expansion coefficients between BTO and Si. Thus, thick BTO layers present more a-oriented domains. Besides, when using a thick STO buffer, c-oriented BTO tends to be obtained, because the impact from the Si thermal expansion on the BTO orientation is reduced and the compressive strain dominates. Therefore, we are able to control the BTO orientation by engineering the thickness of the BTO layer and STO buffer. Then, we exploited ellipsometry to compare the EO effect in 100-nm-thick c-oriented and a-oriented BTO grown on Si(001) substrates using a 40 nm and 10 nm STO buffer respectively. Using a top-down electrode configuration, the a-oriented BTO layer is found to exhibit a larger index difference $\delta n_{BTO}$ compared to c-oriented BTO when applying 1 V. Since the optical axis of the a-oriented BTO is orthogonal to the electric field, this

configuration allows to use the strong $r_{51}$ component in the Pockels tensor. The c-oriented BTO sample on the other hand, with its optical axis parallel to the electric field shows a weaker EO response because it relies on the smaller $r_{13}$ and $r_{33}$ components.

Furthermore, the use of c-oriented and a-oriented BTO for optical modulators using various electrode configurations with TE- and TM-polarized light were discussed. Since $r_{51}$, $r_{31}$ and $r_{33}$ are all used, a-oriented BTO using in-plane electrodes for TE modulation was found to be the optimal scheme. Different from earlier reported waveguide structures, in this work, we have grown 170 nm BTO directly on patterned SOI substrates with c-Si waveguides. However, since the patterns on the substrate result in a temperature non-uniformity, the BTO crystallinity is reduced showing a $\Delta\omega$ of $(002)_{BTO}$ ~1.9°. Besides, no light can be transmitted through the BTO waveguide. Through oxygen annealing at 800 °C for 4 hours, the propagation loss of the 600-nm-wide waveguide could be reduced down to 85 dB/cm. Afterwards, hybrid BTO/Si MZR modulators were studied. In earlier reported work, hybrid BTO/Si optical modulators generally showed a hysteresis phenomenon, which is unfavorable for the optical modulator applications. By adding the steps for domain poling in prior to a DC sweeping measurement, we can acquire the stable polarization. Afterwards, when executing a DC measurement, the hysteresis is avoided and a linear EO effect is obtained, showing an average $r_{eff}$ around 185 pm/V (c.f. 30 pm/V in LN). The corresponding $V_{\pi}L$ is evaluated to be ~1.6 Vcm. We also generalized the model from Castera et al by introducing the domain randomness in a-oriented BTO. Based on this generalized model, we found that $r_{eff}$ = 185 pm/V is equivalent to ~100% of the in-plane domains being poled. In addition, the domain poling and switching observed in in-plane PFM on a TEM lamella, are consistent with the results seen in the EO measurement. We also found a correlation between BTO domain size and polarization stability. Summarizing, although the propagation loss in our hybrid BTO/Si waveguides is 85 dB/cm, one order higher than the state-of-the-art result 6 dB/cm, $r_{eff}$ and $V_{\pi}L$ from our results are competitive with other key works.

## 7.2. Perspectives

In optimizing the hybrid BTO/Si optical modulators, there are still many interesting parts to be explored:

### 7.2.1. BTO Thin Film Preparation

The behavior and ultimate performance of hybrid BTO/Si optical modulators is highly dependent on the domain orientation, polarization strength and polarization stability of the BTO layer. We demonstrated that thickness engineering of the BTO layer and STO buffer allows to control the trade-off between the compressive strain from the BTO/STO lattice mismatch and the tensile strain from the BTO/Si thermal expansion difference. We also observed that there is a correlation between the domain size and the polarization stability observed in PFM. The key to further optimizing hybrid BTO/Si optical modulators will be finding ways to manipulate the strain in the BTO thin film and achieving BTO domain sizes larger than the few tens of nanometers that we have currently. For c-oriented BTO, a stable and consistent compressive strain exerted on the BTO can be used to further improve the material properties for the modulator applications. One possible approach is to prepare a superlattice of BTO and STO layers on Si(001). [1]. From the reported work, the BTO/STO superlattice has a $r_{eff}$ of 73 pm/V which is larger than 23 pm/V observed in the BTO layer without the superlattice structure. For obtaining a-oriented BTO, tensile strain along the same direction is favorable. In order to obtain this, using a mis-cut substrate might be a possible approach. Although there are only a few works discussing the BTO growth on a vicinal substrate, other perovskite oxides show promising results. For instance, $BiFeO_3$ grown on a mis-cut STO substrate, showed a purely single domain in the thin film [2].

### 7.2.2. Modulator Device Design and Integration Process

In this thesis, we gave a summary of the different possible device configurations for c-oriented and a-oriented BTO and their expected performance. However, these discussions were only based on the strength of $r_{eff}$ without considering the electric field arising from an applied bias voltage. To design optimal hybrid BTO/Si optical modulators, using TCAD simulation software to evaluate the different cases from the summary is necessary. Besides, the current device demonstrations, including our own work, are all based on blanket BTO and STO layers because patterning these layers is not straightforward. From our preliminary etching tests using diluted $HF:H_2O_2$, we believe BTO and STO can be etched. However, more work is needed to tune the recipe and control the

etching rate. If high quality patterning of the BTO and STO layers can be achieved, novel designs for the hybrid BTO/Si optical devices can be imagined. Very recently, Messner et al [3] have successfully demonstrated monolithic ferroelectric plasmonic optical modulators with 72 Gb/s using dry-etching to pattern the BTO layer.

# References

[1] J. Hiltunen et al., "BaTiO3–SrTiO3 multilayer thin film electro-optic waveguide modulator," Applied Physics Letters, vol. 89, no. 24, p. 242904, 2006.

[2] Y. H. Chu et al., "Domain Control in Multiferroic BiFeO3 through Substrate Vicinality," Advanced Materials, vol. 19, no. 18, pp. 2662-2666, 2007.

[3] A. Messner et al., "Integrated Ferroelectric Plasmonic Optical Modulator," in Optical Fiber Communication Conference Postdeadline Papers, Los Angeles, California, 2017, p. Th5C.7: Optical Society of America.

.

# A

# EO Response in Single-Domain BTO/Si Hybrid Waveguides

## A.1. EO Effect in BTO

Since BTO is an uniaxially anisotropic material, it exhibits ordinary ($n_o$) and extraordinary indices ($n_e$) with respect to the crystal axes. The BTO crystal orientation determines the optical axis (OA). Defining the Z axis along the OA, the index ellipsoid, shown in Figure A.1, without applied E-field can be described as:

$$(\frac{1}{n_o^2})x^2 + (\frac{1}{n_o^2})y^2 + (\frac{1}{n_e^2})z^2 = 1 \tag{A.1}$$

When an electric field is applied, the index ellipsoid will be deformed and can be described as:

$$(\frac{1}{n_o^2} + r_{13}E_z)x^2 + (\frac{1}{n_o^2} + r_{13}E_z)y^2 + (\frac{1}{n_e^2} + r_{33}E_z)z^2 + 2r_{51}E_x\text{xz} + 2r_{51}E_y\text{yz} = 1 \tag{A.2}$$

with the Pockels tensor for p4mm crystal symmetry

$$r_{ij} = \begin{bmatrix} 0 & 0 & r_{13} \\ 0 & 0 & r_{23} \\ 0 & 0 & r_{33} \\ 0 & r_{42} & 0 \\ r_{51} & 0 & 0 \\ 0 & 0 & 0 \end{bmatrix} \tag{A.3}$$

in which components for bulk BTO crystals are reported as $r_{42}$=$r_{51}$=800 pm/V and $r_{23}$=$r_{13}$=8 pm/V and $r_{33}$=28 pm/V [1]. The EO response in various Si-integrated

waveguides in combination with different BTO domain orientations and different electrode configurations will be analyzed in the following sections.

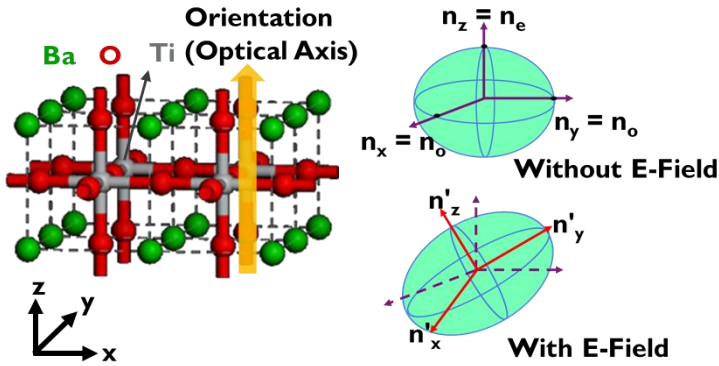


**Figure A.1:** Lattice structure for c-oriented BTO and its index ellipsoid without and with applied electric field.

## A.2. c-Oriented BTO/Si Hybrid Waveguides Using Vertical Electrodes

Figure A.2 shows a Si waveguide integrated with c-Oriented BTO and vertical electrodes. For convenience, and without loss of generality, the y axis is designated as the direction of the waveguide. Given the vertical electrode configuration, the external electric field is applied along the z-axis (i.e. parallel to the OA) and hence only the component $E_z$ is non zero. The index ellipsoid described in Equation A.2 then becomes:

$$(\frac{1}{n_o^2} + r_{13}E_z)x^2 + (\frac{1}{n_o^2} + r_{13}E_z)y^2 + (\frac{1}{n_e^2} + r_{33}E_z)z^2 = 1 \qquad \text{(A.4)}$$

where the indices along x, y and z components ($n_x$, $n_y$ and $n_z$) are all dependent on the external electric field. The $n_x$ can be calculated from

$$\frac{1}{n_x^2} = \frac{1}{n_o^2} + r_{13}E_z \qquad \text{(A.5)}$$

Then, assuming $r_{13}E_z << n_o^{-2}$ and using the differential relation

$$\mathrm{dn} = -\frac{1}{2}n^3 d(\frac{1}{n^2}) \qquad \text{(A.6)}$$

gives

$$n_x = n_o - \frac{1}{2} n_o^3 r_{13} E_z \quad \text{(A.7)}$$

Similarly,

$$n_y = n_o - \frac{1}{2} n_o^3 r_{13} E_z \quad \text{(A.8)}$$

$$n_z = n_e - \frac{1}{2} n_e^3 r_{33} E_z \quad \text{(A.9)}$$

can be obtained.

For **TE-polarized** light, having its electric field along x, the index $n_x$ (with $n_x = n_o$ without applied field), is modulated by the effective Pockels coefficient $r_{eff}$ equal to $r_{13}$, according to the relation:

$$\Delta n_x = -\frac{1}{2} n_x^3 r_{eff} E \quad \text{(A.10)}$$

For **TM-polarized** light, the indices along z component ($n_z$) and y component ($n_y$)[a] are modulated by the effective Pockels coefficient $r_{eff} = r_{33}$ and $r_{eff} = r_{13}$, respectively.

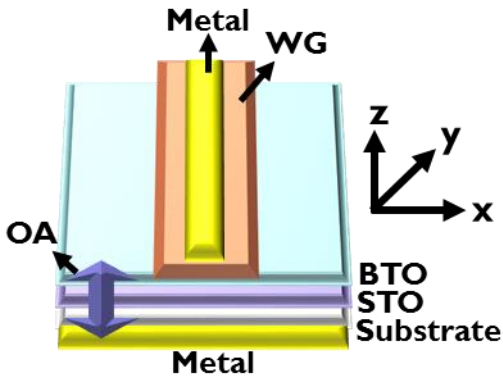


**Figure A.2:** The schematic of the Si-integrated waveguide using the c-oriented BTO and vertical electrode configuration.

## A.3. c-Oriented BTO/Si Hybrid Waveguides Using In-Plane Electrodes

Figure A.3 presents a schematic for c-oriented BTO/Si hybrid waveguides using in-plane electrodes. The electrodes are aligned along the waveguide, applying the electric field only along the x axis. Therefore, the index ellipsoid in Equation A.2 can be described as

[a]In slab, it is antisymmetric so averages to zero. However, in our structure, this is no longer true and the $E_y$ component has to be taken into account. Full mode calculations are needed however to determine the detailed contribution of this component.

$$(\frac{1}{n_o^2})x^2 + (\frac{1}{n_o^2})y^2 + (\frac{1}{n_e^2})z^2 + 2r_{51}E_x\text{xz} = 1 \qquad \text{(A.11)}$$

Opposite to the case in Equation A.4, all the indices along x, y and z are independent of the applied electric field $E_x$. Therefore, there is no modulation neither in TE nor in TM mode.

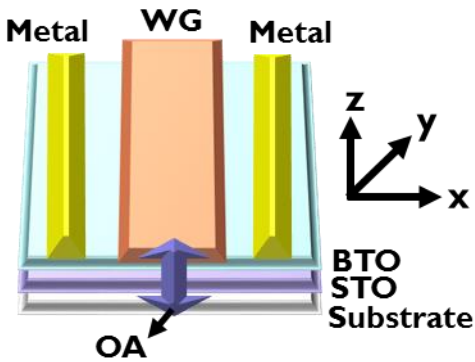


**Figure A.3:** The schematic of the Si-integrated waveguide using the c-oriented BTO and in-plane electrode configuration.

## A.4. a-Oriented BTO/Si Hybrid Waveguides Using Vertical Electrodes

In this section, the EO response in a Si waveguide integrated with a-oriented BTO and vertical electrodes will be discussed. Figure A.4 describes the device and defines the coordinate system. The x axis now points out of the waveguide plane, parallel to the external applied electric field. The OA in the a-oriented BTO lies in the waveguide plane and is set as the z-axis. The index ellipsoid defined by Equation A.2 takes on exactly the same form as Equation A.11. Since the $n_x$, $n_y$ and $n_z$ terms are independent of the electric field, no modulation is observable neither in TE nor in TM mode.

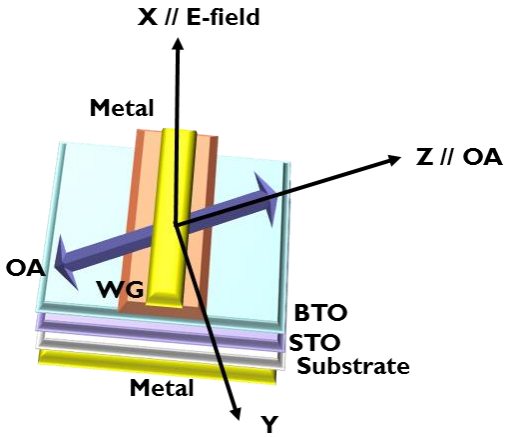


**Figure A.4:** The schematic of the Si-integrated waveguide using the a-oriented BTO and vertical electrode configuration.

## A.5. a-Oriented BTO/Si Hybrid Waveguides Using In-Plane Electrodes

Figure A.5(a) shows the schematic of an a-oriented BTO/Si hybrid waveguides using in-plane electrodes. The electrodes are supposed to be parallel to the waveguide direction. The angle between the electric field and the OA is defined as ϕ. Then, in Figure A.5(b), the x-y-z coordinate system is defined in the same way as in Figure A.4. To investigate the EO response in this device, it is more convenient to define a new coordinate system along the direction of the applied electric field and light propagation direction, denoted y' and z', respectively. Therefore, the index ellipsoid based on the x-y'-z' coordinate can be transformed by inserting:

$$y = \mathrm{y}' \cos\varphi - z' \sin\varphi \tag{A.12}$$

$$z = \mathrm{y}' \sin\varphi + z' \cos\varphi \tag{A.13}$$

and inserting $E_x$=0, $E_y$=$E_z$'sinϕ and $E_z$=Ez'cosϕ into Equation A.2. The new form of the index ellipsoid becomes:

$$\left(\frac{1}{n_x^2} + r_x E_{z'}\right) x^2 + \left(\frac{1}{n_{y'}^2} + r_{y'} E_{z'}\right) y'^2 + \left(\frac{1}{n_{z'}^2} + r_{z'} E_{z'}\right) z'^2 + \boldsymbol{C} y' z' = 1 \tag{A.14}$$

where

$$\boldsymbol{C} = \left\{\left(\frac{2cos\phi sin\phi}{n_e^2} - \frac{2cos\phi sin\phi}{n_o^2}\right) + 2E_{Z'}[cos^2\phi sin\phi(r_{33} - r_{13}) + sin\phi(cos^2\phi - sin^2\phi)r_{51}]\right\} \quad (A.15)$$

For **TE-polarized** light, the index along the z' component ($n_{z'}$) is

$$n_{z'} = \frac{n_o n_e}{\sqrt{n_o^2 cos^2\phi + n_e^2 sin^2\phi}} \quad (A.16)$$

, which is modulated by

$$r_{Z'} = [(r_{33}cos^3\phi) + (r_{13} - 2r_{51})sin^2\phi cos\phi] \quad (A.17)$$

For **TM-polarized** light, the index along the x component ($n_x$) is

$$n_x = n_o \quad (A.18)$$

, which is modulated by

$$r_x = r_{13}cos\phi \quad (A.19)$$

The index along y' component ($n_{y'}$) is

$$n_{y'} = \frac{n_o n_e}{\sqrt{n_e^2 cos^2\phi + n_o^2 sin^2\phi}} \quad (A.20)$$

, which is modulated by

$$r_{y'} = [(r_{13}cos^3\phi) + (r_{33} + 2r_{51})sin^2\phi cos\phi] \quad (A.21)$$

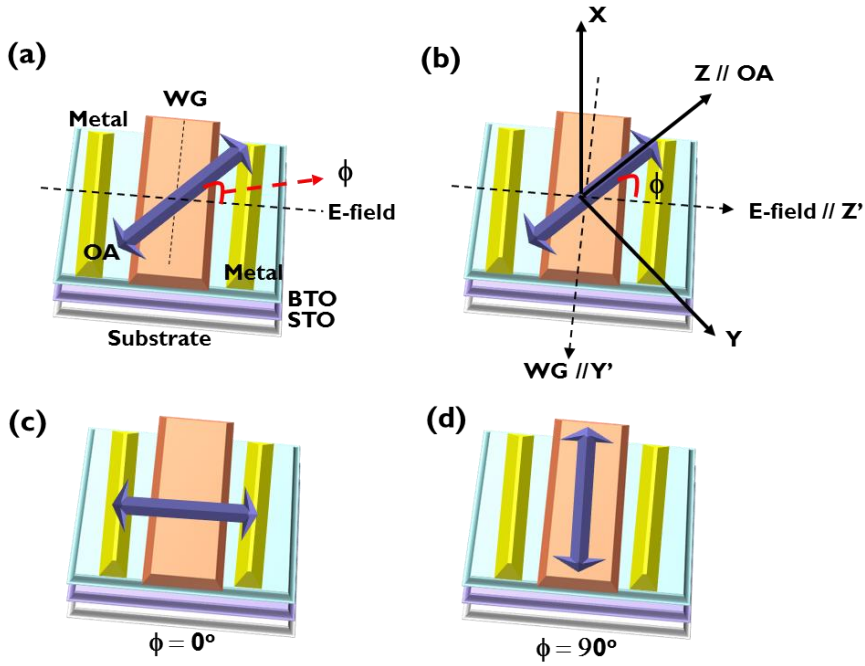


**Figure A.5:** (a) The schematic of the Si-integrated waveguide using the a-oriented BTO and in-plane electrode configuration. (b) The definitions for the x-y-z- and x-y'-z' coordinates. The device when (c) $\phi=0^o$ and (d) $\phi=90^o$

In Figure A.5(c), the special configuration with $\phi=0^o$ is shown. In this case $r_{13}$ and $r_{33}$ modulate the indices along the x and y' directions respectively, for TM-polarized modulation. The index along z' for TE-polarized light is modulated by $r_{33}$. The condition $\phi=90^o$ as plotted in Figure A.5(d) shows no modulation for any polarizations.

# References

[1] P. Castera, D. Tulli, A. M. Gutierrez, and P. Sanchis, "Influence of BaTiO3 ferroelectric orientation for electro-optic modulation on silicon," Opt Express, vol. 23, no. 12, pp. 15332-42, Jun 15 2015.

.